Interferometric GNSS-R processing: modeling and analysis of advanced processing concepts for altimetry

Francisco Martín Alemany

Departament de Teoria del Senyal i Comunicacions

Universitat Politècnica de Catalunya

PhD. Thesis Advisor:

Prof. Adriano Camps Carmona

Barcelona 2015

UNIVERSITAT POLITÈCNICA DE CATALUNYA
BARCELONATECH
Escola de Doctorat

Acta de qualificació de tesi doctoral

Curs acadèmic:

Nom i cognoms

Programa de doctorat

Unitat estructural responsable del programa

Resolució del Tribunal

Reunit el Tribunal designat a l'efecte, el doctorand / la doctoranda exposa el tema de la seva tesi doctoral titulada

_____

_____.

Acabada la lectura i després de donar resposta a les qüestions formulades pels membres titulars del tribunal, aquest atorga la qualificació:

☐ NO APTE ☐ APROVAT ☐ NOTABLE ☐ EXCEL·LENT

(Nom, cognoms i signatura) President/a	(Nom, cognoms i signatura) Secretari/ària	
(Nom, cognoms i signatura) Vocal	(Nom, cognoms i signatura) Vocal	(Nom, cognoms i signatura) Vocal

_____, _____ d'/de _____ de _____

El resultat de l'escrutini dels vots emesos pels membres titulars del tribunal, efectuat per l'Escola de Doctorat, a instància de la Comissió de Doctorat de la UPC, atorga la MENCIÓ CUM LAUDE:

☐ SÍ ☐ NO

(Nom, cognoms i signatura) President de la Comissió Permanent de l'Escola de Doctorat	(Nom, cognoms i signatura) Secretari de la Comissió Permanent de l'Escola de Doctorat

Barcelona, _____ d'/de _____ de _____

Acknowledgements

This Ph.D. Thesis is the result of the support and effort done by several people. My sincere acknowledgement to all of them:

First of all to my advisor, Prof. Adriano Camps, for his keen guidance, dedication, support (above all in the hard moments), and for offering the opportunity to work with him. In addition, I want to express my gratitude to my ESA supervisors, Salvatore D'Addio, and Manuel Martin-Neira, for their support done during my two stages at ESTEC, and for doing that both stages were an awesome experience.

I want to acknowledge the collaboration of the people from the Earth Observation group at ICE- CSIC/IEEC, in particular to Antonio Rius (head of the group), and Fran Fabra. Specially for allowing me to use their data from their experimental campaigns (second Baltic flight, and TIGRIS), and for their advises during the different meetings that we had during the data processing, which have been always enriching. In this sense I want also to acknowledge the contribution from Weiqiang Li, from the School of Electronic and Information Engineering (SEI), in BeiHang, China.

To Valery Zavorotny, Maria Paola Clarizia and Juan Fernando Marchan, for their participation as external reviewers, and above all, for their constructive observations, comments and suggestions done, which have been very useful in order to improve the current contents of this Ph.D. Thesis.

I want also to acknowledge Jordi Corbera, who was my supervisor during two years at ICC, and who was one of the persons that did possible that I started the PhD (among with Adriano).

To Francesco Sarti, for bringing me the opportunity to do my Master Thesis at ESRIN, who encourage me to pursue a PhD, and who has still suporting me after my stage in ESRIN. In addition, I want to acknowledge to Andrea dela Vechia, Andrea Minchella, and Domenico Solimini, who among with Francesco Sarti, guided my work during my stage in ESRIN.

To Pablo Soto Pacheco, who was my Bachelor final work advisor, and who placed the first foundation stone.

To my colleagues at UPC (Alberto, Ali, Dani, Domenico, Giuseppe, Hyuk, Jorge, Raul, and Roger), with whom I have shared nice work discussions, and my time at UPC, as well to my colleagues at ESTEC.

To finish to my family, specially to my father, who always was a big support, and a reference for me.

Abstract

This PhD dissertation is focused on the use of the oportunity signals from the Global Navigation Satellite Systems (GNSS) that scatter-off the Earth's surface for perform ocean mesoscale altimetry (the so-called GNSS-R technique). Specially, this work analyses the capablities of the interferometric approach (iGNSS-R) originally proposed for PARIS IoD (which will be implemented on GEROS-ISS), comparing its performance with the one obtained by the conventional approach (cGNSS-R). The main content of this PhD dissertation, includes:

A comprehensive analysis of the GNSS-R cross-correlation waveform properties, analyising the impact that the observation geometry and system parameters have on the GNSS-R observables, where parameters such as the receiver bandwidth, observation geometry, sea-state, and thermal and speckle noises are analysed.

A detailed derivation of the statistics for both the voltage and power cross-correlations (for both conventional and interferometric processing cases), validated all of them with both simulated and real data from ground-based, airborne, and spaceborne experiments.

Study of the performance model of the altimetry precision based on the Cramer-Rao Bound statistical estimator theory. This study has been carried out for a wide variety of parameters concerning the overall observation system, including instrument, on-board and on-ground processing aspects, for both the conventional and interferometric GNSS-R techniques.

Analysis of experimental data from the Typhoon Investigation using GNSS-R Interferometric Signals (TIGRIS) experiment. This analysis has been used to determine and stablish the boundaries and capabilities of GNSS-R towards remote sensing of typhoons. In this part, aspects such as the mitigation of the direct cross-talk contamination, GNSS multipath contamination, and preliminary results (including a novel observable) are presented.

The main results obtained during this dissertation, will be useful in order to assess the performance of future European GNSS-R space mission, such as the GEROS-ISS interferometric altimeter.

This PhD dissertation has been performed in the framework of the ESA NPI program, Ref. 155-2010, and by grants ref. AYA2011-29183-C02-01 AROSA-Advanced Radio Ocultations and Scatterometry Applications using GNSS and other opportunity signals, AYA 2010-22062-C05-02 MIDAS-6: SMOS ocean and salinity products. Improvements and applications demonstration, and AYA 2012-39356-C05-01 MIDAS-7: Advance products and applications for SMOS and future missions of the Spanish Ministry of Economy and Competitiveness.

Contents

List of Figures

Chapter 1

Introduction

In this Chapter a brief introduction to this PhD thesis is presented. Section 1.1 presents the motivation of this work. In Section 1.2 a summary of the GNSS rEflectometry Radio Occultation and Scatterometry onboard International Space Station (GEROS-ISS) mission is provided (focussing in the framework of the PARIS concept), showing the systems constraints, system concept, instrument architecture, and instrument design. Ending with Section 1.3 that enumerates the goals of this PhD thesis.

1.1 Motivation

Traditionally, mesoscale ocean altimetry was performed by nadir-looking radar altimeters. The first Ku-band pulse-limited spaceborne radar altimeter (S-193 Radscat) dates from the 1960's. In 1973, the S-193 was flown on board the Skylab. The next radar altimeters were flown on board GEOS-C (1975), and on board SeaSAT-A (1978) [1].

After these succesful missions, GEOSAT in 1985, TOPEX/Poseidon in 1992 (which was the precursor of the Poseidon series hosted on Jason), GFO in 1998, ERS-1 in 1991, ERS-2 in 1995, ENVISAT in 2002 (which includes the RA-2, a dual-frequency Ku and S band altimeter), and Jason complete the list of satellites that target ocean altimetry applications.

One of the major drawbacks associated with these first radar altimeters, was related to the spatial and temporal sampling of the ocean. In fact, in [2] it has been demonstrated that, in order to monitor the mesoscale variability at high space and temporal resolutions at least two altimetry missions would be required, since with a single altimetry mission is not possible to resolve the main space and time scales of the ocean circulations. Hence, the ocean currents derived from a single nadir altimeter

is a limited representation of the actual surface flow, limiting the application to the study of very large scale ocean currents, due to the large distance between successive tracks.

This minimum requirement has been met in 1992 with the NASA/CNES TOPEX/ Poseidon (T/P), ESA ERS-1, ERS-2, Jason-1, and ENVISAT [3]. Thus, the 5 complementary sampling of two or more altimeter missions allows to achieve the precise measurements needed to monitor the ocean mesoscale variability (space scales of 50-500 km in time scales of 10-100 days, and currents of a few km/h). At present there are 4 altimetry missions in service, Jason-2, Cryosat-2, Hy-2, and Saral, 2 future missions are planned for next 2015, Sentinel-3, and Jason-3, and 2 additional missions are envisioned, Jason-CS for 2017, and SWOT for 2020.

However, in any case, merging a multi-satellite data sets is not an easy task, since it requires homogeneous and inter-calibrated sea surface height (SSH) data sets. It is also necessary to extract consistent sea level anomalies (SLA) data from different satellites, and finally advanced interpolation techniques are required to map the SLA data onto a regular space/time grids.

On the other hand in 1990, a study about a satellite constellation of pulse limited radar altimeters was conducted by ESA, considering the requirements of the scientific community. This study was finished in 1992, and concludes that to achieve mesoscale observations with seven-day revisit time, and 50-km spatial resolution a constellation of eight satellites will be needed [4]. However the difficulty to implement a constellation like this, and the high cost required, made that an alternative implementations be searched.

Thus, and with the appearance of the Global Navigation Satellite Systems (GNSS) in 1988, Hall and Cordey proposed the use of the Earth-reflected GNSS signals as a means to sense the ocean surface [5]. In 1993, a new concept for perform ocean altimetry was proposed by Martn-Neira [6]. It consisted of taking the navigation signals reflected off the ocean surface as signals of opportunity for ranging. Those signals will be sensed by an airborne or spaceborne receiver in a bistatic radar geometry. Thus, as in traditional altimeters, echo waveforms can be generated and analyzed in order to derive three important descriptors of the ocean surface, the bistatic path delay (from which the ocean height can be derived), the ocean surface wind, and the ocean significant wave height. By means of this approach many reflections could be simultaneously received (as many as visible GNSS satellites, typically more than 10, but is expected more than 40 simultaneous received signals in the next decade, since four GNSS constellations will be fully operational). Hence, GNSS-R has the potential

to offer an exceptional spatial-temporal sampling of the Earth, making GNSS-R very attractive for low-Earth-orbit spaceborne missions for ocean mesoscale altimetry.

Since then, the use of GNSS-R for Earth Remote Sensing has been proposed for many other applications. Several experiments carried out from aircrafts, towers and balloons, have preliminary demonstrated sensitivity of GNSS-R observations to retrieve the sea surface height [7], [8], sea wind speed and direction [9]-[12], soil moisture [13], [14], dry snow and sea ice thickness [15], [16].

In 2003 the feasibility of using reflected GPS signals for remote sensing applications have been proved from space, with the United Kingdom - Disaster Monitoring Constellation (UK-DMC) [18], [19], where a GPS reflectometer was equipped on one of the satellites that forms the small constellation. Despite the UK-DMC only received the L1 signals (hence ionospheric errors could not be corrected) and the antenna gain was too low (< 12 dBi) to provide a good signal-to-noise ratio (SNR), it was demonstrated that reflected GPS signals could be reliable retrieved over oceans of varying degrees of roughness.

After that, PARIS IoD Phase-A was conceived to demonstrate the scientific applications of the GNSS-R technique. PARIS IoD Phase-A was mainly aimed to altimetry, including as a secondary objectives scatterometry, ice altimetry, soil moisture, and biomass. Nowadays, the GNSS Reflectometry Radio Occultation and Scatterometry (GEROS) on board the Internatioanl Space Station (ISS)[17], has been proposed to the European Space Agency (ESA). GEROS-ISS will perform mesoscale ocean altimetry, using the opportunity Global Navigation Satellite Systems (GNSS) reflected signals, and based on the study done during the Phase A of the PARIS IoD.

1.2 The GNSS Reflectometry Radio Occultation and Scatterometry on board the International Space Station

GEROS-ISS is a new and innovative experiment, proposed to ESA based on the exploitation of the reflected signals of opportunity from the GNSS satellites at L-band. GEROS has two main objectives. The primary objective is to retrieve key parameters of the ocean surface (i.e the altimetric sea surface height, or the scalar ocean surface mean square slope mss, related with the sea surface roughness, wind speed and direction). The secondary objectives, is obtain global atmosphere, and ionosphere observations using radio occultations, as well the monitoring of land surface

parameters using the GNSS signals. Figure 1.1 shows the schematic overview of the GEROS experiment.

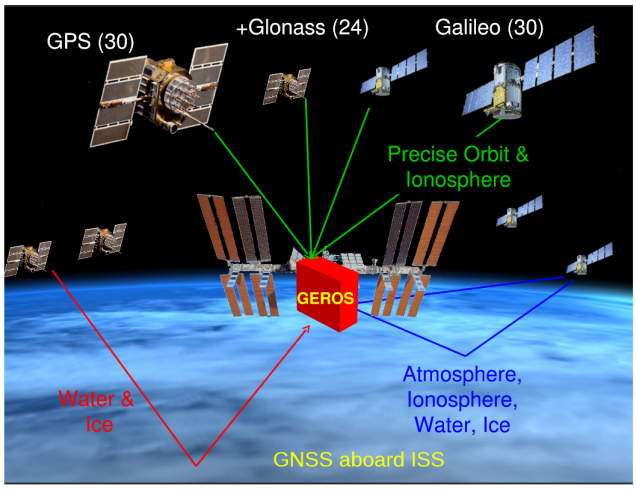

Figure 1.1: Schematic overview of the GEROS experiment. Red lines indicate the scatterometry measurements for water, ice, and land surface monitoring. Blue lines indicate GNSS-RO, and coherent reflectometry observations, and the green lines represent the GNSS signals, received from zenith for Precise Orbit Determination (POD) of the GEROS payload and 3D upside ionosphere monitoring (credits: J. Wickert)[17].

1.2.1 Mission Specifications

GEROS payload will be installed on the Exposed Platform of the ISS Columbus module, with an orbit altitude of 375 $\sim$ 425 km, an orbital period of $\sim$ 92 min, and an orbit inclination of $\sim$ 52°. Figure 1.2 shows the initial location of the payload onboard the ISS.

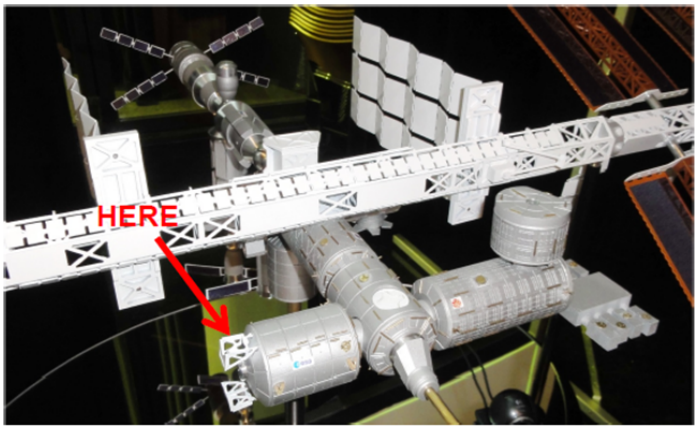

Figure 1.2: Payload location on-board the ISS (credits: J. Wickert)[17].

The payload onboard GEROS will have a mass lower than 375 kg (including the Columbus External Payload Adpater (CEPA) (117 kg)), which corresponds to a volume smaller than 931 mm×787 mm×1193 mm, with a power consumption lower than 420 W. It is foreseen that the mission will be operational during more than 1 year, with a possible extension of up to 5 years, and a storage life on ground of 4 years.

1.2.2 System concept

Initially GEROS will be composed by two Signal Processing Units (SPU-A and SPU-B). The SPU-A will implement the so called interferometric technique (iGNSS-R), in which the received reflected signal is cross-correlated with the received direct signal, whereas in the SPU-B will be implement the conventional o classical technique (cGNSS-R), in which the received reflected signal is correlated with a clean replica of the GPS C/A code. Is important to stretch that the SPU-A will require beamforming of the uplooking antenna.

GEROS will use the same phased array antennas with four high gain beams in both up- and down-link channels. The reason to use high-gain antennas in both channels, is because in the interferometric technique as the correlation is performed directly between the direct and the reflected signals, the processing gain achieved in the conventional technique (around 20 dBs), is lost. Hence, in order to compensate this loss, a higher antenna gain is needed in both channels.

On the other hand, GEROS will be use dual-frequency observations in order to allow precise estimation of the ionospheric delay and will incorporate precise on-board delay and amplitude calibration. To achieve this, the two antenna arrays (up- and down-looking) will be mounted back-to-back minimizing their physical separation with corresponding elements being paired through a mutual calibration switch circuit, allowing them, and the analogue beamforming networks, to be fully characterized.

Summarizing, the equipment to be built will include:

1. up- and down-looking antennas;
2. radio-frequency front-ends;
3. analogue beamforming networks;
4. harness between front-ends and beamformers;
5. down-converter and analog-to-digital converter;

6. correlator unit;

7. instrument controller;

8. downlink system;

9. deployment mechanism.

The antennas will be around 110 cm in diameter, and will consist of 31 elements arranged in an 1-6-12-12 hexagonal grid. For the beamforming network, suitable monolithic microwave integrated circuits will be used, including some developed in previous ESA contracts. The correlator unit can be largely based on a field-programmable-gate-array (FPGA) based signal processor, but using a suitable radiation-tolerant device, or on application-specified integrated-circuit technology.

1.2.3 Instrument Design

GEROS ISS will be designed in order to be able to receive any of the different GNSS systems (i.e the U.S GPS, the European Galileo, the Chinese BeiDou, the Russian Glonass, the Indian INSS, or the Japanese QZSS).

As previously proposed for PARIS IoD, the initial antenna design, will consist of two identical phased arrays, mounted back-to-back, with the front-end and electronics housed between them. With these antennas it will be possible to generate and steer four up-looking and four down-looking high-gain beams (the up-looking beams will steer towards the transmitting satellites, whereas the down-looking ones will track the corresponding reflected points over the ocean or over the Earth's surface).

With respect to the array design, it will be designed in order to maximize the minimum SNR in reception of the reflected signals. Considering that the SPU-A unit of GEROS is based on the interferometric processing, and assuming an altitude of $\sim$ 400-km, an antenna gain of around 23 dBi will be required. That gain can be achieved initially with an hexagonal array of 1.1 m, consisting of 31 elements, where each element will have a directivity of 8 dB. Figure 1.3 shows the initial design of the antenna arrays.

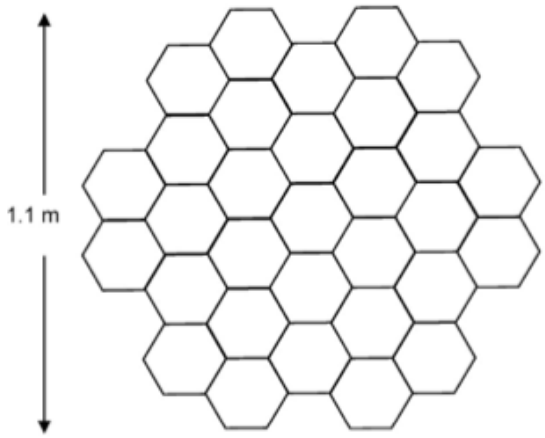

Figure 1.3: Proposed phased array antenna (credits: M. Martin-Neira)[36].

The different elements of the array will be designed with the objective of receive the lowest and highest navigation bands (currently L1-E1 and L5-E5a, respectively for GPS and Galileo), in order to provide the best estimation of the ionospheric delay. The field of view of each element will be between 25^o and 35^o around the boresight to ensure the coverage at the same time that the altimetric performance is preserved.

On the other hand, a back-to back mechanical arrangement of both phased arrays is proposed (Fig. 1.4), achiving that the phase center of both antennas being in close proximity (less than 10 cm as it can be appreciated in Fig. 1.4), minimizing their impact on the altimetry performance. Also, a compact layout of the front-end electronics between the two arrays is achieved. This issue can be better appreciated in Fig. 1.5, where it can be noted that each uplooking element is paired up with one downlooking element. However, the major advantage obtained with this configuration, is that both the direct and reflected signals can be easily routed via pressure connectors from each antenna array element to a calibration switch circuit inserted between them and their low noise amplifiers (LNAs), allowing accurate delay and amplitude calibration, which at the end is essential in order to achieve the scientific goals of the GEROS ISS.

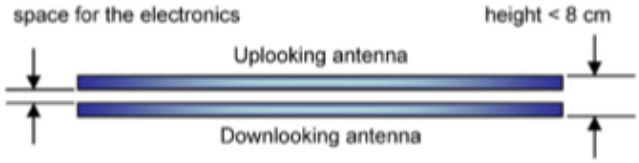

Figure 1.4: Back-to-back double phased array antenna (credits: M. Martin-Neira)[36].

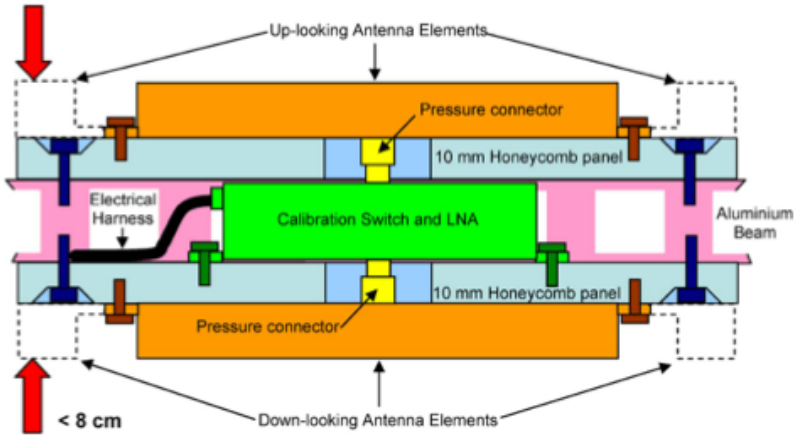

Figure 1.5: Cross section of the PARIS antenna sandwich showing the element pairing through the calibration switch and LNA front-end electronics (credits: M. Martin-Neira).

1.3 Goals of this PhD Thesis

The objective of this PhD activity is to investigate the adoption of advanced Delay/Doppler processing concepts for a PARIS interferometric altimeter in order to improve the instrument altimetry performance and spatial resolution. This shall be achieved by carrying out a solid review and consolidation of the GNSS-R theory, performance models and possible retracking algorithms. This is of high relevance for the definition of future operational GNSS-R missions, aiming an altimetry accuracy of ∼20 cm. Current processing techniques (considered in the frame of the PARIS IoD Phase A), lead to about 20 cm accuracy.

In the following are described the tasks carried out by the student during the PhD Thesis:

- Deep review of the GNSS-R theory in order to consolidate, and refine it.
- Critical review of the Cross-Correlation Waveform model, including the derivation of the statistics for both the voltage and power cross-correlations.
- Study of performance models describing the interferometric processing.
- Study of performance model of the altimetry precision, based on statistical estimator theory such as the Cramer Rao Bound (CRB).

- Study of candidate waveform retracking algorithms (optimum or quasi-optimum from the statistical point of view).
- Analysis and determination of the system/instrument parameters which optimize the altimetric performance of a conventional and interferometric altimeter.
- Processing data from satellite, airborne and ground-based experiments as a preliminary proof of concept of the technique.
- Processing data from the Typhoon Investigation using GNSS-R Interferometric Signals (TIGRIS) experiment, in order to evaluate the capabilities of the GNSS-R technique for typhoon monitoring.

Chapter 2

Background

This chapter provides a general description on the use of GNSS signals for ocean mesoscale altimetry. Section 1 describes the main characteristics of the GPS, GLONASS, Galileo and BeiDou 2 signals. In Section 2, the main principles of the GNSS-R over the ocean are presented.

2.1 Ocean mesoscale altimetry using GNSS signals of opportunity

Global Navigation Satellite Systems (GNSS) are satellite constellations that cover the entire Earth transmitting navigation signals to provide time and position information to users located on or near the Earth's surface. Such systems are used nowadays in a wide range of everyday situations, such as fleet management, search and rescue, wildlife tracking, vehicle guidance or leisure interactive maps, among many others. Different GNSS satellite constellations can be found, as for example the American GPS, the Russian GLONASS, the European Galileo, the Chinese BeiDou-2, the Indian IRNSS, and the Japanese QZSS. Altogether, more than 100 GNSS satellites will be available when all the current planned systems them will be fully deployed (note that some of the constellations are partially deployed as for example Galileo and BeiDou-2). The availability of all those signals has made them become a valuable source of opportunity for Earth remote sensing. Figure 2.1 shows the spectral allocation of the major GNSS signals.

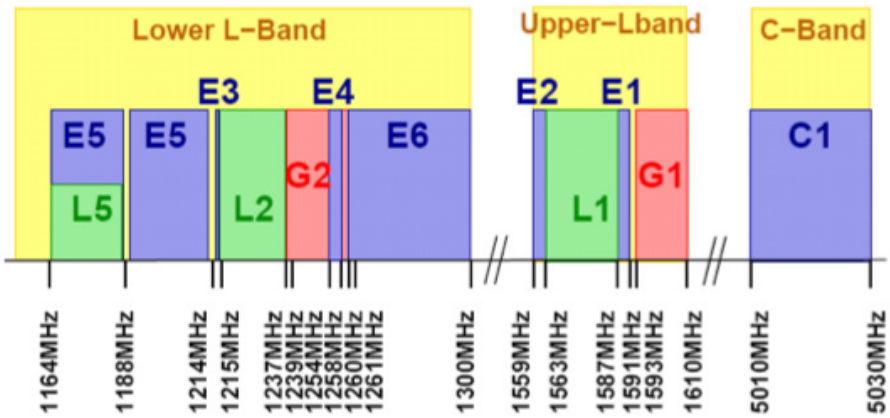

Figure 2.1: Radio Navigation Satellite Service band distribution after the World Radio Conference, Istambul, 8 May-2 June 2000, which discussed the allocation of the GALILEO signal spectrum. E and C bands (blue) are assigned to GALILEO, L bands (green) are for GPS, and G bands (red) are reserved for the GLONASS signals [22].

2.1.1 The GPS signal

The American Global Positioning System (GPS) was designed to provide 3D positioning anytime anywhere on Earth. To fulfill that goal at least four satellites have to be observed simultaneously at a given place and moment. In order to ensure the service even when one satellite fails it is necessary to consider a minimum of five visible satellites. These considerations result in a constellation of at least 24 satellites distributed in six orbital planes spaced 60° through the Equator with an inclination of 55°. The satellites in the same orbital plane are not equally spaced, but distributed so that the effects of a single satellite failure are minimized. Their orbital period is of 12 sidereal hours, which implies that the ground track repeats daily with a time shift of four minutes. The near circular orbits (eccentricity smaller than 0.02) have a medium height of 20163 km above the Earth's surface, and results in a mean satellite speed of 3.87 km/s approximately. The actual satellite visibility depends on the latitude, but there is always a minimum of 5 satellites in view, and this minimum number is 7 for more than 80 % of the time [20].

2.1.1.1 Transmitted GPS signal

GPS uses a Binary Phase Shift Keying (BPSK) modulation [21], which is a simple digital signaling scheme, where the carrier phase changes instantaneously by 180°,

over succesive intervals in time. A BPSK modulated signal can be written as:

$$S_{PSK}(t) = \sqrt{2P}a(t)\cos(w_c t)d(t), \tag{2.1}$$

where P is the signal power, $a(t)$ is the bi-phase Pseudo-Random Noise (PRN) code spreading signal, $d(t)$ is the bi-phase data signal, and $w_c(t)$ is the carrier frequency.

Additionally to the BPSK, there is the Binary Offset Carrier (BOC) modulation, for the military L1 and L2 signals. A BOC modulation basically is a rectangular subcarrier modulation (sine or cosine) of the PRN spreading code, and it is denoted as BOC(f_s,f_c), where f_s is the subcarrier frequency and f_c is the PRN code chipping rate. Both f_s and f_c are multiples of 1.023 MHz. Thus, the BOC signal can be represented as:

$$S_{BOC}(t) = \sqrt{2P}b(t)\cos(w_c t)d(t), \tag{2.2}$$

where $b(t) = a(t)s(t)$, being $s(t)$ the square wave subcarrier.

The overall transmitted signal can be represented as a Quadrature Phase Shift Keying (QPSK) signal. In QPSK, the two signals are generated using RF carriers that are in-phase and quadrature (have a relative phase difference of 90°), and are simply added together. Therefore, the transmitted signal can be expressed as:

$$s(t) = s_I(t)\cos(2\pi f_c t) - s_Q(t)\sin(2\pi f_c t), \tag{2.3}$$

where $s_I(t)$ and $s_Q(t)$ are the in-phase and quadrature components, expressed as,

$$s_I(t) = \sqrt{2P_I}s_1(t)\cos(m) - \sqrt{2P_Q}s_2(t)\sin(m), \tag{2.4}$$

and

$$s_Q(t) = \sqrt{2P_Q}s_3(t)\cos(m) - \sqrt{2P_I}s_1(t)s_2(t)s_3(t)\sin(m), \tag{2.5}$$

being $s_1(t)$, $s_2(t)$ and $s_3(t)$ the three desired signals, f_c the carrier frequency and m an index that is set in conjuction of the power parameters P_I and P_Q to achieved the desired power levels.

2.1.1.2 GPS signal structure

Figure 2.2 represents the block diagram of the GPS satellite signal structure for the L1 and L2 frequencies, respectively $154f_o$ and $120f_o$, being f_o the fundamental frequency (10.23 MHz). As it can be appreciated, the L1 frequency is modulated by two PRN codes, the C/A code, and the P code, plus the navigation message

data, whereas the L2 frequency is modulated by only one PRN code. As it has been commented, the nominal reference frequency (f_o) is 10.23 MHz, but in order to compensate some relativistic effects, an offset of $4.467 \cdot 10^{-10}$ should be considered. Therefore $f_o = 10.22999999453$ MHz [23]. On ground the C/A code has a chip rate equal to $1.023 \cdot 10^6$ chips per second (equivalent to $f_o/10 = 1.023$ MHz), whereas the P code has a chip rate equal to $10.23 \cdot 10^6$ chips per second (equivalent to $f_o = 10.23$ MHz).

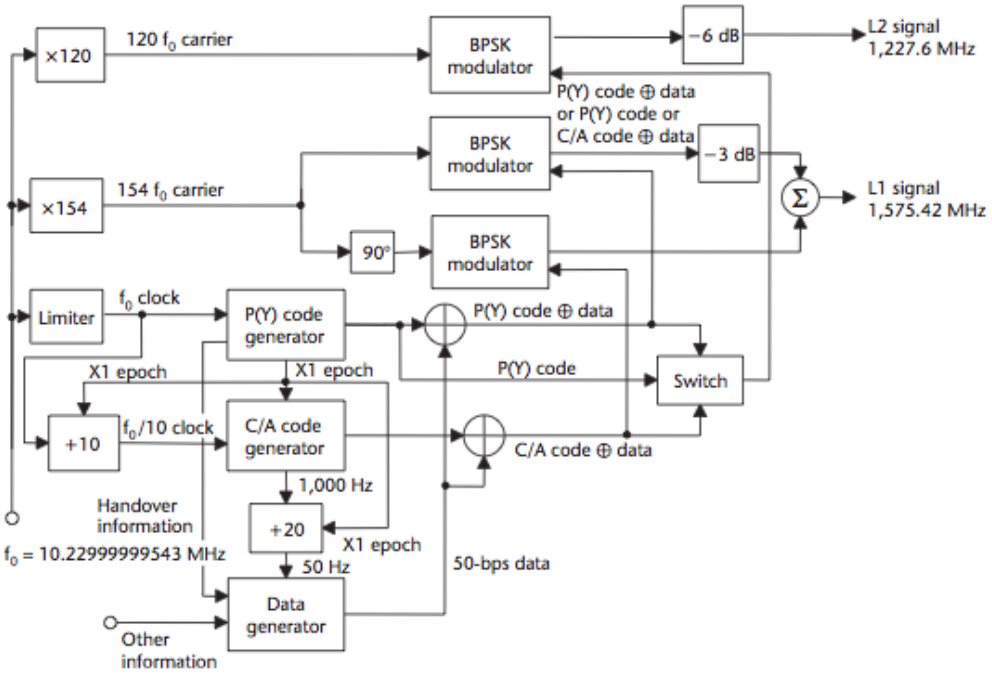

Figure 2.2: GPS satellite signal structure [24].

It is important to remark that the P code only is available for the Payroll Personnel System (PPS) users (primarily military), since the P code is encrypted (with the so-called Y-code). For this reason, sometimes the acronym used for the precise (encrypted) code is the P(Y) code. Note that the chip rate of the P(Y) is exactly the same of the P code.

Also, it is important to comment that a 50-bps navigation message data is combined with both the C/A and P(Y) codes, before modulating the L1 carrier (an exclusive -or logic gate is used to perform the modulation). Ending, as the C/A and P(Y) codes are both synchronous operations, the bit transition rate cannot exceed the chip rate.

2.1.1.3 Generation of the C/A, P, and M codes

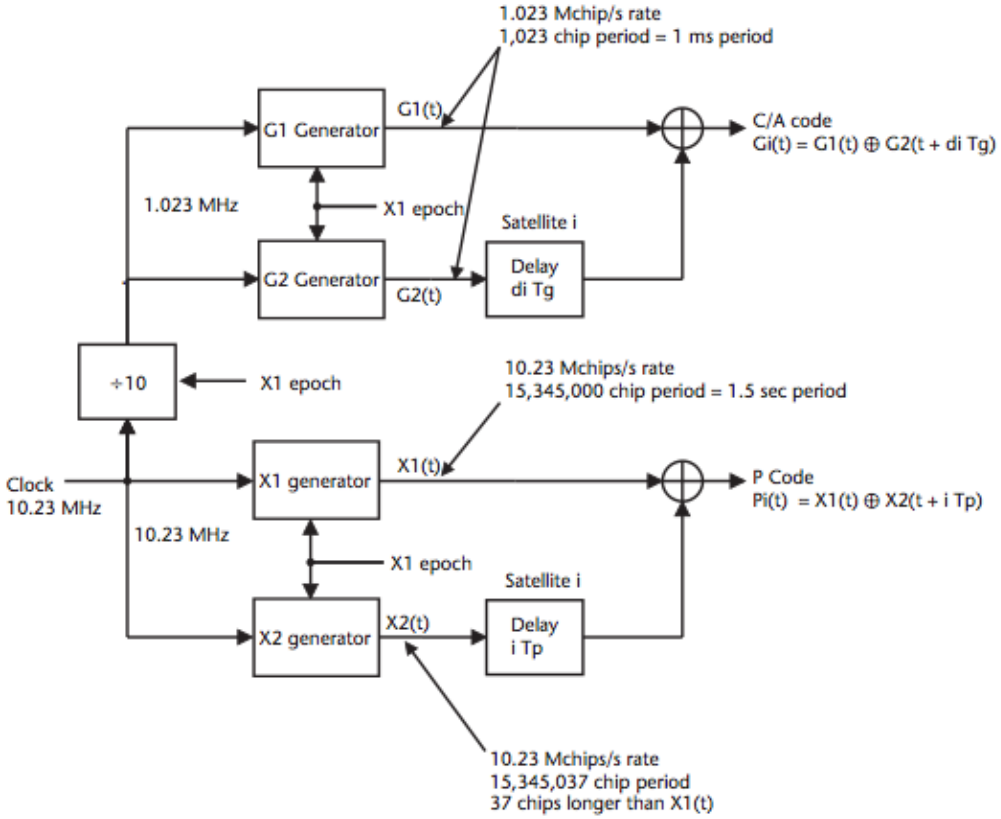

Figure 2.3: GPS code generators [24].

Figure 2.3 represents the high-level block diagram of the direct sequence of the PRN code generator used to generate the GPS C/A and P codes.

The GPS C/A code is a Gold code [27], which a sequence lenght of 1023 bits (chips). As the chip rate of the C/A code is 1.023 MHz, the C/A code has a period of 1 ms ($1023/(1.023 \cdot 10^6)$Hz). As it can be appreciated from Fig. 2.4, there are two shift registers of 10 bits each one (G1 and G2), which generate PRN codes with a length of 1023 bits ($2^{10} - 1$). Figure 2.4 represents with higher level of detail the C/A code generator.

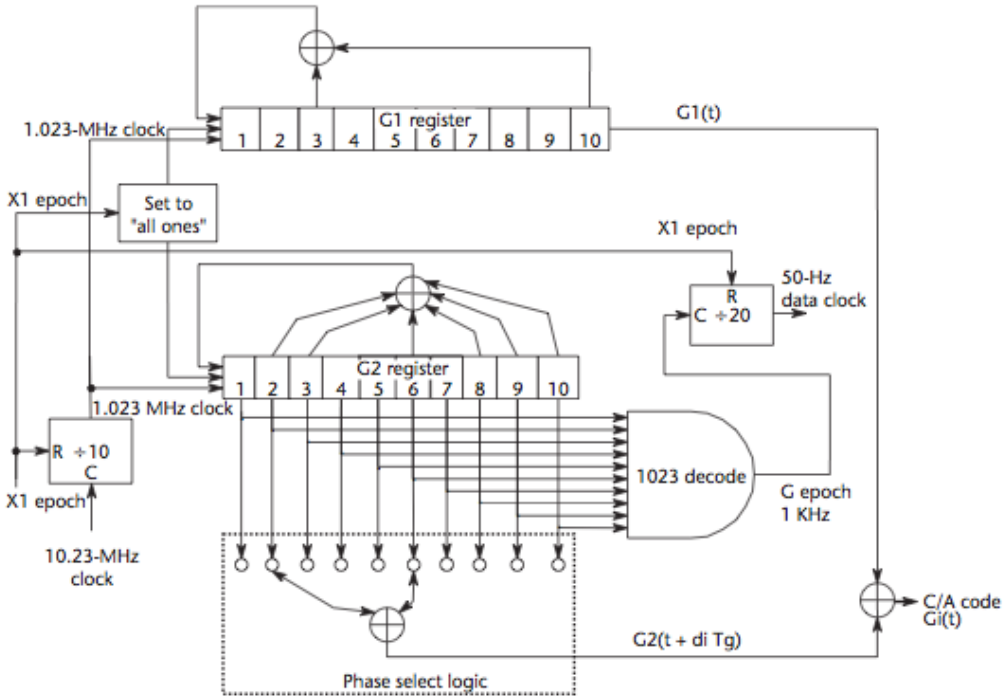

Figure 2.4: C/A code generator [24].

On the other hand, the GPS P code is a PRN sequence generated using four 12-bit shift registers designated as X1A, X1B, X2A, and X2B. A detailed block diagram of this shift register architecture is shown in Fig. 2.5. Is important to note that the output of the register X1A is combined by an exclusive-or circuit with the output of the register X1B in oder to form the X1 code generator. In a similar way the output of the register X2A is combined by an exclusive-or circuit with the output of the register X2B to form the X2 code generator. The P code is formed by combining an exclusive -or the resultant X2 code fed to a shift register delay, with the resulting X1 composite code. In this case the length of the P code is $6.1871 \cdot 10^{12}$ chips with a week period (the P-code is reset every week as it can be appreciated on Fig. 2.5).

To end, the M code employs a BOC modulation, specifically a BOC (10,5) signal. The first parameter denotes the frequency of an underlying square wave subcarrier, which is $10 \cdot 1.023$ MHz, and the second parameter denotes the underlying M code generator code chip rate, which is $5 \cdot 1.023$ Mchip/s. Figure 2.6 depicts a high level block diagram of the M code generator.

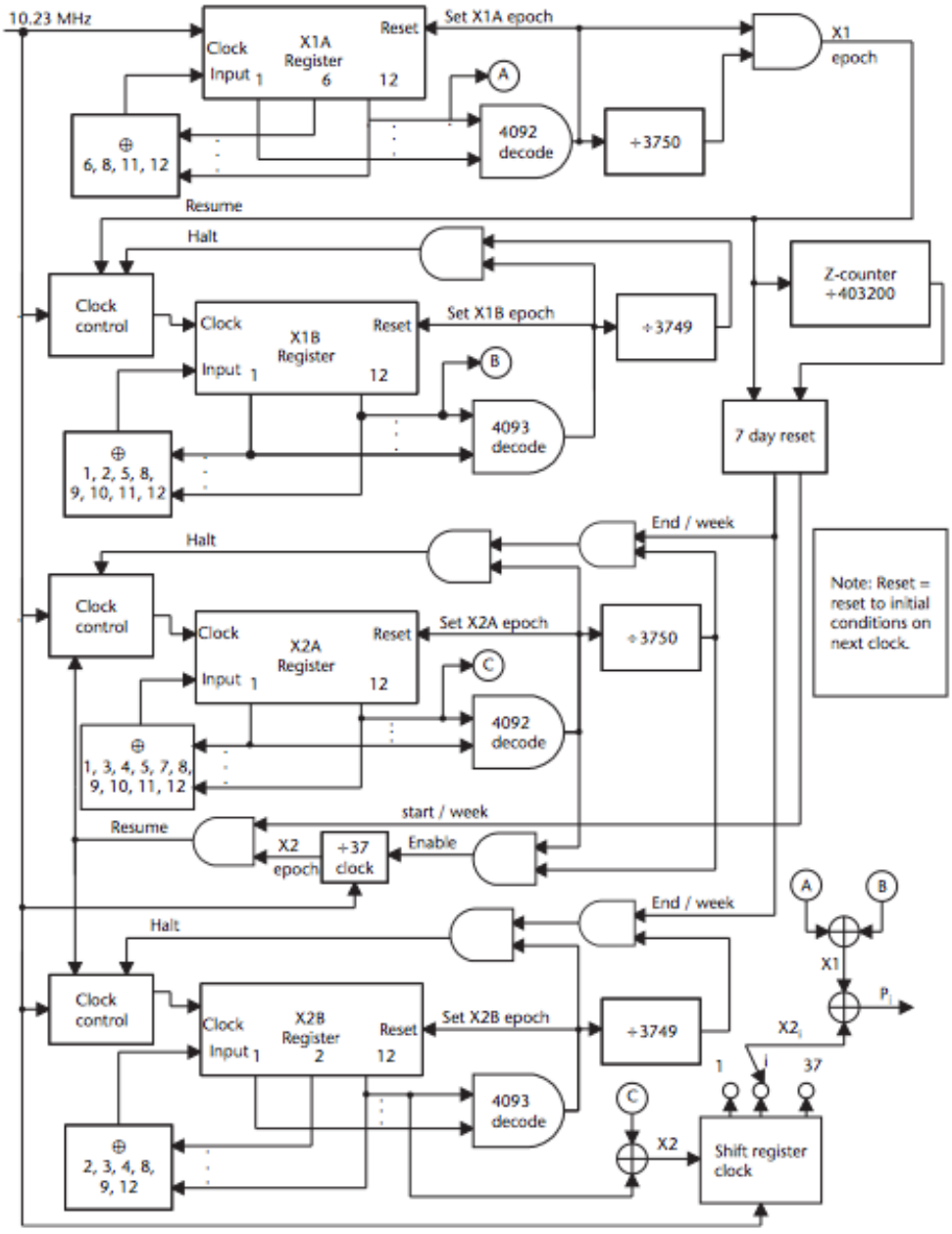

Figure 2.5: P-code generator [24].

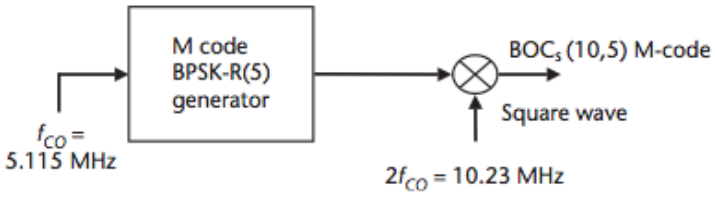

Figure 2.6: M code signal generator [24].

2.1.1.4 The GPS L2c signal

The L2 civil (L2c) signal presents a similar power spectrum than the C/A code (i.e., 2.046 MHz null-to-null bandwidth), but presents some differences respect to the C/A code. The first one, is that L2c uses two different PRN codes per satellite. The first one is referred as the civil moderate (CM), because employs a sequence that is repeated every 10230 chips, whereas the second one referred as civil long (CL), extremely long, and presenting a length of 767250 chips.

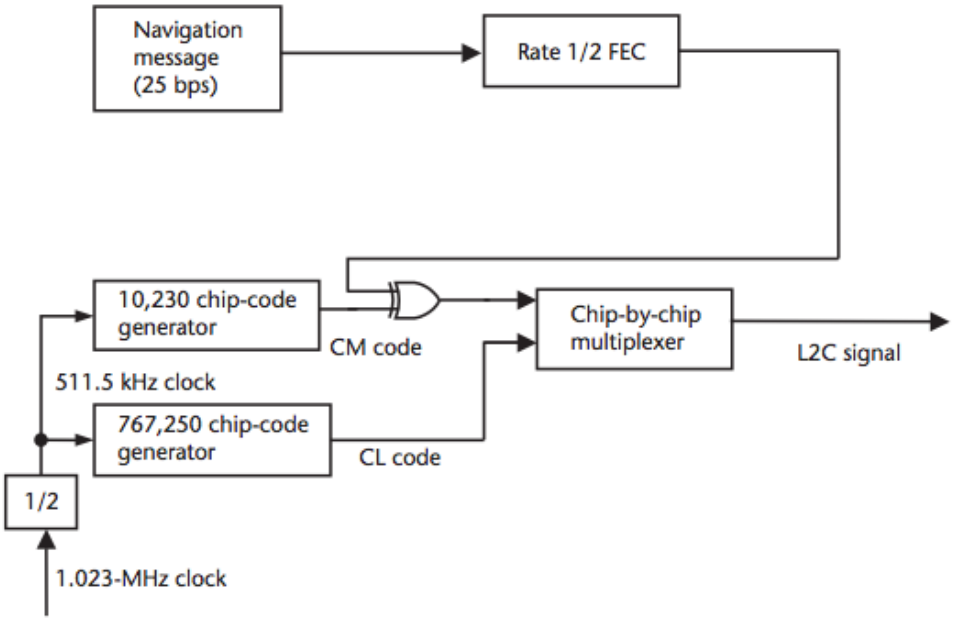

Figure 2.7: L2c code generator [24].

The L2C signal has an overall chip rate of 1.023 Mchip/s (equivalent to $2 \cdot 511.5$ Kchip/s rate), which is the reason of the similarity with the power spectrum of the C/A code. In any case, it is important to consider that as both CM and CL codes are much longer than the C/A code (1023 chips), the maximum lines in the L2c code power spectrum are far lower than the ones in the C/A case, allowing to obtain robustness against the presence of narrowband interferences.

2.1.1.5 The GPS L5 signal

In August 2002, the US in coordination with the International Telecommunication Union Radio communication Sector (ITU-R) proposed the transmission of a new civil signal, the L5 signal (transmitted at 1176.45 MHz), as a part of the modernization of the GPS.

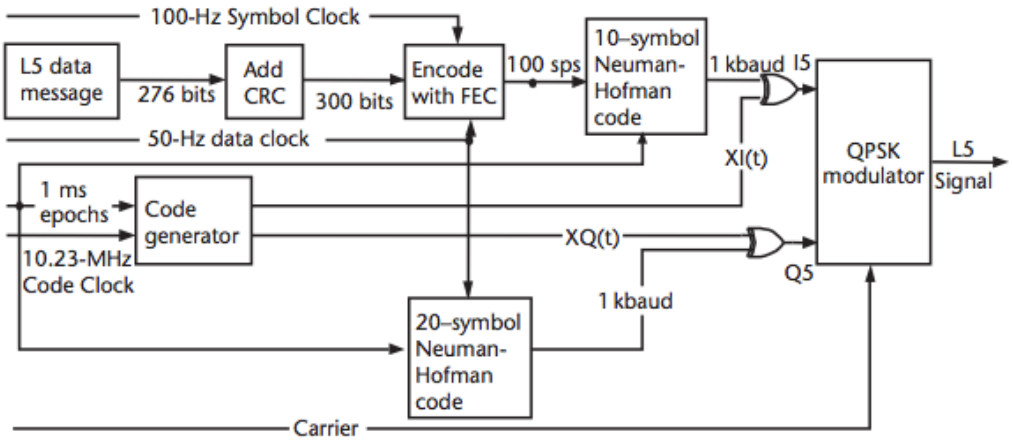

Figure 2.8: L5 signal generation [24].

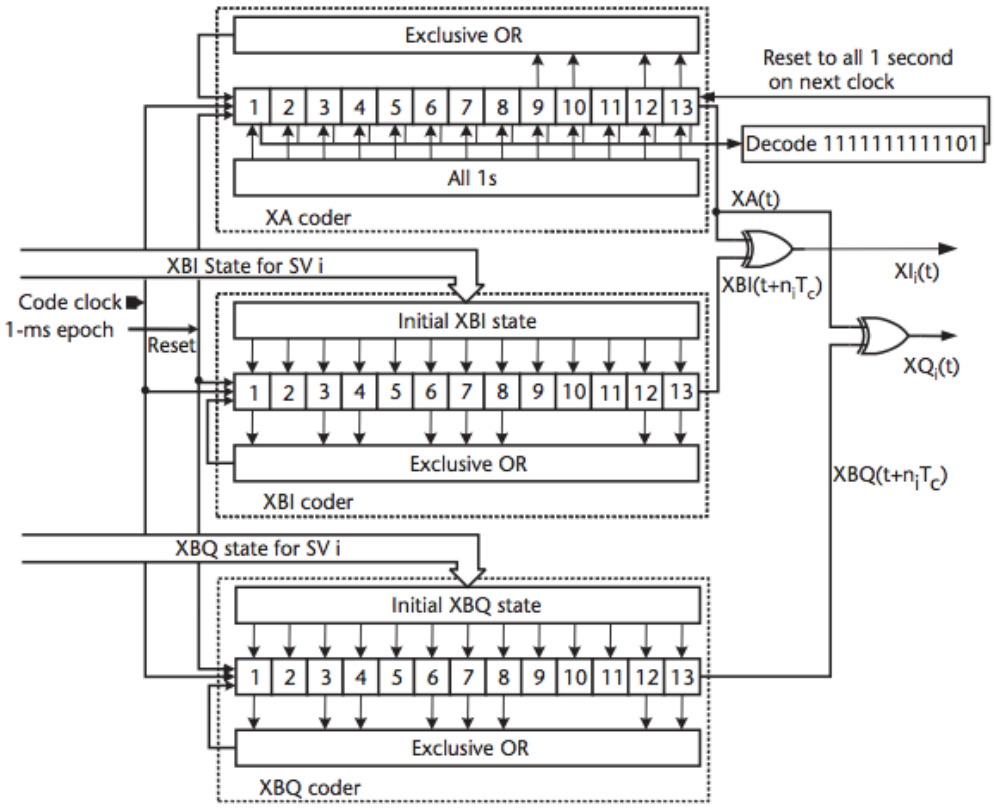

Figure 2.9: PRN code generator for the in-phase and quadrature L5 signal components [24].

The structure of the new GPS L5 signal consists of two carrier components signals, both in-phase and quadrature, with the same power level, and with different, but nearly orthogonal, and time-synchronized PRN codes [25]. The quadrature channel

is a data-less channel, transmitting only a pilot signal modulated with the specific satellite PRN (useful when the coherent integration time is long), whereas the in-phase channel, is where the navigation message is modulated (with 100 symbols per second). By using different PRN codes, possible tracking biases are prevented. To finish the L5 signal uses a chip rate of 10.23 MHz (as the P-code), providing thus a null-to-null bandwidth of 20.46 MHz. Figure 2.8 shows the GPS L5 signal generator, whereas Fig. 2.9 shows the PRN code generator for the in-phase and quadrature L5 signals.

2.1.2 The GLONASS signal

The Russian GLONASS (GLObalnaya NAvigatsionnaya Sputnikovaya Sistema) started to be developed in 1976 by the Soviet Union, achieving the full orbital constellation of 24 satellites in 1995. Later, between 2003 and 2011, and under the Russian Federal Space Agency, the system was completely replaced by a second generation of satellites (GLONASS-M). Currently, a third generation of space vehicles (GLONASS-K) is already in orbit. The full constellation of 24 satellites is deployed in 3 orbital planes separated by 120°, being the orbits nearly circular, with a height of 19100 km and an orbital period of 11 h 15 m approximately.

2.1.2.1 GLONASS signal characteristics

GLONASS has many similarities with GPS in terms of system architecture. Hence, it has its origin as a military system, uses similar terminology (C/A-code, P-code), use two types of service (standard precision (SP) and high precision (HP), having the HP signal 10 times more bandwidth than the SP one) at both L1 and L2 bands, and both are multiplexed in-phase and quadrature. However, some differences can also be found between GPS and GLONASS. For example, the characteristics of the C/A and P codes are different. In GLONASS the C/A code has a maximal length of 9 shift registers, with a code rate of 0.511 Mchips/s (1.023 Mchips/s in GPS), a code length of 511 chips (1023 chips in GPS), and a period of 1 ms, whereas the P code has a maximal length of 25 shift registers, a code rate of 5.11 Mchips/s, a code length of 33554432 chips, and a period rate of 1 sec (exactly the period is 6.57 seconds, but the chipped sequence is truncated resulting in a period equal to 1 sec). But the main difference between GLONASS and GPS relies in the technique used. As a difference of GPS in where each satellite transmits a unique PRN code on the same frequency (code division multiple access or CDMA), GLONASS transmits the same PRN code pair on different frequencies (frequency division multiple access or FDMA).

Signals are right-hand circularly polarized. The 24 satellites employ only 15 frequency channels according to the following equation,

$$f = (178.0 + \frac{K}{16})Z, \tag{2.6}$$

being K an integer value between -7 and 12 (between 0 and 12 through 1998, between -7 and 12 between 1998 and 2005, and between -7 and 4 after 2005), and $Z = 9$ for L1 and $Z = 7$ for L2. Note that since antipodal satellite pairs use identical frequencies, an Earth-located receiver will never receive both satellites simultaneously. To finish, the navigation signal is contained in a 50-bps data signal.

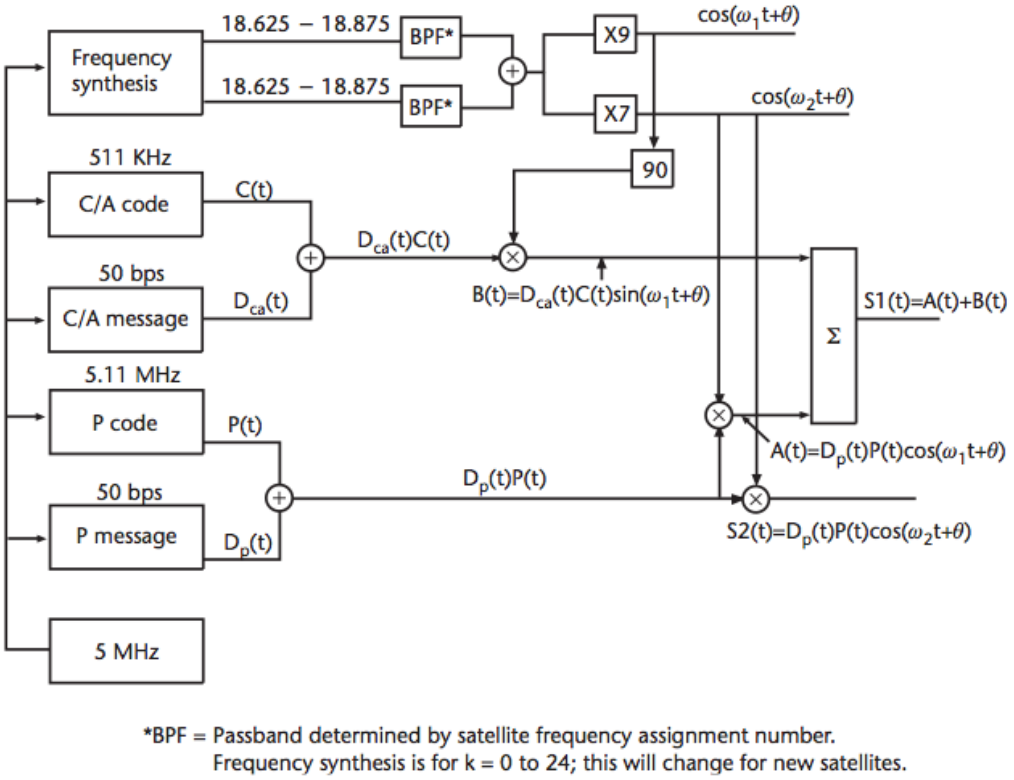

Figure 2.10: GLONASS signal generator [24].

2.1.3 The Galileo signal

The European GALILEO GNSS was conceived as an alternative to both GLONASS and GPS, since Russia or the USA could deny the access to their respective navigation systems in case of war or political disagreement. The first GALILEO satellite was launched in December 2005, with the aim of having a fully deployed the 30 element constellation (27 operational + 3 active spares). With 4 In-Orbit Validation (IOV)

and 2 Full Operational Capability (FOC) space vehicles already launched, the full completion of the 30 satellites constellation is expected by 2019 [26].

The satellites are distributed in 3 orbital planes with an inclination of 56°. The Open Service (OS) will perform similarly to the GPS C/A service, whereas the encrypted Commercial Service (CS) will be available under subscription. Two additional Public Regulated Service (PRS), and Safety of Life Service (SoL) modes will be available.

2.1.3.1 Galileo frequency plan and signal design

Galileo will provide six navigation signals with RHCP polarization in the following frequency ranges.

- E5-band (1.165-1.215 MHz), which includes the E5a and E5b. The E5a is an open access signal, including a data channel, and a pilot channel. E5a has unencrypted ranging codes and data accessible by all the users, transmitting the basic data to support the navigation and timing functions, using a relatively low data rate (25-bps), enabling a more robust data modulation and supporting OS. The E5b is an open access signal too, including as the E5a signal unencrypted ranging codes and navigation data accessible to all users. The E5b contains a data stream, integrity messages and encrypted commercial data. The data rate in this case is a bit higher (125 bps), supporting OS and SoL.

- E6-band (1.265-1.3 MHz), which includes the E6c and the E6p. The E6c is a dedicated signal to support the commercial service. E6c, includes a data channel, and a pilot channel. The data and ranging codes in this case are encrypted, using a commercial algorithm and a data rate of 500 bps. On the other hand the E6p is a restricted access signal, being in this case the ranging codes and data encrypted, using a governmental encryption algorithm.

- E2-L1-E1-band (usually referred as L1-band (1.559-1.592 MHz)), which includes the L1f and L1p. The L1f is an open access signal, comprising a data channel and a pilot channel, containing also integrity messages and encrypted commercial data. The ranging codes and navigation data are unencrypted. As in the case of the E5b signal, the data rate is 125 bps, and supports OS and SoL. The L1p as the E6p is a restricted acces signal, using a governmental encryption algorithm for encrypting the ranging codes and data. L1p supports PRS.

Is important to remark, that all satellites will make use of the same carrier frequencies with different range codes through the CDMA multiplexing technique.

2.1.3.2 Galileo modulation scheme

2.1.3.2.1. E5

The transmitted GALILEO E5 signal ($S^{tx}_{E5}(t)$) results from multiplexing the four E5 components (E5a data channel, E5a pilot channel, E5b data channel, and E5b pilot channel).

- The E5a data channel is a modulo-two combination of the E5a navigation data stream ($d_{E5a}(t)$) with the E5a data channel PRN code sequence ($c_{E5a\cdot d}(t)$).
- The E5a pilot channel, is a PRN code sequence ($c_{E5a\cdot p}(t)$).
- The E5b data channel in a similar way of the E5a, is a modulo-two combination of the E5b navigation data stream ($d_{E5b}(t)$) with the E5b data channel PRN code sequence ($c_{E5b\cdot d}(t)$).
- The E5b pilot channel, is as the E5a a PRN code sequence ($c_{E5b\cdot p}(t)$

The chip rate of the four E5 components is 10.23 MHz, and multiplexing the four channels is achieved by means of the AltBOC (15,10) modulation as,

$$s^{tx}_{E5}(t) = Re[s^{tx}_{E5}]\cos(2\pi f_{E5}t) - Im[s^{tx}_{E5}]\sin(2\pi f_{E5}t), \tag{2.7}$$

with

$$\begin{aligned} s^{tx}_{E5}(t) =& \frac{1}{2\sqrt{2}}(s^{tx}_{E5a-d}(t) + js^{tx}_{E5a-p}(t))[sc_{E5d}(t) - jsc_{E5d}(t - T_{sc_{E5}}/4)] \\ &+ \frac{1}{2\sqrt{2}}(s^{tx}_{E5b-d}(t) + js^{tx}_{E5b-p}(t))[sc_{E5d}(t) - jsc_{E5d}(t - T_{sc_{E5}}/4)] \\ &+ \frac{1}{2\sqrt{2}}(s^{-tx}_{E5a-d}(t) + js^{-tx}_{E5a-p}(t))[sc_{E5p}(t) - jsc_{E5p}(t - T_{sc_{E5}}/4)] \\ &+ \frac{1}{2\sqrt{2}}(s^{-tx}_{E5b-d}(t) + js^{-tx}_{E5b-p}(t))[sc_{E5p}(t) - jsc_{E5p}(t - T_{sc_{E5}}/4)], \end{aligned} \tag{2.8}$$

2.1.3.2.2. E6

The transmitted GALILEO E6 signal ($S^{tx}_{E6}(t)$) consists of three components (E6c data channel, E6c pilot channel, and the E6p).

- The E6c data channel is a modulo-two combination of the E6c navigation data stream ($d_{E6c}(t)$) with the E6c data channel PRN code sequence ($c_{E6c\cdot d}(t)$), resulting in a binary phase shift keyed onto the E6 carrier at $5.115 \cdot 106$ chip/s (BPSK-R(5)).

- The E6c pilot channel, results from modulating the PRN code sequence ($c_{E6c\cdot p}(t)$), which as the E6c data channel is a binary phase shift keyed onto the E6 carrier at $5.115 \cdot 106$ chip/s (BPSK-R(5)).

- The E6p channel, is a modulo-two combination of the E6p navigation data stream ($d_{E6p}(t)$) with the E6p data channel PRN code sequence ($c_{E6p}(t)$) and the binary E6p subcarrier ($sc_{E6p}(t)$). The result is a binary phase shift keyed onto the E6 carrier with a code chipping rate of $5.115 \cdot 106$ chips/s and a subcarrier of 10.23 MHz (BOCc(10,5)).

The E6 signal components are multiplexed onto the E6 carrier signal by means of a modified hexaphase modulation, where the E6c signal channels are modulated onto the in-phase component, and the E6p channels are modulated on to the quadrature component of the E6 carrier signal,as

$$\begin{aligned} s^{tx}_{E6}(t) =& \sqrt{2P^{tx}_{E6}}[\alpha_{E6} s^{tx}_{E6c_d}(t) - \alpha_{E6} s^{tx}_{E6c_p}(t)] \cos(2\pi f_{E6} t) \\ & - \sqrt{2P^{tx}_{E6}}[\beta_{E6} s^{tx}_{E6p}(t) + \gamma_{E6} s^{tx}_{E6_{int}}(t)] \sin(2\pi f_{E6} t). \end{aligned} \tag{2.9}$$

2.1.3.2.3. L1

The transmitted GALILEO L1 signal ($S^{tx}_{L1}(t)$) consists of the multiplexing of three L1 components (L1f data channel, L1f pilot channel, and the L1p channel),

- The L1f data channel, results from the modulo-two combination of three components, the L1f navigation data stream ($d_{L1f}(t)$), the L1f-d channel PRN code sequence ($c_{L1f-d}(t)$) and the L1f-d subarrier ($sc_{L1f-d}(t)$). The signal modulation corresponds to a BOC subcarrier with a sine phase (BOCs(1,1)), modulated by the d-channel code sequence and the d- channel data signal.

- The L1f pilot channel, results from a modulo-two combination of the L1f channel PRN code sequence ($c_{L1f-p}(t)$) with the L1f subcarrier ($sc_{L1f-p}(t)$). As in the case of the L1f data channel, the signal modulation corresponds to a BOC subcarrier with a sine phase (BOCs(1,1)), modulated by the p-channel code sequence.

- The L1p channel, results from a modulo-two combination of three components, the L1p navigation data stream ($d_{L1p}(t)$), the L1p channel PRN code sequence ($c_{L1p}(t)$) and the L1p subcarrier ($sc_{L1p}(t)$). The BOC subcarrier has cosine phasing, corresponding to a BOCc(15,2.5) cosine modulation by the code sequence and data signal.

The L1 signal components are multiplexed into the L1 carrier using the modified hexaphase modulation, where the L1f signal is modulated onto the carrier in-phase component while the L1p signal is modulated onto the quadrature component. The composite signal can be expressed as:

$$\begin{aligned} s^{tx}_{L1}(t) =& \sqrt{2P^{tx}_{L1}}[\alpha_{L1} s^{tx}_{L1f_d}(t) - \alpha_{L1} s^{tx}_{L1f_p}(t)] \cos(2\pi f_{L1} t) \\ & - \sqrt{2P^{tx}_{L1}}[\beta_{L1} s^{tx}_{L1p}(t) - \gamma_{L1} s^{tx}_{L1_{int}}(t)] \cos(2\pi f_{L1} t). \end{aligned} \tag{2.10}$$

2.1.4 The BeiDou 2 signal

The Chinese Compass (or Beidou 2) is an independent system similar to GPS or Galileo. It uses a CDMA scheme to discriminate between satellites and it will offer two levels of service: open and restricted (for military purposes). The whole constellation consists of 5 Geostationary Earth Orbit (GEO) satellites, 27 Medium Earth Orbit (MEO) and three Inclined Geosynchronous Satellite Orbit (IGSO). The GEO satellites operate in a 35786 kilometres height orbit and positioned at 58.75°E, 80°E, 110.5°E, 140°E and 160°E respectively. The MEO satellites operate at a 21528 kilometres orbit height and an inclination of 55° to the equatorial plane. Ending the IGSO satellites operate in orbit at an altitude of 35786 kilometres and an inclination of 55° to the equatorial plane [28].

2.1.4.1 Beidou Signal Characteristics

The BeiDou signal is composed of the carrier frequency, ranging code, and the NAV message. The BeiDou signals B1 and B2, are the sum of the in-phase and quadrature channels, and can be expressed as:

$$\begin{aligned} S^j_{B1}(t) =& A_{B1I} C^j_{B1I}(t) D^j_{B1I}(t) \cos(2\pi f_1 t + \varphi^j_{B1I}) \\ & + A_{B1Q} C^j_{B1Q}(t) D^j_{B1Q}(t) \sin(2\pi f_1 t + \varphi^j_{B1Q}), \end{aligned} \tag{2.11}$$

$$\begin{aligned} S^j_{B2}(t) =& A_{B2I} C^j_{B2I}(t) D^j_{B2I}(t) \cos(2\pi f_2 t + \varphi^j_{B2I}) \\ & + A_{B2Q} C^j_{B2Q}(t) D^j_{B2Q}(t) \sin(2\pi f_2 t + \varphi^j_{B2Q}). \end{aligned} \tag{2.12}$$

The B1I has a carrier frequency of 1561.098 MHz, whereas the B2I has a carrier frequency of 1207.140 MHz. The signal is transmitted in a RHCP, presenting a QPSK modulation mode, and a CDMA signal multiplexing mode. The 1dB Bandwidth (BW) is 4.092 MHz for the B1I, and 20.46 MHz for the B2I both centered at their respective carrier frequencies.

2.1.4.2 Beidou Code Characteristics

The B1I and B2I present a chip rate of 2.046 Mchips/s, being the length equal to 2046 chips. The B1I and B2I ranging codes (hereinafter referred to as CB1I and CB2I) are a balanced Gold code truncated with the last one chip. The Gold code is generated by means of Modulo-2 addition of G1 and G2 sequences which are respectively derived from two 11-bit linear shift registers. The generator polynomials for G1 and G2 are,

$$\begin{aligned} G1(X) =& 1 + X + X^7 + X^8 + X^9 + X^{10} + X^{11} \\ G2(X) =& 1 + X + X^2 + X^3 + X^4 + X^5 + X^8 + X^9 + X^{11}, \end{aligned} \tag{2.13}$$

with the 01010101010 as the initial phases for both G1(X) and G2(X). Figure 2.11 shows the ranging code generator for B1I and B2I.

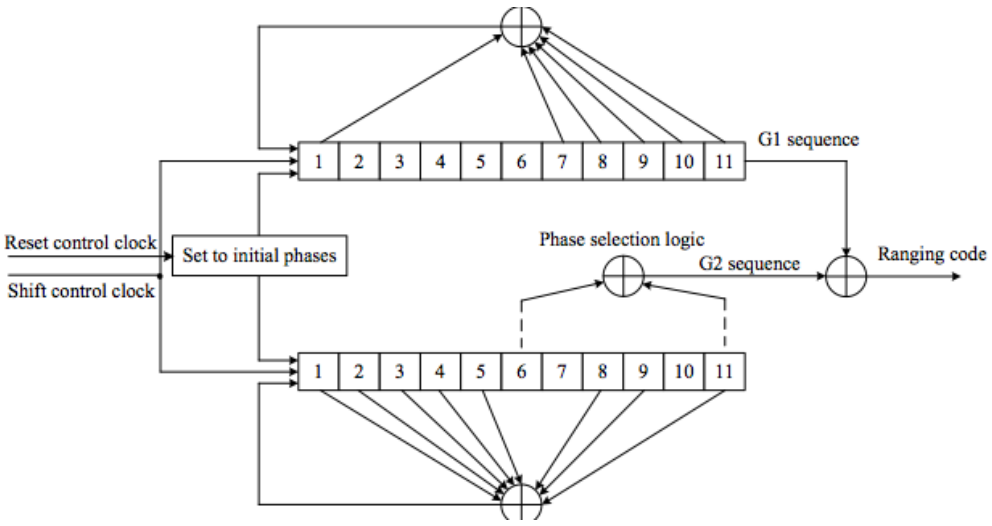

Figure 2.11: BeiDou ranging code generator.

The different phase shift of G2 sequence is accomplished by respective tapping in the shift register generating G2 sequence. By means of Modulo-2 addition of G2 with different phase shift and G1, a ranging code is generated for each satellite.

2.2 Principles of GNSS-R over the ocean

The GNSS-R approach allows retrieving geophysical parameters related to the observed surface. This is possible because the scattering process that watermarks the incoming GNSS signal depends on the surface characteristics. Therefore, it is necessary to understand the underlying scattering mechanism in order to perform the geophysical retrievals.

2.2.1 Derivation of the scattered field

GNSS-R is able to retrieve geophysical parameters through the scattering process where the signal interacts with the surface. Several models exist to describe the electromagnetic process over the ocean surface, which basically are assymptotic solutions of the Maxwell equations. Hence, two limits are usually considered, the Kirchoff Method (KM) [29], and the Small Pertubation Method (SPM) [30]. Aditionally there is a third one, the Two Scale Composite Model (2SCM), which combines both the KM and the SPM models. From the different models the most accepted and widely used is the Kirchoff Method under the Geometric Optics aproximation [11].

In the Kirchoff approximation, only the fields scattered by the large-scale surface component are taken into account. Considering the relatively low power and remoteness of GPS transmitters, it can be expected that only the signal scattered from the area around the specular point (the so-called glistering zone) will be received, dominating thus the quasi-specular reflections. According to the two-scale (or composite) roughness model [31], [32], this type of scattering is produced mostly by a large-scale (larger than several radio wavelengths) component of the surface. On the other hand, around the periphery of the glistering zone, the power scattered toward the receiver has been decreased significantly, being here where the Bragg resonant scattering from a small-scale surface component starts to be relevant. However, this kind of scattering is too weak, in order to be detected by the current receivers. Therefore it can be not considered in the analysis.

According to this, the scattered field based in the Kirchhoff approximation can be expressed as [11]

$$u(\vec{R}_r, t) = \frac{1}{4\pi} \int D(\vec{R}_s, t) \Re \frac{\partial}{\partial N} [U(\vec{R}_s) \exp(\frac{jKR}{R})], \tag{2.14}$$

where $D(\vec{R}_s)$ is the footprint function of the receiving antenna in terms of complex amplitudes, $\Re$ is the polarization sensitive reflection coeeficient, $\frac{\partial}{\partial N}$ is the normal

derivative, $U(\vec{R}_s)$ is the incident electric field at $\vec{R}_s$ on the large-scale rough surface, $K = K(f) = 2\pi f/c$, and R is the distance from the receiver to the point $\vec{R}_s$.

Assuming that the rough surface Σ within some limited area can be represented as a single-valued function $\zeta(\vec{r}, t)$ of the plane vector $\vec{r} = (x, y, 0)$ with $\langle \zeta \rangle = 0$, the integration over the surface Σ can be computed in function of the vector $\vec{r}$.

On the other hand, the complex amplitude U of the GNSS signal transmitted at the receiver position $\vec{R}_r$, can be written as,

$$U(\vec{R}_r, t) = \frac{1}{R_d} a(t - \frac{R_d}{c} \exp(j(KR_d - 2\pi f_c t))), \tag{2.15}$$

where R_d is the distance from a transmitter at R_t to the receiver at R_r, $a(t)$ is the code sequence (i.e C/A code), c is the speed of light, and f_c is the carrier frequency (i.e for the GPS L1 $f_c = 154 f_o$, where $f_o = 10.23$MHz). It is important to note that the modulation signal $a(t)$ as well the carrier wave propagates at the speed of light. On the other hand, is also important to consider that both the receiver and the transmitter are moving. These relative motions are producing a Doppler shift in the received signal. Thus Eqn.(2.15) can be expressed as,

$$U(\vec{R}_r, t) = U(\vec{R}_r, t_o) \exp(-j2\pi(f_c + f_D)t), \tag{2.16}$$

where f_D is the Doppler done by,

$$f_D(t_o) = |\vec{V}_t(t_o) - \vec{V}_r(t_o)|\vec{\kappa}(t_o)/\lambda, \tag{2.17}$$

being $\vec{V}_t$ and $\vec{V}_r$ the velocity vectors of the transmitter and the receiver, respectively, and $\vec{\kappa}(t_o)$ the unit vector pointing from a transmitter to a receiver.

Hence if the derivative $\frac{\partial}{\partial N}$ of Equ. (2.14) is computed as a function of Eqn. (2.16) and the derivatives of the slow-changing functions are neglected, Eqn. (2.14) becomes,

$$u(\vec{R}_r, t) = \int D(\vec{r}) a[t - (R_o - R)/c] g(\vec{r}, t) d\vec{r}, \tag{2.18}$$

where R_o is the distance from the transmitter at R_t to the point R_s on the rough surface, and $g(\vec{r}, t)$ is a complex random variable that accounts for the surface geometry

$$g(\vec{r}, t) = -\Re \frac{\exp(-j2\pi f t)}{j4\pi R_o R} \exp[jK(R_o + R)] \frac{q^2}{q_z}, \tag{2.19}$$

being q the scattering vector, and q_z the z component of the scattering vector.

If all the possible causes for a Doppler shift in the scattered signal are considered, Eqn. (2.19) becomes

$$g(\vec{r}, t_o + t') = g(\vec{r}, t_o) \exp(-j2\pi[f + f_D(\vec{r}, t_o)]t'), \tag{2.20}$$

where f_D is the total Doppler shift as the sum of the contribution of the Doppler shift due to the transmitter and receiver motions (Eqn. (2.17)), and the Doppler shift caused by the intrinsic motion of the surface. Respect this second term, considering that for an ocean surface the main contribution is given by the vertical component of the velocity of the surface gravitity waves, it can be expressed as:

$$f_s \approx q_z v_z / 2\pi, \tag{2.21}$$

2.2.2 Derivation of the Range-Coded Doppler-Limited Footprint Function

The voltage waveform $Y(t_o, \tau)$ at a given delay τ with respect to the specular delay t_o results from the cross-correlation between the scattered electric field obtained from the down-looking antenna and either (a) a locally generated replica of the open access code (for example, C/A code for GPS L1), up-converted to f_c and delayed by τ (in case of cGNSS-R) or (b) the direct signal transmitted by the GNSS satellite captured by an up-looking antenna (in case of iGNSS-R). Thus the voltage waveform can be expressed as [11]:

$$Y(t_o, \tau) = T_c \int D(\vec{r})[\chi(t_o, \delta\tau(\vec{r}), \delta f(t_o + \tau)]g(\vec{r}, t_o + \tau)d^2r, \tag{2.22}$$

where T_c is the coherent integration time, and $\chi(t_o, \delta\tau, \delta f)$ is the Woodward Ambiguity Function (WAF) [33]. The WAF can be expressed as:

$$\chi[t_o, \delta\tau, \delta f] = 1/T_c \int a(t_o + t')a(t_o + t' + \delta\tau) \exp(j2\delta f t')dt', \tag{2.23}$$

where

$$\delta\tau(\vec{r}) = \tau - |R_o(\vec{r}) + R(\vec{r})|/c, \tag{2.24}$$

and

$$\delta f(t_o + \tau) = f_D(t_o + \tau) - f_c. \tag{2.25}$$

If it is assumed that the Doppler frequency does not change significantly over time, so $\delta f(t_o + \tau)$ can be simplified as $\delta f(t_o)$, and thus $\chi(t_o, \delta\tau(\vec{r}), \delta f(t_o + \tau))$ as

$\chi(t_o, \delta\tau(\vec{r}), \delta f(t_o))$. For the sake of brevity, from now the WAF will be referred as $\chi(\delta\tau, \delta f)$.

On the other hand, due to the complexity to obtain an analytical expression for the WAF, a simple model is often used by separating the frequency and time variables and relying in the analytical behaviour along the temporal and frequency axes [11]. Therefore, at $\delta f = 0$, $\chi(\delta\tau, \delta f)$ is transformed in

$$\chi(\delta\tau, 0) = \frac{1}{T_c} \int a(t_o + t')a(t_o + t' + \delta\tau)dt', \tag{2.26}$$

which at the end is the Autocorrelation Function (ACF) of the code sequence (i.e. C/A code for the conventional case, and C/A, P and M codes for the interferometric case). At $\delta\tau = 0$, $\chi(\delta\tau, \delta f)$ becomes:

$$\chi(0, \delta f) = \frac{1}{T_c} \int \exp(-j2\pi\delta f t)dt = \frac{sin(\pi\delta f T_c)}{\pi\delta f T_c} \exp(-j\pi\delta f T_c), \tag{2.27}$$

which is the sinc function. Therefore the WAF can be approximated as the convolution between the ACF, and the sinc function (S) as:

$$\chi(\delta\tau, \delta f) = ACF(\tau)S(\delta f), \tag{2.28}$$

Hence, Eqn. (2.22) can be rewritten as:

$$Y(t_o, \tau) = T_c \int D(\vec{r})ACF[\delta\tau(t_o, \vec{r})]S[\delta f(t_o, \vec{r})]g(\vec{r}, t_o)d^2r. \tag{2.29}$$

In order to obtain the power waveform $|Y|^2$, some simplifications are required. Thus, according to [11] the functions over the integrated are expanded into Taylor series over ζ, withholding zero-order terms in slow functions $\Re$, D, a, and $\frac{1}{R_o R}$, and the first-order terms in the exponential. Therefore, the time-delayed average power waveform can be initially expressed as:

$$\begin{aligned}\left\langle |Y|^2 \right\rangle =& T_c^2 \int \left\langle (D \cdot ACF \cdot S \cdot g)'(D \cdot ACF \cdot S^* \cdot g^*)'' \right\rangle d^2r' d^2r'' \\ =& \frac{T_c^2}{16\pi^2} \int \Phi(\vec{r'}, \vec{r''})(\frac{D \cdot ACF \cdot S \cdot \Re \cdot q^2}{R_o R q_z})'(\frac{D \cdot ACF \cdot S^* \cdot \Re^* q^2}{R_o R q_z})'' \\ & \cdot \exp(jK(R_o' + R' - R_o'' - R''))d^2r' d^2r''. \end{aligned} \tag{2.30}$$

It is important to note that here the statistical averaging is related only to the surface elevations. This averaging produces $\Phi = \left\langle \exp(-jq_z'\zeta(\vec{r'}) + jq_z''\zeta(\vec{r''})) \right\rangle$. Φ will be computed considering the case of diffuse scattering regime characterized by the large Rayleigh parameter ($q_z^2(\zeta) >> 1$) applying thus the geometric optics limit. Note

that when the Rayleigh parameter is small ($q_z^2(\zeta^2) < 1$, i.e low winds), the function Φ tends to $\left\langle \exp[-jq_z'\zeta(\vec{r'})]\right\rangle\left\langle \exp[jq_z''\zeta(\vec{r''})]\right\rangle$, which is the coherent component of the scattered power, neglected here.

Introducing now the variables $\vec{\xi} = \vec{r'} - \vec{r''}$, and $\vec{\rho} = t(\vec{r'} + \vec{r''})/2$, and expanding $K(R_o' + R' - R_o'' - R'')$ into a Taylor series over $\vec{\xi}$ witholding only the linear term $-\vec{q}_\perp(\vec{\rho})\vec{\xi}$, and assuming $q_z' \approx q_z'' \approx q_z(\vec{\rho})$, Eqn. (2.30) can be written as:

$$\left\langle |Y(\tau)|^2 \right\rangle = T_c^2 \int \frac{D^2(\vec{\rho})ACF^2(\tau - (R_o + R)/c)|S[f_D(\rho) - f_c]|^2\sigma_o(\vec{\rho})}{4\pi R_o^2 R^2} d^2\rho, \quad (2.31)$$

with:

$$\sigma_o(\vec{\rho}) = \frac{|\Re(\vec{\rho})|^2}{4\pi}\frac{q^4(\vec{\rho})}{q_z^2(\vec{\rho})}\int \exp[-j\vec{q}_\perp(\vec{\rho})\vec{\xi}]\Phi(\vec{\xi},\vec{\rho})d^2\xi, \quad (2.32)$$

where:

$$\Phi(\vec{\xi},\vec{\rho}) = \left\langle exp\{-jq_z[\zeta(\vec{\rho} + \vec{\xi}/2) - \zeta(\vec{\rho} - \vec{\xi}/2)]\}\right\rangle. \quad (2.33)$$

Note that $\sigma_o(\vec{\rho})$ over ρ determines the so-called glistering zone of the surface. Based on the geometric optics limit, and thus, on the fact that only a small area $\xi \leq l_\phi$ significantly contributes to the integration over ξ, and expanding the different elevations ζ into a Taylor series over ξ, and withholding a linear term, Eqn. (2.33) becomes:

$$\Phi(\vec{\xi},\vec{\rho}) = \left\langle exp[-jq_z\zeta \bigtriangledown_\perp \zeta(\vec{\rho})]\right\rangle, \quad (2.34)$$

which allows to express Eqn. (2.32) as a function of the probability density function (PDF) of slopes ($P(\vec{s})$), as

$$\sigma_o(\vec{\rho}) = \pi\frac{|\Re|^2 q^4}{q_z^4}P(\frac{-q_\perp}{q_z}), \quad (2.35)$$

To finish, taking into account Eqn. (2.35), Eqn. (2.31) can be rewritten as:

$$\left\langle |Y(\tau)|^2 \right\rangle = T_c^2 \int \frac{|\Re|^2 D^2(\vec{\rho})ACF^2(\tau - (R_o + R)/c)|S[f_D(\rho) - f_c]|^2 q^4}{4R_o^2 R^2 q_z^4} P(-\frac{\vec{q}_\perp}{q_z})d^2\rho, \quad (2.36)$$

2.3 Conclusions

This chapter has provided a general description on the use of GNSS signals for ocean measoscale altimetry, where the main characteristics of the GPS, GLONASS, Galileo, and BeoDou 2 signals have been introduced. Additionally the main principles of the GNSS-R over the ocean has been described.

Chapter 3

Cross-correlation Waveform Analysis

This Chapter provides a critical review of the cross-correlation waveform model, addressing issues such as the correlation characteristics, the bandwidth, the observation geometry, and the thermal and speckle noises. It also provides a comprehensive and systematic overview of the impact of all the effects of system parameters on the GNSS-R observables. The results presented provide a reference set of analyses, useful to assess accurately the performance of cGNSS-R and iGNSS-R spaceborne and airborne systems.

3.1 Introduction

As it has been introduced previously, the use of GNSS signals to perform mesoscale ocean altimetry was proposed back to 1993 [6] as an alternative to a constellation of conventional nadir-looking altimeter satellites. Since then, different airborne, spaceborne and ground-based experiments have proven the feasibility of use GNSS reflectometry (GNSS-R) concept.

One of the main advantages that GNSS-R systems present with respect to classical altimetry is the possibility to track several GNSS reflections simultaneously (as many as GNSS satellites are in view, (including GPS, GALILEO, GLONASS, BEIDOU, etc)). This allows a wider coverage and higher temporal resolution than classical nadir-looking radar altimeters, with only one receiving satellite instead of eight nadir-looking altimeters required to achieve mesoscale observations with a seven-day revisit time, and a 50-km spatial resolution [35].

However, considering that in cGNSS-R altimetry the reflected signals are cross-correlated with local replicas of the open navigation signals (i.e. the GPS C/A code),

the lower power, and narrower bandwidth of GNSS signals by comparison to those used by conventional altimeter, lead to poorer per-pulse altimetry precision, accuracy and resolution. In order to improve the current altimetry performance obtained by cGNSS-R, ESA proposed the PARIS IoD mission [36], an implementation of the so-called interferometric processing (iGNSS-R) originally put forward in [6].

The interferometric processing consists of the measurement of the complex cross-correlation between the direct and reflected signals, instead of using a locally-generated clean replica of the transmitted signal. This should allow the exploitation of the full power spectrum of the transmitted GNSS signals, maximizing thus the height estimation precision, and improving the ranging precision. Nevertheless in this case the impact of thermal noise is higher than in cGNSS-R due to the presence of noise in both channels (up-looking, and down-looking). Therefore, for the same system parameters, the Signal-to-Noise (SNR) ratio obtained will be poorer in the iGNSS-R, than in the cGNSS-R [37], impacting thus the altimetric performance.

Several are the aspects that should be considered in the performance of the iGNSS-R technique. Hence, the first part of this PhD thesis, presents a deep review of the cross-correlation waveform model, where issues such as the autocorrelation properties of the signal, impact of the receiver bandwith, impact of the thermal and speckle noises, impact of the observation geometry (e.g, altitude, incidence angle, wind speed, etc) are addressed.

3.2 Cross-correlation

Considering that the C/A codes are basically PRN codes generated from two 10 bits linear feedback shift registers (LFSR), with a length of 1023 chips, and a period of 1 ms, the ACF can be approximated by a triangle function [11],

$$ACF_{CA}(\tau) = A^2(1 - \frac{|\tau|}{T_c}) \qquad \text{for} |\tau| \leq T_c. \tag{3.1}$$

On the other hand, the ACF(τ) of the composite L1 signal includes also the GPS P and M components, where the ACF of the P code can be also approximated by a triangle function, resulting in a 10 times narrow ACF respect the C/A one (since the $f_s = 10.23$ MHz), whereas the ACF function of the M code can be approximated as [34],

$$ACF_M(\tau) = \int_{-B/2}^{B/2} S_{BOC}(f) e^{j2\pi f\tau} d\tau, \tag{3.2}$$

where B is the bandlimited complex bandwidth and $S_{BOC}(f)$ is the power spectral density of the M code.

Therefore, it translates into an ACF much narrower for the L1 composite signal than for the L1 C/A due to the combination of these ACFs. Figure 3.1 shows the ideal magnitude-squared Auto-Correlation Function (ACF) obtained, with the GPS L1 composite signal (composed by the C/A, P and M components distributed in-phase and quadrature), and with the GPS L1 C/A component only.

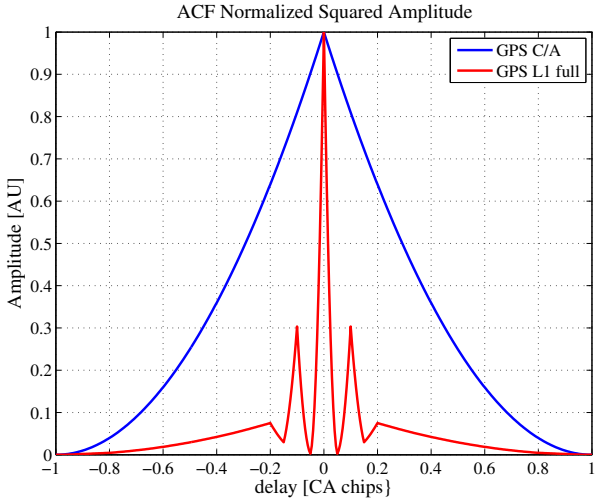

Figure 3.1: Squared ACF comparison of the C/A code (red), and the L1 GPS composite signal (blue).

On the other hand, the power spectra density of the C/A and P codes, can be expressed as:

$$S_{BPSK}(f) = A^2 T_c \left(\frac{\sin(\pi f T_c)}{\pi f T_c}\right)^2, \tag{3.3}$$

being $T_c = 1$ ms/1023 and $T_c = 1$ ms/10230, for the C/A and P codes, respectively. In the case of the M code, as it is a BOC (10,5) modulation, with $k = 2(T_c/T_s)$, the power spectrum can be expressed as:

$$S_{BOC}(f) = T_c \left(\frac{\sin(\pi f T_c)}{\pi f T_c}\right)^2 \tan^2\left(\frac{\pi f}{2 f_s}\right), \tag{3.4}$$

Figure 3.2 plots the normalized spectra of the C/A, P and M codes (top), and the spectrum of the GPS L1 composite signal (bottom). From it, it can be observed that the signal bandwidth of the C/A code at RF is 2.046 MHz (1.023 MHz at Base Band (BB)), and for the P code is 10 times the C/A (20.46 MHz), as expected. For

the GPS L1 composite signal the spectrum extends up to approximately 40 MHz, although the effective rms bandwidth (Gabor bandwidth) is smaller.

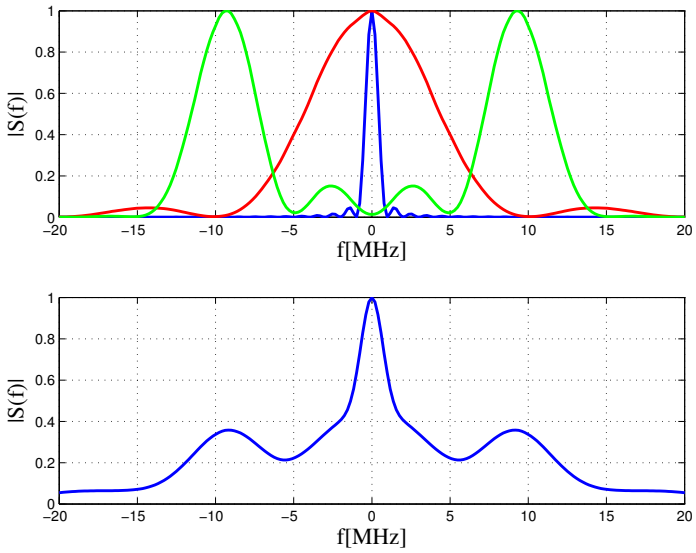

Figure 3.2: Normalized Spectra of the C/A (blue), P (red) and M codes (green) (top) and the L1 composite GPS signal (bottom).

Therefore, the narrower ACF obtained for the L1 composite signal, together with the wider bandwidth of the L1 composite signal, will in principle turn into a higher altimetry precision (note that the end performance will also depend on the SNR).

The reflected power waveforms ($|Y(\tau)|^2$) have been simulated for the L1 composite signal, and for the L1 C/A, considering a spaceborne observation scenario (the main system parameters are summarized in Table 5.6). In order to perform the simulation, a GNSS-R scenario has been defined using a local Cartesian coordinate system centered at the specular point, with the Transmitter-Specular Point- Receiver plane parallel to the Y-Z plane. Initially the positions of the receiver, transmitter, and an arbitrary surface point have been defined as:

$$\vec{R_t} = (0, \frac{h_o}{tan(\theta_{elev})}, h_o), \tag{3.5}$$

$$\vec{R_t} = (0, \frac{-h}{tan(\theta_{elev})}, h), \tag{3.6}$$

$$\vec{r} = (x, y, z), \tag{3.7}$$

where h_0 and h are the transmitter and receiver heights over the tangent plane at the specular point. In a spaceborne scenario, the Earth′s curvature is introducing

some effect on the surface scattering (which will increase with the altitude). Thus, the Earth′s surface should be consider to a first approximation as spherical surface. It can be easily done, computing the mean surface height (z_{mean}) as [62]:

$$z_{mean} = \sqrt{R_e^2 - x^2 - y^2} - R_e, \tag{3.8}$$

note that in the case of the tangent plane approximation $z_{mean} = 0$.

Figure 3.3 shows the reflected power waveform ($|Y(\tau)|^2$) simulated for the L1 composite signal (blue line) and for the L1 C/A (red line). As it can be appreciated at the zero delay point (which in the simulation it has been intentionally set to the delay that would have been observed for the specular point), the L1 composite waveform is much steeper than the L1 C/A waveform, leading thus for the same SNR to a better altimetric precision.

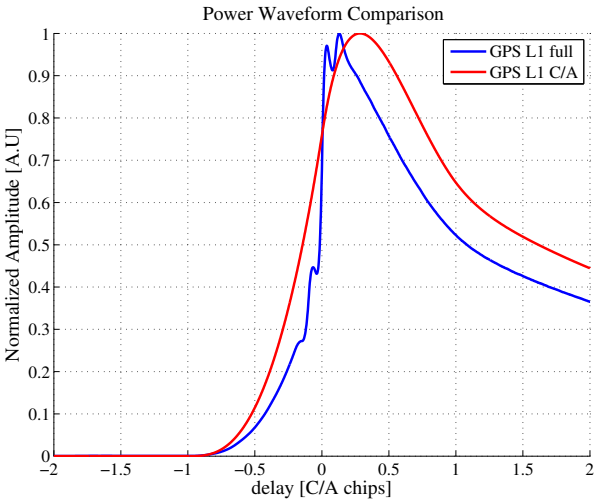

Figure 3.3: Sample normalized Power Waveforms for the GPS L1 composite (blue) and C/A (red).

On the other hand Fig. 3.4 represents the derivative of the waveforms relative to the GPS L1 case. As it can be appreciated there is a difference between the amplitude of the derivative for the interferometric and conventional waveforms, being the slope of the composite signal around 6 times larger than the one of the C/A code. Note that this difference is due basically to the steeper leading edge of the L1 composite power waveform.

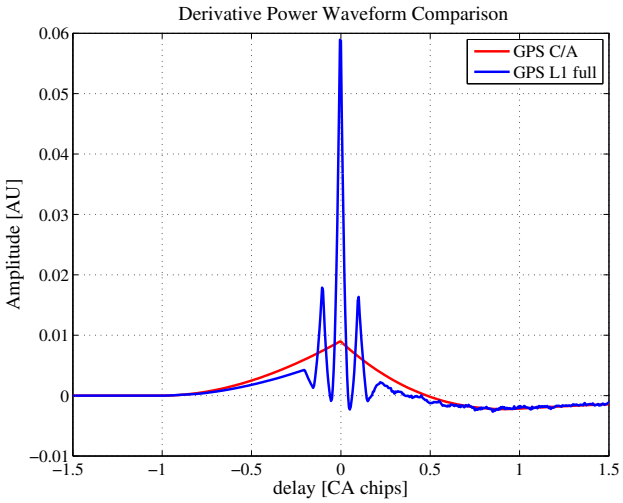

Figure 3.4: Waveforms derivative relative to the GPS L1 case.

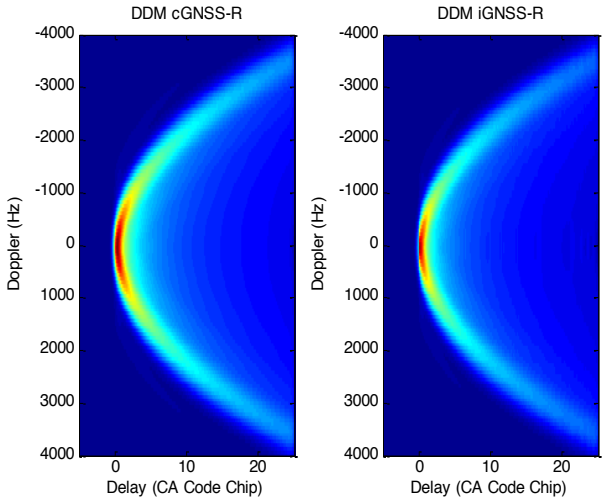

Figure 3.5: Noise- and speckle-free normalized DDMs derived with conventional GNSS-R (left) and with the interferometric GNSS-R (right) using the system parameters summarized in Table 5.6.

To finish, Fig. 3.5 shows the Delay Doppler Map (DDM) for both GPS L1 composite signal and GPS C/A. Note that the DDM is the reflected power waveform as a function of the relative delay, and the Doppler shift ($|Y(\tau, f_d)|^2$).

3.3 Bandwidth impact

As it has been introduced previously, the interferometric processing consists of performing the complex cross-correlation between the received direct and reflected sig-

Table 3.1: Simulation System Parameters

Parameter	**Value**	**Unit**
GPS altitude	20200	km
Receiver altitude	700	km
GPS velocity	3.87	km/s
Receiver velocity	7.5	km/s
Incidence angle (θ_i)	0	deg
Directivity (D)	19	dBi
Wind Speed (U_{10})	10	m/s
Coherent Int. Time (T_c)	1	ms

nals. Using this approach, an accurate estimation of the relative delay is possible, since all the codes embedded in a given GNSS frequency (including also the restricted access codes) are contributing to the cross-correlation shape (as shown in the previous section). Thus, the interferometric processing allows to exploit the full power spectral density of the GNSS signals. However, in the interferometric processing (iGNSS-R) the bandwidth (BW) is a critical parameter. On one hand, considering that both chains (up- and downlooking) have thermal noise, the SNR can be analytically expressed according to as [36]:

$$SNR = \frac{SNR_{cr}}{[1 + \frac{1+SNR_R}{SNR_D}]}, \tag{3.9}$$

where SNR_{cr} is the SNR at the output of the cross-correlator that would be obtained in the cGNSS-R case, and where SNR_R and SNR_D are the SNRs of the reflected and direct signals respectively, given by,

$$SNR_R = \frac{P_R}{kT_{Nr}BW}, \tag{3.10}$$

$$SNR_D = \frac{P_D}{kT_{Nd}BW}, \tag{3.11}$$

being P_R and P_D the total reflected power received in the main antenna beam at the input of the cross-correlator, and the power of the received direct signal respectively, k the Boltzman constant, and T_{Nd} and T_{Nr} are the system's noise temperature in the up- and down- chains respectively).

Rewritting Eqn. (3.9) only as a function of the BW, the impact that the BW has on the SNR can be computed (Eqn. 3.12). Figure 3.6 shows the SNR as a function of the BW. From it, it is possible to estimate the impact that the BW has on the SNR, which can be up to 30 dB for a BW = 100 MHz ($SNR_{BW=100MHz} - SNR_{BW=0.1MHz}$).

$$SNR = \frac{1}{[1 + \frac{1+(\frac{1}{BW})}{(\frac{1}{BW})}]}, \tag{3.12}$$

Hence, considering the impact that has the BW on the SNR ($\Delta SNR = SNR_{BW} - SNR_{BW=0.1MHz}$), and the expression given in [36] for the height precision, it is possible to compute the impact that the BW has on the height precision as,

$$\Delta\sigma_h = \sqrt{\left(1 + \frac{1}{\Delta SNR}\right)^2 + \left(\frac{1}{\Delta SNR}\right)^2} \tag{3.13}$$

Figure 3.18 plots the impact that has the BW in the height precision (computed only as a function of the SNR). As it can be observed, the degradation in the height precision can be around 22.5 cm approximately for BW equals to 100 MHz (Fig. 3.18). It is important to remark that this impact has been computed considering the impact that the bandwidth has on the SNR, considering the same system parameters for the different bandwidths. It means that this impact could be lower if other system parameters are considered, i.e antenna gain .

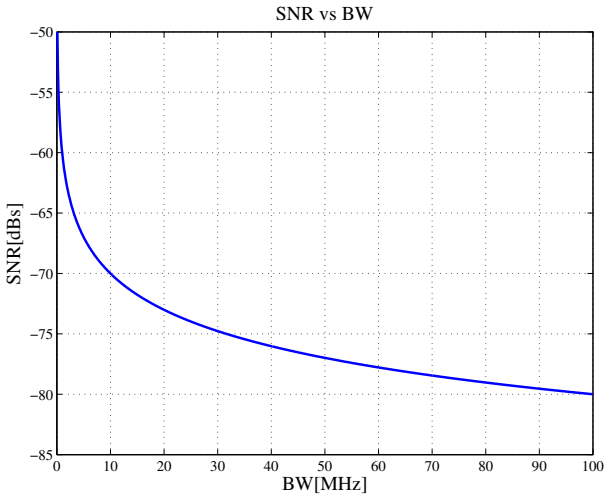

Figure 3.6: Impact that has the BW in the SNR.

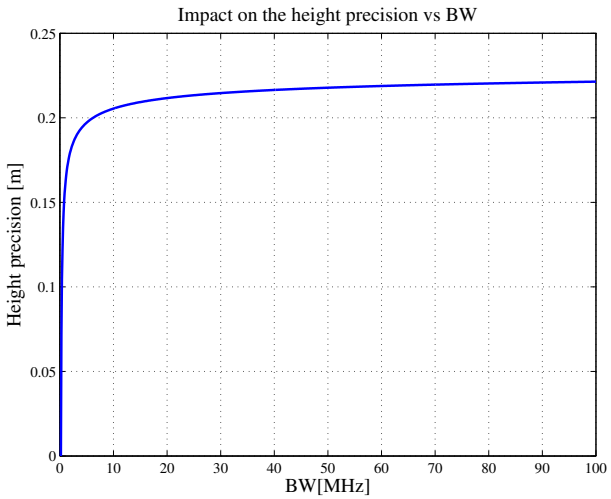

Figure 3.7: Impact that has the BW in the height precision.

On the other hand, the BW will also impact the ACF shape and thus the shape of the received power waveform. Hence, Fig. 3.8 shows the impact of the receiver's bandwidth in the ACF shape. As it can be appreciated the impact obtained for an IF bandwidth of 20 MHz (40 MHz at RF) is practically negligible as it can be expected, since as it has been shown that the GPS L1 composite signal extends up to about 20 MHz (40 MHz at RF). The impact at 10 MHz (20 MHz at RF) starts to be noticeable, and significant at 5 MHz (10 MHz at RF) and at 2.5 MHz (5 MHz at RF). From this bandwidth the ACF shape tends to become wider, yielding to lose of the accuracy gain introduced by the interferometric processing with respect to the conventional case. In fact the ACF shape tends to be closer to the one obtained with the C/A code only, as it can be observed. The impact that the instrument's bandwidth has on the ACF will translate into an impact in the Power Waveform obtained, as it can be observed in Fig. 3.9.

Therefore according to Figs. 3.8 and 3.9, as the bandwidth is reduced, the waveform shape tends to the one obtained by means of the cGNSS-R, being the waveform in the zero delay point less steeper, and thus getting a worse altimetry performance.

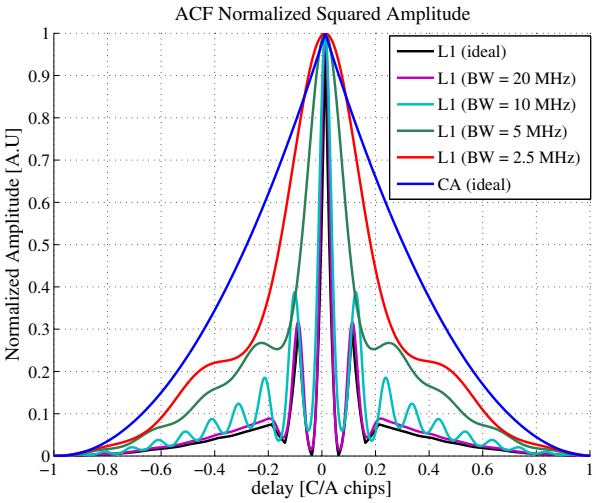

Figure 3.8: Squared normalized ACF for different band pass bandwidths.

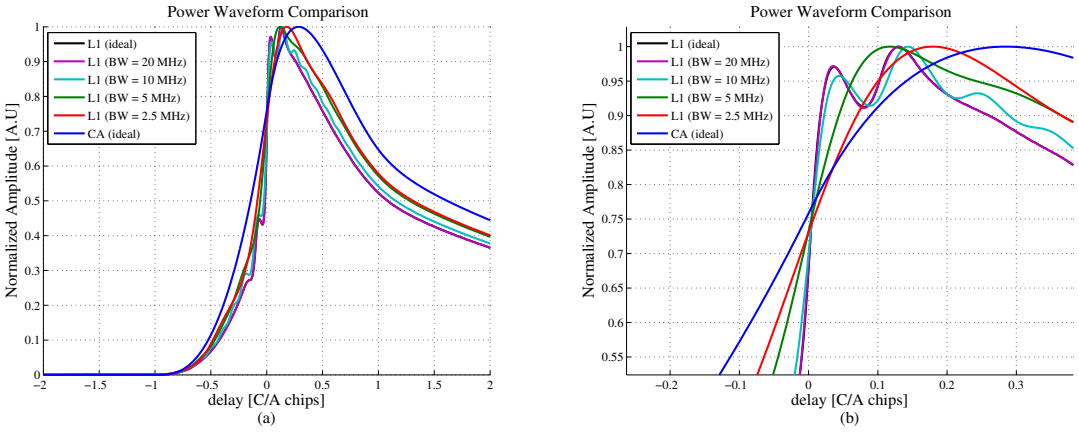

Figure 3.9: (a) Normalized Power Waveforms for differents band pass bandwidths, (b) Zoom of the centered part.

In order to determine the impact of the Radio Frequency (RF) bandwidth on the altimetry performance, the derivative of the waveform is plotted. The peak of the derivative determines a biased estimator of the specular point [38]. This bias is dependent on several filters, and also on the sea state. The unbiased specular delay will be computed from the biased estimator, and then corrected empirically [38].

For the sake of simplicity, in this section the displacement produced in the peak of the derivative due to the impact of the RF bandwidth is evaluated. The displacement has been computed with respect to the case where no filtering is applied. Figure 3.10 shows the derivatives of the waveforms of Fig. 3.9 around $\tau = 0$ with respect to the case of infinite bandwidth. As it can be appreciated, the differences around the

maximum derivative point used to define the biased specular reflected point are very low for the bandwidths of 20 and 10 MHz (40, and 20 MHz at RF). These differences start to be considerable at 5 MHz (10 MHz at RF), and are significant at 2.5 MHz (5 MHz at RF).

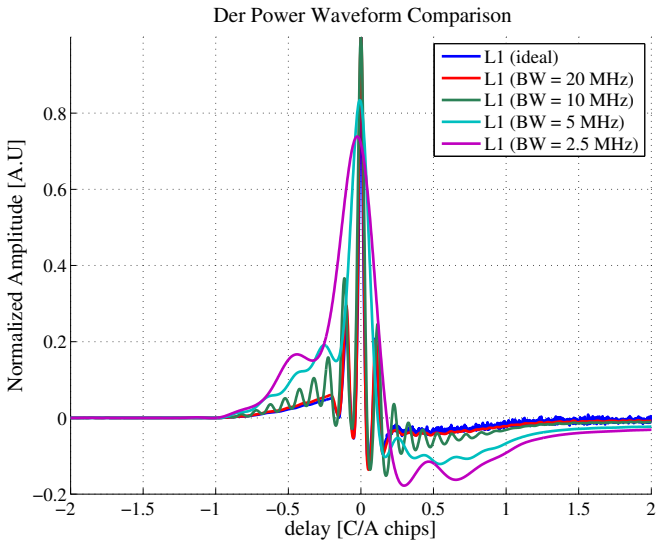

Figure 3.10: Derivatives of the Waveforms of Fig. 3.9 ($\tau = 0$ is relative to the peak derivative of the ideal Power Waveform).

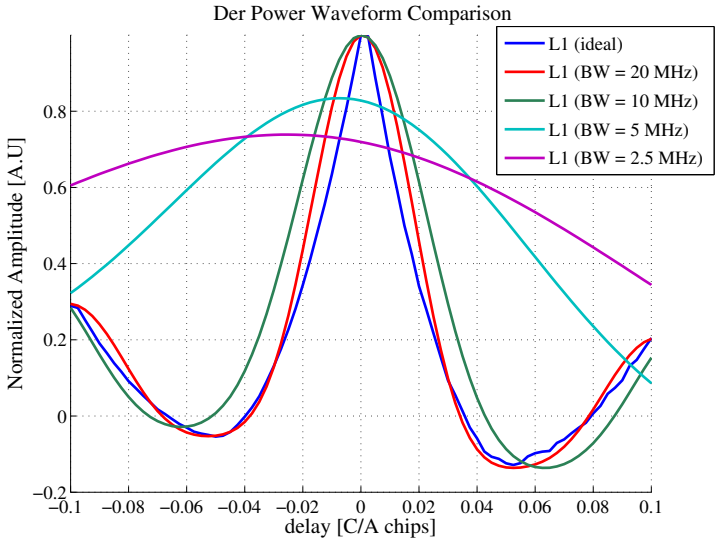

Figure 3.11: Zoom of the Waveform's derivatives of Fig. 3.10 around $\tau = [-0.1, 0.1]$.

The main displacements in the maximum derivative point with respect to the ideal case (where no filtering is applied), are summarized in Table 3.2. As mentioned

above, it can be concluded that the displacement is small for 20 MHz (40 MHz in RF) (around 14 cm approx.). At 10 MHz (20 MHz in RF) the displacement obtained is around 25 cm, which starts to be relevant, considering that oceanographers are looking at a few cm altimetry accuracy. For the lower receiver bandwidths are rather significant. In the next sections, the bias will be evaluated as a function of the sea state, considering different BWs.

Table 3.2: Displacement of the maximum derivative point respect to the original case (no filtered).

BW (MHz)	**Shift Max. Deriv. (C/A chips)**	**Shift Max. Deriv. (m)**
20	$\sim -4.63 \cdot 10^{-4}$	~ -0.14
10	$\sim -8.35 \cdot 10^{-4}$	~ -0.25
5	~ -0.0075	~ -2.26
2.5	~ -0.0242	~ -7.27

On other hand, as it can be expected, reducing the bandwidth the peak of the derivative function decreases, thus causing a proportional loss in range estimation accuracy, as it has been commented in the previous section. This reduction is practically negligible for 20 and 10 MHz (40 and 20 in RF), being for 5 MHz (10 MHz in RF) around 1.3%. For 2.5 MHz (5 MHz in RF) this reduction is higher being around 14.4%, whereas for 1 MHz (2 MHz in RF) this reduction is about 25.5%, which may have a significant impact on the altimetry performance.

3.4 Observation geometry

The shape of the waveform also depends on the observation geometry (i.e. altitude of the receiver, elevation of the transmitter, etc) and on the state of the observed scene (e.g. sea state) [39]. Figure 3.12 shows a comparison between different power waveforms computed as function of the geometry and sea state. Information on the peak value of the power waveform is also provided. The results obtained in these graphs will be analysed in the next sub-sections.

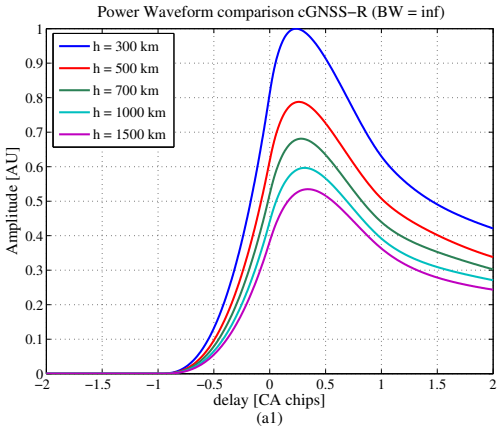

(a1)

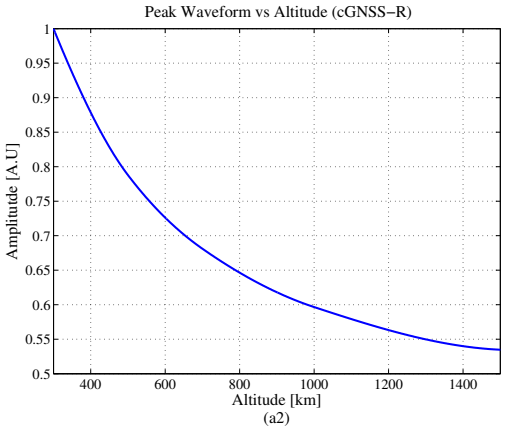

(a2)

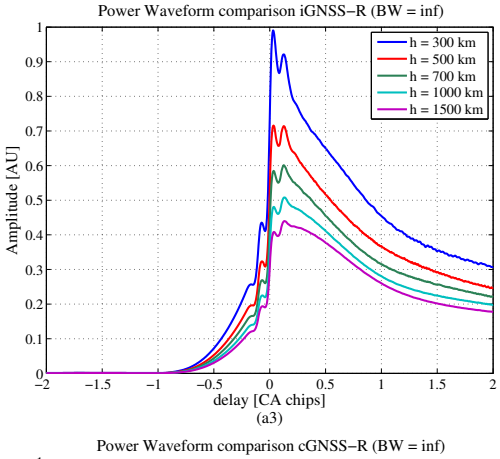

(a3)

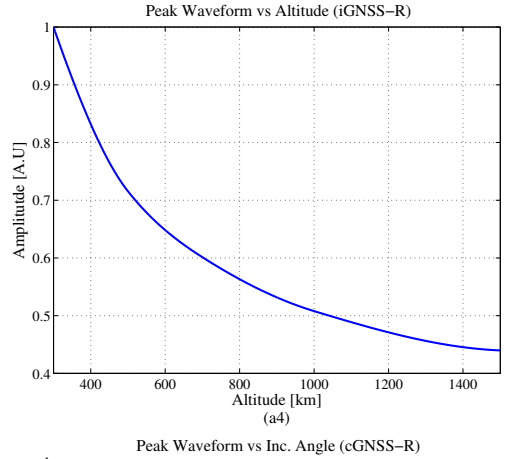

(a4)

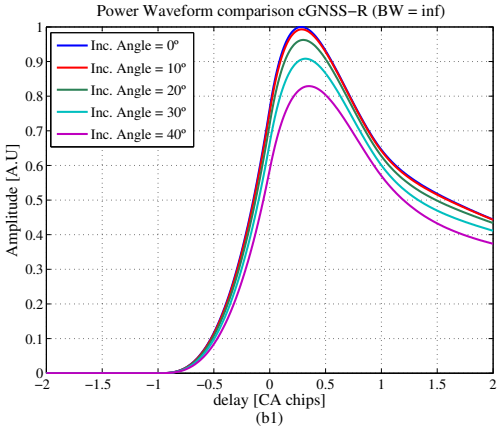

(b1)

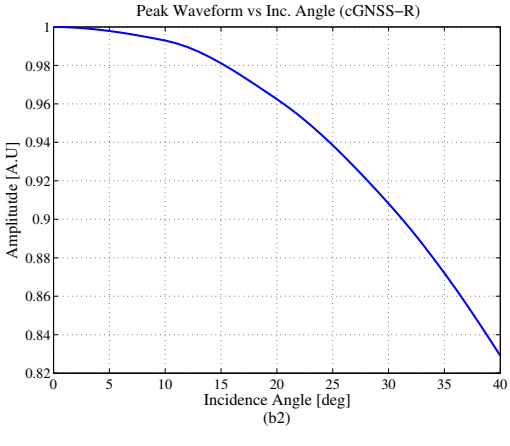

(b2)

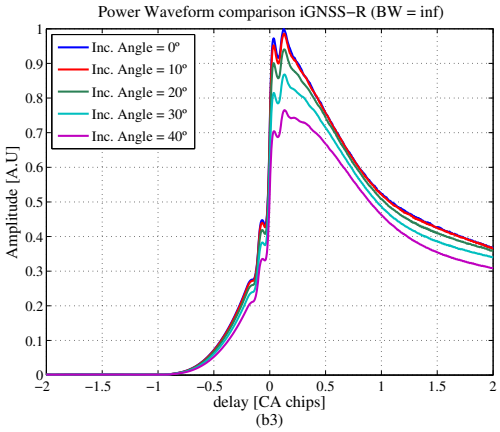

(b3)

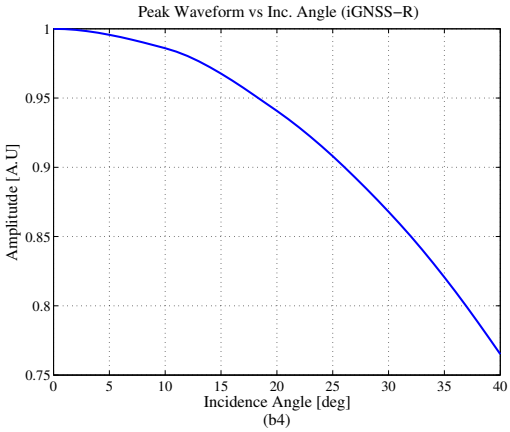

(b4)

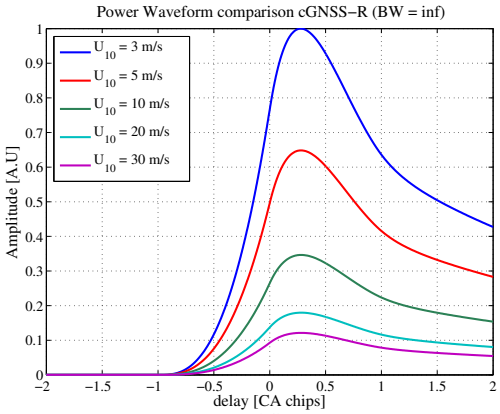

(c1)

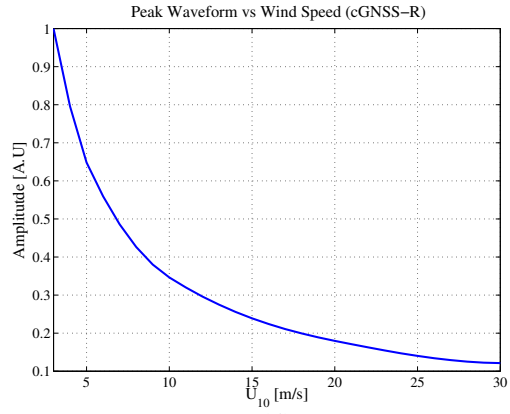

(c2)

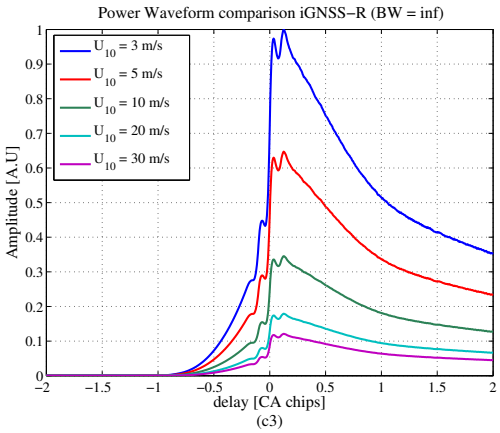

(c3)

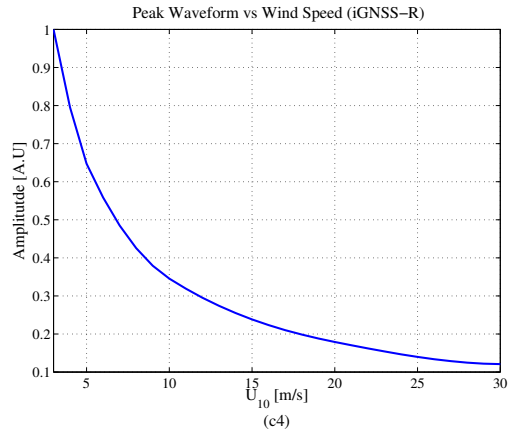

(c4)

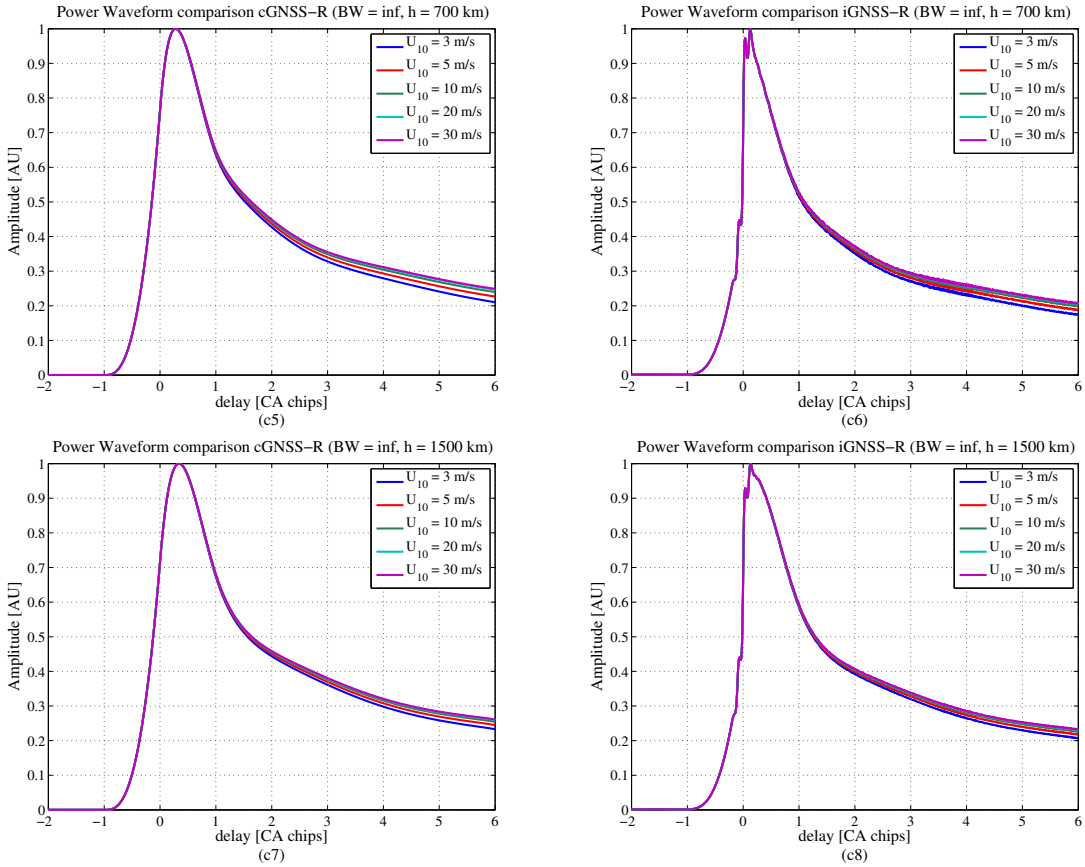

Figure 3.12: (a1) Normalized Power Waveforms (cGNSS-R) for different altitudes, relative to h=500 km, (a2) Normalized Peak Waveform evolution in function of the receiver altitude (cGNSS-R) relative to h=500 km (a3) Normalized Power Waveforms (iGNSS-R) for different altitudes relative to h=500 km, (a4) Normalized Peak Waveform evolution in function of the receiver altitude (iGNSS-R) relative to h=500 km, (b1) Normalized Power Waveforms (cGNSS-R) for different incident angles, relative to $\theta_{inc} = 0°$, (b2) Normalized Peak Waveform evolution in function of the incidence angle (cGNSS-R) relative to $\theta_{inc} = 0°$, (b3) Normalized Power Waveforms (iGNSS-R) for different incident angles, relative to $\theta_{inc} = 0°$, (b4) Normalized Peak Waveform evolution in function of the incidence angle (iGNSS-R) relative to $\theta_{inc} = 0°$, (c1) Normalized Power Waveforms (cGNSS-R) for different wind speeds, relative to $U_{10} = 3m/s$, (c2) Normalized Peak Waveform evolution in function of the wind speed (cGNSS-R) relative to $U_{10} = 3m/s$, (c3) Normalized Power Waveforms (iGNSS-R) for different wind speeds relative to $U_{10} = 3m/s$, (c4) Normalized Peak Waveform evolution in function of the wind speed (iGNSS-R) relative to $U_{10} = 3m/s$, (c5) Normalized Power Waveforms (cGNSS-R) for different wind speeds considering h=700 km and $\theta_{inc} = 0°$, (c6) Normalized Power Waveforms (iGNSS-R) for different wind speeds, considering h=700 km and $\theta_{inc} = 0°$, (c7) Normalized Power Waveforms (cGNSS-R) for different wind speeds, considering h=1500 km and $\theta_{inc} = 0°$, (c7) Normalized Power Waveforms (iGNSS-R) for different wind speeds, considering h=1700 km and $\theta_{inc} = 0°$.

3.4.1 Receiver height

In this section, very simple considerations on the dependence of the waveform properties with respect to the receiver height are studied for completeness. Figure 3.12 plots the power waveforms for different receiver heights, where Fig. 3.12 a1 shows it for the cGNSS-R case and Fig. 3.12 a3 for the iGNSS-R. From them, the first issue that can be observed is that, as it can be expected, the level of the power waveform decreases inversely to the receiver height. The evolution of the peak of the power waveform has been plotted in Fig. 3.12 a2 (cGNSS-R) and in Fig. 3.12 a4 (iGNSS-R). In both cases the trend is similar, being this reduction a bit higher in the iGNSS-R for the highest altitudes, but in any case, the difference is not too large). This decay can be fitted in both cases with a $\sim 95\%$ of precision by a negative exponential ($Peak\_Waveform = a \cdot \exp(h/b)$), where $a = 1.354$ and $b = -1381.2$ for the iGNSS-R case and $a = 1.261$ and $b = -1730.4$ for the cGNSS-R.

On the other hand as it can be observed in Fig. 3.12 a3, the shape of the peak of the waveforms changes. This is due on one hand to the distribution of the delay and the power scattered, which is different for the different altitudes considered, and on the other hand to the shape of the ACF in the iGNSS-R (see Fig.3.1).

3.4.2 Incidence Angle

The incidence angle plays an important role, and different issues can be affected by the incidence angle (θ_i). Hence, according to [36], as the incidence angle increases, the error in the range measurements ($\delta\rho$) increases, resulting in a larger height error (δh) as:

$$\delta h = -\frac{\delta\rho}{2cos\theta_i}. \tag{3.14}$$

Also, if the incidence angle increases, the slant path accross the ionosphere increases, and hence the ionospheric delay and refraction, leading, as a consequence, the larger ionospheric residual errors. Additionally, as the downlooking antenna is pointing to nadir, its gain will be reduced with increasing incidence angles, resulting thus in noisier range observations. On the other hand, the number of reflections points increases with the incidence angle and the swath (coverage and revisit time) improves.

Figures 3.12 c1 and c3 show the Power Waveforms for the cGNSS-R and for the iGNSS-R cases as a function of the incidence angle, and Figs. 3.12 c2 and c4 show the Peak Waveform evolution as a function of the incidence angle. It is worth reporting

that, apart from the typical effects due to change of the observation geometry, the incidence angle has an effect on the Fresnel reflection coefficient ($\Re_{lr}$), defined as:

$$\Re_{LR} = \frac{1}{2} \cdot (R_{VV} - R_{HH}), \tag{3.15}$$

where $\Re_{VV}$ and $\Re_{HH}$ are:

$$\Re_{VV} = \frac{\varepsilon \cos\theta_i - \sqrt{\varepsilon - \sin^2\theta_i}}{\varepsilon \cos\theta_i + \sqrt{\varepsilon - \sin^2\theta_i}}, \tag{3.16}$$

$$\Re_{HH} = \frac{\cos\theta_i - \sqrt{\varepsilon - \sin^2\theta_i}}{\cos\theta_i - \sqrt{\varepsilon - \sin^2\theta_i}}, \tag{3.17}$$

being θ_i the incidence angle and ε the dielectric constant. Figure 3.13 shows the evolution of ($\Re_{lr}$) as a function of the incidence angle. In the range from $\theta_i = 0°$ to 35°, the decrease of $\Re_{LR}$ is just $\sim 0.4\%$, thus it can be considered negligible in front of other factors.

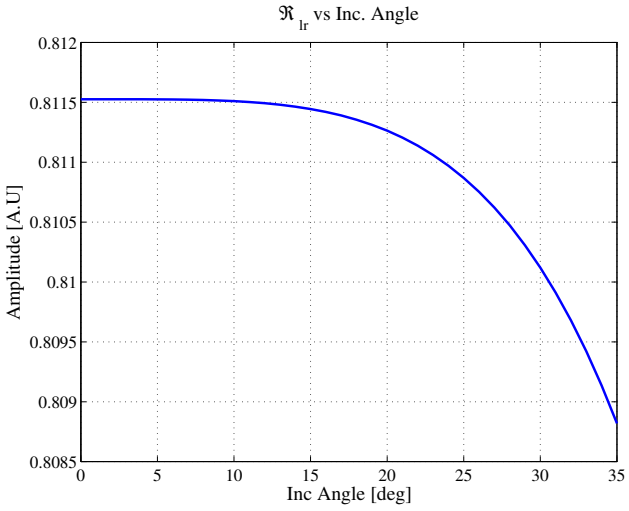

Figure 3.13: Impact of the θ_{inc} on $\Re_{lr}$.

3.4.3 Wind Speed

This section presents an analysis of the wind speed effects on the power Waveforms. In the simulations performed, the scattering coefficient has been computed according to [11] based on the Kirchhoff Approximation - Geometric Optics (KA-GO). Considering the KA-GO approximation, the radar cross-section density (σ_o) can be expressed as a function of the probability density function (pdf) of the slopes ($P(\vec{s})$) as:

$$\sigma_o(\vec{\rho}) = \frac{\pi |\Re|^2 q^4}{q_z^4} P(-\frac{\vec{q_\perp}}{q_z}), \tag{3.18}$$

where $\Re$ is the Fresnel polarization coefficient, and q_z and $q_\perp$ are the vertical and horizontal components of the scattering vector (q) respectively defined as:

$$q = k(\vec{n} - \vec{m}), \tag{3.19}$$

where $k = 2\pi/\lambda$, and $\vec{n}$ and $\vec{m}$ are the unit vector of the scattered and incident waves respectively. Assuming that sea surface slope pdf has a normal distribution, and expressing it as a function of the up-wind and cross-wind components, it can be written as a:

$$P(-\frac{\vec{q_\perp}}{q_z}) = \frac{1}{2\pi\sqrt{\sigma_u}\sqrt{\sigma_c}} exp[-\frac{1}{2}(\frac{k_x^2}{\sigma_u^2} + \frac{k_y^2}{\sigma_c^2})], \tag{3.20}$$

being σ_u and σ_c the mean square slopes in the up- and cross-wind directions respectively, and $k_x = -q_x/q_z$ and $k_y = -q_y/q_z$. According to [40] the mean square slope variations respect to the wind speed (including winds above 35 meters per second), can be modelled easy as,

$$\sigma_u(U_{10}) = 0.45 \cdot (0.000 + 0 - 00316 \cdot f(U_{10})), \tag{3.21}$$

$$\sigma_c(U_{10}) = 0.45 \cdot (0.003 + 0 - 00192 \cdot f(U_{10})), \tag{3.22}$$

with $f(U_{10})$ being a function of the wind speed as,

$$\begin{aligned} f(U_{10}) &= U_{10}, && 0 < U_{10} < 3.49 \\ f(U_{10}) &= 6\ln(U_{10}) - 4.0, && 3.49 < U_{10} < 46, \\ f(U_{10}) &= 0.411 \cdot U_{10}, && 46 < U_{10} \end{aligned} \tag{3.23}$$

Figures 3.12 c1-c4 show the waveforms derived for different wind speeds considering an altitude of 700 km and an incidence angle of 0°. As it can be observed, the maximum peak power is obtained for a wind speed of 3 m/s (in which case the reflection is nearly specular), decreasing it with the wind speed. On the other hand it can be appreciated that the waveform peak power tends to saturate for high wind speeds. This is basically due to the logarithmic dependence of the relationship between sea surface slopes and wind speed as presented in Eqn. (3.23).

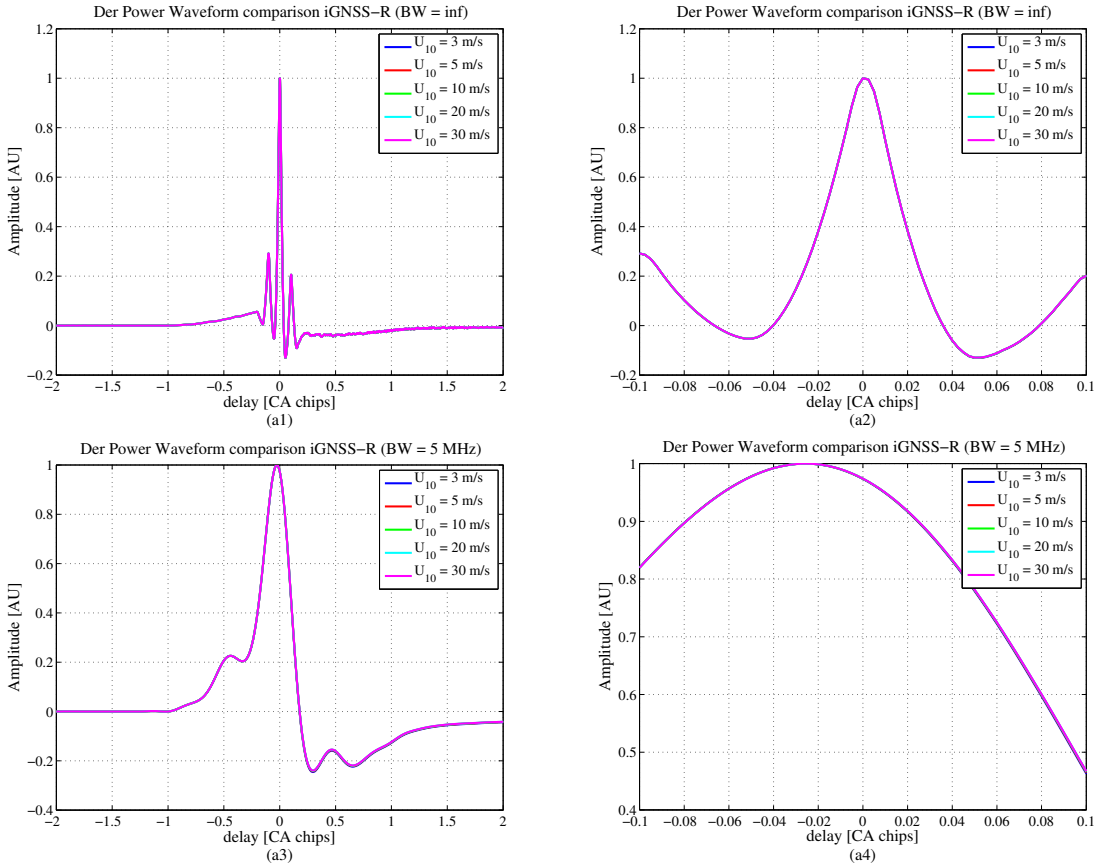

Figure 3.14: (a1) Power Waveform derivative for different wind speeds considering an infinite bandwidth, (a2) Zoom of the derivatives computed in a1 between -0.1 and 0.1 CA chips, (a3) Power Waveform derivative for different wind speeds considering a 5 MHz bandwidth, (a4) Zoom of the derivatives computed in a3 between -0.1 and 0.1 CA chips.

Figures 3.12 c5-c8 depict the normalized power waveforms for the cGNSS-R and iGNSS-R cases considering a nadir observation and receiver altitudes of 700 and 1500 km, respectively. It can be clearly noticed that the wind speed mainly affects the trailing edge of the normalised power waveforms. It is important to highlight that the sensitivity of the trailing edge to wind speed is lower for higher altitudes.

Figure 3.14 plots the point of the Waveform's maximum derivative as a function of the wind speed. From Figs. 3.14 a1 and a2, the maximum derivative point obtained seems not to be sensitive to wind speed, suggesting that it is potentially a very good observable for altimetry. The latter analysis has been repeated applying the receiver filtering. Also in this case, as depicted in Figs. 3.14 a3 and a4, significant changes in the maximum derivative point are not observed.

Figure 3.15a presents the position of the peak derivative as a function of the wind

speed for different receiver bandwidths. From Fig. 3.15a significant changes are not observed in the position of the peak derivative due to the wind speed. On the other hand Fig. 3.15b plots the position of the peak as a function of wind speed, but now focusing in the case of a receiver bandwidth of 20 and 2.5 MHz (40 and 5 MHz in RF). From it, a displacement of $\sim$ 2 cm in the position of the peak occurs for the 20 MHz (40 MHz in RF) case between the lower and higher wind speed considered in this case, whereas for the 2.5 MHz (5 MHz in RF) the displacement obtained is a bit higher (around 6-7 cm). Thus the displacement of the peak derivative due to the wind speed tends to increase as the receiver bandwidth is reduced. In any case this displacement is negligible even more if it is compared to the displacement due to the receiver bandwidth.

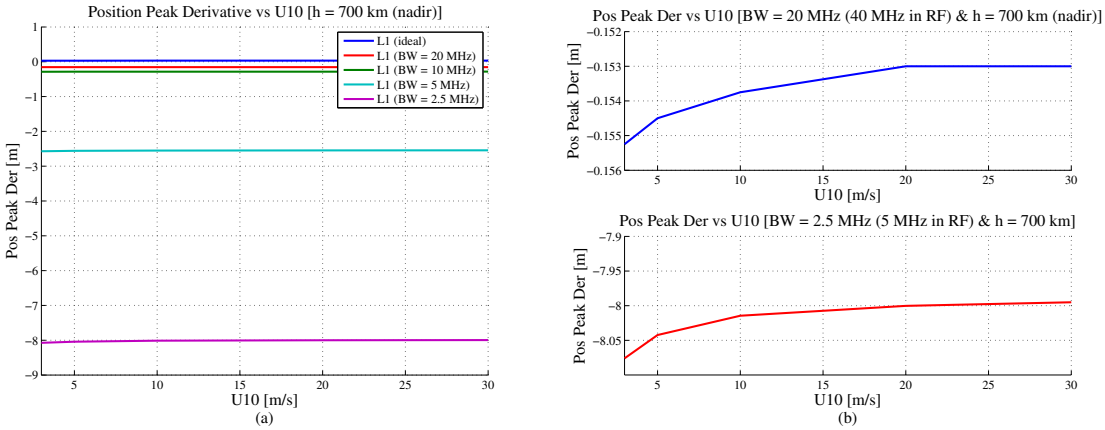

Figure 3.15: (a) Position of the peak derivative as a function of the wind speed for different receiver bandwidths, (b) Position of the peak derivative as a function of the wind speed for the 20 MHz (top) and 2.5 MHz (bottom) receiver bandwidths.

To finish, Fig. 3.16 plots the position of the peak derivative as a function of the wind speed, computed for different altitudes, and incidence angles (for a 20 MHz and 2.5 MHz receiver bandwidths). As it can be appreciated, the position of the peak derivative tends to change with the receiver altitude and with the incidence angle, being the impact of the receiver altitude more important than the incidence angle. From Fig. 3.16, a displacement of 20 cm in the position of the peaks occurs between the lower and higher reciver altitude for a 20 MHz receiver bandwidth (40 MHz in RF), whereas for a 2.5 MHz receiver bandwithd (5 MHz in RF), the displacement is around 5 meters. In the case of the incidence angle, the displacement obtained between the lower and upper values considered in the simulations is around 6 cm for a receiver bandwidth of 20 MHz (40 MHz in RF) and about 1.2 m for a receiver

bandwidth of 2.5 MHz (5 MHz). Therefore the impact that the receiver bandwidth has in the position of the derivative peak, varies as a function of the receiver altitude and incidence angle as well

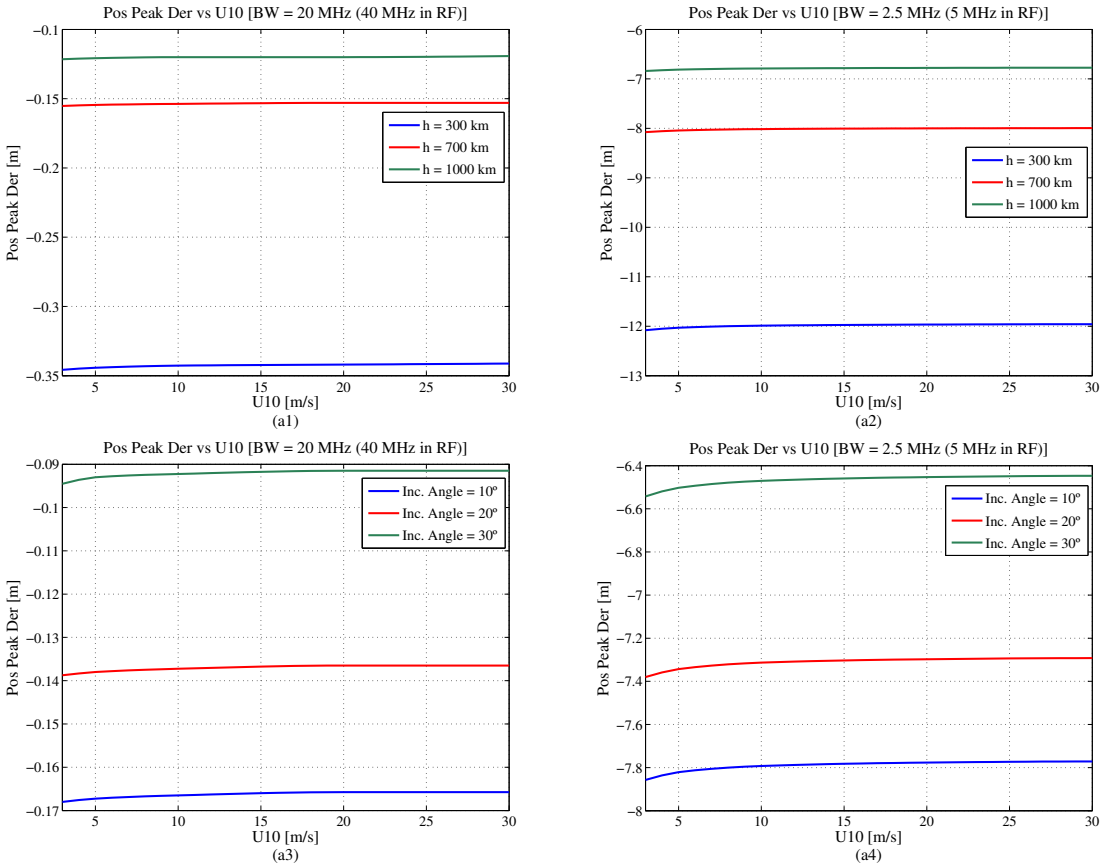

Figure 3.16: Position of the peak derivative in function of the wind speed for different altitudes (nadir case) for a bandwidth of 20 MHz (40 MHz in RF)(a1) and 2.5 MHz (5 MHz in RF)(a2), and position of the peak derivative in function of the wind speed for different incidence angles (at 700 km) for a bandwidth of 20 MHz (40 MHz in RF) (a3) and 2.5 MHz (5 MHz in RF) (a4).

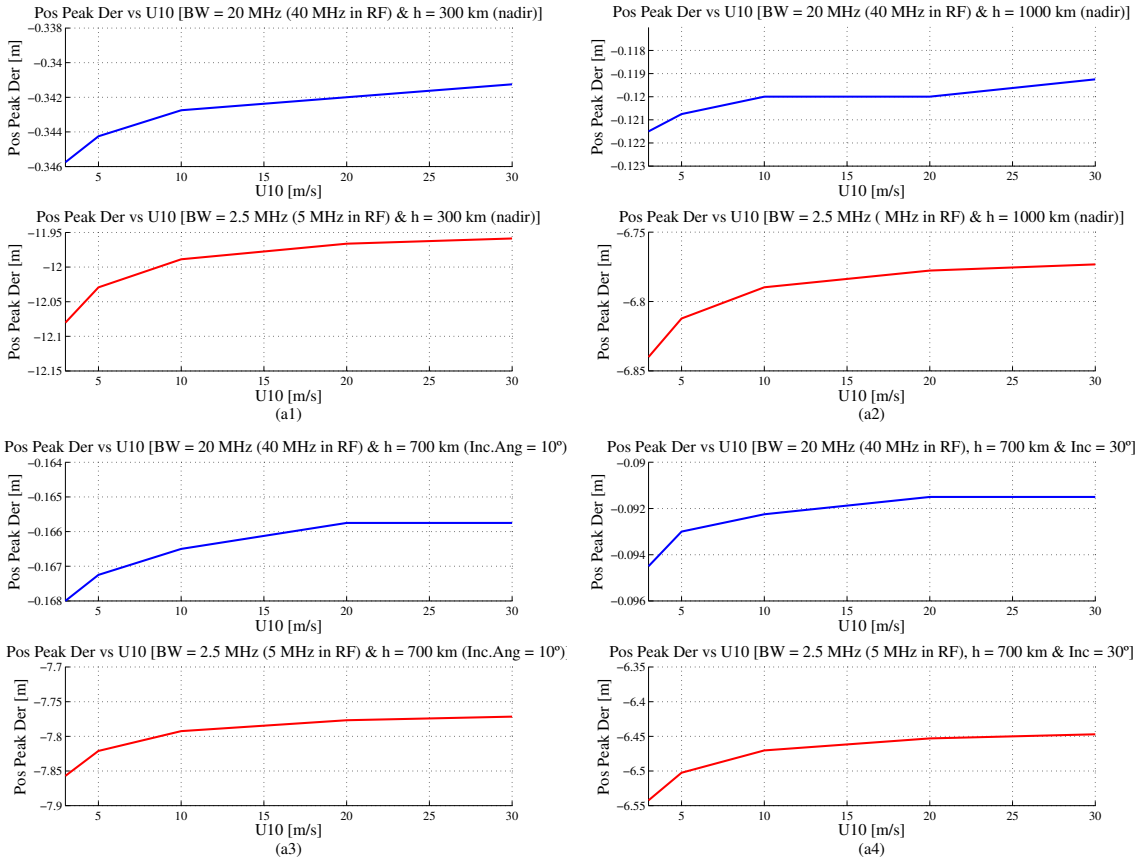

Figure 3.17: Position of the peak derivative in function of the wind speed for for 300 km (a1), and 1000 km (a2) receiver altitudes (both at nadir), and for an incidence angles of 10° (a3), and 30° (a4) at 700 km.

On the other hand Fig. 3.17 shows clearly the impact that the wind speed has as a function of the altitude and incidence angle. It can be appreciated that the displacement due to the wind speed, for a 20 MHz receiver bandwidth (40 MHz in RF), is very low, just a few milimeters. Thus, for a large receiver bandwidth, the impact that has the incidence angle in the displacement caused by the wind speed is practically negligible (2 mm), whereas the impact of the altitude is a bit higher when is considered the 300 km case (4-5 mm). In any case the displacement still negligible as compared to other sources affecting the altimetry error budget [53]. As the receiver bandwidth decreases, the displacement due to the wind speed increases. Hence for an altitude of 300 km this displacement is around 15 cm, whereas for an altitude of 1000 km is around 8 cm. In the same way for the incidence angles are obtained a displacement of 8 cm for an incidence angle of 10° and 10 cm for an incidence angle of 30°. In any case, that displacement still small even more if it is compared with the one due to the receiver bandwidth.

Therefore, as a first approximation, it can be concluded that the bias obtained in the previous section, is an instrumental bias and can it be accurately characterized and calibrated. Is important consider that in the simulations performed has not been taken into account the effect of the swell, and the electromagnetic bias resulting from the non linear nature of the ocean waves [42]-[44].

3.5 Thermal Noise

Thermal noise is an additive Gaussian noise, whose power at the input of the cross-correlator is given by:

$$\left\langle |n(t)|^2 \right\rangle = kT_{sys}B, \tag{3.24}$$

where k is the Boltzmann constant ($k = 1.38 \cdot 10^{-33}$ J/K), T_{sys} is the system noise temperature ($T_{sys} = T_A + T_R$), being T_A the antenna temperature, T_R the receiver noise temperature, and B the receiver's noise bandwidth.

At the output of the cross-correlator the thermal noise is reduced by the coherent integration time according to:

$$\left\langle |n(t)|^2 \right\rangle = kT_{sys}/T_c, \tag{3.25}$$

3.5.1 Conventional GNSS-R

In the cGNSS-R, the received ocean scattered GNSS signal is cross-correlated with a clean replica of the C/A code generated on board the satellite. Thus, in this case the cross-correlation output can be written as,

$$Y(t,\tau) = \frac{1}{T_c}\int_{-T_c/2}^{T_c/2} v_r(t+t')v_d^*(t+t'-\tau)dt', \tag{3.26}$$

where v_r is the received ocean scattered GNSS signal, formed by the useful signal and the noise terms ($v_r(t) = s_r(t) + n(t)$), and v_d is the direct signal, in this case the clean replica generated on board ($v_d(t) = s_d(t)$). Note that it has been assumed that the replica is exactly equal to the transmitted signal, while it may show some small deviations with respect to the real transmitted signal.

According to [45], the received power can be expressed as the sum of two components (the useful signal and the noise component):

$$\left\langle |Y(t,\tau)|^2 \right\rangle = \left\langle |Y_s(\tau)|^2 \right\rangle + \left\langle |Y_n(\tau)|^2 \right\rangle. \tag{3.27}$$

3.5.2 Interferometric GNSS-R

For the interferometric processing, the effect of thermal noise may become more relevant in terms of the achievable performance, since it is present in both the up-looking and down-looking channels. Considering that both thermal noise components are uncorrelated, the cross-correlation output can be written again as Eqn. (3.26), where now both the received direct and reflected signals ($v_{r/d}$) are the sum of the useful signal $s(t)$ and the thermal noise $n(t)$ components ($v_{r/d}(t) = s_{r/d}(t) + n_{r/d}(t)$). Thus, the cross-correlation output can be represented as,

$$Y(t,\tau) = Y_s(\tau) + Y_{Nd}(\tau) + Y_{Nr}(\tau) + Y_{Ndr}(\tau), \tag{3.28}$$

where $Y_s(t,\tau)$ is the signal voltage cross-correlation, $Y_{Nd}(t,\tau)$ is the reflected signal and up-looking noise voltage cross-correlation, $Y_{Nr}(t,\tau)$ is the direct signal and down-looking noise voltage cross-correlation and $Y_{Ndr}(t,\tau)$ is the up-looking noise and down-looking noise voltage cross-correlation. From it, and considering that the signal and the thermal noise components present in both channels (up and down) are uncorrelated, the average power can be expressed as the sum of four power terms [36]:

$$\left\langle |Y(t,\tau)|^2 \right\rangle = \left\langle |Y_s(\tau)|^2 \right\rangle + \left\langle |Y_{Nd}(\tau)|^2 \right\rangle + \left\langle |Y_{Nr}(\tau)|^2 \right\rangle + \left\langle |Y_{Ndr}(\tau)|^2 \right\rangle, \tag{3.29}$$

where $\langle |Y_s(\tau)|^2 \rangle$ is the reflected average power waveform, $\langle |Y_{Nd}(\tau)|^2 \rangle$ is the product of the reflected signal average power at the input of the cross-correlator and the down-looking noise power at the output of the cross-correlator, $\langle |Y_{Nd}(\tau)|^2 \rangle$ is the product of the direct signal average power at the input of the cross-correlator and the up-looking noise power at the output of the cross-correlator, and $\langle |Y_{Ndr}(\tau)|^2 \rangle$ is the product of the down-looking and up-looking channel noise power.

3.6 Speckle Noise

Speckle noise (also known as fading) is an important factor affecting the performance of radars. Speckle arises when a radar pulse coherently illuminates a certain surface area consisting of many elementary point scatterers (distributed scattering). In these conditions, the returned echo consists of the coherent addition of the echoes from the elementary scatterers, which is thus very sensitive to the viewing observation geometry.

It can be shown that the resultant complex echo signal has a zero-mean two dimensional Gaussian probability density function (pdf) in the complex plane [46]. Hence,

the absolute value of the complex speckle (the envelope) has a Rayleigh distribution, and the power has a negative exponential distribution. Taking into account the property of the Rayleigh random variables ($\mu/\sigma = 1.91$, where μ is the mean and σ is the variance of a Rayleigh random variable), it means that the signal to speckle noise ratio is equal to 5.6 dB (20·log 1.91) [48].

$$\begin{aligned} \mu(x) &= \sigma\sqrt{\frac{\pi}{2}} \approx 1.253\sigma, \\ \sigma(x) &= \frac{4-\pi}{2}\sigma^2 \approx 0.429\sigma^2, \\ \frac{\mu(x)}{\sigma(x)} &\approx \frac{1.253\sigma}{\sqrt{0.429\sigma^2}} \approx 1.91. \end{aligned} \tag{3.30}$$

As the speckle noise is a multiplicative noise (proportional to the waveform amplitude), it cannot be reduced by increasing the transmitted signal power. In order to mitigate it, incoherent averaging should be applied. The effectiveness of the incoherent averaging will depend on the correlation between consecutive waveforms. In order to consider that the different waveforms are uncorrelated, it is necessary that the reflecting surface or viewing geometry changes significantly. For Low Earth Orbits (LEO) altitudes, the peak correlation time has been estimated on the order of 1 ms [18] and [47], for a conventional GNSS-R system based on C/A code signal reception. If the receiver is moving faster, the coherent correlation time will shorten, and if it slows it will lengthen. However, even in the case of a stationary receiver the sea surface movement will change sufficiently to decorrelate the samples eventually.

In this section, the correlation time between consecutive waveforms at the same delay and Doppler has been evaluated considering different scenarios. Here, the correlation time has been computed as the interval over which the magnitude of the autocorrelation diminishes by a factor of e, where the autocorrelation of the complex waveforms, has been defined as,

$$|R_Y(\tilde{t})| = E\{Y(t+\tilde{t})Y^*(t)\}, \tag{3.31}$$

In Fig.3.18 the correlation time has been computed for a spaceborne case (LEO orbit) using the UK-DMC data (L1 C/A component only) [19] and [68]. As it can be appreciated the correlation time between consecutive waveforms for the UK-DMC data, is less than 1 ms (the level of correlation decreases very quickly being practically zero at 1 ms). It is important to note that the results presented here correspond to a space-borne scenario, with an altitude of 700 km, and a wind speed of 7.8 m/s.

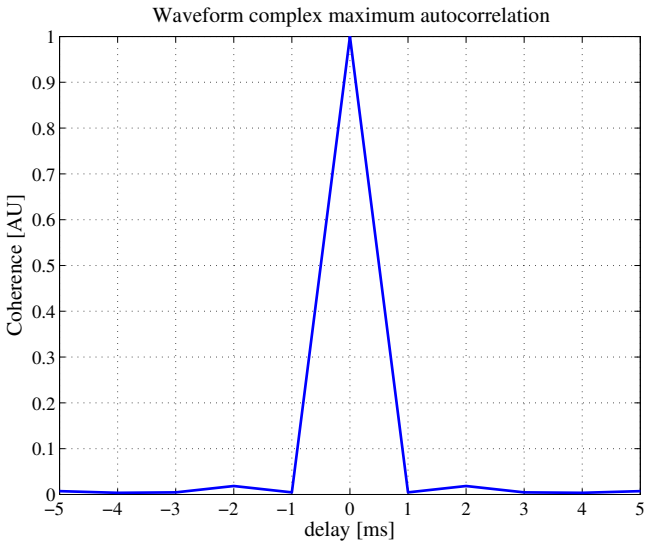

Figure 3.18: Coherence of the speckle computed from UK-DMC data.

In the same way, the correlation time will vary as a function of the receiver altitude, incidence angle or state of the sea. As an example Figs. 6.15 shows the correlation time computed from an airborne case ($h \approx 3000$ km) for both the cGNSS-R (GOLD-RTR data) and iGNSS-R (PIRA data) techniques. The data is from a two-hour long airborne experiment performed over the Gulf of Finland near Helsinki on Nowember 11^{th} 2011 [51]. As it can be observed, in this case the correlation time between consecutive waveforms is higher than in the spaceborne case, being around 6 ms in both cases, in agreement with [52].

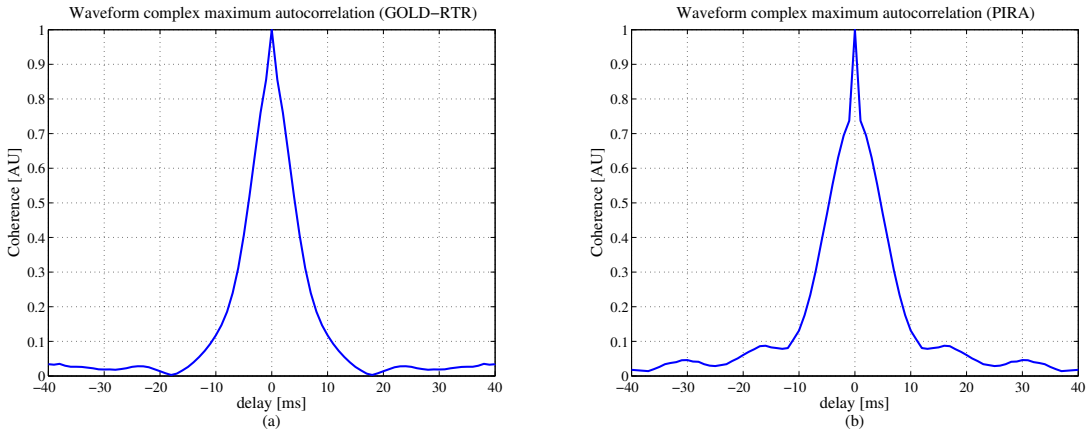

Figure 3.19: Coherence of the speckle computed from PIT-POC data.

3.7 Impact of Thermal and Speckle Noises

A general introduction to thermal and speckle noise in GNSS-R has been given in previous sections. It has been discussed that for the iGNSS-R approach the thermal noise may have an important effect on the SNR, since it is present in both channels. Nevertheless, the actual impact of thermal noise has to be analysed case-by-case. For example, for the space-borne case studied (UK-DMC case), the thermal noise is an important contributor to the final performance. This is basically due to the low antenna gain that is present in the UK-DMC instrument, which leads to a low/moderate SNR at waveform level, as it can be appreciated in Fig. 3.20, where the power waveforms obtained for a T_{coh} =1ms are plotted (a) without incoherent averaging, and (b) after averaging incoherently 10000 independent waveforms. Hence from Fig. 3.20 it can be noted that the waveform without averaging is very noisy (being the thermal noise the dominant term), still even after the incoherent averaging.

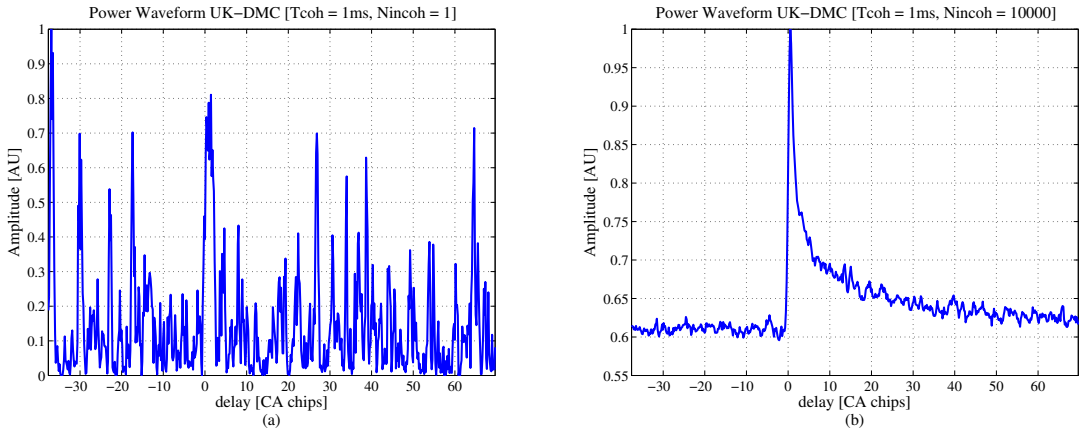

Figure 3.20: UK-DMC Power Waveform obtained for T_{coh} =1 ms, N_{incoh} =1 (a), and T_{coh} =1ms, N_{incoh} =10000 (b).

On the other hand for the PIT-POC data shown in Fig. 3.21, thermal noise is not a limiting factor of the instrument performance, being the system not limited by SNR (due to the very low height of the receiver, 3 km in the present case), also in the iGNSS-R technique (PIRA data). It is worth mentioning that the PIT-POC case presents higher peak antenna gains (of about 15 dBi) than the UK-DMC case. On the other hand, it is clearly visible that, for the airborne scenario, being the signal to thermal noise ratio SNR rather good, the waveform can be easily identified even in a single 1 ms snapshot (which is clearly not the case for the spaceborne scenario presented in Fig 3.20).

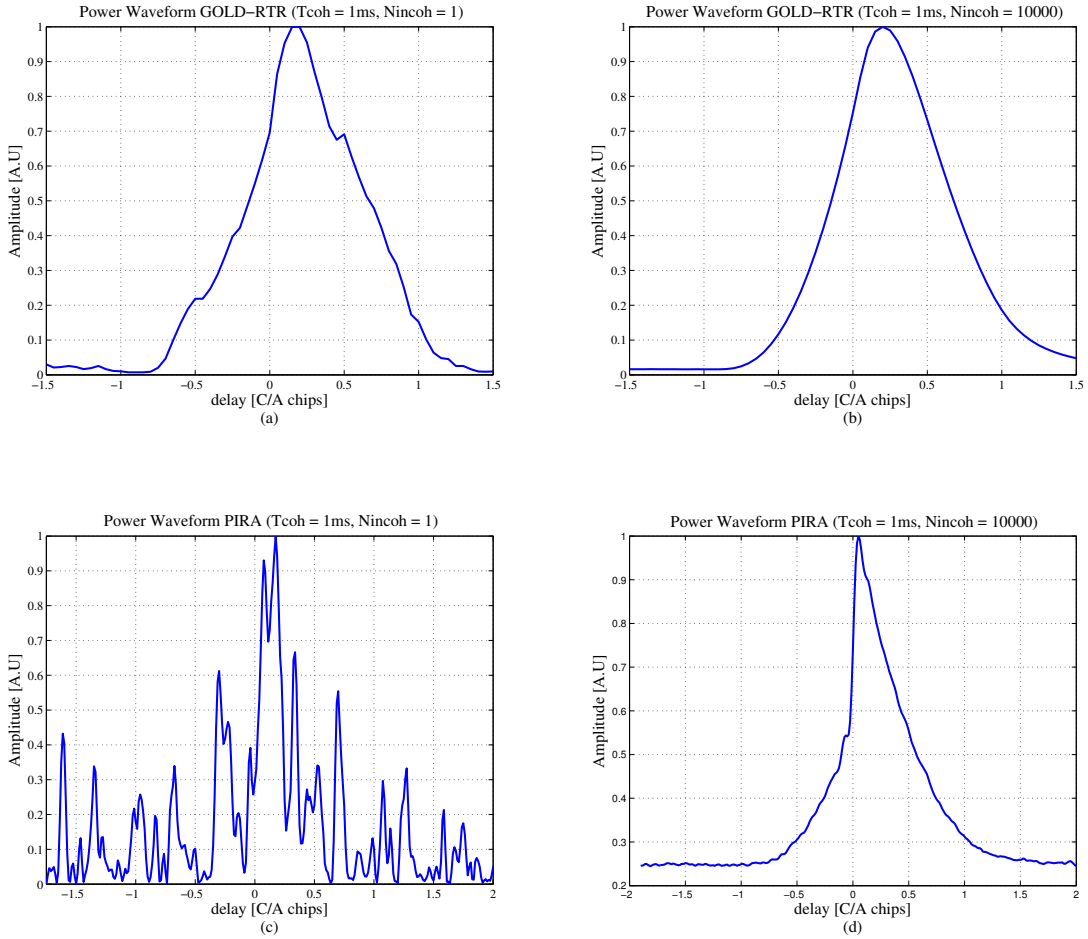

Figure 3.21: PIT-POC Power Waveform obtained for T_{coh} =1ms, N_{incoh} =1 (cGNSS-R) (a), (iGNSS-R) (c), and T_{coh} =1ms, N_{incoh} =10000 (cGNSS-R) (b), (iGNSS-R) (d).

3.7.1 Noise reduction factor by incoherent averaging

In order to reduce the standard deviation of the amplitude of the reflected power waveforms due to the speckle and thermal noises, incoherent averaging is applied [36]. In the case of thermal noise, the reduction achieved in the standard deviation is proportional to $\sqrt{N}$ as it is uncorrelated from sample to sample, whereas in the speckle noise case, the effectiveness of the incoherent averaging depends on the level of correlation between consecutive waveforms, which as it has been shown, it varies with the geometry and the sea state conditions. On the other hand this effectiveness will be also dependent on the lag position, since the level of correlation is not the same for all the lags, as it is presented in [50] and [52].

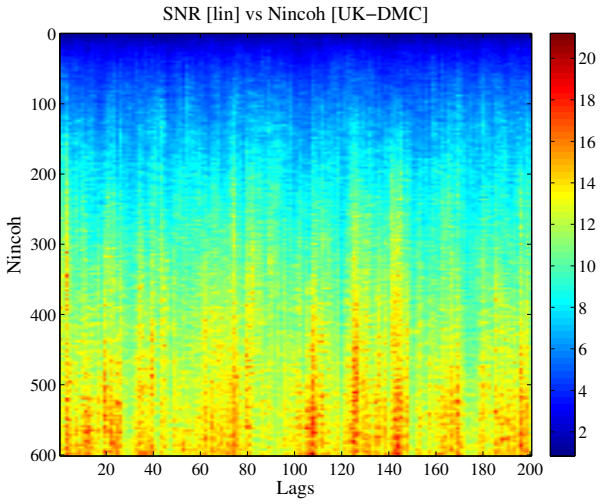

Figure 3.22: SNR [lin] of each Waveform bin for different incoherent averages from 1 to 200 Waveforms, in steps of 1.

Figure 3.22 shows the evolution of the SNR in linear units and in 1 unit increment step of N_{incoh} =1 for the UK-DMC data. Note that here the SNR has been defined as the ratio between the average value and the standard deviation of each waveform bin for a T_{incoh} = 1ms. As in this case the Power Waveforms are uncorrelated, the SNR evolves proportionally to $\sqrt{N_{incoh}}$, for all the lags.

Figure 3.23 shows the evolution of the SNR as a function of the $\sqrt{N_{incoh}}$ for lag 1 (dominated by thermal noise) and for lag 64 (peak of the waveform, where speckle noise is more important). Figure 3.23 agrees with the previous results, and confirms that in this case the speckle noise is uncorrelated.

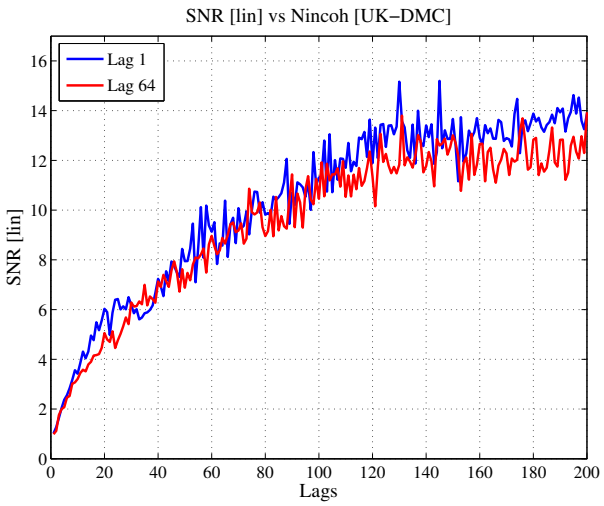

Figure 3.23: SNR for the lag=1 and lag=64.

The same procedure has been repeated for the PIT-POC data (GOLD-RTR, and PIRA). The main results are presented in Fig. 3.24, where as it can be appreciated now the SNR increases as $\sqrt{N_{incoh}}$ except for the central part (dominated by speckle noise) in which case the SNR increases approximately as $\sqrt{N_{incoh}/R}$, where $R = N_{incoh}/N_{incoh,eff}$, that can be interpreted as the effective number of incoherent averages. For the peak of the power waveform, this value is around 6. These results in agreement with the ones published at [50] and [52].

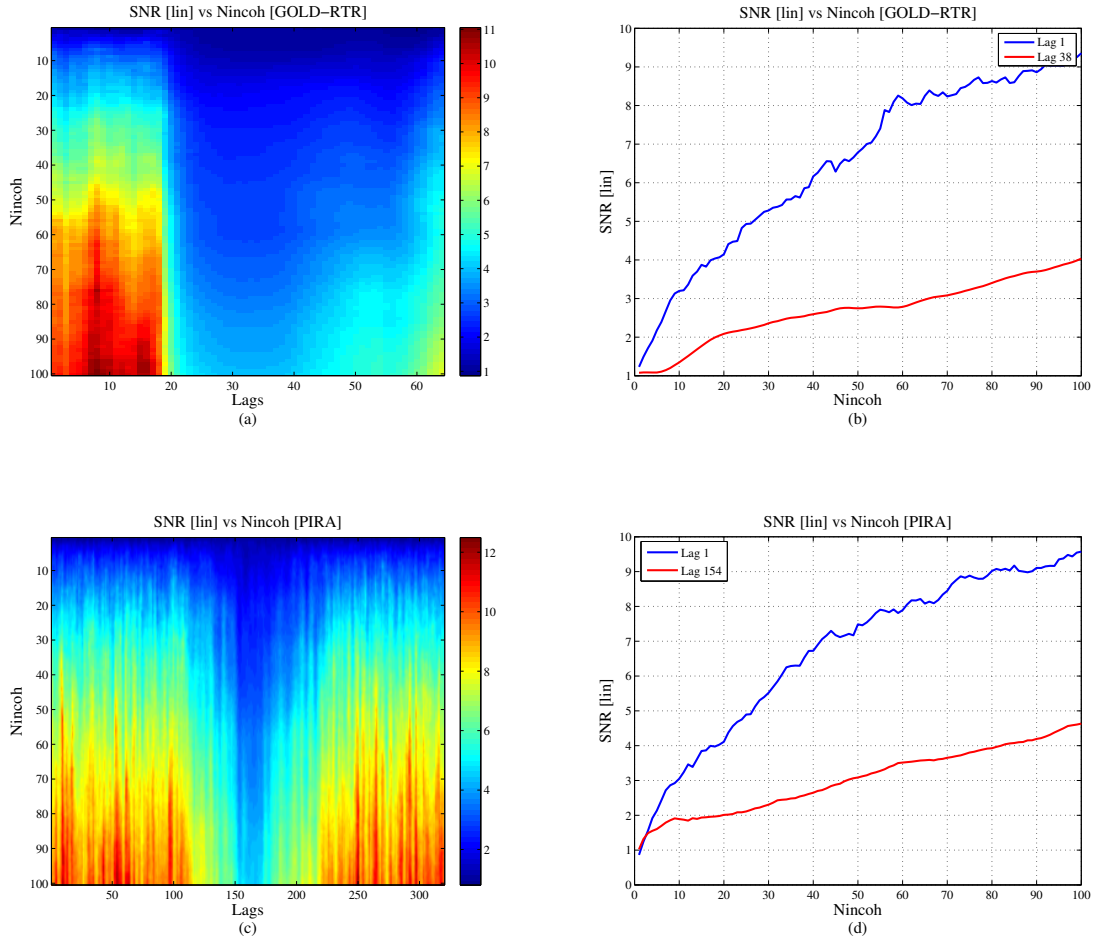

Figure 3.24: SNR [lin] of each Waveform bin for different incoherent averages from 1 to 200 Waveforms, in steps of 1 for the GOLD-RTR (a), and PIRA (c) data, SNR for the bin=1 and bin=38 (GOLD-RTR)(b), and SNR for the bin=1 and bin=154 (GOLD-RTR)(d).

Figure 3.25, shows the ratio as a function of the correlation lag for two instants times (5:33 am and 5:37 am). Two main conclussions can be extracted. The first one is that the ratio is around 1 in the part dominated by the thermal noise (uncorrelated), and increases in the central part of the waveform, where the speckle noise dominates.

On the other hand, the differences between the ratio obtained at 5:33 am and at 5:37 am, can be related to changes in the geometry (i.e altitude, incidence angle, wind speed).

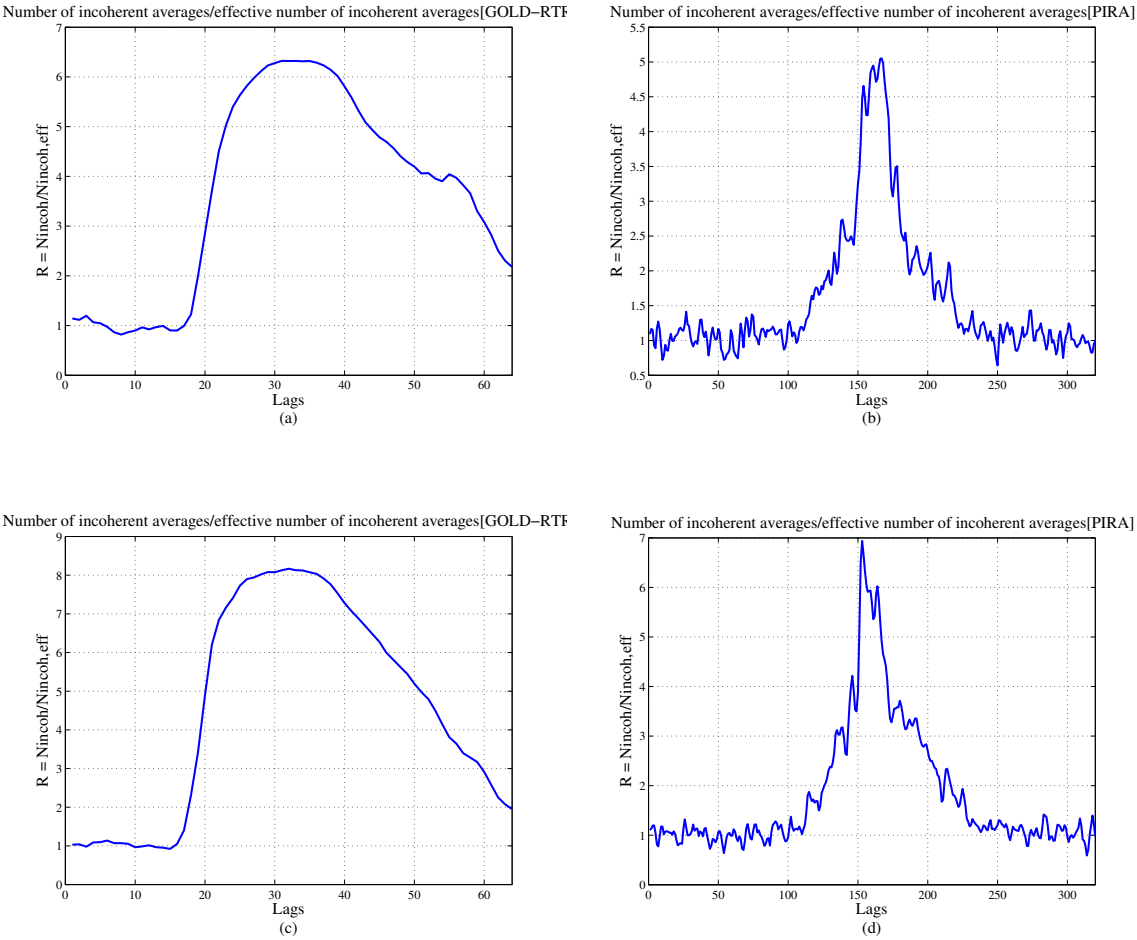

Figure 3.25: Estimated ratio (R) of the number of incoherent averages, and the effective number of incoherent averages as a function of the waveform lag, GOLD-RTR at 5:33 am (a) and at 5:37 am (c), and PIRA at 5:33 am (b), and at 5:37 am (d).

3.8 Conclusions

This chapter has performed a comprehensive analysis of the GNSS-R cross-correlation waveform properties, focusing mainly on the impact that observation and system parameters have on the GNSS-R observables. Parameters such as the receiver bandwidth, the observation geometry, the sea-state and the thermal and speckle noise have been analysed. From this study the following main conclusions can be extracted:

3.8.1 ACF and Waveform shapes

As expected, due to the larger bandwidth, the ACF of the L1 composite signal is much narrower than the C/A code only. It is translated in a steeper power waveform for the L1 composite case with respect to the C/A code case, which should lead to an improvement of the altimetry precision.

The bandwidth has an important impact in the shape of the ACF. As the bandwidth is reduced, the ACF becomes wider, and the waveform shape approximates to the conventional GNSS-R approach, using the C/A code only. The displacement produced is small for 20 (40 MHz in RF) (around 14 cm approx.). At 10 MHz (20 MHz in RF) the displacement obtained is around 25 cm, which starts to be relevant. It has been shown that other sources of bias have not been identified as critical (such for example sea-state in which case the shift produced in the peak of the derivative is less than the one produced by the receiver bandwidth). On the other hand as the receiver's bandwidth is reduced, the slope of the leading edge on the power waveform degrades as well. Thus, from the derivatives it can be noted a reduction in the amplitude of a 15% for the 5 MHz bandwidth (10 MHz in RF), whereas for the 2.5 is around the 22.5% with its consequent loss in altimetry performance.

3.8.2 Sea State

The wind speed dependence of the power waveform is seen in two aspects. On one hand, the waveform peak power decreases with increasing the wind speed. However, for large wind speeds, the sensitivity of the peak power to wind speed decreases significantly, due to the logarithmic relationship between sea surface slopes and wind speed. On the other hand, the wind speed has also a visible impact on the waveform trailing edge. The sensitivity of the trailing edge to wind speed reduces with increasing receiver heights.

3.8.3 Bias

The displacement of the peak derivative due to the wind speed tends to increase with decreasing the receiver bandwidths. On the other hand, the receiver bandwidth and wind speed impact in the position of the peak derivative position, varies as a function of the receiver altitude and incidence angle.

In any case considering that the bias due to the wind speed is quite small, even more if it is compared to the bias introduced by the receiver bandwidth, as a first

approximation, it can be concluded that the bias is an instrumental bias, and it can be accurately characterized and compensated for.

3.8.4 Noise

Thermal and speckle noises have been introduced and analysed for both the interferometric and conventional processing.

The correlation of the speckle noise between consecutive waveforms has been computed with real measurements from UK-DMC and PIT-POC data. It has been verified that the speckle noise correlation is about 1 ms for the cGNSS-R, considering an altitude of 700 km. For the cGNSS-R and iGNSS-R considering an altitude of 3 km, the speckle noise correlation has been estimated to be about 6 ms. For space-borne scenarios, the thermal noise is an important contributor to the final performance. For altimetry applications, antenna gains larger than 15-18 dBi are needed, otherwise a low/moderate SNR will be observed at waveform level.

For airborne scenarios, thermal noise is not a limiting factor to instrument performance, being the system not limited by thermal SNR (due to the very low height of the receiver, 3 km in the present case), even if moderate antenna gains of about 15 dBi are employed.

Chapter 4

Modelling and Analysis of GNSS-R Waveforms Sample-to-Sample Correlation

The knowledge of the statistical properties of GNSS-R waveforms is of fundamental importance to define the retrieval algorithms to estimate the geophysical parameters, and to optimize the accuracy of these estimations. In this chapter a comprehensive and general derivation of the analytical model that describes the fast-time statistics of GNSS-R waveforms is presented, for both the cGNSS-R and iGNSS-R techniques, and considering both complex and power waveforms. The models here presented include both the signal and thermal noise components. Hence, the model for the complex waveforms, is presented in section II (and detailed in the Appendix A (for the cGNSS-R case) and B(for the iGNSS-R case)). The models presented in Section II, have been validated with real data acquired on-board the UK-DMC satellite, and from the PIT-POC November 11^{th}. Section III presents the statistics for the power waveforms (and detailed in the Appendix D (for the cGNSS-R case) and E (for the iGNSS-R case)). Real data from the UK-DMC satellite, and from the PIT-POC are used again to validate the models.

4.1 Introduction

In order to know the accuracy of the geophysical parameters derived from the GNSS-R waveforms (sea surface height, wind speed, soil moisture, etc.) the knowledge of the statistical properties is required. The statistical properties can be divided in two groups, the so-called slow-time statistics, and the so-called fast-time statistics. The slow-time statistics represent the correlation between GNSS-R waveforms acquired

at different time instants (Fig. 4.1). On the other hand, the fast-time or sample-to-sample statistics represent the correlation between the different samples of a given GNSS-R waveform acquired at one time instant (Fig. 4.2).

The modeling and analysis of the slow-time statistical properties have been subject of previous works. An initial model can be found in [54], further expanded in [55]. On the other hand, the fast-time statistics of GNSS-R waveforms have been introduced in [56]. In [56] a model for the correlation between waveforms samples at different delays (samples) is modeled, and then implemented in a simulator. The waveforms obtained from the simulator are tested with experimental measurements collected from an airborne experiment. Results show that the covariance matrix obtained with the simulated waveforms agree quite well with the processed ones from experimental waveforms.

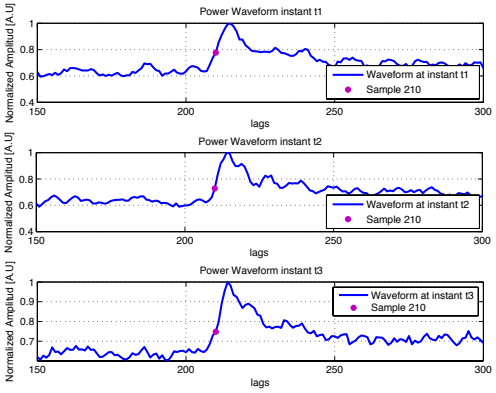

Figure 4.1: Slow Statistics.

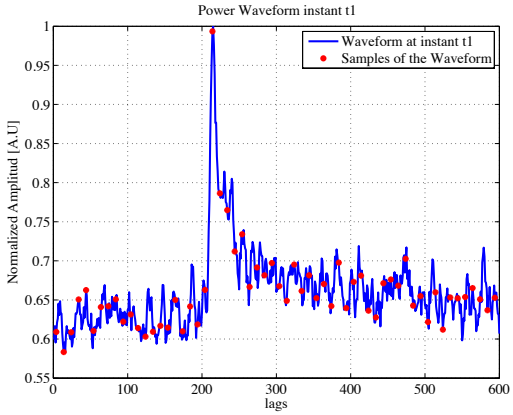

Figure 4.2: Fast Statistics.

In this chapter a comprehensive and general derivation of the analytical model that describes the fast-time statistics of GNSS-R waveforms is presented, including both signal and thermal noise components.

4.2 Sample to sample correlation model for Complex Waveforms

This section describes the fast-time statistics of GNSS-R waveforms, based on the use of the complex cross-correlation statistics of the signal [36].

4.2.1 cGNSS-R Sample to sample correlation model

The direct complex cross-correlation at the output of the correlator at a given delay τ, and acquired at a time instant t, can be defined as the complex cross-correlation between the received direct signal and the received reflected signal as,

$$Y(t,\tau) = \frac{1}{T_c}\int_{-\frac{T_c}{2}}^{\frac{T_c}{2}} v_r(t+t')v_d^*(t+t'-\tau)dt', \tag{4.1}$$

where T_c is the cross-correlation integration time, and where v_r is the received reflected signal and v_d is the received direct signal.

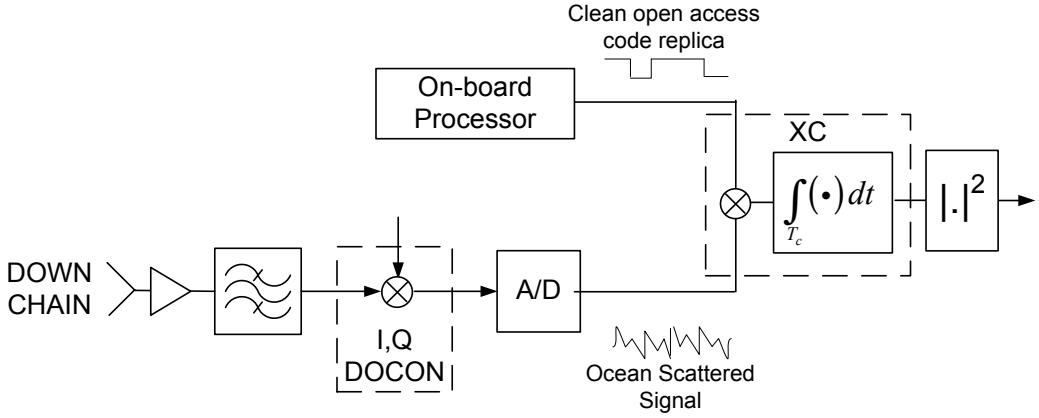

Figure 4.3: Schematic diagram of a classical GNSS-R altimeter processor.

Figure 4.3 represents the schematic diagram for the conventional GNSS-R approach. In this approach, the received reflected signal is band pass limited, down converted (DOCON), digitalized by the Analog-to-Digital conversor (A/D), and then is cross-correlated by the cross-correlator (XC) with a clean replica of the C/A code.

Therefore, the received direct signal in this case is the clean replica generated on-board the satellite ($v_d = s_d$), whereas the received reflected signal is the sum of the received ocean scattered GNSS signal (s_r) and the thermal noise introduced by the receiver in the down-looking chain (n_r). Therefore, Eqn. (4.1) can be expressed as

$$Y(t,\tau) = \frac{1}{T_c}\int_{-\frac{T_c}{2}}^{\frac{T_c}{2}} s_{r,c}(t+t')s_{d,c}^{*}(t+t'-\tau)dt' + \frac{1}{T_c}\int_{-\frac{T_c}{2}}^{\frac{T_c}{2}} n_{r,c}(t+t')s_{d,c}^{*}(t+t'-\tau)dt'$$
$$= Y_s(t,\tau) + Y_{Nr}(t,\tau), \tag{4.2}$$

where $Y_s(t,\tau)$ is the Signal Voltage Cross-Correlation and $Y_{Nr}(t,\tau)$ is the Noise Voltage Cross-Correlation. The signals $s_{r,c}(t)$, $v_{d,c}(t)$, and $n_{r,c}(t)$ are defined as:

$$s_{d,c}(t) = \sqrt{2}u(t-T_s)e^{j\varphi_o}e^{j2\pi f_s(t-T_s)}, \tag{4.3}$$

$$s_{r,c}(t) = \sqrt{2}\int_{\theta,\phi} W_{\theta,\phi,t}u(t-\tau_{r,\theta,\phi,t})e^{-j2\pi f_o\tau_{r,\theta,\phi,t}e^{j\varphi_o}}d\Omega, \tag{4.4}$$

and

$$n_{r,c}(t) = n_r(t)e^{j\varphi_o}e^{-j2\pi f_o t}, \tag{4.5}$$

where $u(t)$ is the complex baseband-modulated open navigation signal of a particular GNSS system, φ_o is the phase of the local oscillator (LO), T_s is a time shift introduced in the clean replica in order to align it with the reflected signal, f_s is a frequency shift introduced to the clean replica in order to match the Doppler frequency response corresponding to the specular point, $W_{\theta,\phi,t}$ is a complex amplitude factor which includes all the radar equation parameters, f_o is the nominal centre frequency, and $d\Omega = \sin\theta d\theta d\phi$ is the elementary solid angle. Thus, considering Eqns. (4.3), (4.4) and (4.5), the Signal Voltage Cross-Correlation ($Y_s(t,\tau)$) and the Noise Voltage Cross-Correlation ($Y_{Nr}(t,\tau)$) can be expressed as:

$$Y_s(t,\tau) = 2\int_{\theta,\phi} W_{\theta,\phi,t}\chi(\Delta\tau,\Delta f,t)e^{-j2\pi f_o\tau_{r,\theta,\phi,t}}e^{-j2\pi f_s(t-\tau-T_s)}d\Omega, \tag{4.6}$$

$$Y_{Nr}(t,\tau) = \frac{\sqrt{2}}{T_c}\int_{\theta,\phi} n_{r,c}(t+t')e^{-j2\pi f_o(t+t')}u^{*}(t+t'-\tau-T_s)e^{-j2\pi f_s(t+t'-\tau-T_s)}dt', \tag{4.7}$$

From Eqns. (4.6) and (4.7), the Complex Cross-Correlation Statistics can be expressed as,

$$C = \langle Y(\tau_1), Y^{*}(\tau_2)\rangle$$
$$= 4\int_{\theta,\phi}\left\langle |W_{\theta,\phi,t}|^2\right\rangle \chi(\Delta\tau,\Delta f,t)\chi^{*}(\Delta(\tau+\tilde{\tau}),\Delta f,t)e^{-j2\pi f_s\tilde{\tau}}d\Omega$$

$$+\frac{2}{T_c}2kT_{Nr}\Lambda(\Delta\tau)e^{-j2\pi f_s\tilde{\tau}}, \tag{4.8}$$

where $\chi(\Delta\tau, \Delta f, t)$ is the Woodward Ambiguity Function (WAF) (it is worth mentioning that the WAF has a slight dependence on the PRN impacting mainly on the sidelobes outside the main correlation region), T_c is the receiver coherent integration time, k is the Boltzmann constant, T_{Nr} is the equivalent input noise temperature of the downlooking chain, and $\Lambda(\Delta\tau)$ is the particularization of $\chi(\Delta\tau, \Delta f, t)$ for $\Delta f = 0$. In the appendix all the mathematics related to the derivation of the cross-correlation statistics are detailed. Equation (4.8) can be divided in two terms, the signal statistics and the noise statistics as:

$$\langle Y_s(\tau_1), Y_s^*(\tau_2)\rangle = 4\int_{\theta,\phi}\left\langle |W_{\theta,\phi,t}|^2\right\rangle \chi(\Delta\tau, \Delta f, t)\chi^*(\Delta(\tau+\tilde{\tau}), \Delta f, t)e^{-j2\pi f_s\tilde{\tau}}d\Omega, \tag{4.9}$$

and

$$\langle Y_{Nr}(\tau_1), Y_{Nr}^*(\tau_2)\rangle = \frac{2}{T_c}2kT_{Nr}\Lambda(\Delta\tau)e^{-j2\pi f_s\tilde{\tau}}, \tag{4.10}$$

Figure 4.4a plots the signal-to-signal statistics (signal component covariance matrix), Fig. 4.4b the noise statistics (thermal noise component covariance matrix), and Fig. 4.4c the complex cross-correlation statistics as the sum of both the signal statistics and the noise statistics (complete covariance matrix including both the signal and noise components). The different covariance matrices computed and plotted in this section or in the following sections have been normalized, thus the maximum amplitude is equal to one. The computation of the Complex Cross-Correlation Statistics has been performed based on the UK-DMC system parameters (Table 4.2).

Table 4.1: Simulation System Parameters

Parameter	**Value**	**Unit**
GPS altitude	20200	km
Rec. altitude	700	km
GPS velocity	3.87	km/s
Rec. velocity	7.5	km/s
Inc. angle (θ_i)	13.9	deg
Directivity (D)	13	dBi
Wind Speed (U_{10})	7.8	m/s
Coh. Int. Time (T_c)	1	ms

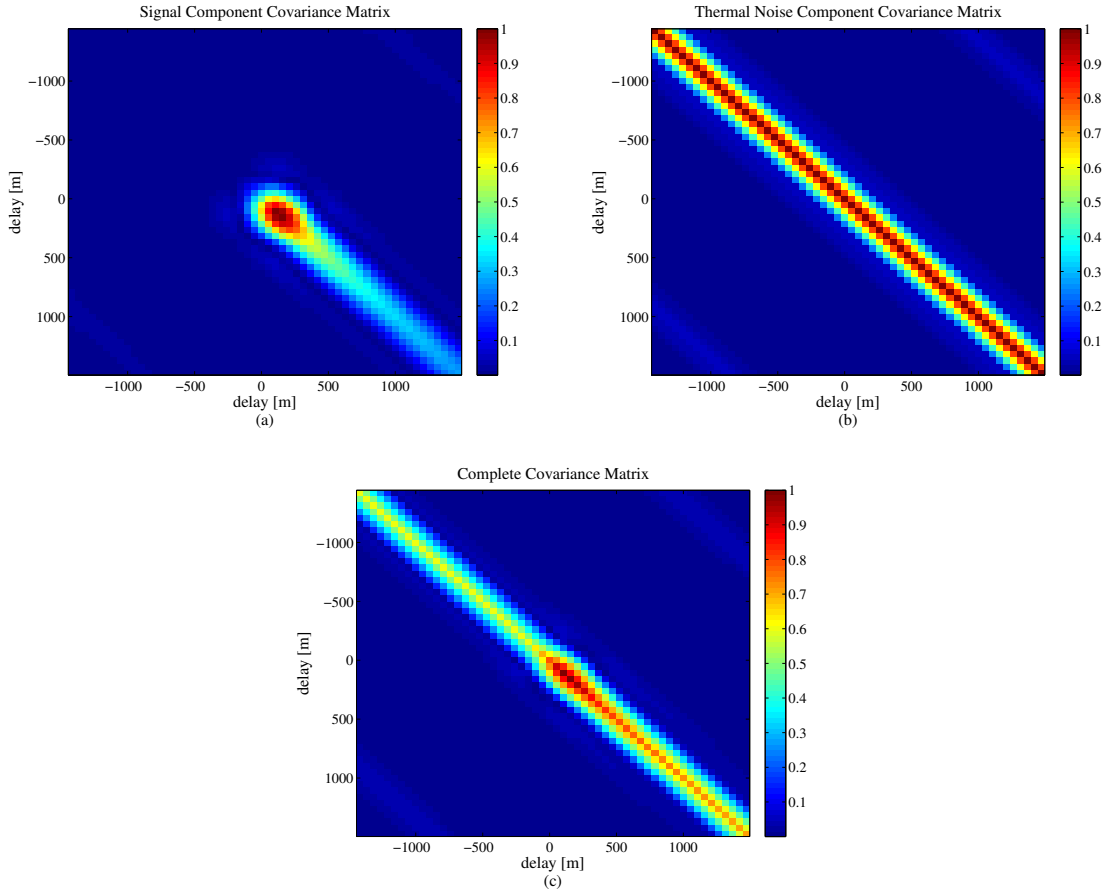

Figure 4.4: (a) Signal component covariance matrix (signal statistics), (b) Thermal noise component covariance matrix (noise statistics), (c) Complete covariance matrix (complex cross-correlation statistics, including both signal and noise terms).

As it can be observed from Figs. 4.4a and 4.4b both covariance matrices present different properties. The first one is that the noise component is present in all the delays, while clearly this is not the case for the signal term (since it is dependent on the backscattered signal). On the other hand, the covariance noise term follows the shape of the ACF, as described in Eqn. (4.7) (it can be clearly seen in Fig. 4.5, where the minor diagonal of this term is represented (minor is referred to the main diagonal rotated 90°)). On the other hand, the covariance signal term is dependent on the complex multiplication of the ACF at delays τ_2 and τ_1, as shown in Eqn. (4.6).

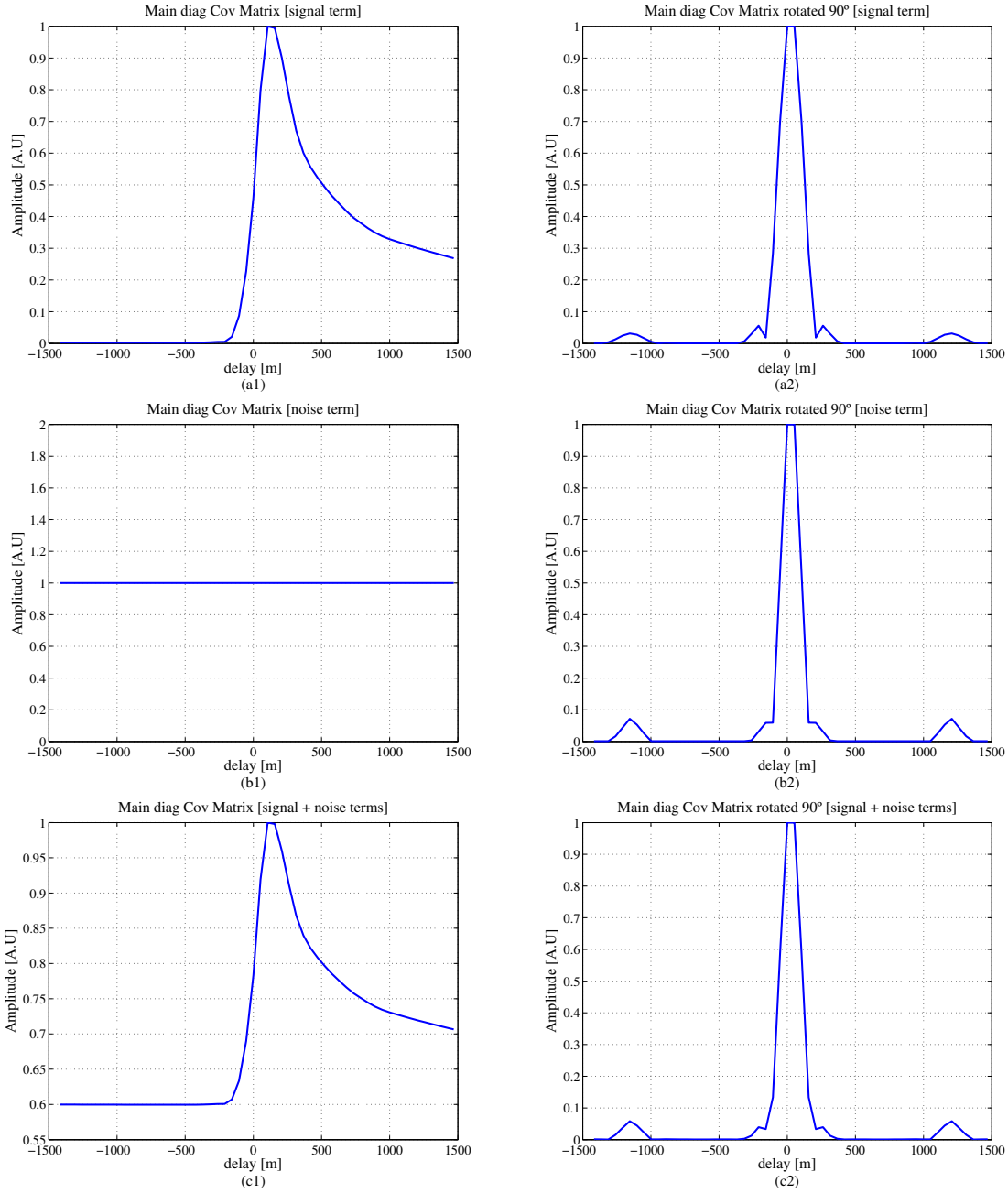

Figure 4.5: Diagonal of the covariance matrix derived from the analytical model for the signal term (a1), noise term (b1) and for the signal and noise terms (c1), and Minor Diagonal of the covariance matrix derived from the analytical model for the signal term (a2), noise term (b2), and for the signal and noise terms (c2).

Figure 4.5 shows the main and minor diagonals of the covariance matrices, for the signal term, the noise term and for the combination of the signal, and noise. As it can be observed, when signal is present (cases (a1) and (c1)), the main diagonal depicts the Power Waveform. Figure 4.5.b1 shows, as expected, that the thermal noise is

constant and not depending on the delay. The plots of the minor diagonal show that the covariance of the noise term follows the shape of the ACF while the covariance of the signal term follows the shape of the squared ACF, as expected and described in Equ. 4.9 and Equ. 4.10.

4.2.1.1 Model Validation with real data

In this section real data from the UK-DMC satellite [19] and [68] and from the PIT-POC November 11^{th}, 2011 flight [51] have been used to validate the analytical model presented on Section II.

For the data processed here, it is important to take into account the variation of the length of the specular path as the satellite progresses along its orbit. If the range model used on-board for the correlation does not take this variation into account, consecutive waveforms will be drifting in delay. Averaging of these waveforms without correcting for the geometry will cause an artificial spread of the final averaged waveform, and a reduction of the peak amplitude, which must be avoided. Hence, the original UK-DMC data set available to the authors was subject to this delay drift, which needed correction for proper comparison with simulated data. Therefore, the complex waveforms have been corrected by applying a delay shift every 500 ms to compensate for this delay drift. Figure 4.6 shows the projected position of the GPS transmitter, the UK-DMC receiver and the specular point for each second of the available data.

Figure 4.7 shows the normalized power waveforms computed before and after the delay correction. As it can be appreciated, the delay introduced by the geometry variation not only affects the waveform's shape (i.e. width), but it also degrades the SNR.

In this case, the complex cross-correlation statistics (covariance matrix) can be easily computed as:

$$\mathbf{C}(\theta) = E[(\tilde{\boldsymbol{x}} - \boldsymbol{\mu}(\theta))(\tilde{\boldsymbol{x}} - \boldsymbol{\mu}(\theta))^H], \tag{4.11}$$

where $\tilde{\boldsymbol{x}}$ is a complex random vector ($\tilde{\boldsymbol{x}} = [\tilde{x}_1, \tilde{x}_2, \cdots, \tilde{x}_N]^T$) with $\tilde{x}_1 = u + jv$, $\boldsymbol{\mu}$ is the mean ($\boldsymbol{\mu}(\theta) = E[\boldsymbol{u}] + jE[\boldsymbol{u}]$), and θ is the parameter to be estimated (range in this case).

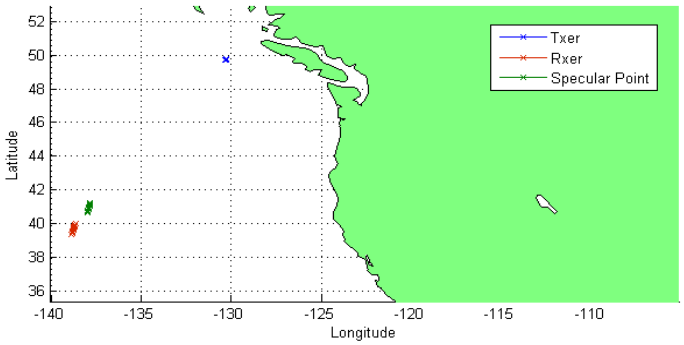

Figure 4.6: GPS transmitter, UK-DMC receiver and specular point.

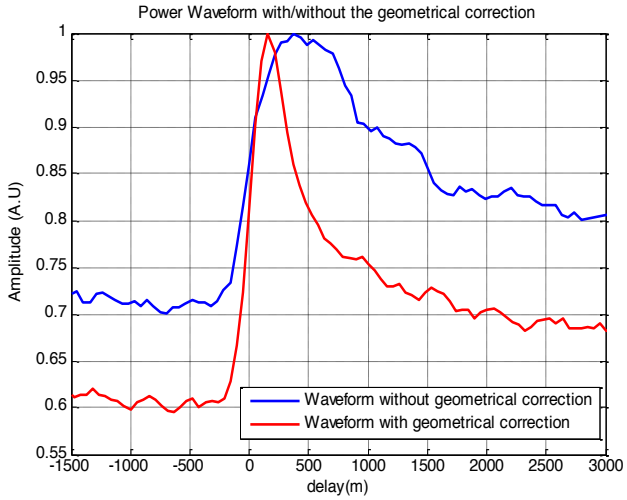

Figure 4.7: Sample waveforms over the ocean derived from UK-DMC, without and with applying the geometrical correction.

Figures 4.8.a1, 4.8.b1 and 4.8.c1 show the difference between the covariance matrices obtained from the UK-DMC data and the analytical model employing different receiver bandwidths (infinite (i.e. no filtered), 3 MHz and 1 MHz). On the other hand in Fig. 4.8.a2, 4.8.b2 and 4.8.c2 the Power Waveforms obtained from the analytical model and from the real data are depicted. From those figures, it can be observed that the results obtained with the analytical model fit very well with those obtained from the real data, with maximum deviations reaching only about 10%. Important differences can be attributable to non-perfect modeling of the receiver bandwidth, which, is an important parameter that must be taken into account, and it is not publically available.

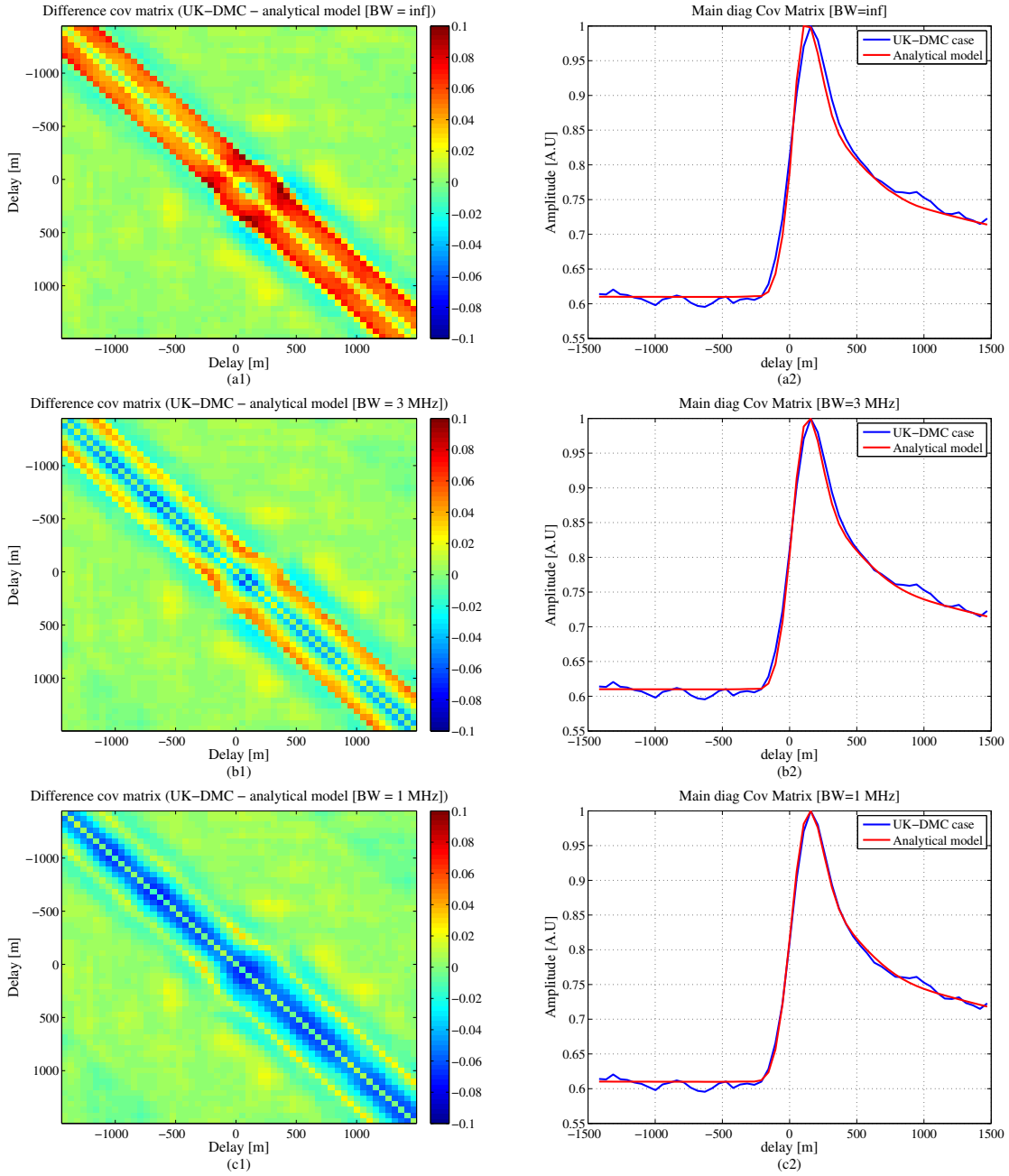

Figure 4.8: (a1), (b1), (c1) Difference between the covariance matrix computed from the UK-DMC data and from the analytical model for an infinite, 3 MHz and 1 MHz bandwidths, (a2), (b2), (c2) Main diagonal of the covariance matrix comparison derived from the UK-DMC data and the analytical model, for an infinite, 3 MHz and 1 MHz bandwidths.

The receivers bandwidth not only impacts the shape of the Covariance (dependent on the Autocorrelation Function (ACF)), but also the altimetry performance, as it will be shown in the following sections. In fact the differences across Figs. 4.8.a2,

4.8.b2 and 4.8.c2 are due to the fact that a narrowband filter tends to widen the ACF of the C/A code . For example, in Fig. 4.8.a2 the analytical model considers an infinite receiver bandwidth and therefore the corresponding ACF shape is the triangle function whereas for the UK-DMC, due to the receiver bandwidth, the ACF broadens a bit, resulting in a clear deviation. However in Fig. 4.8.c2 the opposite effect is observed, since in this case, the receiver filter of the model is narrower (1 MHz) than the one used in the UK-DMC. Now the ACF for the analytical model is wider than that for the UK-DMC, and thus the difference between data and model will tend towards negative values.

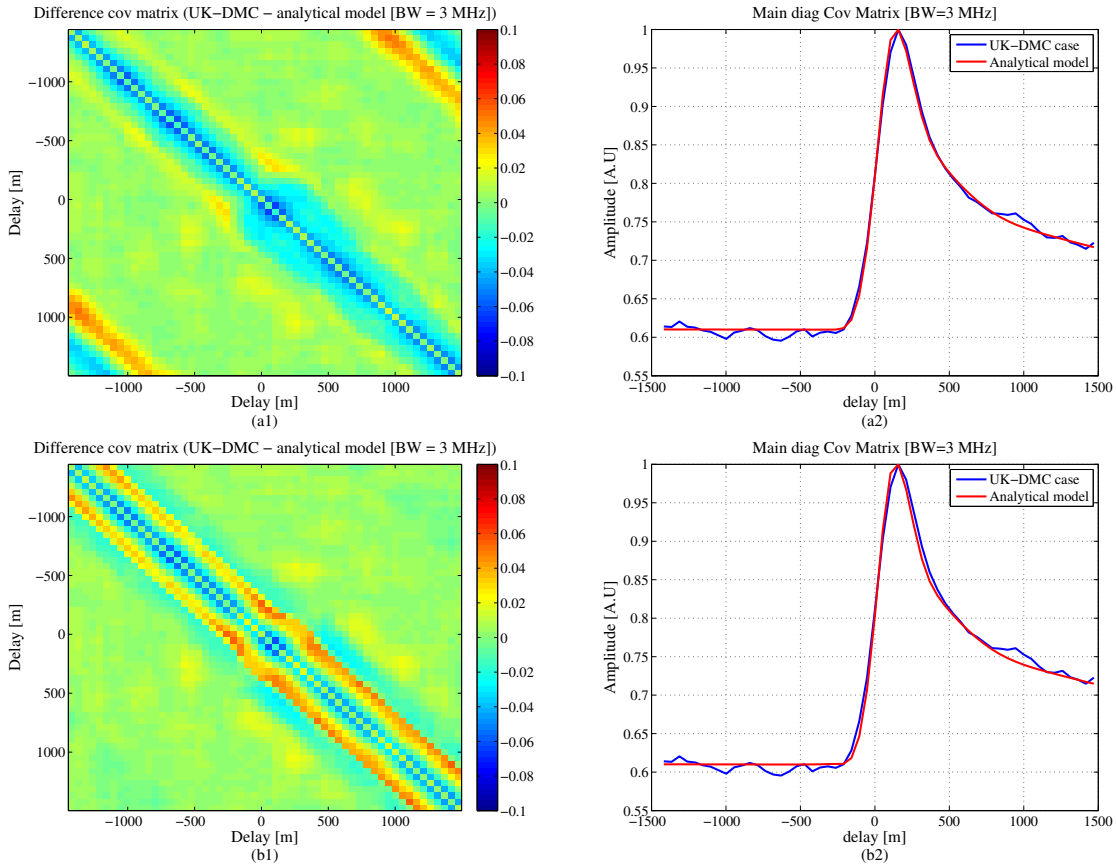

Figure 4.9: (a1), (b1), Difference between the covariance matrix computed from the UK-DMC data and from the analytical model for SV1 and SV22, (a2), (b2), Main diagonal of the covariance matrix comparison derived from the UK-DMC data and the analytical model, for SV1 and SV22.

The covariance matrices presented have been computed considering GPS SV-22 (as in the UK-DMC data). As an additional test case, the covariance matrix has been calculated by adopting a different GPS PRN. For example, by adopting in the model

the GPS SV-1 PRN, it can be seen that the modeled covariance matrix presents some deviations with respect to the real data, as it can be observed in Fig. 4.9 a1. The large errors occurring off the main diagonal are in this case mainly due to the different sidelobes structure of the ACF of SV-1 (used in the model) and SV-22 (real data). It can be appreciated that the selection of different PRNs does not have a major impact on the main diagonal of the covariance matrix.

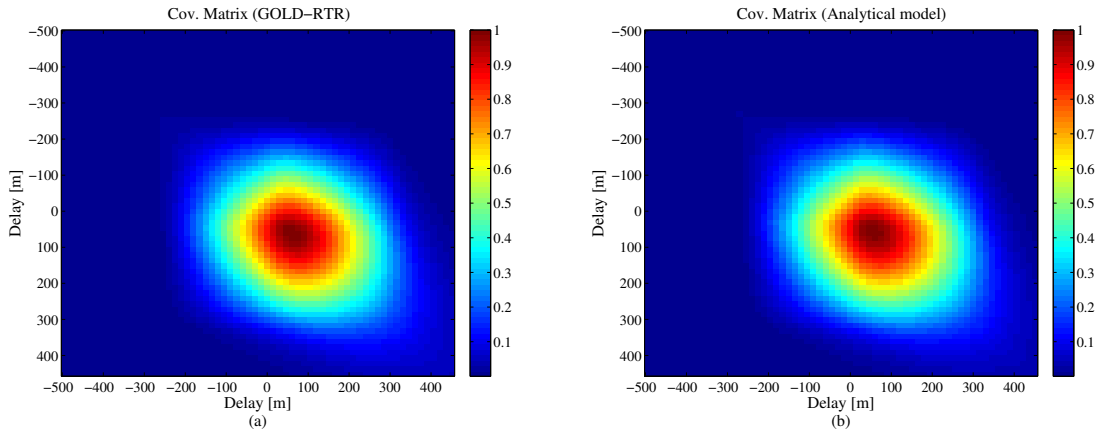

Figure 4.10: Covariance Matrices obtained from (a) GOLD-RTR data, (b) Analytical model.

To finish the PIT-POC data (GOLD-RTR) has been also used to validate the model. The main system parameters are summarized in Table 4.2 . Figures 4.10.a and 4.10.b show the Covariance Matrices obtained from the GOLD-RTR data and from the analytical model considering the system parameters of the GOLD-RTR data. As it can be appreciated both covariance matrices are practically identical. On the other hand Fig 4.11a shows the difference between the covariance matrix obtained from the GOLD-RTR data and the analytical model. As it can be observed, the difference is quite small, even smaller than the ones obtained for the UK-DMC data, being around a 2%. In the same way if the diagonals of both covariance matrices are compared, it can be observed that both match pretty well.

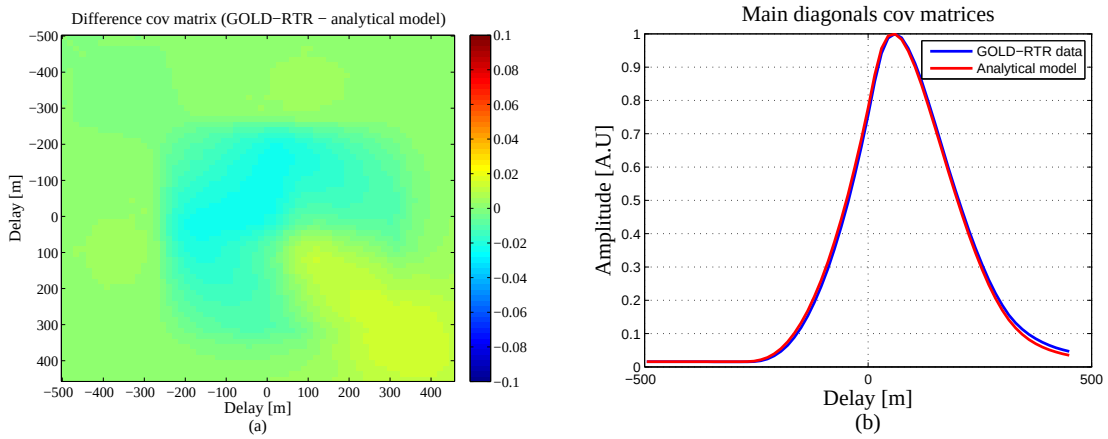

Figure 4.11: (a) Difference between the covariance matrix computed from the GOLD-RTR data and from the analytical model, (b) Main diagonal of the covariance matrix comparison derived from the GOLD-RTR data and the analytical model.

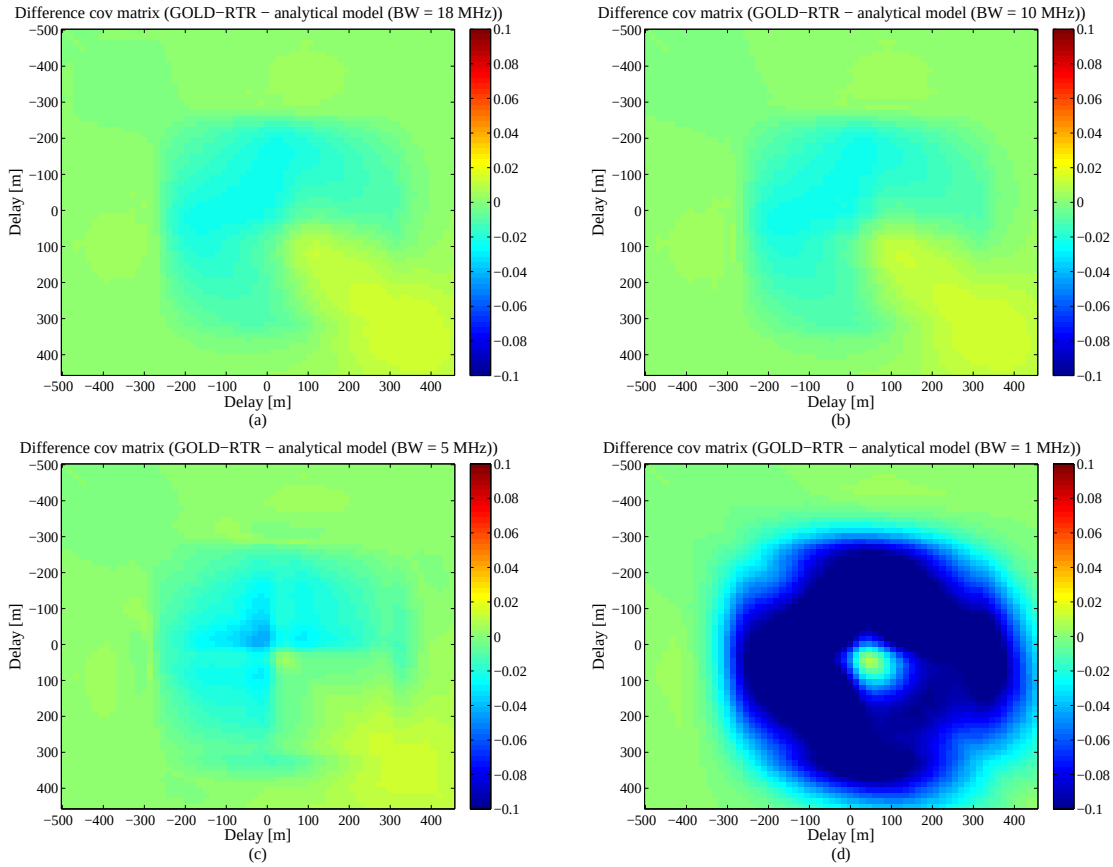

Figure 4.12: Difference between the covariance matrix computed from the GOLD-RTR data and from the analytical model for a (a) BW = 18 MHz, (b) BW = 10 MHz, (c) BW = 5 MHz, (d) BW = 1 MHz.

The last results have been obtained adjusting the receiver bandwidth used in

the simulations to the one used by the GOLD-RTR receiver. If now the receiver bandwidth is modified, the differences between the covariance matrices obtained from the model and from the GOLD-RTR data will increase. It can be clearly appreciated in Fig. 4.12, where the difference between the covariance matrix obtained from the model and from the GOLD-RTR has been plotted for four different bandwidths (18 MHz, 10 MHz, 5 MHz, and 1 MHz). Differences between them start to be relevant for bandwidths lower than 5 MHz. In the same way Fig. 4.13 shows the main diagonals for the covariance matrices.

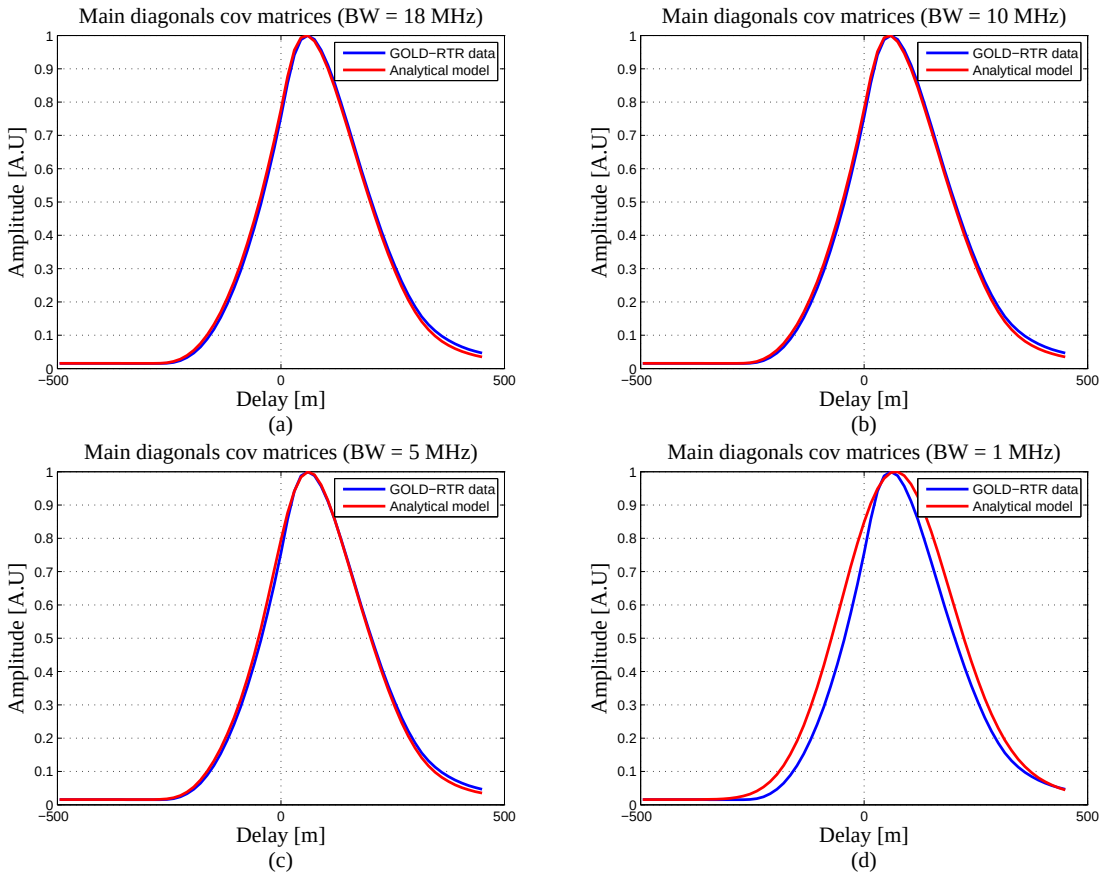

Figure 4.13: Comparison of the main diagonal of the covariance matrix derived from the GOLD-RTR data and the analytical model for: a (a) BW = 18 MHz, (b) BW = 10 MHz, (c) BW = 5 MHz, and (d) BW = 1 MHz.

Table 4.2: Simulation System Parameters

Parameter	**Value**	**Unit**
GPS altitude	20200	km
Rec. altitude	3	km
GPS velocity	3.87	km/s
Rec. velocity	55	m/s
Inc. angle (θ_i)	13.9	deg
Directivity (D)	11.8	dBi
Wind Speed (U_{10})	4.25	m/s
Coh. Int. Time (T_c)	1	ms

4.2.1.2 Simulated data vs real data

Additionally, in this section complex waveforms have been simulated. Therefore, taking as a reference the system parameters of the UK-DMC data, 12 seconds of complex waveforms have been simulated. The simulated data include the impact of the speckle noise (multiplicative noise inherent to the signal) and the thermal noise (additive noise independent to the signal and related to the receiver). From this geometry, the complex waveforms are generated considering the random nature of the scattering from the ocean, as

$$Y(t_o, \tau) = e^{j\varphi_o} T_c \int_{\theta,\phi} W_{\theta,\phi,t} \chi(\Delta\tau, \Delta f, t) d\Omega, \tag{4.12}$$

where T_c is the integration time, $W_(\theta, \phi, t)$ is the footprint function of the receiving antenna including all the radar equation parameters, and $\chi(\Delta\tau, \Delta f, t)$ is the Woodward Ambiguity Function as previously introduced.

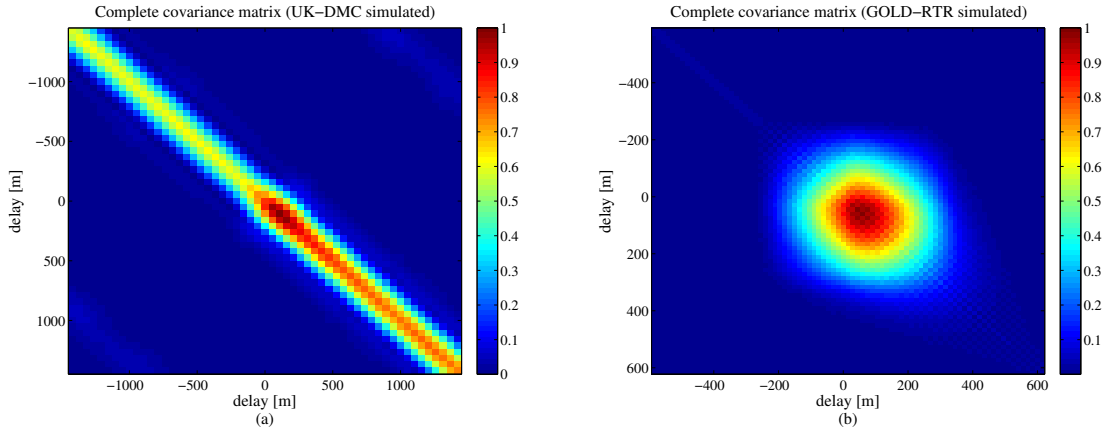

Figure 4.14: Complete covariance matrix using simulated data (a) UK-DMC data, (b) GOLD-RTR data.

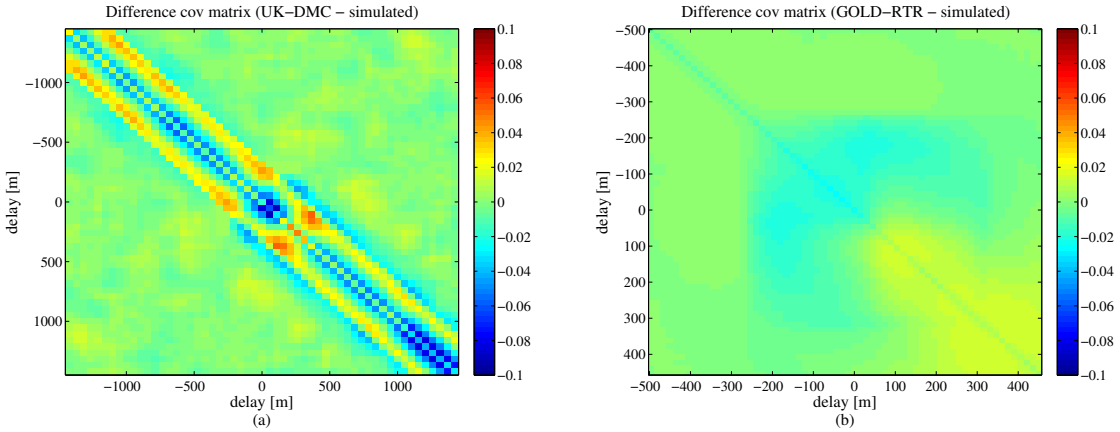

Figure 4.15: Power Waveforms comparison from simulation and measured data (a) UK-DMC data, (b) GOLD-RTR data.

As for the case of the real data, the cross-correlation statistics (covariance matrix) are computed by applying Eqn. (4.11). Figure 4.14 shows the complete covariance matrix derived for the simulated data (for both the UK-DMC and GOLD-RTR system parameters). As it can be observed, both covariance matrices present different shapes, due basically to the different geometry (satellite vs airborne). On tbe other hand, the covariance matrix obtained for the UK-DMC is noisier than the one obtained for the PIT-POC case. Despite the differences between both covariances matrices, it can be appreciated that the shape of the covariance matrices obtained from the simulated data are in agreement with the ones obtained previously with the real data. Figure 4.15 shows the deviation plots, as it can be observed, the maximum difference is lower than a 10%

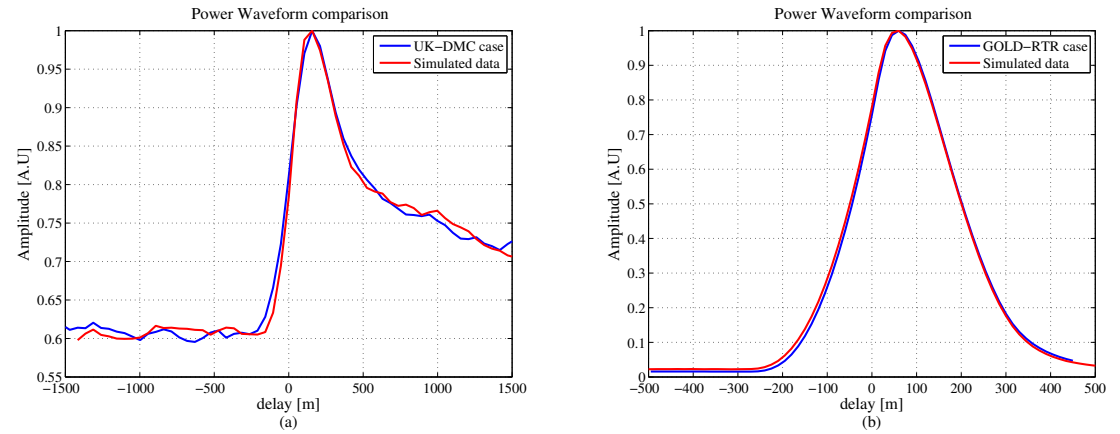

Figure 4.16: Comparison of Power Waveforms derived from simulation and from measured data (a) UK-DMC data, (b) GOLD-RTR data.

Ending Fig. 4.16 show the Power Waveform obtained along the main diagonal of the cross-correlation statistics. It can be observed that there is also an excellent agreement between the simulated and the measured data power waveforms.

4.2.2 iGNSS-R Sample to sample correlation model

This section describes the fast-time statistics of the GNSS-R waveforms, based on the use of the complex cross-correlation statistics of the signal for the interferometric technique [36]. In this case, as a difference to the conventional GNSS-R approach, the received reflected signal is cross-correlated with the received direct signal.

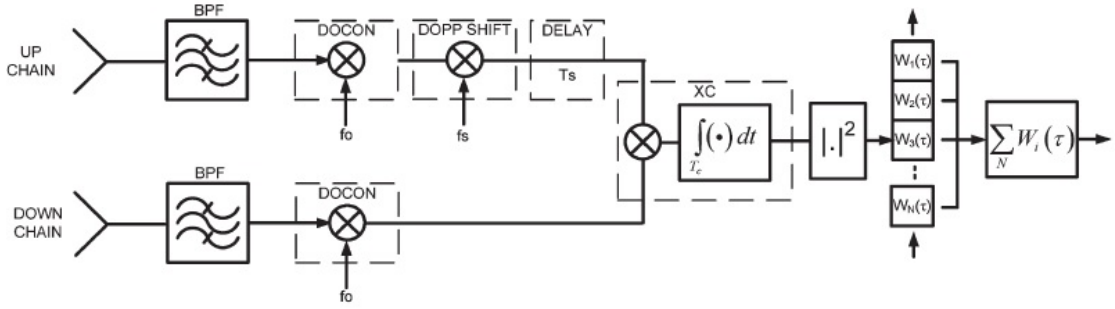

Figure 4.17: Block diagram of a classical GNSS-R altimeter processor.

Figure 4.17 represents the block diagram for the iGNSS-R approach. In this case the received direct signal v_d is bandpass filtered, down-converted, Doppler-shifted, and time-delayed, in the same way as the reflected received signal. An important issue of the iGNSS-R technique, is that the thermal noise is present in both channels in contrast with the cGNSS-R technique, where it is present only in the down-looking channel. Thus, the interferometric complex waveform can be expressed as:

$$\begin{aligned} Y(t,\tau) = & \frac{1}{T_c}\int_{-\frac{T_c}{2}}^{\frac{T_c}{2}} s_r(t+t')s_d^*(t+t'-\tau)dt' \\ & + \frac{1}{T_c}\int_{-\frac{T_c}{2}}^{\frac{T_c}{2}} s_r(t+t')n_d^*(t+t'-\tau)dt' \\ & + \frac{1}{T_c}\int_{-\frac{T_c}{2}}^{\frac{T_c}{2}} n_r(t+t')s_d^*(t+t'-\tau)dt' \\ & + \frac{1}{T_c}\int_{-\frac{T_c}{2}}^{\frac{T_c}{2}} n_r(t+t')n_d^*(t+t'-\tau)dt' \\ = & Y_s(t,\tau) + Y_{Nd}(t,\tau) + Y_{Nr}(t,\tau) + Y_{Ndr}(t,\tau), \end{aligned} \tag{4.13}$$

where $Y_s(t,\tau)$ is the Signal Voltage Cross-Correlation, $Y_{Nd}(t,\tau)$ is the Reflected Signal-Uplooking Noise Voltage Cross-Correlation, $Y_{Nr}(t,\tau)$ is the Direct Signal-Down-looking Noise Voltage Cross-Correlation, and $Y_{Ndr}(t,\tau)$ is the Up-looking Noise-Down-looking Noise Voltage Cross-Correlation. $s_{r,c}(t)$, and $n_{r,c}(t)$ have been introduced previously, whereas $s_{d,c}(t)$ and $n_{d,c}(t)$ can be defined as:

$$s_{d,c}(t) = \sqrt{2}A_d u(t-\tau_d-T_s)e^{-j2\pi f_o\tau_d}e^{j\phi_o}e^{j2\pi f_s(t-T_s)}, \tag{4.14}$$

$$n_{d,c}(t) = n_d(t-T_s)e^{j\phi_o}e^{-j2\pi(f_o-f_s)(t-T_s)}, \tag{4.15}$$

where A_d is an amplitude factor (includes the GNSS signal transmitted power, the voltage antenna pattern of transmitting and receiving antennas, and the free-space loss), $u(t)$ is the complex baseband-modulated open navigation signal of a particular GNSS system, φ_o is the phase of the local oscillator (LO), T_s is a time shift introduced in the direct signal in order to align it with the reflected signal, and f_s is a frequency shift introduced to the direct signal in order to match the Doppler frequency response corresponding to the specular point. Thus, considering Eqns. (4.14-4.15), $s_{r,c}(t)$ and $n_{r,c}(t)$ (introduced on section 2.1), the Signal Voltage Cross-Correlation ($Y_s(t,\tau)$) , the Reflected Signal-Uplooking Noise Voltage Cross-Correlation ($Y_{Nd}(t,\tau)$), the Direct Signal-Down-looking Noise Voltage Cross-Correlation ($Y_{Nr}(t,\tau)$), and the Up-looking Noise-Down-looking Noise Voltage Cross-Correlation ($Y_{Ndr}(t,\tau)$) terms can be expressed as [36]

$$Y_s(t,\tau) = 2A_d\int_{\theta,\phi} W_{\theta,\phi,t}U(\Delta\tau,\Delta f,t)e^{j2\pi f_o(\tau_{d,t-\tau}\tau_{r,\theta,\phi})}e^{-j2\pi f_s(t-\tau-T_s)}d\Omega, \tag{4.16}$$

$$\begin{aligned} Y_{Nd}(t,\tau) =& \frac{\sqrt{2}}{T_c}\int_{\theta,\phi} W_{\theta,\phi}\int_{-\frac{T_c}{2}}^{\frac{T_c}{2}} u(t+t'-\tau_{r,\theta,\phi,t+t'})n_d^*(t+t'-\tau-T_s) \\ &\cdot e^{j2\pi f_{Dr,\theta,\phi}t'}e^{j2\pi(f_o-f_s)t'}dt'e^{-j2\pi f_o\tau_{r,\theta,\phi}t}e^{j2\pi(f_o-f_s)(t-\tau-T_s)}d\Omega, \end{aligned} \tag{4.17}$$

$$\begin{aligned} Y_{Nr}(t,\tau) =& \frac{\sqrt{2}A_d}{T_c}\int_{-\frac{T_c}{2}}^{\frac{T_c}{2}} n_r(t+t')u^*(t+t'-\tau-\tau_{d,t+t'-\tau}) \\ &\cdot e^{-j2\pi f_o(t+t')}e^{j2\pi f_o\tau_{d,t+t'-\tau}}e^{-j2\pi f_s(t+t'-\tau-T_s)}, \end{aligned} \tag{4.18}$$

$$\begin{aligned} Y_{Ndr}(t,\tau) =& \frac{1}{T_c}\int_{-\frac{T_c}{2}}^{\frac{T_c}{2}} n_r(t+t')n_d^*(t+t'-T_s-\tau) \\ & e^{-j2\pi f_o(t+t')}e^{j2\pi(f_o-f_s)(t+t'-\tau-T_s)}dt', \end{aligned} \tag{4.19}$$

From Eqns. (4.16 to 4.19), and considering that the signal and the up- and donw-looking thermal noise components are uncorrelated to each other, the Complex Cross-Correlation Statistics can be expressed as,

$$\begin{aligned}\big\langle Y(\tau_1)Y^*(\tau_2)\big\rangle = \big\langle Y_s(\tau_1)Y_s^*(\tau_2)\big\rangle + \big\langle Y_{Nd}(\tau_1)Y_{Nd}^*(\tau_2)\big\rangle \\ + \big\langle Y_{Nr}(\tau_1)Y_{Nr}^*(\tau_2)\big\rangle + \big\langle Y_{Ndr}(\tau_1)Y_{Ndr}^*(\tau_2)\big\rangle,\end{aligned} \tag{4.20}$$

where the different terms in Eqn. (4.20) are given by:

$$\big\langle Y_s(\tau_1)Y_s^*(\tau_2)\big\rangle = 4A_d^2\big\langle W_{\theta,\phi,t}W_{\theta,\phi,t}^*\big\rangle U(\Delta\tau,\Delta f,t)U^*(\Delta\tau,\Delta f,t)e^{j2\pi(-f_{Dd,t-\tau}+f_s)\tilde{\tau}}, \tag{4.21}$$

$$\big\langle Y_{Nd}(\tau_1)Y_{Nd}^*(\tau_2)\big\rangle = 2\big\langle W_{\theta,\phi,t}W_{\theta,\phi,t}^*\big\rangle 2\frac{kT_{Nd}}{T_c}ACF(\tau)e^{-j2\pi(f_o-f_s)(-\tilde{\tau})}, \tag{4.22}$$

$$\big\langle Y_{Nr}(\tau_1)Y_{Nr}^*(\tau_2)\big\rangle = 4A_d^2\frac{kT_{Nr}}{T_c}ACF(\Delta\tau)e^{j2\pi(f_{Ddt}-f_s)(\tilde{\tau})}, \tag{4.23}$$

$$\begin{aligned}\big\langle Y_{Ndr}(\tau_1)Y_{Ndr}^*(\tau_2)\big\rangle =& \frac{4kT_{Nr}kT_{Nd}}{T_c^2}\int_{-\frac{T_c}{2}}^{\frac{T_c}{2}}\int_{-\frac{T_c}{2}}^{\frac{T_c}{2}}\frac{sin(2\pi B(t'-t''))}{\pi(t'-t'')} \\ &\cdot\frac{sin(2\pi B(t'-t''+\tilde{\tau}))}{\pi(t'-t''+\tilde{\tau})}e^{j2\pi(f_o+f_s)(t''-t')}e^{j2\pi f_s(\tilde{\tau})}dt'dt'',\end{aligned} \tag{4.24}$$

The different cross-correlations are plotted in Fig. 4.18.

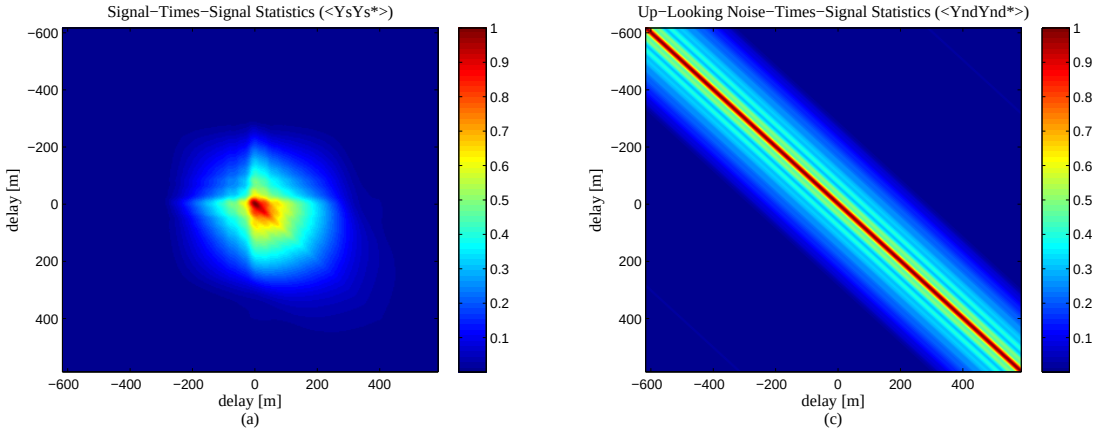

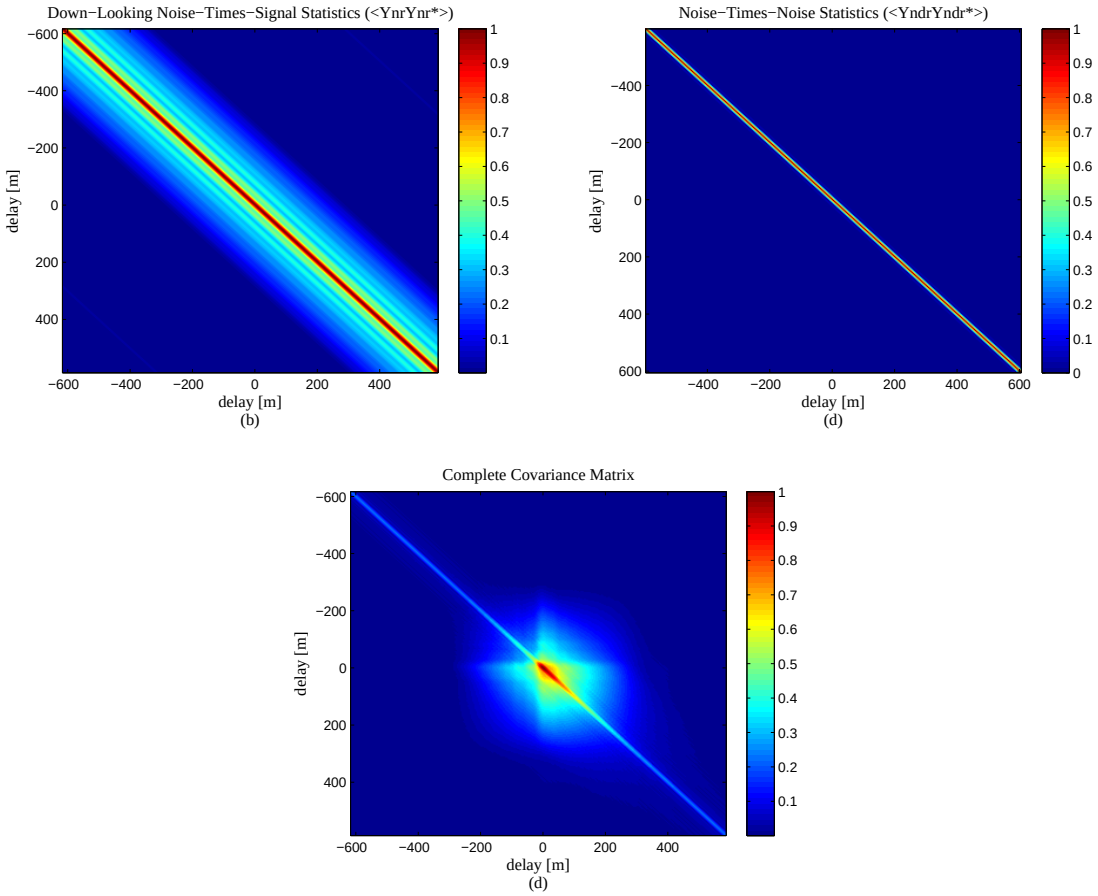

Figure 4.18: Covariance matrices (a) Signal-Times-Signal Statistics ($\langle Y_s Y_s \rangle$), (b) Up-Looking Noise-Times-Signal Statistics ($\langle Y_{nd} Y_{nd} \rangle$), (c) Down-Looking Noise-Times-Signal Statistics ($\langle Y_{nr} Y_{nr} \rangle$), (d) Noise-Times-Noise Statistics ($\langle Y_{ndr} Y_{ndr} \rangle$), (e) Complete covariance matrix (complex cross correlation statistics, including both signal and noise terms).

Figure 4.18 plots the covariance matrices obtained for each of the four cross-correlation products (Signal-Times-Signal Statistics ($\langle Y_s Y_s \rangle$), Up-Looking Noise-Times-Signal Statistics ($\langle Y_{nd} Y_{nd} \rangle$), Down-Looking Noise-Times-Signal Statistics ($\langle Y_{nr} Y_{nr} \rangle$), and Noise-Times-Noise Statistics ($\langle Y_{ndr} Y_{ndr} \rangle$)), as well for the complete covariance matrix (the sum of the four). The computation of the Complex Cross-Correlation Statistics has been performed based on the PIT-POC systems parameters. Addressing to the results shown, it is important to remark the importance of the noise terms on the shape of the complete covariance matrix (specially the term related to the noise-times-noise statistics). On the other hand Fig. 4.21 shows the minor diagonal (main diagonal rotated 90°) for the four components, and the main diagonal for the complete covariance matrix. As it can be appreciated, the signal-times-signal statis-

tics shows a dependency with the squared ACF (note that the shape is affected by the receiver bandwidth), whereas the up/down-looking noise shows a dependency with the ACF. The noise-times-noise statistics shows a dependency with squared sinc. On the other hand, the main diagonal of the complete covariance matrix, is the power waveform. Figures 4.20 and 4.21 shows now the covariance matrices and diagonals considering a ground base case. Table 4.3 summarizes the main system parameters employed in this case, which has been adjusted to the ones from the TIGRIS (Typhon Investigation using GNSS-R Interferometric Signals) Experiment conducted at the East of China (Xichong Bay) [59].

Table 4.3: Simulation System Parameters

Parameter	**Value**	**Unit**
GPS altitude	20200	km
Rec. altitude	120	m
GPS velocity	3.87	km/s
Rec. velocity	0	m/s
Elevation. angle (θ_e)	30	deg
Directivity (D)	15	dBi
Wind Speed (U_{10})	7.5	m/s
Coh. Int. Time (T_c)	1	ms

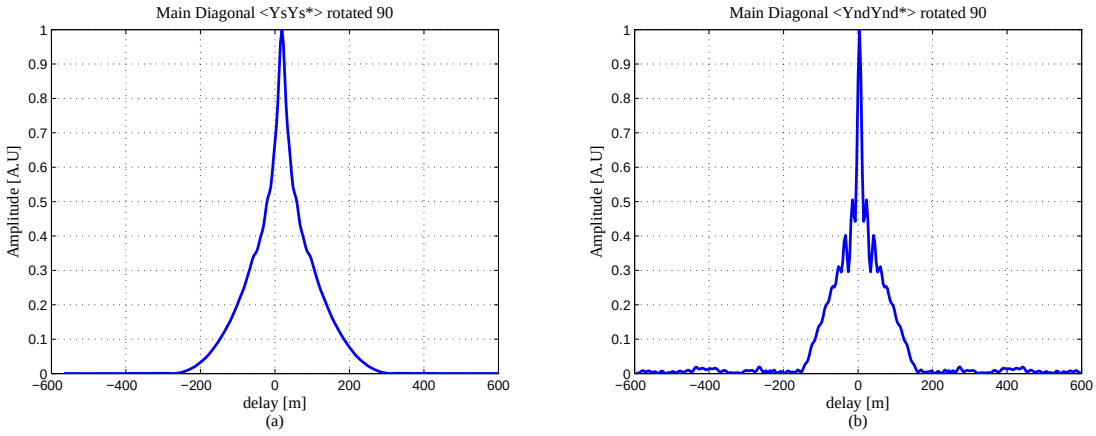

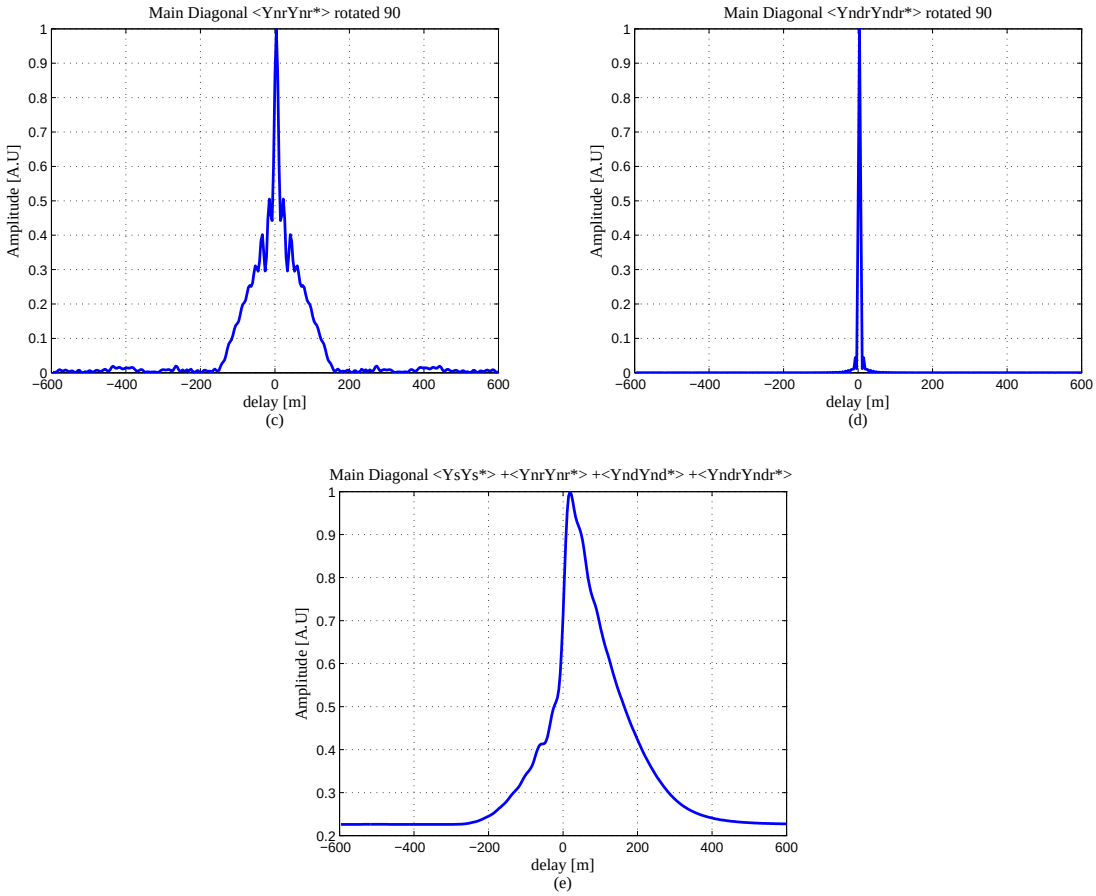

Figure 4.19: Minor Diagonals (a) ($\langle Y_s Y_s \rangle$), (b) ($\langle Y_{nd} Y_{nd} \rangle$), (c) ($\langle Y_{nr} Y_{nr} \rangle$),(d) ($\langle Y_{ndr} Y_{ndr} \rangle$), and (e) Main diagonal Complete covariance matrix (complex cross correlation statistics, including both signal and noise terms).

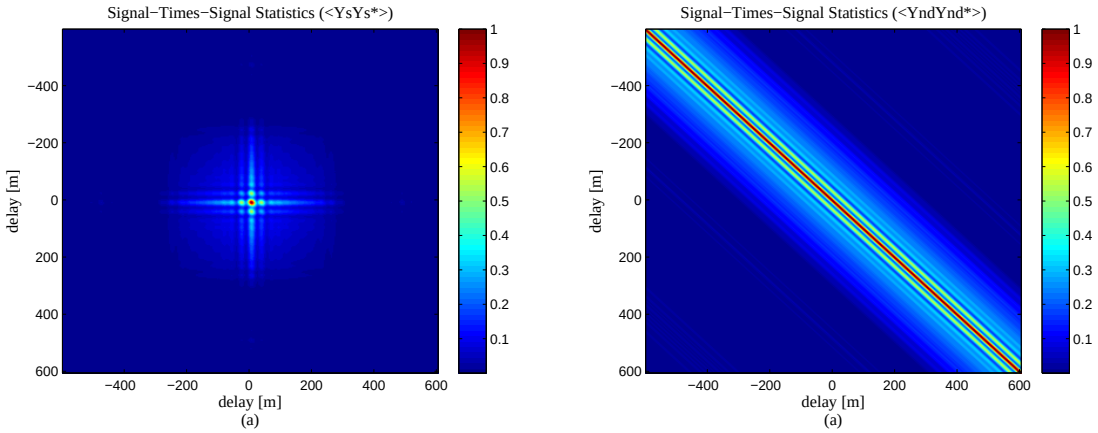

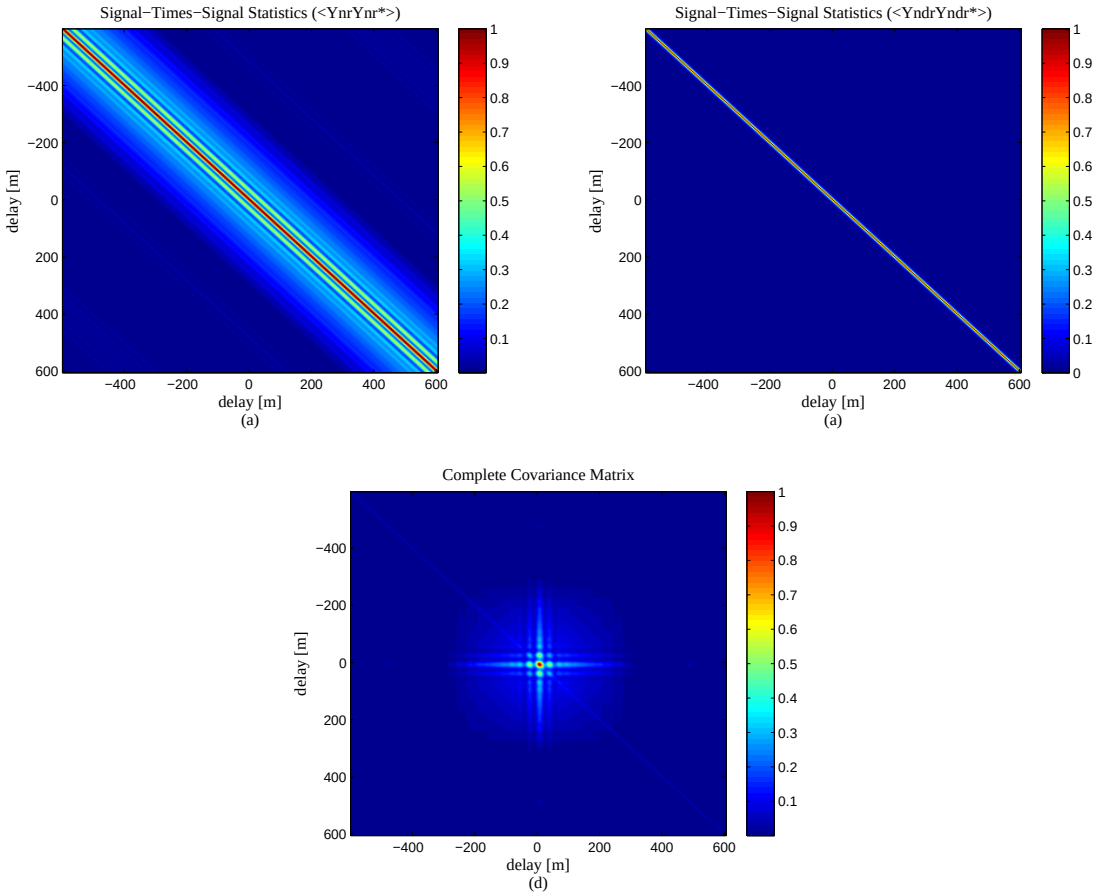

Figure 4.20: Covariance matrices (a) Signal-Times-Signal Statistics ($\langle Y_s Y_s \rangle$), (b) Up-Looking Noise-Times-Signal Statistics ($\langle Y_{nd} Y_{nd} \rangle$), (c) Down-Looking Noise-Times-Signal Statistics ($\langle Y_{nr} Y_{nr} \rangle$), (d) Noise-Times-Noise Statistics ($\langle Y_{ndr} Y_{ndr} \rangle$),(c) Complete covariance matrix (complex cross-correlation statistics, including both signal and noise terms).

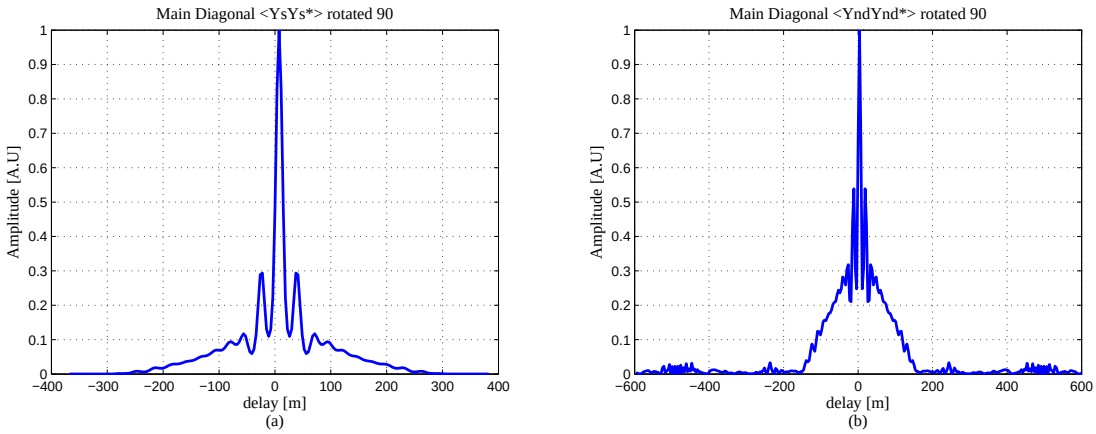

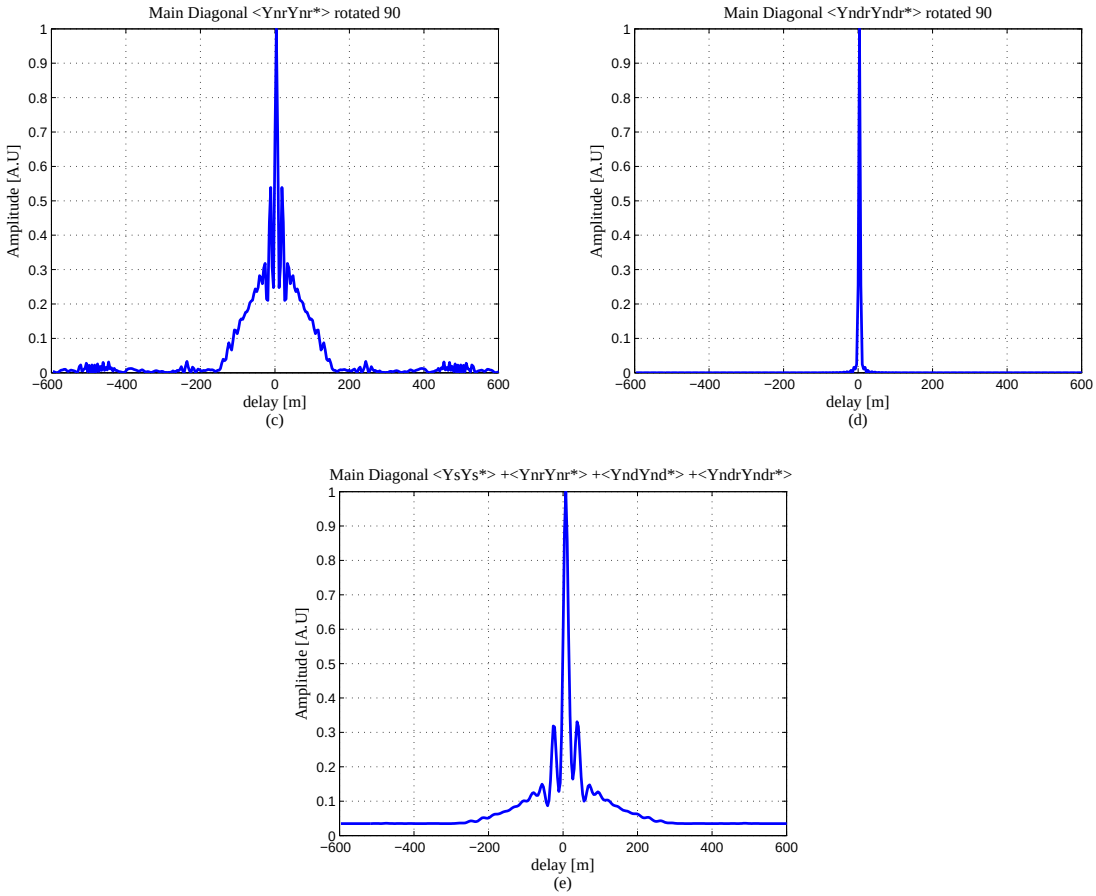

Figure 4.21: (a) Diagonal ($\langle Y_s Y_s \rangle$) rotated 90°, (b) Diagonal ($\langle Y_{nd} Y_{nd} \rangle$) rotated 90°, (c) Diagonal ($\langle Y_{nr} Y_{nr} \rangle$) rotated 90°,(d) Diagonal ($\langle Y_{ndr} Y_{ndr} \rangle$) rotated 90°,(c) Main diagonal Complete covariance matrix (complex cross-correlation statistics, including both signal, and noise terms).

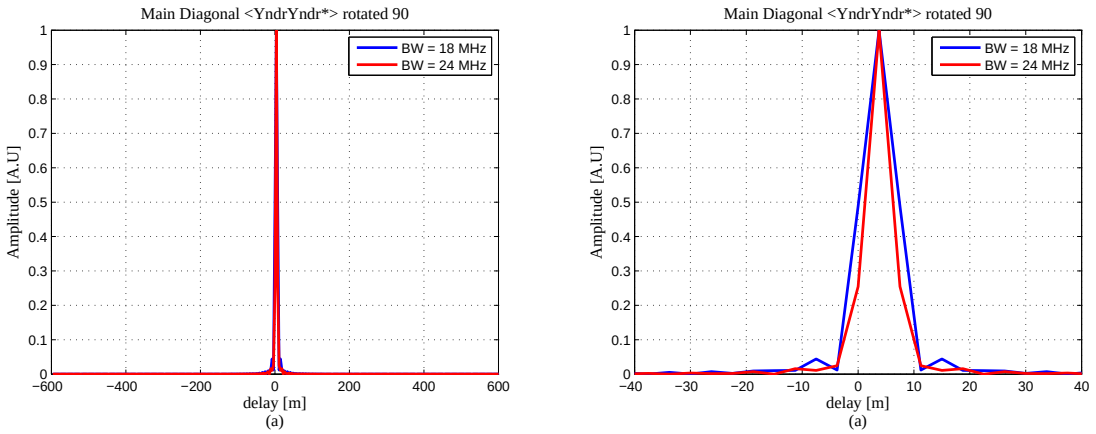

Figure 4.22: (a) Noise-Times-Noise Statistics ($\langle Y_{ndr} Y_{ndr} \rangle$),(c) Minor diagonal, (b) Zoom of Noise-Times-Noise Statistics ($\langle Y_{ndr} Y_{ndr} \rangle$), (c) diagonal rotated.

The main differences obtained in the shape of the covariance matrices, are because in this case the scattered signals are more specular, than in the airborne case. This issue can be clearly appreciated in Fig. 4.21, where the minor and the main diagonals are plotted. Focussing in the main diagonal (equivalent to the power waveform), it is equivalent to the squared ACF (consider that the power waveform basically is the 2D convolution between the squared WAF and the scattered signal, which in this case is close to a delta function). On the other hand, in the minor diagonals it can be observed better the dependency with the squared ACF (for the Signal-Times-Signal Statistics), and with the ACF (for the Up-Looking Noise-Times-Signal Statistics and the Down-Looking Noise-Times-Signal Statistics). Also, the minor diagonal of the noise-times-noise statistics is a bit narrower (it can be observed better on Fig. 4.22). The reason is because the squared exponential dependency of this term, as a function of the receiver bandwidth (ideally it is a delta function when the signal is not filtered, and spreads as the receiver bandwidth is reduced).

4.2.2.1 Model validation with real data

In this section data from the PIT-POC November 11^{th} flight and from the TIGRIS experiment have been used to validate the analytical model presented on Section I.

Figures 4.23 show the complete full covariance matrix obtained from the analytical model, and the ones obtained from the PIT-POC and TIGRIS experiments. As it can be appreciated, both covariances matrices (the ones obtained with the analytical model, and the ones obtained from the real data), are quite similar (practically identical). Figure 4.24 shows the difference obtained between the analytical model and the real data. As it can be observed maximum deviations around 10% are obtained. Thus, the model are in good agreement with real observations

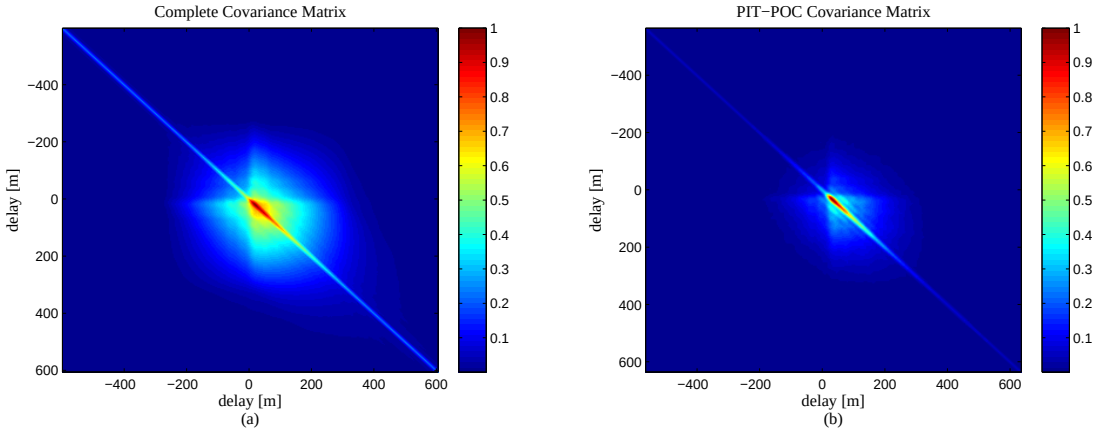

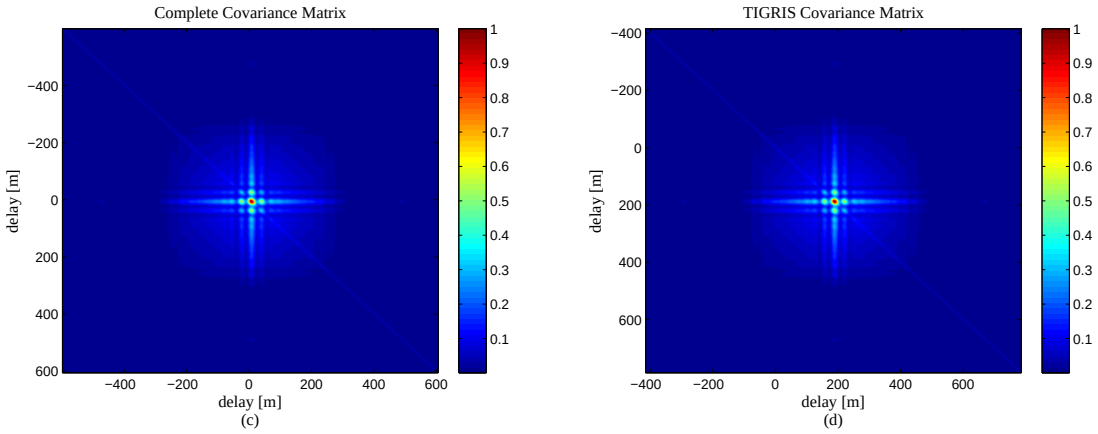

Figure 4.23: (a) Covariance matrix analyitical model, (b) Covariance matrix derived from the PIT-POC data, (c) Covariance matrix analyitical model, (d) Covariance Matrix derived from the TIGRIS data.

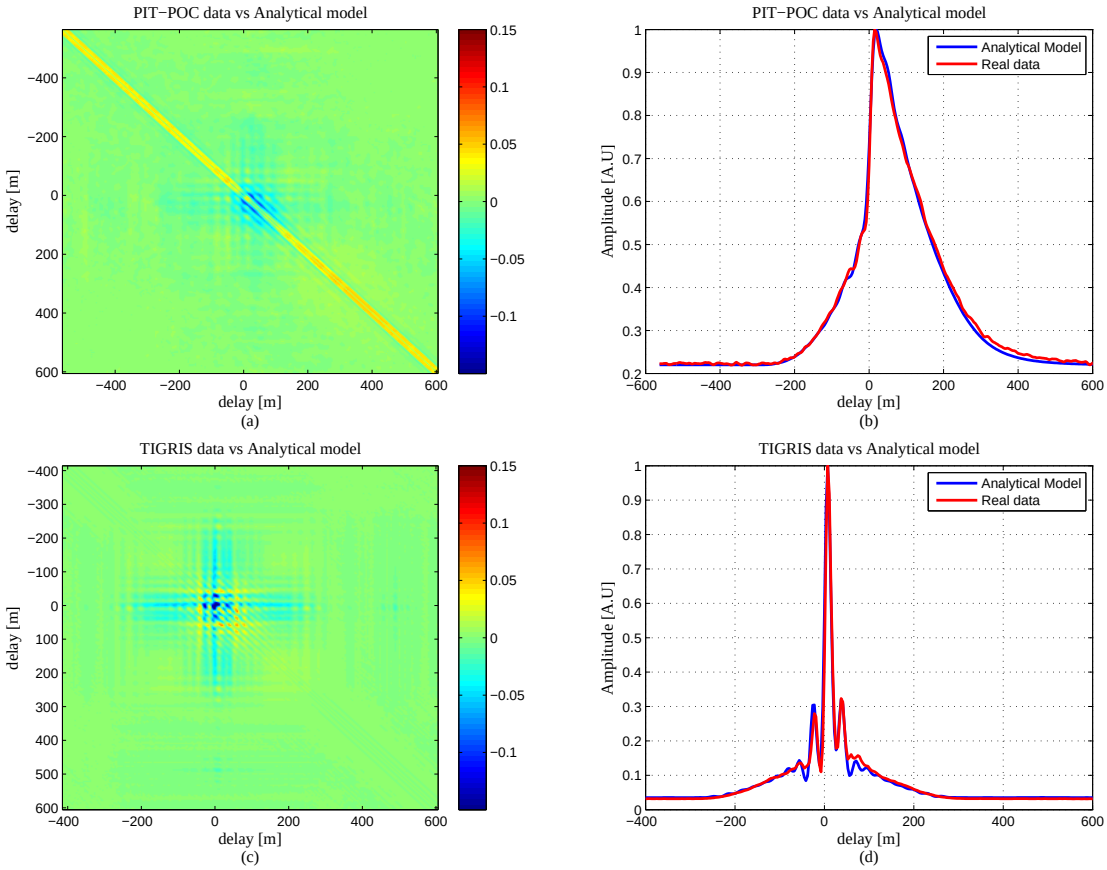

Figure 4.24: (a) Difference between the covariance matrix computed from the PIT-POC data and from thw analytical model, (b) Main diagonal comparison (PIT-POC - Analytical model), (c) Difference between the covariance matrix computed from the TIGRIS data and from the analytical model, (d) Main diagonal comparison (TIGRIS - Analytical model).

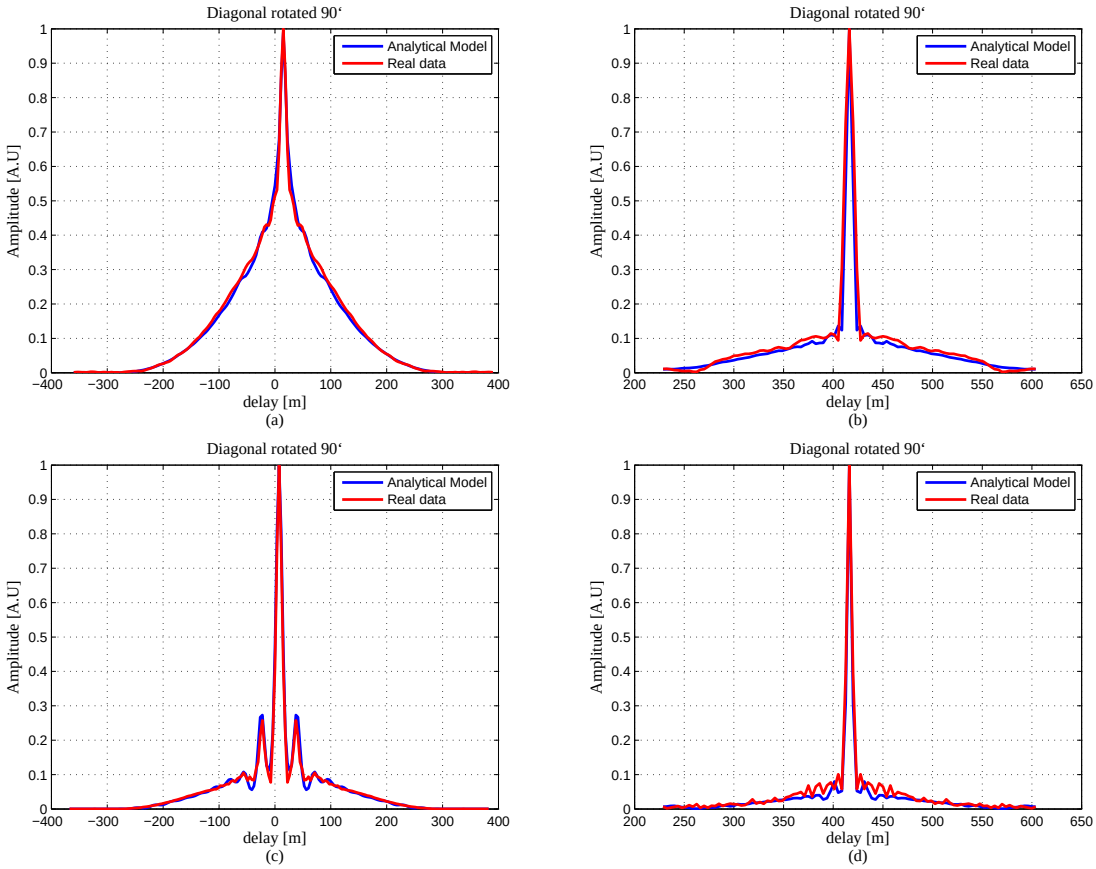

Figure 4.25: Comparison of the diagonals rotated 90° (a) analytical model vs. PIT-POC centered in the signal part, (b) analytical model vs. PIT-POC centered in the noisy part, (c) analytical model vs. TIGRIS centered in the signal part, (d) analytical model vs. TIGRIS centered in the noisy part.

4.2.2.2 Simulated data vs real data

In this section, complex waveforms have been simulated. Therefore, taking as a reference the system parameters of the PIT-POC second fligth, and TIGRIS experiment [59], data have been simulated. As for the cGNSS-R case, the simulated data include the impact of the speckle noise, and the thermal noise.

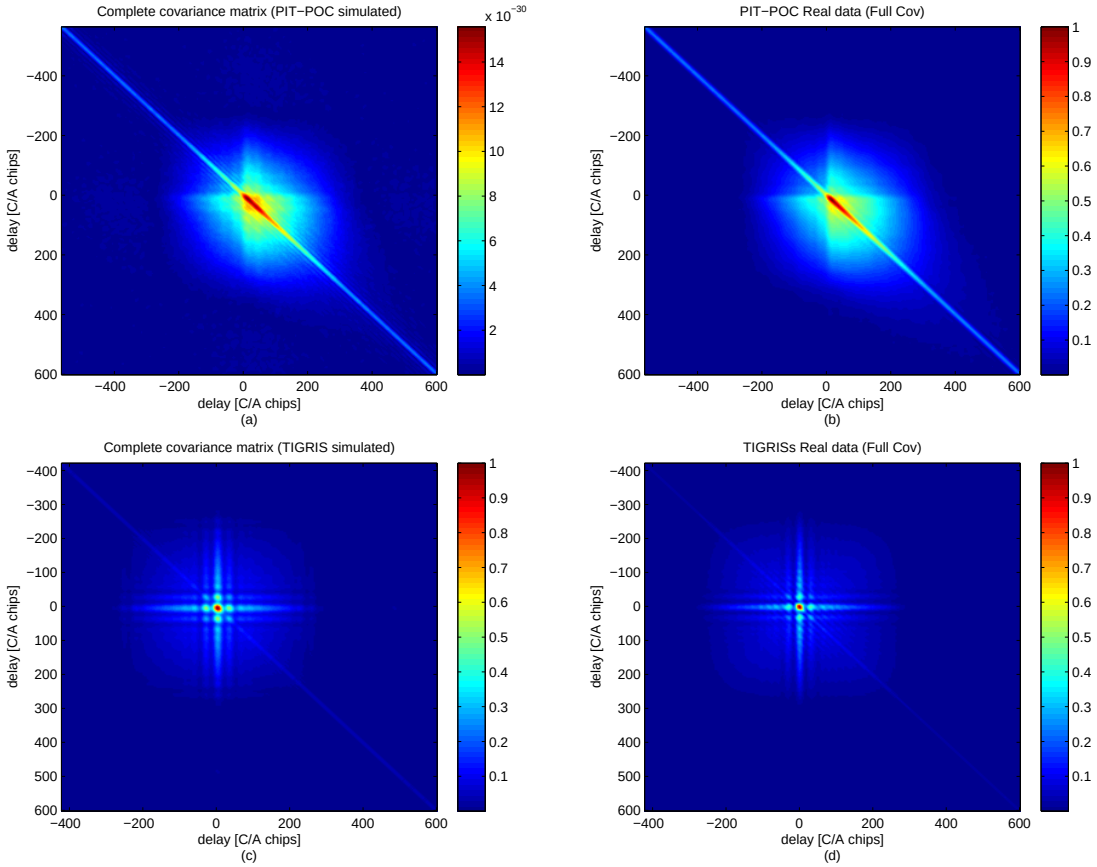

Figure 4.26: (a) Covariance matrix from simulated data, (b) Covariance matrix derived from the PIT-POC data, (c) Covariance matrix from simulated data, (d) Covariance matrix derived from the TIGRIS data.

Figures 4.26 shows the complete covariance matrices obtained from simulated data, and the ones obtained from the PIT-POC and TIGRIS experiments. As can be appreciated, the covariance matrices obtained by the simulated data are quite similar to the ones obtained from the real data. Figures 4.27 shows the difference obtained between the simulated and real data. From it, the maximum deviations obtained are a bit higher than the ones obtained from the analytical model, being in this case around 12% approximately. In any case, it can be concluded that the simulated data, is in agreement with real observations.

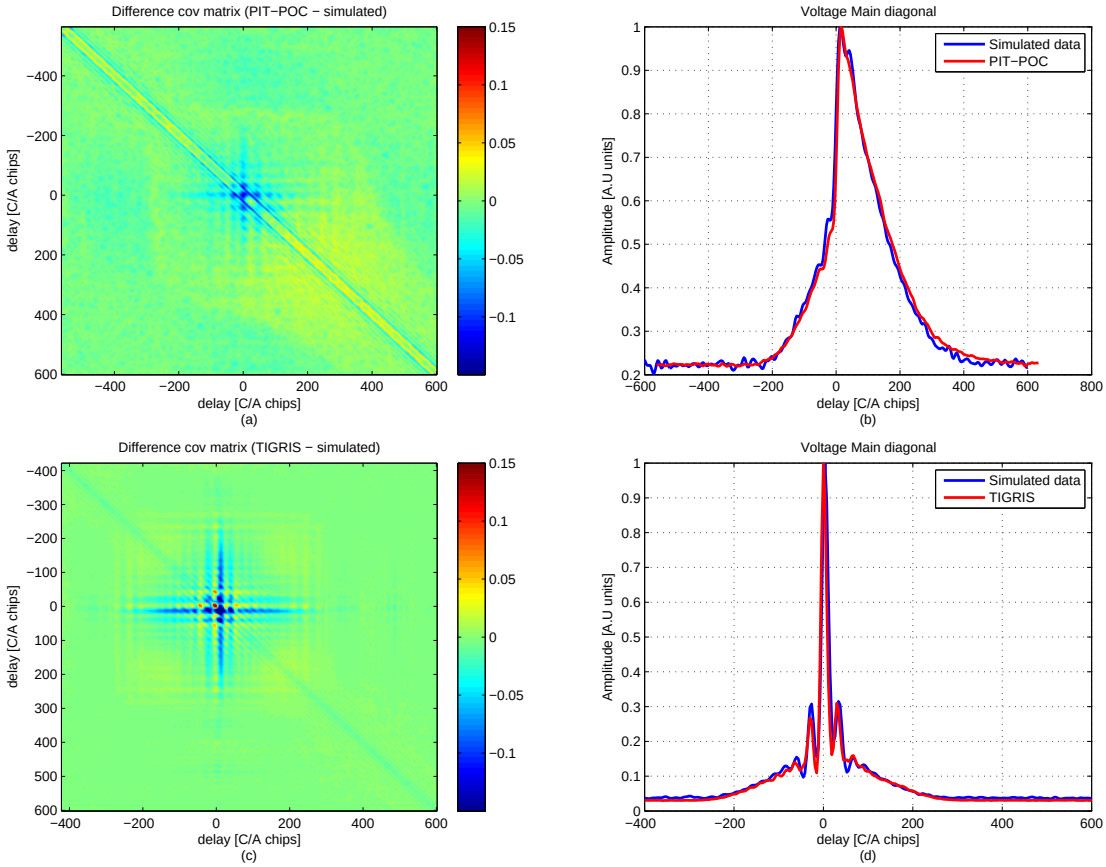

Figure 4.27: (a) Covariance matrix from simulated data, (b) Covariance matrix derived from the PIT-POC data, (c) Covariance matrix from simulated data, (d) Covariance matrix derived from the TIGRIS data.

4.3 Sample to sample correlation model for Power Waveforms

In the previous section an accurate model for the sample-to-sample correlation model (fast time correlation) within complex GNSS-R waveforms, including both the iGNSS-R and the cGNSS-R tehcniques, has been presented and validated. In this section the previous analytical model is extended and validated for the case of power GNSS-R waveforms.

4.3.1 cGNSS-R Sample to sample correlation model for Power Waveforms

As it has been introduced on Section 2, the complex cross-correlation at the output of the correlator at a given delay τ and acquired at a time instant t can be expressed

as the sum of two terms as,

$$Y(t,\tau) = Y_s(t,\tau) + Y_{Nr}(t,\tau), \tag{4.25}$$

where $Y_s(t,\tau)$ is the Signal Voltage cross-correlation and $Y_{Nr}(t,\tau)$ is the Noise Voltage cross-correlation. Thus, from Eqn. (4.25), the power waveform obtained at the output of the cross-correlator can be written as:

$$\begin{aligned}|Y(t,\tau)|^2 =& |Y_s(t,\tau) + Y_{Nr}(t,\tau)|^2, \\ =& |Y_s(t,\tau)|^2 + |Y_{Nr}(t,\tau)|^2 + Y_s(t,\tau)Y_{Nr}^*(t,\tau) + Y_s^*(t,\tau)Y_{Nr}(t,\tau)\end{aligned} \tag{4.26}$$

Therefore, the cross-correlation statistics are given by:

$$\begin{aligned}C =& \big\langle |Y(\tau)|^2 |Y(\tau+\tilde{\tau})|^2 \big\rangle \\ =& \big\langle (|Y_s(\tau)|^2 + |Y_{Nr}(\tau)|^2 + Y_s(\tau)Y_{Nr}^*(\tau) + Y_s^*(\tau)Y_{Nr}(\tau)) \\ & \cdot (|Y_s(\tau+\tilde{\tau})|^2 + |Y_{Nr}(\tau+\tilde{\tau})|^2 + Y_s^*(\tau+\tilde{\tau})Y_{Nr}(\tau+\tilde{\tau}) + Y_s(\tau+\tilde{\tau})Y_{Nr}^*(\tau+\tilde{\tau})) \big\rangle\end{aligned} \tag{4.27}$$

Considering that the signals are circular complex random Gaussian variables (see Appendix C), the fourth-order moments, can be expressed as [60],

$$\big\langle Y_1 Y_2 Y_3^* Y_4^* \big\rangle = \big\langle Y_1 Y_3^* \big\rangle \big\langle Y_2 Y_4^* \big\rangle + \big\langle Y_1 Y_4^* \big\rangle \big\langle Y_2 Y_3^* \big\rangle \tag{4.28}$$

and hence, the cross-correlation statistics can be expressed as (Math detailed in Appendix D),

$$\begin{aligned}C =& \big\langle |Y(\tau)|^2 |Y(\tau+\tilde{\tau})|^2 \big\rangle \\ =& |C_{Y_s}(\tilde{\tau})|^2 + |C_{Y_{Nr}}(\tilde{\tau})|^2 + 2C_{Y_s}(\tilde{\tau})C_{Y_{Nr}}(\tilde{\tau}) \\ & + |C_{Y_s}(0)|^2 + |C_{Y_{Nr}}(0)|^2 + 2C_{Y_s}(0)C_{Y_{Nr}}(0),\end{aligned} \tag{4.29}$$

where

$$|C_Y(\tilde{\tau})|^2 = \big\langle Y(\tau)Y^*(\tau+\tilde{\tau}) \big\rangle \big\langle Y(\tau+\tilde{\tau})Y^*(\tau), \big\rangle \tag{4.30}$$

$$|C_Y(0)|^2 = \big\langle Y(\tau)Y^*(\tau) \big\rangle \big\langle Y(\tau+\tilde{\tau})Y^*(\tau+\tilde{\tau}), \big\rangle \tag{4.31}$$

note that $C_{Y_s}(\tilde{\tau})$ and $C_{Y_{Nr}}(\tilde{\tau})$ have been previously defined on Section 2 (as the signal-to-signal, and the down-looking noise-times-signal statistics).

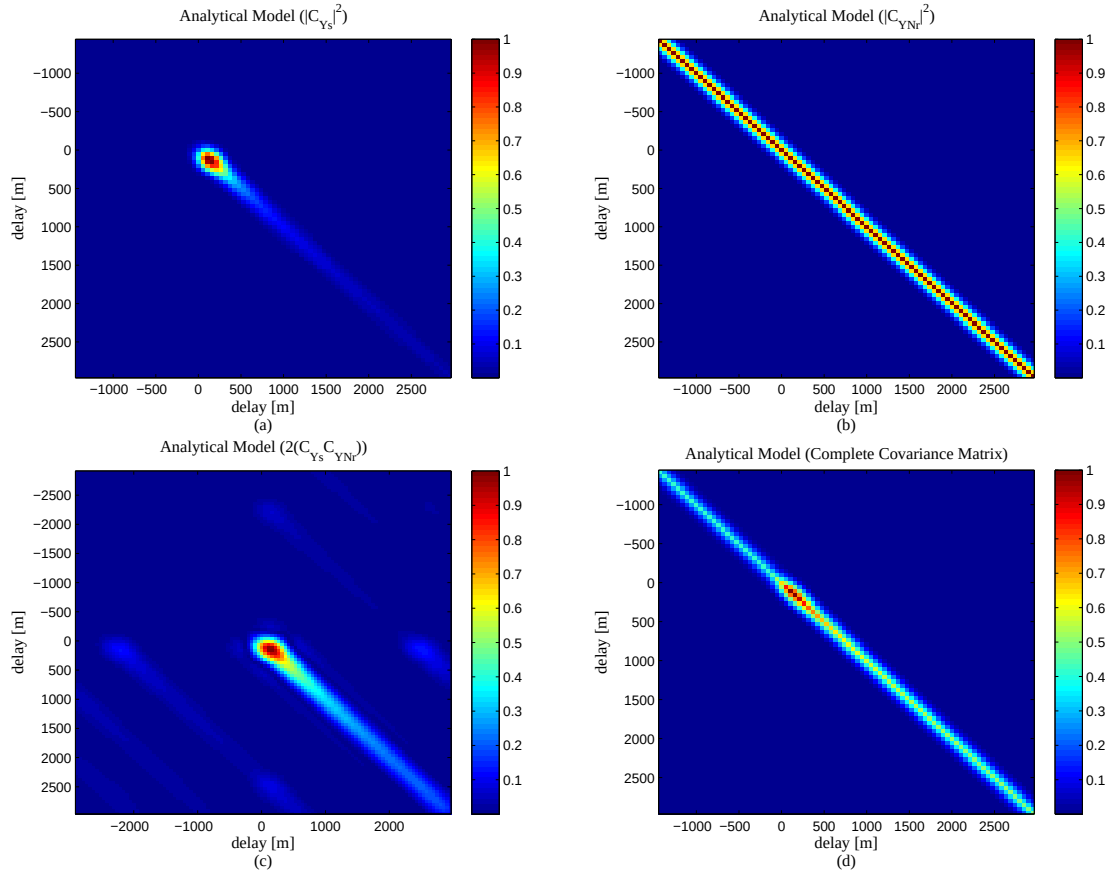

Figure 4.28: Covariance Matrices from the analytical model: (a) $|C_{Y_s}|^2$ term, (b) $|C_{Y_{Nr}}|^2$ term, (c) $2C_{Y_s}C_{Y_{Nr}}$ term, (d) Complete Covariance Matrix ($|C_{Y_s}|^2$ + $|C_{Y_{Nr}}|^2$ + $2C_{Y_s}C_{Y_{Nr}}$).

Figure 4.28 plots the covariance matrices computed from the analytical model for the power waveforms case. From them, many differences can be observed with respect to the complex waveforms case. The first one is that now the complete covariance matrix presents a high SNR with respect to the complex waveforms case. This is basically due to the third term ($2C_{Y_s}C_{Y_{Nr}}$), which is a function of the signal and noise terms. Hence, if instead of the three terms, only the two first terms ($C_{Y_s}|^2$ + $|C_{Y_{Nr}}|^2$) are considered, the new covariance matrix will present a worst SNR (worst also than the one obtained for the complex waveforms), as it can be observed in Fig. 4.28. It is important to note that, for the correct computation of the complete covariance matrix, the three terms should be taken into account.

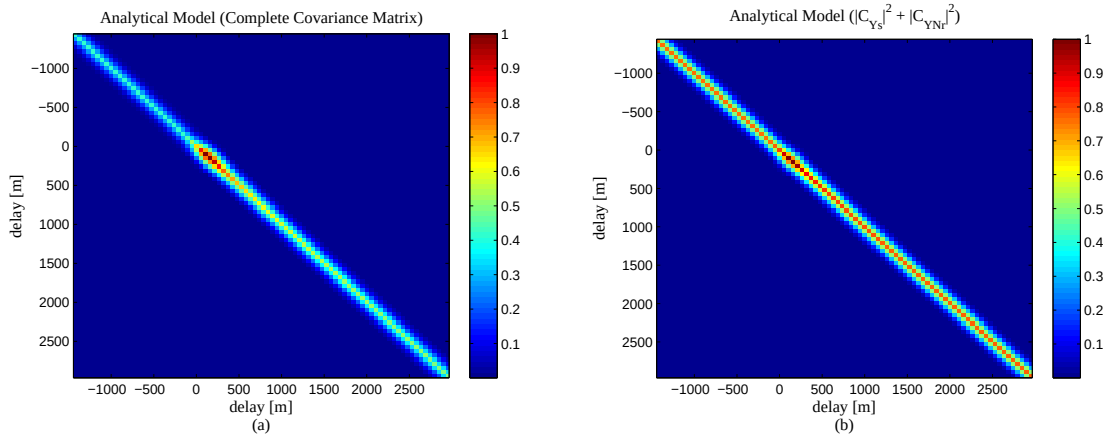

Figure 4.29: Covariance matrices from the analytical models: (a) ($|C_{Y_s}|^2 + |C_{Y_{Nr}}|^2 + 2C_{Y_s}C_{Y_{Nr}}$), (b) ($|C_{Y_s}|^2 + |C_{Y_{Nr}}|^2$).

On the other hand the new complete covariance matrix is narrower, than the one obtained for the same system parameters for the complex waveforms. The reason is because now the signal term ($|C_{Y_s}|^2$), depends on the fourth WAF (for the complex waveforms case it was depending on the squared WAF), whereas $|C_{Y_{Nr}}|^2$ depends on the squared ACF (for the complex waveforms case it was depending on the ACF), since:

$$
\begin{aligned}
|C_{Y_s}(\tilde{\tau})|^2 =& \big\langle Y_s(\tau)Y_s^*(\tau+\tilde{\tau})\big\rangle\big\langle Y_s(\tau+\tilde{\tau})Y_s^*(\tau)\big\rangle \\
=& \Big\langle 2\int_{\theta_i\phi_i} W_{\theta_i,\phi_i}\chi(\Delta\tau,\Delta f,t)e^{-j2\pi f_o\tau_{ri,t}}e^{-j2\pi f_s(t-\tau-T_s)}d\Omega_i \\
& \cdot 2\int_{\theta_j\phi_j} W^*_{\theta_j,\phi_j}\chi^*(\Delta(\tau+\tilde{\tau}),\Delta f,t)e^{j2\pi f_o\tau_{rj,t}}e^{j2\pi f_s(t-\tau-\tilde{\tau}-T_s)}d\Omega_j\Big\rangle \\
& \Big\langle 2\int_{\theta_i\phi_i} W_{\theta_i,\phi_i}\chi(\Delta(\tau+\tilde{\tau}),\Delta f,t)e^{-j2\pi f_o\tau_{ri,t}}e^{-j2\pi f_s(t-\tau-\tilde{\tau}-T_s)}d\Omega_i \\
& \cdot 2\int_{\theta_j\phi_j} W^*_{\theta_j,\phi_j}\chi^*(\Delta\tau,\Delta f,t)e^{j2\pi f_o\tau_{rj,t}}e^{j2\pi f_s(t-\tau-T_s)}d\Omega_j\Big\rangle \\
=& 4\big\langle|W_{\theta,\phi}|^4\big\rangle|\chi(\Delta\tau,\Delta f,t)\chi(\Delta(\tau+\tilde{\tau}),\Delta f,t)|^2, \qquad (4.32)
\end{aligned}
$$

and

$$
|C_{Y_{Nr}}(\tilde{\tau})|^2 = \big\langle Y_{Nr}(\tau)Y_{Nr}^*(\tau+\tilde{\tau})\big\rangle\big\langle Y_{Nr}(\tau+\tilde{\tau})Y_{Nr}^*(\tau)\big\rangle
$$

$$
\begin{aligned}
=&\Big\langle \frac{\sqrt{2}}{T_c}\int_{-\frac{T_c}{2}}^{\frac{T_c}{2}} n_r(t+t')u^*(t+t'-\tau-T_s)e^{-j2\pi f_o(t+t')}e^{-j2\pi f_s(t+t'-\tau-T_s)}dt' \\
&\cdot \frac{\sqrt{2}}{T_c}\int_{-\frac{T_c}{2}}^{\frac{T_c}{2}} n_r^*(t+t'')ut+t''-\tau-\tilde{\tau}-T_s)e^{j2\pi f_o(t+t'')}e^{j2\pi f_s(t+t''-\tau-\tilde{\tau}-T_s)}dt''\Big\rangle \\
&\Big\langle \frac{\sqrt{2}}{T_c}\int_{-\frac{T_c}{2}}^{\frac{T_c}{2}} n_r(t+t')u^*(t+t'-\tau-\tilde{\tau}-T_s)e^{-j2\pi f_o(t+t')}e^{-j2\pi f_s(t+t'-\tau-\tilde{\tau}-T_s)}dt' \\
&\cdot \frac{\sqrt{2}}{T_c}\int_{-\frac{T_c}{2}}^{\frac{T_c}{2}} n_r^*(t+t'')u(t+t''-\tau-T_s)e^{j2\pi f_o(t+t'')}e^{j2\pi f_s(t+t''-\tau-T_s)}dt''\Big\rangle \\
=&(\frac{4kT_{Nr}}{T_c})^2|ACF(\Delta\tau)|^2. \qquad (4.33)
\end{aligned}
$$

Figure 4.30 shows this feature, where the rotated main diagonal of C_{Y_s}, $|C_{Y_s}|^2$, $C_{Y_{Nr}}$, and $|C_{Y_{Nr}}|^2$ are compared.

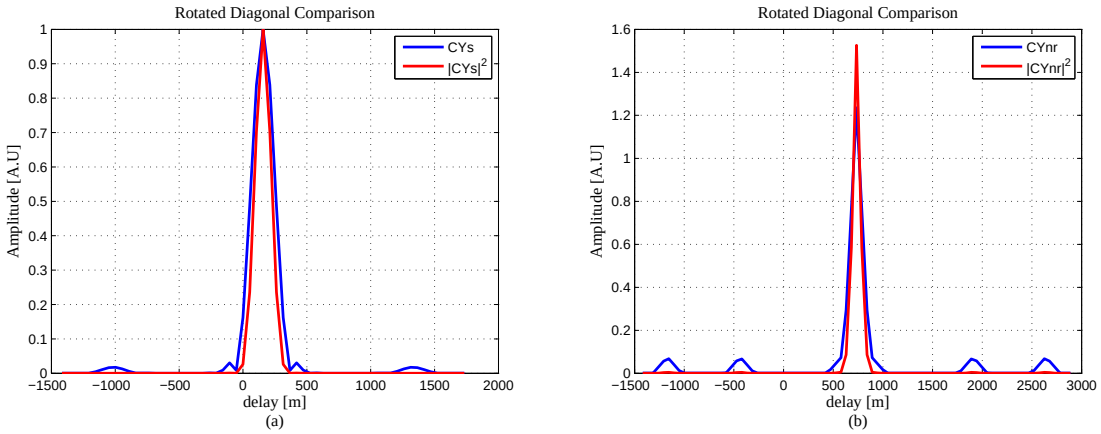

Figure 4.30: Rotated diagonal matrices comparison (a) C_{Y_s} vs. $|C_{Y_s}|^2$, (b) $C_{Y_{Nr}}$, vs. $|C_{Y_{Nr}}|^2$.

On the other hand Eqn. (4.29) can be approximated as:

$$
\begin{aligned}
C =&\big\langle |Y(\tau)|^2|Y(\tau+\tilde{\tau})|^2\big\rangle \\
=&|C_{Y_s}(\tilde{\tau})+C_{Y_{Nr}}(\tilde{\tau})|^2+|C_{Y_s}(0)+C_{Y_{Nr}}(0)|^2, \qquad (4.34)
\end{aligned}
$$

being the difference between this approximation and Eqn.4.29 very small (practically negligible), as it can be appreciated in Fig. 4.31c.

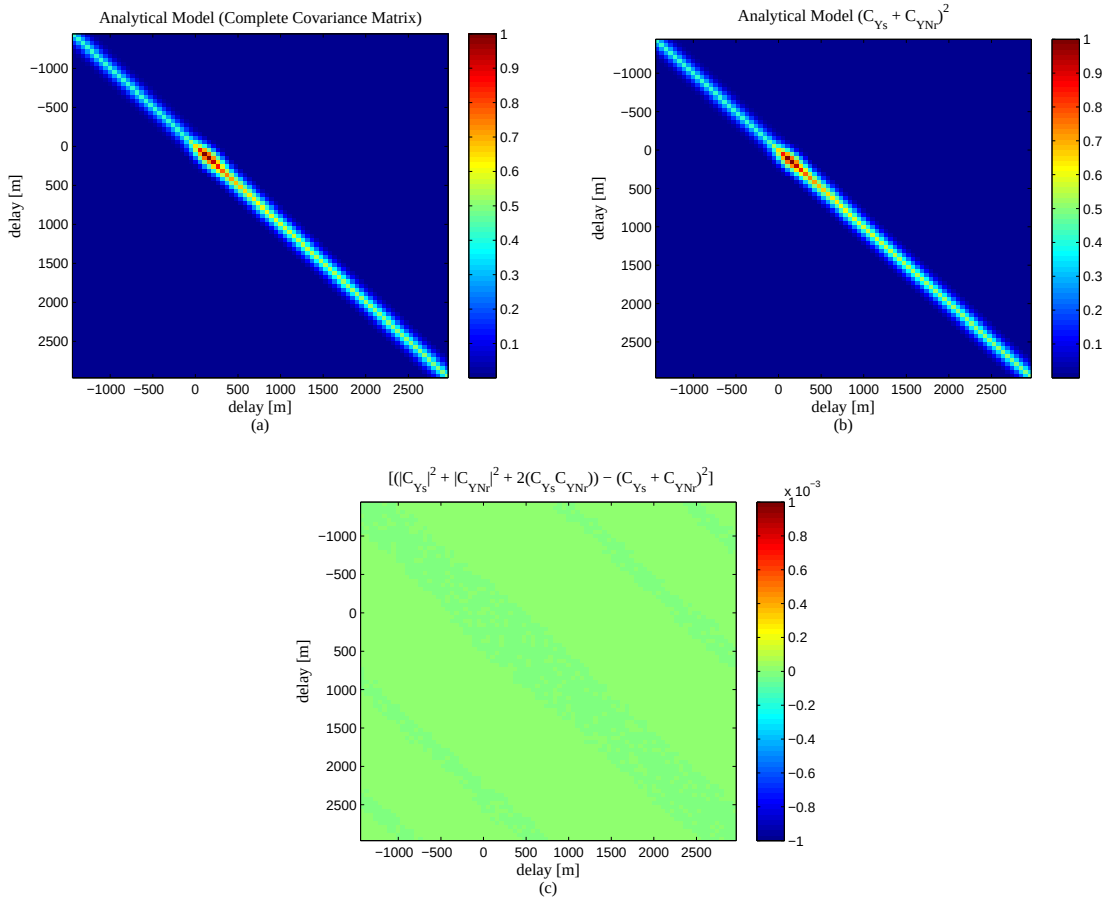

Figure 4.31: (a) Covariance matrix computed from $(|C_{Y_s}|^2 + |C_{Y_{Nr}}|^2 + 2C_{Y_s}C_{Y_{Nr}})$, (b) Covariance matrix computed from $(|C_{Y_s} + C_{Y_{Nr}}|^2$, (c) Difference between (a) and (b).

4.3.1.1 Model validation with real data

In this section data from the UK-DMC satellite has been used to validate the analytical model presented. Figures .4.32 shows the covariance matrices obtained from the UK-DMC data and from the analytical model. As it can be appreciated, both covariance matrices are practically identical, where the difference between them is lower than a 8% (Fig. 4.33). In addition, in Fig. 4.33 it can be observed that both Waveforms (main diagonal of the covariance matrix) are pretty well fitted.

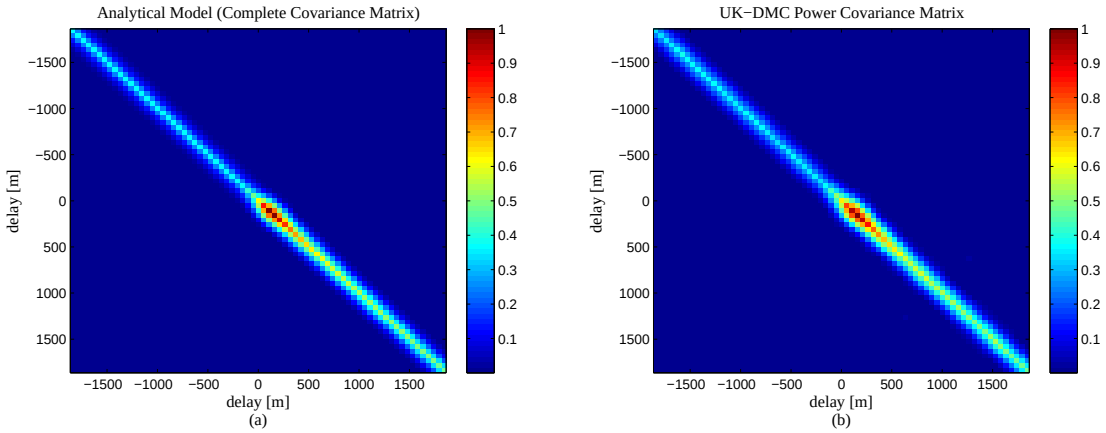

Figure 4.32: (a) Covariance Matrix Analyitical model, (b) Covariance Matrix derived from the UK-DMC data.

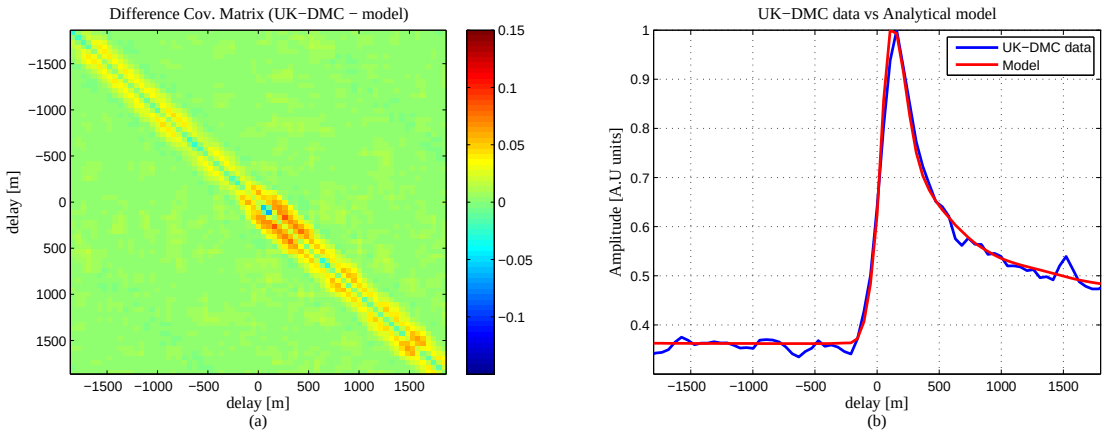

Figure 4.33: (a) Difference between the covariance matrix computed from rhe UK-DMC data and from the analyitical model, (b) Main diagonal of the covariance matrix comparison derived from the UK-DMC data and the analytical model.

4.3.1.2 Model validation with simulated data

In this section the UK-DMC data set is used to validate the simulated Power waveforms. Figures 4.34 shows the covariance matrices obtained from the power waveforms simulated and from the UK-DMC experiment. As it can be appreciated, both matrices are closer, being its maximum deviation lower than a 10%.

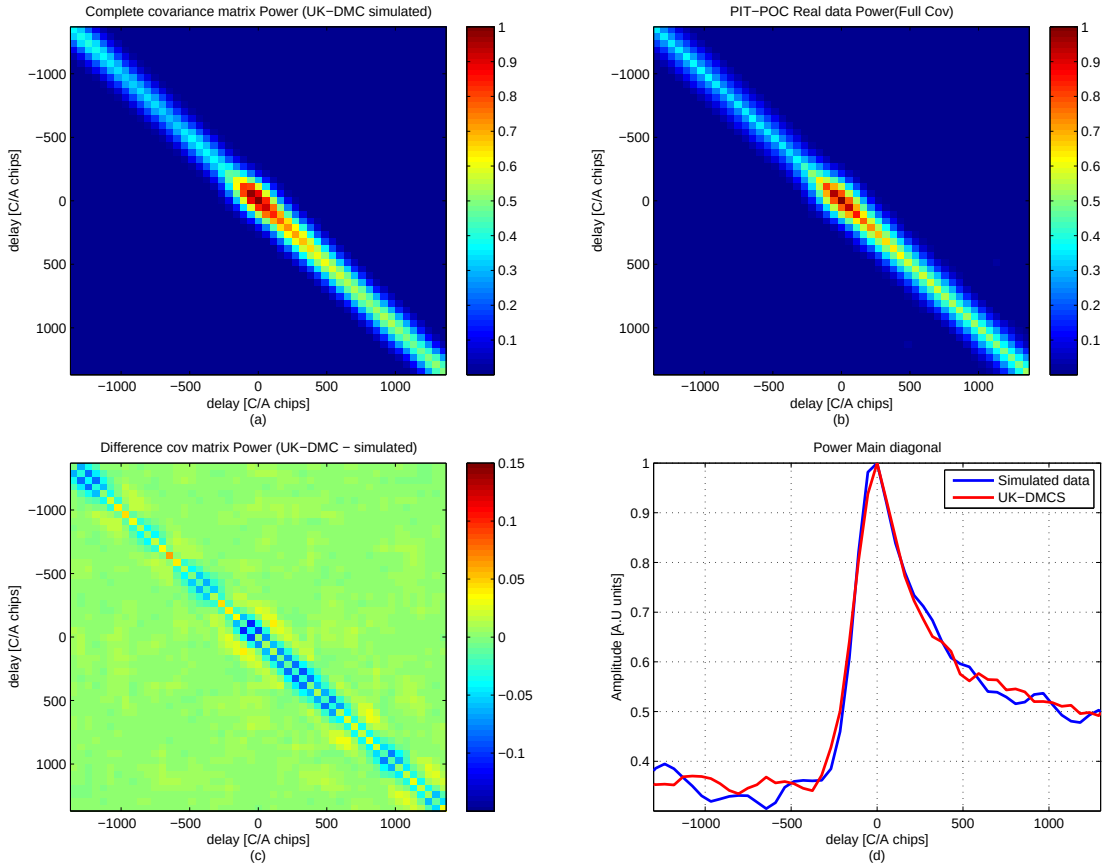

Figure 4.34: (a) Covariance matrix obtained from simulated Power Waveforms, (b) Covariance matrix obtained from UK-DMC data, (c) Difference between the covariance matrix computed from the UK-DMC and from the simulated data, (d) Main diagonal comparison of the covariance matrix comparison derived from the UK-DMC and the simulated data.

4.3.2 iGNSS-R Sample to sample correlation model for Power Waveforms

Following the procedure shown in section 3.1, the cross-correlation statistics for the iGNSS-R technique, considering Power Waveforms, is presented in this section.

As previously introduced, the complex waveform at the output of the cross-correlator can be expressed as the sum of four terms (Y_s, Y_{Nr}, Y_{Nd}, and Y_{Ndr}). Thus, considering this feature, the power waveform obtained at the output can be expressed as,

$$|Y(t,\tau)|^2 = |Y_s(t,\tau) + Y_{Nr}(t,\tau) + Y_{Nd}(t,\tau) + Y_{Ndr}(t,\tau)|^2$$

$$
\begin{aligned}
=&|Y_s(t,\tau)|^2 + Y_s(t,\tau)Y_{Nr}^*(t,\tau) + Y_s(t,\tau)Y_{Nd}^*(t,\tau) + Y_s(t,\tau)Y_{Ndr}^*(t,\tau) \\
&+ Y_{Nr}(t,\tau)Y_{Ns}^*(t,\tau) + |Y_{Nr}(t,\tau)|^2 + Y_{Nr}(t,\tau)Y_{Nd}^*(t,\tau) + Y_{Nr}(t,\tau)Y_{Ndr}^*(t,\tau) \\
&+ Y_{Nd}(t,\tau)Y_{Ns}^*(t,\tau) + Y_{Nd}(t,\tau)Y_{Nr}^*(t,\tau) + |Y_{Nd}(t,\tau)|^2 + Y_{Nd}(t,\tau)Y_{Ndr}^*(t,\tau) \\
&+ Y_{Ndr}(t,\tau)Y_s^*(t,\tau) + Y_{Ndr}(t,\tau)Y_{Nr}^*(t,\tau) + Y_{Ndr}(t,\tau)Y_{Nd}^*(t,\tau) + |Y_{Ndr}(t,\tau)|^2
\end{aligned}
\tag{4.35}
$$

being the cross-correlation statistic given by

$$
\begin{aligned}
C =&\left\langle |Y(\tau)|^2 |Y(\tau+\tilde{\tau})|^2 \right\rangle \\
=&\big\langle (|Y_s(\tau)|^2 + Y_s(\tau)Y_{Nr}^*(\tau) + Y_s(\tau)Y_{Nd}^*(\tau) + Y_s(\tau)Y_{Ndr}^*(\tau) \\
&+ Y_{Nr}(\tau)Y_{Ns}^*(\tau) + |Y_{Nr}(\tau)|^2 + Y_{Nr}(\tau)Y_{Nd}^*(\tau) + Y_{Nr}(\tau)Y_{Ndr}^*(\tau) \\
&+ Y_{Nd}(\tau)Y_{Ns}^*(\tau) + Y_{Nd}(\tau)Y_{Nr}^*(\tau) + |Y_{Nd}(\tau)|^2 + Y_{Nd}(\tau)Y_{Ndr}^*(\tau) \\
&+ Y_{Ndr}(\tau)Y_s^*(\tau) + Y_{Ndr}(\tau)Y_{Nr}^*(\tau) + Y_{Ndr}(\tau)Y_{Nd}^*(\tau) + |Y_{Ndr}(\tau)|^2) \\
&(|Y_s(\tau+\tilde{\tau})|^2 + Y_s^*(\tau+\tilde{\tau})Y_{Nr}(\tau+\tilde{\tau}) + Y_s^*(\tau+\tilde{\tau})Y_{Nd}(\tau+\tilde{\tau}) \\
&+ Y_s^*(\tau+\tilde{\tau})Y_{Ndr}(\tau+\tilde{\tau}) + Y_{Nr}^*(\tau+\tilde{\tau})Y_{Ns}(\tau+\tilde{\tau}) + |Y_{Nr}(\tau+\tilde{\tau})|^2 \\
&+ Y_{Nr}^*(\tau+\tilde{\tau})Y_{Nd}(\tau+\tilde{\tau}) + Y_{Nr}^*(\tau+\tilde{\tau})Y_{Ndr}(\tau+\tilde{\tau}) + Y_{Nd}^*(\tau+\tilde{\tau})Y_{Ns}(\tau+\tilde{\tau}) \\
&+ Y_{Nd}^*(\tau+\tilde{\tau})Y_{Nr}(\tau+\tilde{\tau}) + |Y_{Nd}(\tau+\tilde{\tau})|^2 + Y_{Nd}^*(\tau+\tilde{\tau})Y_{Ndr}(\tau+\tilde{\tau}) \\
&+ Y_{Ndr}^*(\tau+\tilde{\tau})Y_s(\tau+\tilde{\tau}) + Y_{Ndr}^*(\tau+\tilde{\tau})Y_{Nr}(\tau+\tilde{\tau}) + Y_{Ndr}^*(\tau+\tilde{\tau})Y_{Nd}(\tau+\tilde{\tau}) \\
&+ |Y_{Ndr}(\tau+\tilde{\tau})|^2)\big\rangle
\end{aligned}
\tag{4.36}
$$

As in the previous section, the signals are circular complex Gaussian random variables (see Appendix C), hence the fourth-order moments can be computed using Eqn. (4.27) [60]. Therefore Eqn.(4.36) becomes (Appendix E),

$$
\begin{aligned}
C =&\left\langle |Y(\tau)|^2 |Y(\tau+\tilde{\tau})|^2 \right\rangle \\
=&|C_{Y_s}(\tau)|^2 + |C_{Y_{Nr}}(\tau)|^2 + |C_{Y_{Nd}}(\tau)|^2 + |C_{Y_{Ndr}}(\tau)|^2 \\
&+ 2C_{Y_s}(\tau)C_{Y_{Nr}}(\tau) + 2C_{Y_s}(\tau)C_{Y_{Nd}}(\tau) + 2C_{Y_s}(\tau)C_{Y_{Ndr}}(\tau) \\
&+ 2C_{Y_{Nr}}(\tau)C_{Y_{Nd}}(\tau) + 2C_{Y_{Nr}}(\tau)C_{Y_{Ndr}}(\tau) + 2C_{Y_{Nd}}(\tau)C_{Y_{Ndr}}(\tau) \\
&|C_{Y_s}(0)|^2 + |C_{Y_{Nr}}(0)|^2 + |C_{Y_{Nd}}(0)|^2 + |C_{Y_{Ndr}}(0)|^2 \\
&+ 2C_{Y_s}(0)C_{Y_{Nr}}(0) + 2C_{Y_s}(0)C_{Y_{Nd}}(0) + 2C_{Y_s}(0)C_{Y_{Ndr}}(0) \\
&+ 2C_{Y_{Nr}}(0)C_{Y_{Nd}}(0) + 2C_{Y_{Nr}}(0)C_{Y_{Ndr}}(0) + 2C_{Y_{Nd}}(0)C_{Y_{Ndr}}(0)
\end{aligned}
\tag{4.37}
$$

Therefore, these results, in 10 different terms. Figure 4.35, represents each one of these 10 terms, as well the complete covariance matrix.

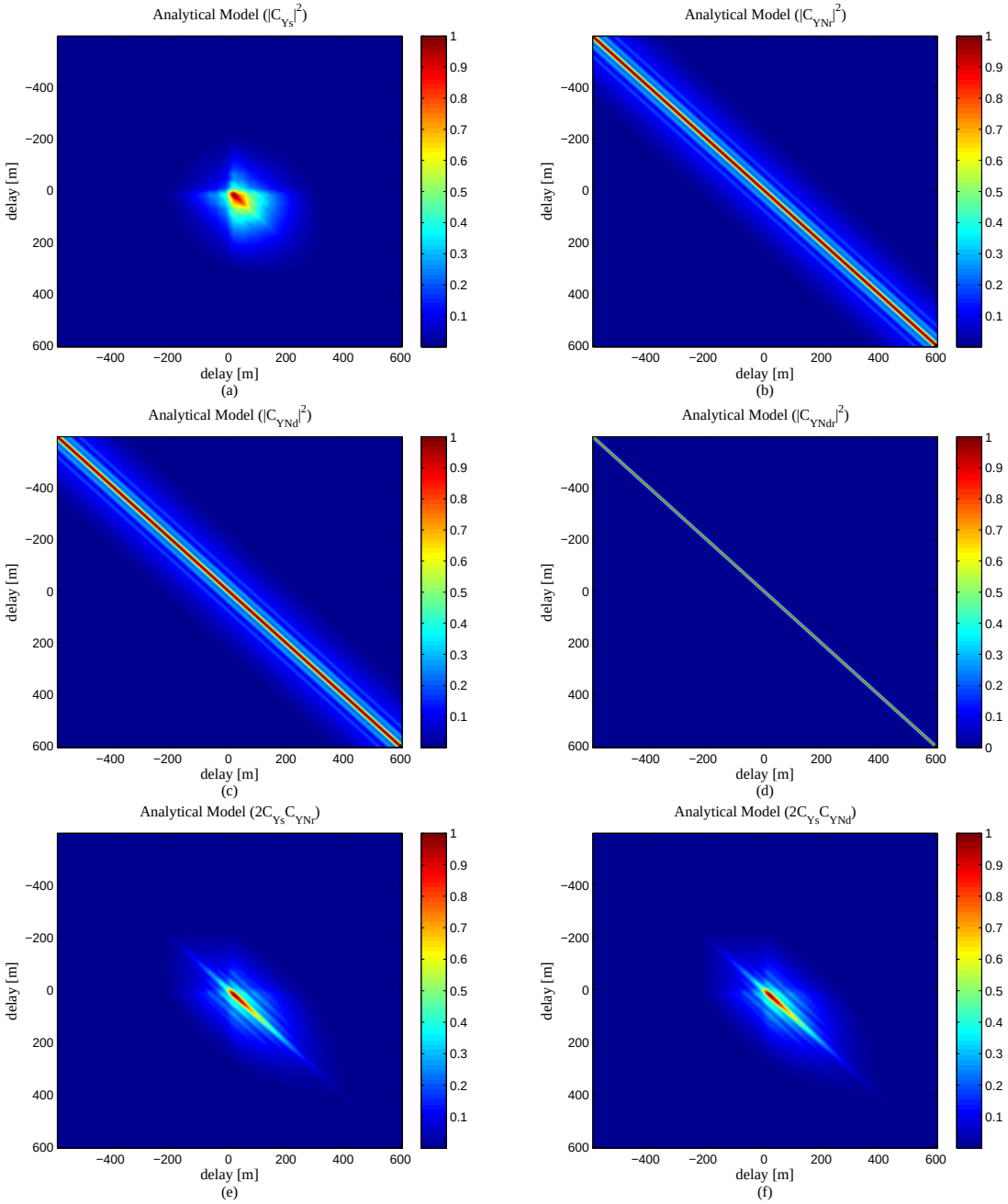
Analytical Model (|C_Ys|^2)
delay [m]
delay [m]
(a)
Analytical Model (|C_YNr|^2)
delay [m]
delay [m]
(b)
Analytical Model (|C_YNd|^2)
delay [m]
delay [m]
(c)
Analytical Model (|C_YNdr|^2)
delay [m]
delay [m]
(d)
Analytical Model (2C_Ys C_YNr)
delay [m]
delay [m]
(e)
Analytical Model (2C_Ys C_YNd)
delay [m]
delay [m]
(f)

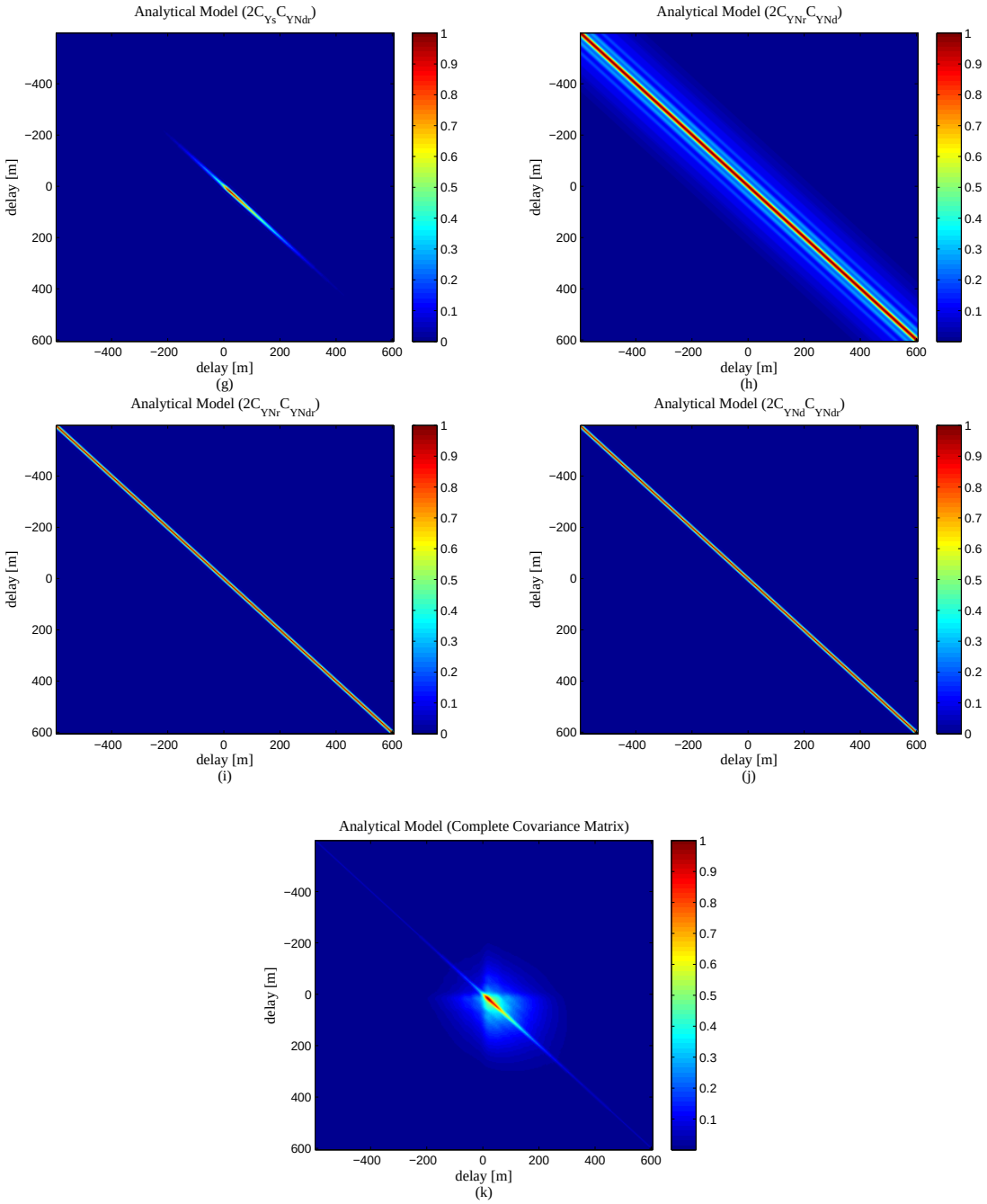

Figure 4.35: Rotated diagonal matrices comparison (a) $|C_{Y_s}|^2$, (b) $|C_{Y_Nr}|^2$, (c) $|C_{Y_Nd}|^2$, (d) $|C_{Y_Ndr}|^2$, (e) $2C_{Y_s}C_{Y_Nr}$, (f) $2C_{Y_s}C_{Y_Nd}$, (g) $2C_{Y_s}C_{Y_Ndr}$, (h) $2C_{Y_Nr}C_{Y_Nd}$, (i) $2C_{Y_Nr}C_{Y_Ndr}$, (j) $2C_{Y_Nd}C_{Y_Ndr}$, and (k) Complete Covariance Matrix.

On the other hand Eqn. (4.37) can be approximated as:

$$\begin{aligned} C =& \left\langle |Y(\tau)|^2 |Y(\tau+\tilde{\tau})|^2 \right\rangle \\ =& |C_{Y_s}(\tilde{\tau}) + C_{Y_{Nr}}(\tilde{\tau}) + C_{Y_{Nd}}(\tilde{\tau}) + C_{Y_{Ndr}}(\tilde{\tau})|^2 \\ &+ |C_{Y_s}(0) + C_{Y_{Nr}}(0) + C_{Y_{Nd}}(0) + C_{Y_{Ndr}}(0)|^2, \end{aligned} \tag{4.38}$$

as it occurs in the cGNSS-R case, the result obtained by the approximation is practically the same to the result obtained using the full analytical model (Eqn. (4.37)), being the difference between it and the fully analytical model practically negligible (Fig. 4.36 c).

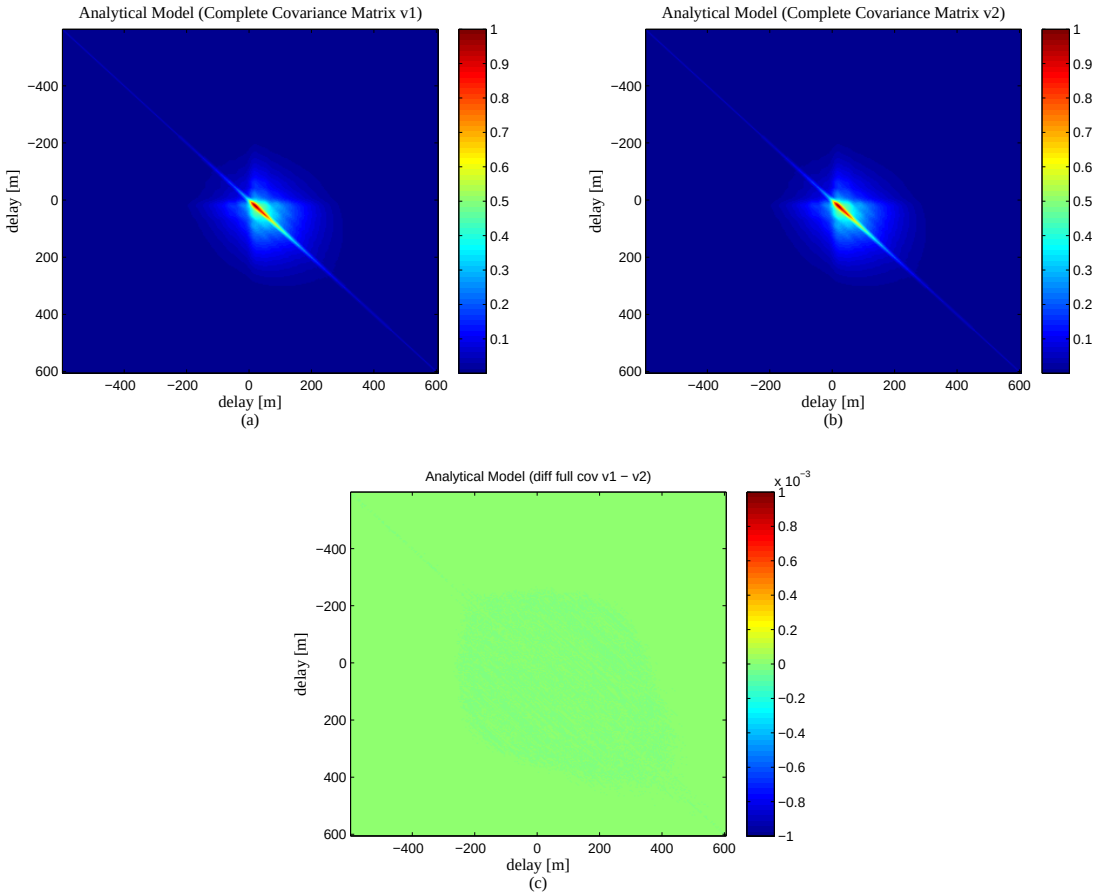

Figure 4.36: (a) Covariance matrix computed from $(|C_{Y_s}|^2 + |C_{Y_{Nr}}|^2 + |C_{Y_{Nd}}|^2 + |C_{Y_{Ndr}}|^2 + 2C_{Y_s}C_{Y_{Nr}} + 2C_{Y_s}C_{Y_{Nd}} + 2C_{Y_s}C_{Y_{Ndr}} + 2C_{Y_{Nr}}C_{Y_{Nd}} + 2C_{Y_{Nr}}C_{Y_{Ndr}} + 2C_{Y_{Nd}}C_{Y_{Ndr}})$, (b) Covariance matrix computed from $(|C_{Y_s} + C_{Y_{Nr}} + C_{Y_{Nd}} + C_{Y_{Ndr}}|^2$, and (c) Difference between (a) and (b).

4.3.2.1 Model Validation with real data

In this section, data from the PIT-POC November 11^{th} 2011 flight and from the TIGRIS experiment have been used again to validate the analytical model presented in section 2.2.

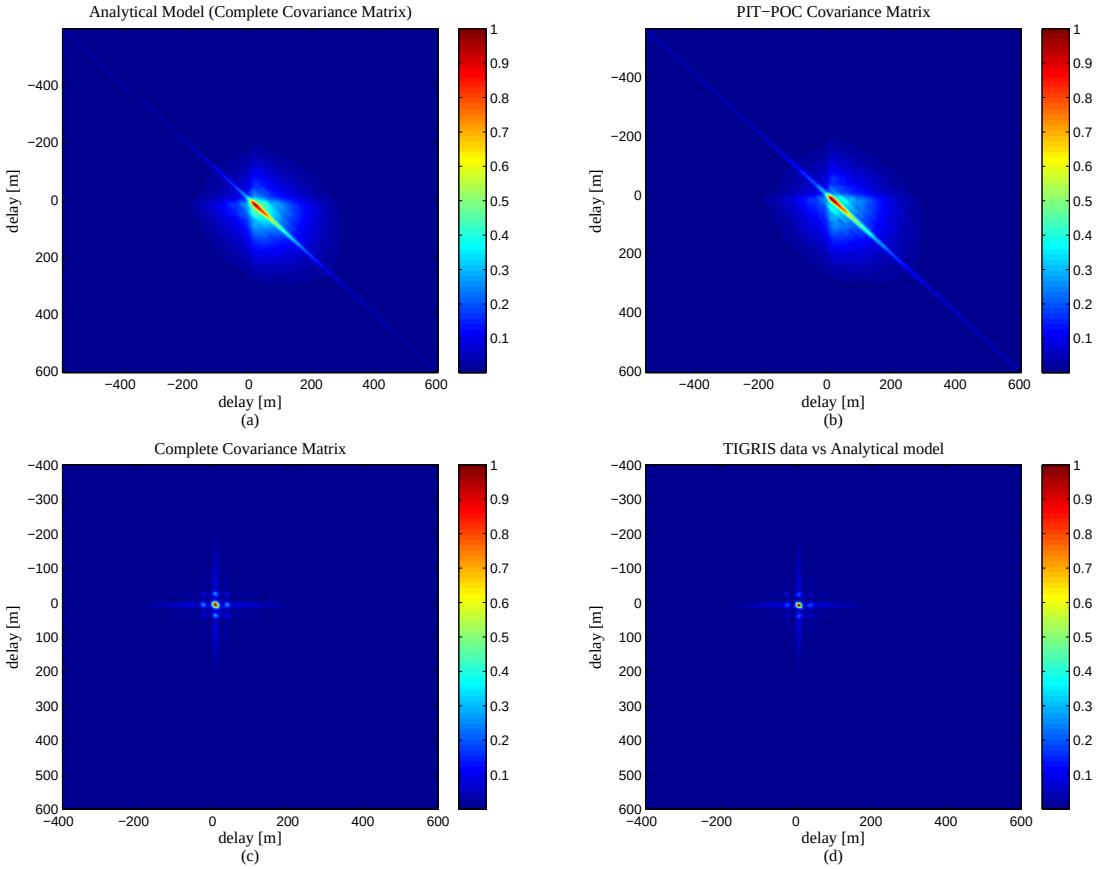

Figure 4.37: (a) Covariance Matrix Analyitical model, (b) Covariance Matrix derived from the PIT-POC data, (c) Covariance Matrix Analyitical model, (d) Covariance Matrix derived from the TIGRIS data.

Figure 4.37 shows the complete full covariance matrix obtained from the analytical model, and the ones obtained from the PIT-POC and TIGRIS experiments. As it occurred in previous sections, the ones obtained with the analytical model, and the ones obtained from the real data, are quite similar (practically identical), where no apparent differences are identified. This can be appreciated in Fig. 4.38, where the difference between the covariance matrices obtained with the analytical model and with the real data are showed. As it can be appreciated, that differences are lower than a 10%

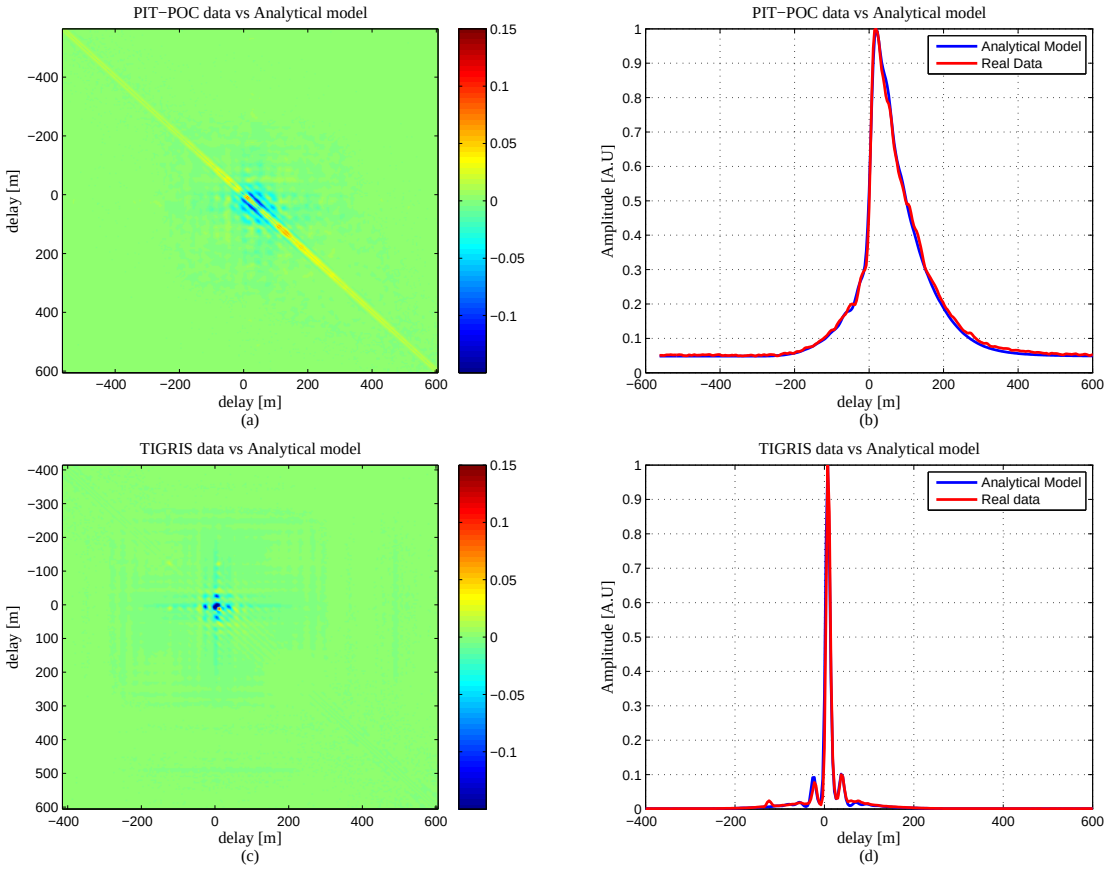

Figure 4.38: (a) Difference between the covariance matrix computed from the PIT-POC data and from the analytical model, (b) Main diagonal comparison (PIT-POC Analytical model), (c) Difference between the covariance matrix computed from the TIGRIS data and from the analytical model, (d) Main diagonal comparison (TIGRIS Analytical model).

To finish, Figs. 4.38b, and 4.38d show the Waveforms (main diagonal) obtained from the analytical model and real data. As it can be appreciated, the ones obtained with the analytical model match pretty well the ones obtained with the real data. The same conclusion can be extracted if the minor diagonals (main diagonal rotated 90°) are compared (Fig. 4.39).

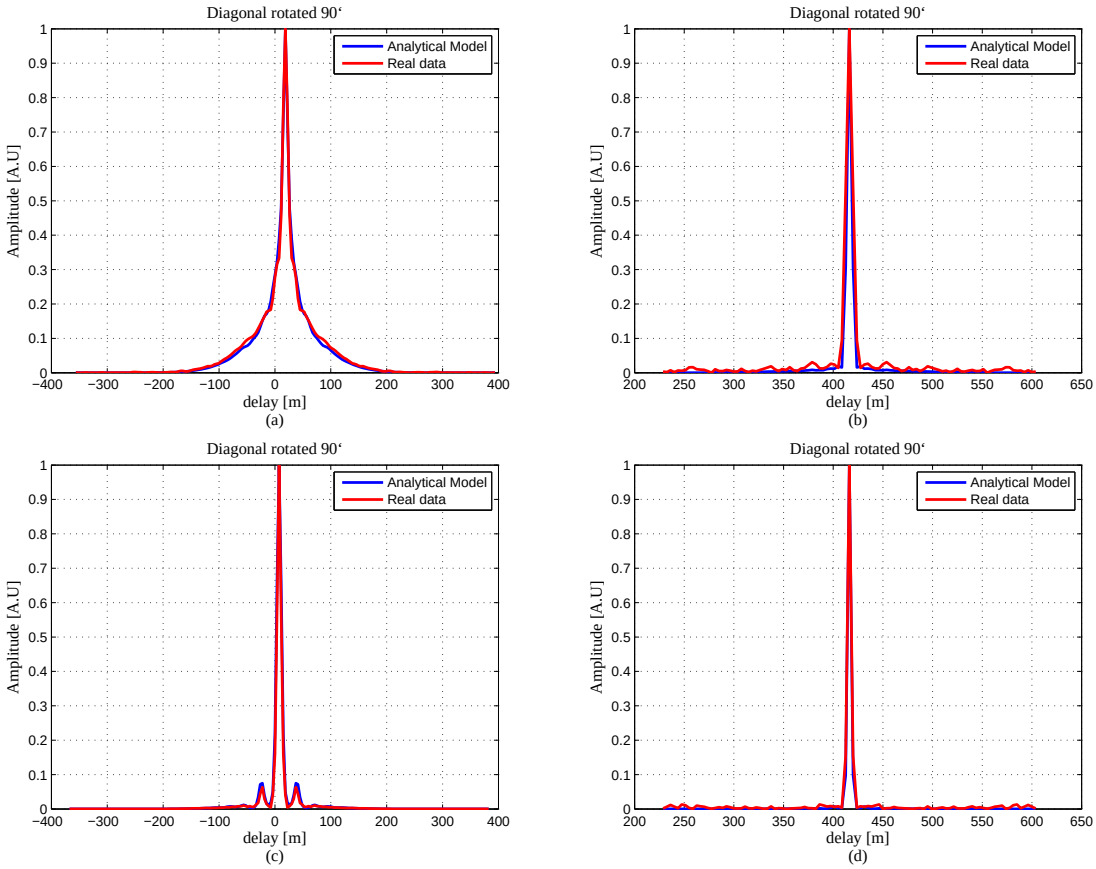

Figure 4.39: Diagonals rotated 90° comparison (a) Analytical model vs. PIT-POC centered in the signal part, (b) Analytical model vs. PIT-POC centered in the noisy part, (c) Analytical model vs. TIGRIS centered in the signal part, (d) Analytical model vs. TIGRIS centered in the noisy part.

4.3.2.2 Model Validation with simulated data

As in the previous section, data from the PIT-POC November 11^{th} 2011 flight and from the TIGRIS experiment is used, for validate the simulated data.

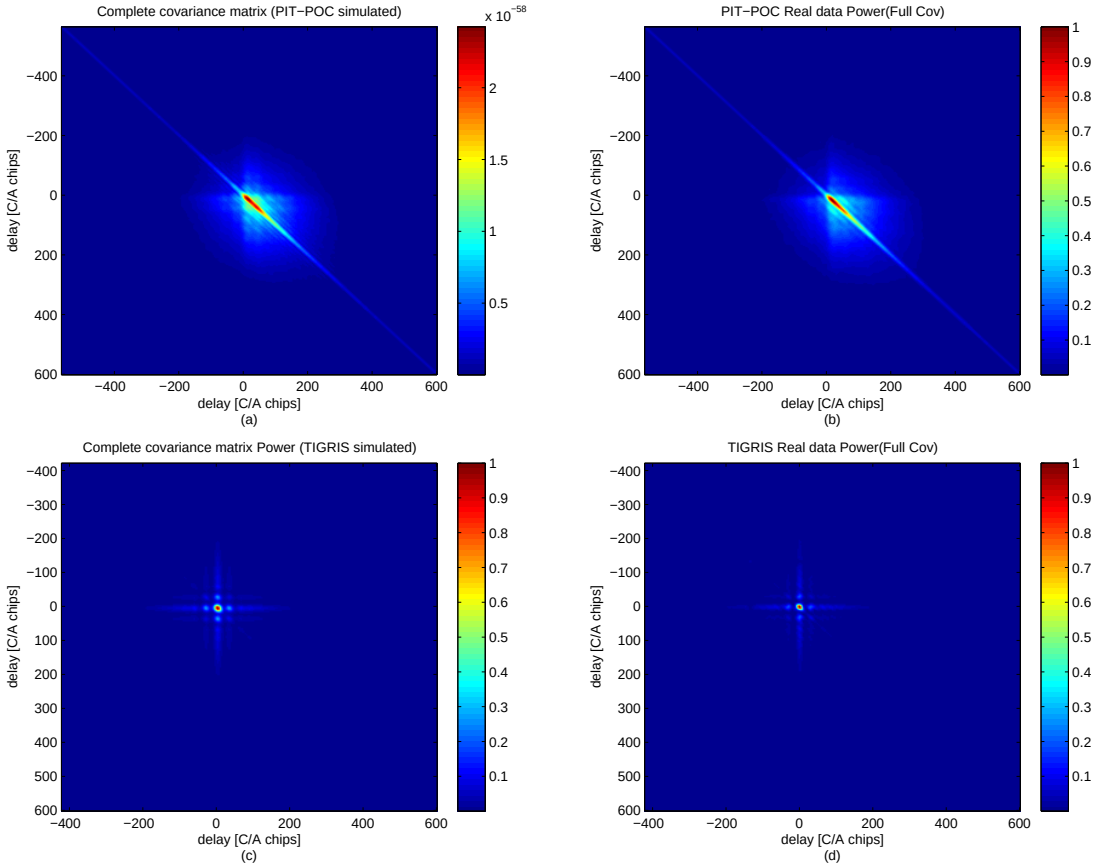

Figure 4.40: (a) Covariance matrix from simulated data, (b) Covariance matrix derived from the PIT-POC data, (c) Covariance matrix from simulated data, (d) Covariance matrix derived from the TIGRIS data.

Figures 4.40 shows the complete covariance matrices obtained from simulated data, and the ones obtained from the PIT-POC and TIGRIS experiments. As can be appreciated, the covariance matrices obtained by the simulated data are quite similar to the ones obtained from the real data.

Figures 4.41 shows the difference obtained between the simulated and real data. As occurs for the complex waveforms case, the maximums deviations obtained are a bit higher than the ones for the analytical model, being around 12% approximately. In any case, it can be concluded that the simulated data, is in agreement with the real observations.

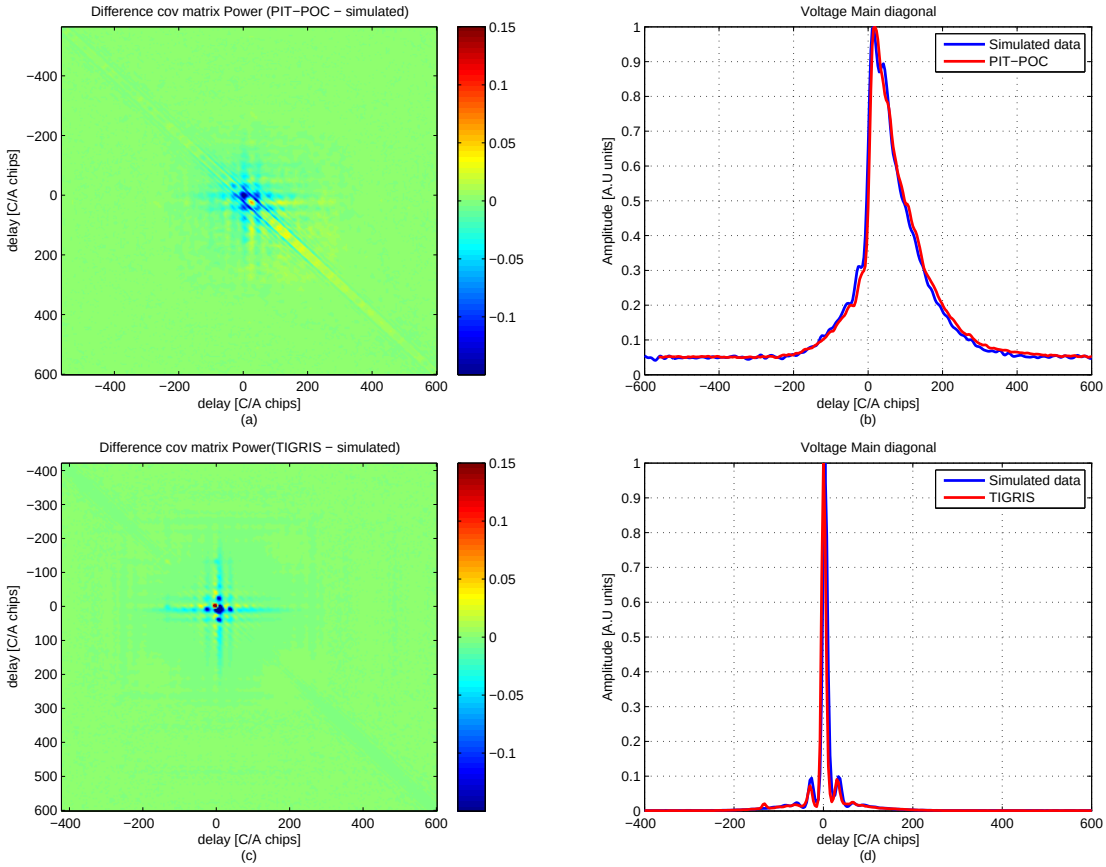

Figure 4.41: (a) Covariance matrix from simulated data, (b) Covariance matrix derived from the PIT-POC data, (c) Covariance matrix from simulated data, (d) Covariance matrix derived from the TIGRIS data.

4.4 Conclusions

This chapter has presented a detailed analytical model of the correlation between samples within a GNSS-R waveform (fast-time correlation), also referred to as the GNSS-R waveform covariance matrix, including complex and power waveforms, and covering both the cGNSS-R and iGNSS-R techniques. The theoretical derivation of the model has been described in detail and a validation against real data from the UK-DMC, PIT-POC second flight and TIGRIS experiment. The model was found to be in very good agreement with real observations, with errors well within 10%. The availability of such detailed covariance model has opened the door to assess the performance of a GNSS-R spaceborne altimeter, as a function of important system parameters. The proposed model can be also adopted to analyse the correlation properties of delay-Doppler Maps (DDM), and to evaluate the benefit of using the full DDM for altimetry applications. The presented method could also be used to

assess the performance of other GNSS-R applications such as scatterometry or soil moisture retrieval.

Chapter 5

Evaluation of the Cramer-Rao Bound (CRB) for GNSS-R waveforms

The previous chapter presented an accurate and validated model for the sample-to-sample correlation (fast-time correlation) within GNSS-R waveforms (i.e. covariance matrix). The knowledge of the covariance matrix can be very useful in order to assess the altimetry performance limit of GNSS-R spaceborne systems, and in general, to optimize the altimetry performance. For example, the covariance matrix can be used to evaluate the Cramer-Rao Bound (CRB) to estimate the range of the specular path from the GNSS-R waveform. Thus, in this chapter the covariance matrix is used to evaluate the Cramer-Rao bound (CRB) for the estimation of the minimum range/delay from the GNSS-R waveform.

5.1 Introduction

To date, the GNSS-R altimetry precision has been analyzed by adopting simple analytical models, which describe in closed form the sensitivity of the height precision as function of system/instrument parameters such as the thermal noise SNR, the observation geometry, the speckle, the autocorrelation properties of composite GNSS transmitted signals and the on ground processor parameters [36].

However, these methods rely on a number of assumptions (for example on the re-tracking Level 1-b processing), and very likely do not represent the true optimal achievable precision. The prediction of the optimal height precision shall instead rely on a method which is independent of the retrieval processing (i.e. employed estimator) and shall inherently make use of the time statistics of the observed signal, e.g. the

covariance matrix. As it is well known from statistical theory, the error variance of any unbiased estimator is low-bounded by its corresponding Cramer-Rao bound [57]. This bound can be easily calculated if the probability density function of the signal (including noise) under analysis is known.

Hence, the Cramer-Rao bound will be used to evaluate a wide variety of parameters concerning the overall observation system. Thus instrument/system parameters such as the sampling frequency, the signal-noise-ratio, or the receiver bandwidth are addressed in this chapter.

5.2 The Cramer-Rao Bound (CRB)

It is well known in estimation theory that the Cramer-Rao Bound provides the minimum variance of an unbiased estimator (if it exists) [57], and it can be evaluated only by knowing the covariance matrix of the observed signal, under the assumption that it is a Circular Gaussian random process [58]. As it will be shown later, the voltage samples of GNSS-R waveforms satisfy this assumption, and therefore the knowledge of the covariance matrix becomes an important tool for the analysis of the performance of GNSS-R systems. In the following, the Cramer-Rao Bound for the estimation of the minimum range/delay from the GNSS-R waveform is analysed. In order to understand the properties of the GNSS-R waveforms, and to optimize the performance of a spaceborne GNSS-R system, the Cramer-Rao Bound has been evaluated for a wide variety of parameters concerning the overall observation system, including instrument, on-board, and on-ground processing aspects. This allows to identify the critical factors driving the performance of GNSS-R systems. It is important to mention that, to date, the GNSS-R altimetry performance has been mainly predicted by means of simple analytical methods [7], [36], which rely on a number of assumptions on the retrieval estimators and do not take into account the correlation between samples within a waveform. Because of these limitations, important system parameters affecting the retrieval such as the sampling frequency and the retracking window have not been subject of trade-off and optimization. On the other hand, the Cramer-Rao Bound does not have these limitations, and allows to provide a solid theoretical analysis.

By means of the Cramer-Rao Bound (CRB), the minimum variance of an unbiased estimator can be evaluated (here it will be the minimum variance of the range

estimation) [19]. The CRB is given by:

$$var(\tilde{\theta}) \geq \frac{1}{I(\theta)}, \tag{5.1}$$

where θ is the parameter to be estimated (in this case the range of the reflected signal), and $I(\theta)$ is the so-called Fisher Information Matrix, that can be expressed as,

$$I(\theta) = -E[\frac{\partial^2 \ln(p(x;\theta)}{\delta\theta^2}], \tag{5.2}$$

The Cramer-Rao Bound can be written as a function of only the covariance matrix if the observed signal follows complex circular Gaussian statistics.

Hence, the observed GNSS-R waveform can be denoted as $\tilde{\boldsymbol{x}} \sim CN(\boldsymbol{\mu(\theta)}, \boldsymbol{C(\theta)})$, where $\tilde{x}$ is a complex random vector ($\tilde{x} = [\tilde{x}_1, \tilde{x}_2, \cdots, \tilde{N}]^T$) with $\tilde{x}_1 = u + jv$. The mean is $\tilde{\mu}(\theta) = E[u] + jE[v]$, and the covariance matrix is an Hermitian Matrix ($C^H(\theta) = C(\theta)$). Therefore the Circular Gaussian probability density function (pdf) can be written as:

$$p(\tilde{\boldsymbol{x}};\boldsymbol{\theta}) = \frac{1}{(\pi)^N |\boldsymbol{C(\theta)}|} \exp[-(\tilde{\boldsymbol{x}} - \tilde{\boldsymbol{\mu}}(\boldsymbol{\theta}))^H \boldsymbol{C}^{-1}(\boldsymbol{\theta})(\tilde{\boldsymbol{x}} - \tilde{\boldsymbol{\mu}}(\boldsymbol{\theta})]. \tag{5.3}$$

Applying Eqn.(5.3) to Eqn.(5.2) the Fisher Information matrix can be written as:

$$\begin{aligned} |\boldsymbol{I}(\boldsymbol{\theta})|_{i,j} =& E\left[\frac{\partial \ln p(\tilde{\boldsymbol{x}}:\boldsymbol{\theta})}{\partial\theta_i}\frac{\partial \ln p(\tilde{\boldsymbol{x}}:\boldsymbol{\theta})}{\partial\theta_j}\right] \\ =& 2\left[\frac{\partial\tilde{\boldsymbol{\mu}}}{\partial\theta_i}\right]^H \boldsymbol{C}^{-1}(\boldsymbol{\theta})\left[\frac{\partial\tilde{\boldsymbol{\mu}}(\boldsymbol{\theta}}{\partial\theta_j}\right] + tr\left(\boldsymbol{C}^{-1}(\boldsymbol{\theta})\frac{\partial\boldsymbol{C}(\boldsymbol{\theta})}{\partial\theta_i}\boldsymbol{C}^{-1}(\boldsymbol{\theta})\frac{\partial\boldsymbol{C}(\boldsymbol{\theta})}{\partial\theta_j}\right). \end{aligned} \tag{5.4}$$

If $\boldsymbol{\theta}$ is a scalar parameter ($\tilde{x} \sim CN(\mu(\theta), C(\theta))$, Eqn. (5.4) can be rewritten as

$$I(\theta) = 2\left[\frac{\partial\tilde{\boldsymbol{\mu}}}{\partial\theta}\right]^H \boldsymbol{C}^{-1}(\theta)\left[\frac{\partial\tilde{\boldsymbol{\mu}}(\theta}{\partial\theta}\right] + tr\left(\left(\boldsymbol{C}^{-1}(\theta)\frac{\partial\boldsymbol{C}(\theta)}{\partial\theta}\right)^2\right). \tag{5.5}$$

By considering that the observed signal has a zero mean, Eqn. (5.5) can be further reduced to:

$$I(\theta) = tr\left(\left(\boldsymbol{C}^{-1}(\theta)\frac{\partial\boldsymbol{C}(\theta)}{\partial\theta}\right)^2\right). \tag{5.6}$$

Thus, Eqn.(5.6) shows that the Cramer-Rao Bound can be written as a function of the covariance matrix of the observed signal, as anticipated above.

The covariance matrix can then be computed by adopting the analytical model presented in chapter 4. As it was presented in the previous chapter the covariance

matrices obtained from the analytical model and simulations closely match that from UK-DMC and GOLD-RTR data, as well as the Power Waveforms derived in each case. **However, the covariance matrix estimated from real data is generally noisier (because an infinite data set for perfect averaging cannot be obtained), and this leads to an incorrect evaluation of the Cramer-Rao Bound, since the noise creates artefacts in the calculation of the derivative of the covariance matrix in Equ. (5.6)**. As a reference, Figs. 5.1a and 5.1b show both the Power Waveforms and their derivatives for the model and real covariance.

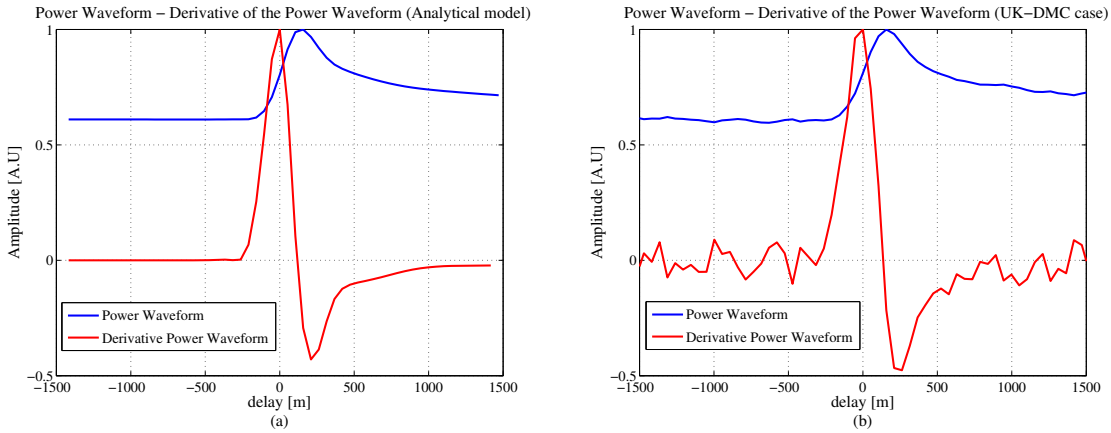

Figure 5.1: Power Waveforms and its derivative computed for (a) the analytical model, and (b) the real data provided by UK-DMC.

5.3 Analysis of the altimetry performance (cGNSS-R case)

In this section, the Cramer-Rao bound is used to evaluate a wide variete of parameters concerning the overall observation system, for the cGNSS-R technique.

5.3.1 Altimetry performance vs tracking-region considered

In this Section, the impact on altimetry performance of the region of the waveform used by the estimator for the retrieval of the range is analyzed. This region is called hereinafter the "tracking-window" used in the range estimation. This analysis is of high importance as it defines the maximum delay range (i.e. observation window) over which it is useful to calculate the altimetry waveform on-board. It is also useful to identify the minimum size of the tracking-window, which simplifies the complexity of the range estimation algorithm. For this purpose, different tracking-window

sizes have been considered, namely 150, 300, 450 and 600 m (80 lags considering a sampling frequency of 40 MHz). For each point of the covariance matrix the altimetry performance has been computed, obtaining a minimum one-shot range precision of 242, 240.1, 239.3, and 238.15 m respectively.. Note that in this analysis, a sampling frequency of 40 MHz, and an SNR = 1.65 (∼2dB) as in the case of UK-DMC observations, has been assumed.

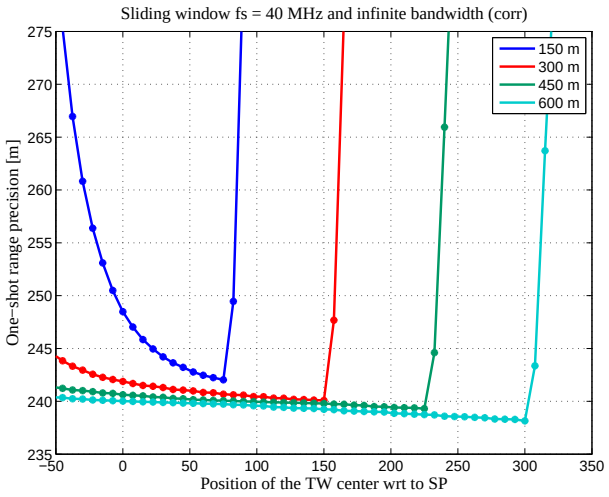

Figure 5.2: One shot Range precision for each point of the sliding windows (TW = Tracking Window, SP = Specular Point).

Figure 5.2 plots the one-shot (i.e. 1 ms observation) range precision obtained for the different Tracking Windows (TW) defined previously. It can be observed that the minimum one-shot range precision is obtained around the specular point, as expected. On the other hand, it is noted that increasing the tracking-window has a small impact on the actual performance (e.g. 238 m precision obtained with 600 m window with respect to 243 m obtained with 150 m).

Figure 5.3 plots the size of the scattering ocean surface contributing to the waveform in a given tracking window. As it can be observed, for tracking windows from 150 m to 600 m, the contributing scattering sea surface extend approximately from 22 to 42 km, for the reference geometry considered. It is important to remark that, the spatial resolution, being defined as the 3 dB footprint of the WAF centered at the specular point [6], [18], does not depend on the size of the adopted tracking window.

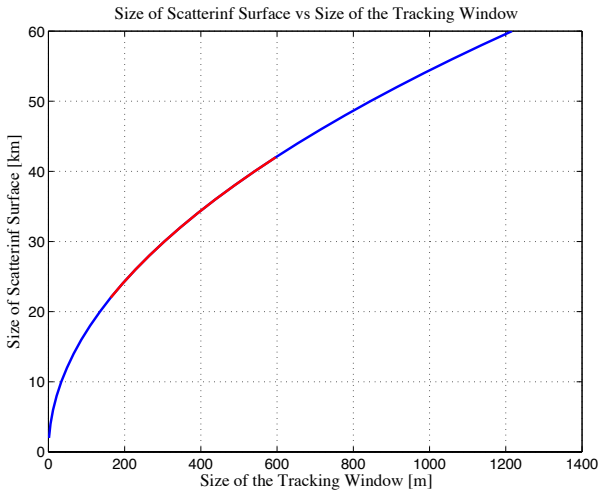

Figure 5.3: Size of the Scattered surface vs Size Tracking Window.

Therefore, from this analysis it can be concluded that increasing the tracking-window size beyond the width of the Auto-Correlation Function (i.e. 300 m) does not bring any improvement in terms of range performance. Although this analysis is presented for the C/A code, it can be directly translated to any other signal with different chip-rate. For example, for a signal with a chip-rate of 10.23 MHz (as GPS L5 or Galileo E5a/b), the optimal size of the tracking window is then 30 m, simply obtained by considering the width of the ACF for this case. It is further clarified that, in this study, other aspects to be taken into account when selecting the width of the tracking window are not discussed. For example, the need to have the reflected signals within some delay limits (delay window) despite the limited knowledge of the geometry is not discussed. These other aspects can be accommodated in a practical instrument by adding some margin to the size of the tracking window found in the present analysis.

5.3.2 Correlation Impact on the Altimetry Performance

The knowledge of the covariance matrix and its use within the CRB also allows to assess the impact on the altimetry performance of the correlation between waveform samples. For example, Fig. 5.4 plots the altimetry performance by considering both that the observed waveform samples are fully uncorrelated (i.e. covariance matrix diagonal), or correlated as predicted by the covariance matrix. The analysis has been conducted by considering the same system parameters of the previous section (same f_s, BW, and SNR), and for a tracking-window of 600 m.

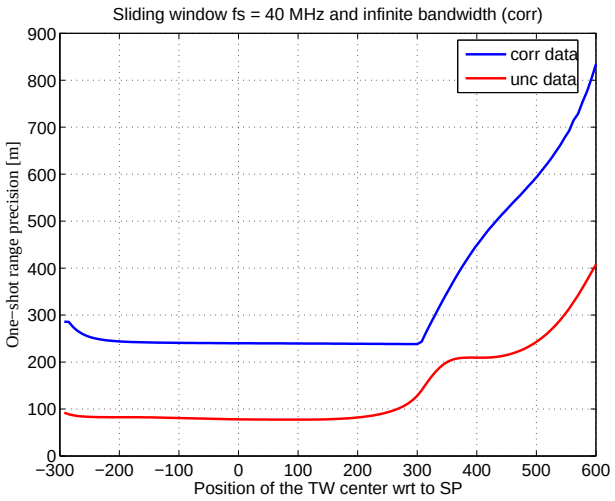

Figure 5.4: One-shot Range precision (T_{coh} = 1ms and N_{incoh} = 1) obtained for the correlated and uncorrelated data.

As it can be observed in Fig. 5.4 the impact due to the correlation between lags for this case is very large, and is about 150 m. It is important to stress that this impact is dependent on the sampling frequency, receiver bandwidth, and SNR, and therefore will vary with these system/instrument parameters. Nevertheless, this analysis gives a preliminary demonstration that it is important to take into account the correlation between samples (i.e. the covariance matrix), when predicting the altimetry performance by using analytical models, otherwise over optimistic results may be obtained.

5.3.3 Altimetry Performance vs Sampling Frequency

In this section the impact of the sampling frequency on the altimetry performance is analyzed. This analysis is very important in order to derive requirements for the sampling to be used on-board for the measured GNSS-R waveform, which drives the instrument complexity and data-rate for data downlink to ground. It is important to mention that the term "sampling frequency" is defined at the waveform level and not at signal level before the correlation. With this purpose, the one-shot range precision has been computed by considering four different sampling frequencies (40, 20, 10 and 5 MHz), and an SNR= 1.65 (∼2 dB) as in previous sections. As an example, Figs. 5.5a and 5.5b show the modelled covariance matrix obtained for the 5 and 40 MHz sampling frequency, respectively.

The next plots show the one-shot range precision computed for the different sampling frequencies using a tracking window of 600 m, by considering both the full

covariance matrix, and the diagonal covariance matrix (i.e. uncorrelated data case).

For the correlated data, as it can be expected, the difference in the one shot range precision obtained for the different sampling frequencies is marginal (there is a difference of only about 5% between the lower and upper sampling frequency approximately). This is expected, since increasing the sampling frequency does not increase the information content of the correlated data (as it can be seen in the covariance matrix plot of Fig. 5.5b).

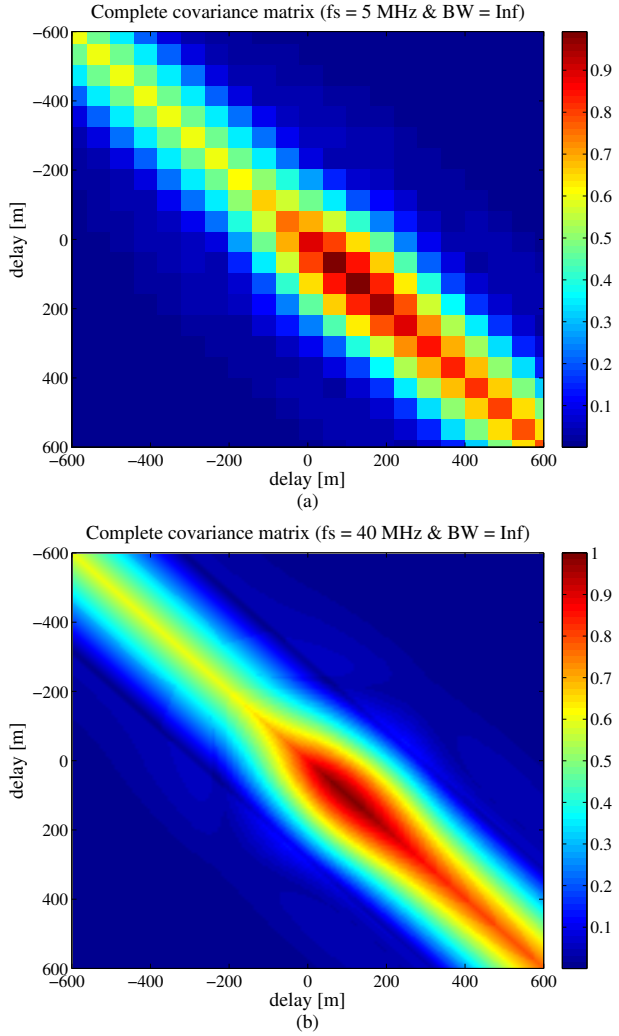

Figure 5.5: Complex cross-correlation statistics (including both signal and noise terms) for a sampling frequency of (a) 5 MHz and infinite bandwidth, and (b) 40 MHz.

On the other hand, although not representative of the true case, the hypothetical case of uncorrelated data is also analysed and shown in Fig. 5.7, for reference. Again, as expected, in this latter case, since the data uncorrelated, increasing the sampling

frequency improves drastically the performance. This hypothetical performance improvement is proportional to the square root of the number of samples, as it would be expected theoretically. For example, going from 40 MHz to a 20 MHz sampling frequency implies a reduction on the altimetry performance of a factor $\sqrt{2}$.

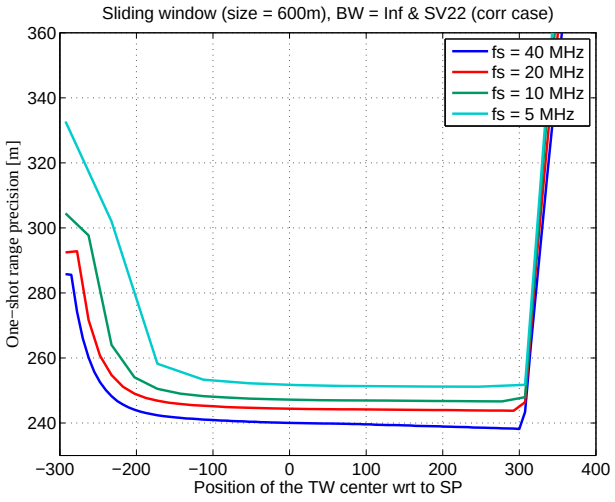

Figure 5.6: One-shot range precision vs. sampling frequency for the correlated data.

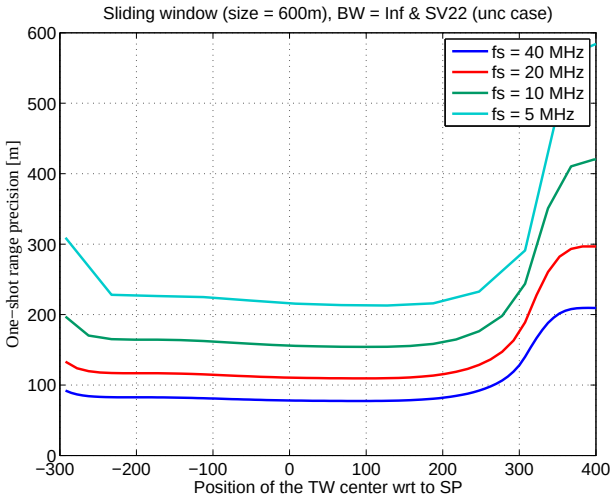

Figure 5.7: One-shot range precision vs. sampling frequency for the uncorrelated data.

5.3.4 Altimetry performance vs SNR

Another parameter of interest that affects the altimetry performance is the Signal-to-Noise Ratio (SNR). Here "noise" refers only to the thermal noise. Previous sections

have considered a SNR= 1.65 (∼2 dBs), in order to represent the case of the UK-DMC observations. In this section the altimetry performance is evaluated by considering different SNR values, in order to determine its impact on the altimetry performance. As in previous sections, this analysis has been conducted for both correlated and uncorrelated cases, and for different sampling frequencies.

Figure 5.8 confirms the importance that the SNR has in altimetry performance. It can be noticed that, for low SNRs a small increase of SNR gives a large improvement in performance. For higher values, increasing the SNR provides only a marginal improvement on altimetry performance, flattening out considerably (see Fig. 5.8, for SNR∼10). As an example, the delta improvement achieved from a SNR of 9 to 10 dB is only about 2 m, whereas this improvement is in the order of ∼ 110 m when the SNR passes from 1 to 2 dB.

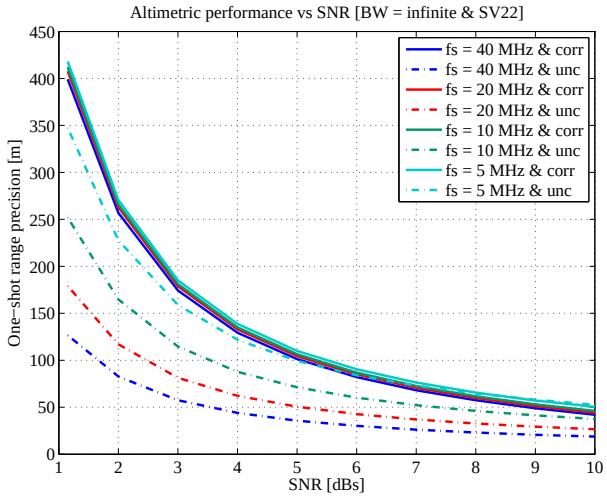

Figure 5.8: One-shot range precision computed vs. SNR for different sampling frequencies, and for the uncorrelated data in function of the SNR.

To finish, the altimetry performance shown in Fig. 5.8 as a function of the SNR, can be approximated as an exponential function, by $\sigma_h = a \cdot \exp(b \cdot x) + c \cdot \exp(d \cdot x)$, where x is the SNR, and where the parameters a, b, c, and d are summarized in the next table.

Table 5.1: Coefficients to parameterize the one-shot range precision as a function of the SNR

	a	b	c	d
fs = 40 MHz (corr)	479	-0.68	164.1	-0.14
fs = 20 MHz (corr)	495	-0.68	166.6	-0.13
fs = 10 MHz (corr)	506.7	-0.67	165.1	-0.13
fs = 5 MHz (corr)	522.5	-0.66	159.6	-0.11
fs = 40 MHz (unc)	163.6	-0.66	47.81	-0.09
fs = 20 MHz (unc)	231.4	-0.66	67.62	-0.09
fs = 10 MHz (unc)	326	-0.66	95.49	-0.09
fs = 5 MHz (unc)	447.4	-0.66	133.2	-0.09

5.3.5 Altimetry performance vs bandwidth

In this section, the impact of receiver bandwidth on the altimetry performance is analyzed. Previous sections have considered the ideal case of infinite receiver bandwidth. The receiver bandwidth is an important parameter that must be considered when analyzing the altimetry performance, since it affects the shape of the autocorrelation function. This change in the ACF translates directly into a spreading of the covariance matrix, as it can be observed in Fig. 5.9.

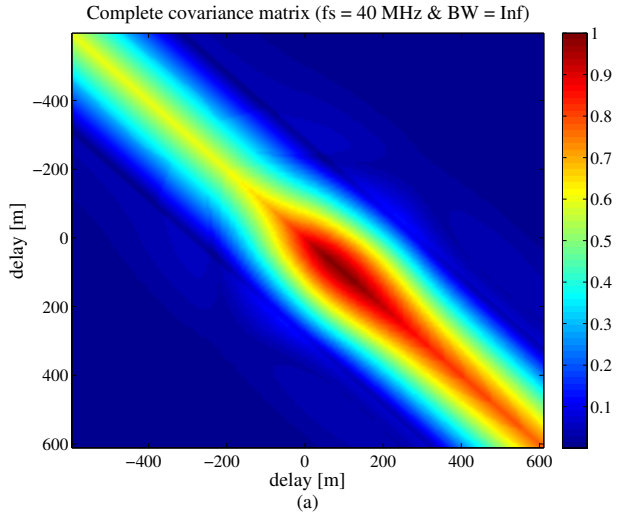

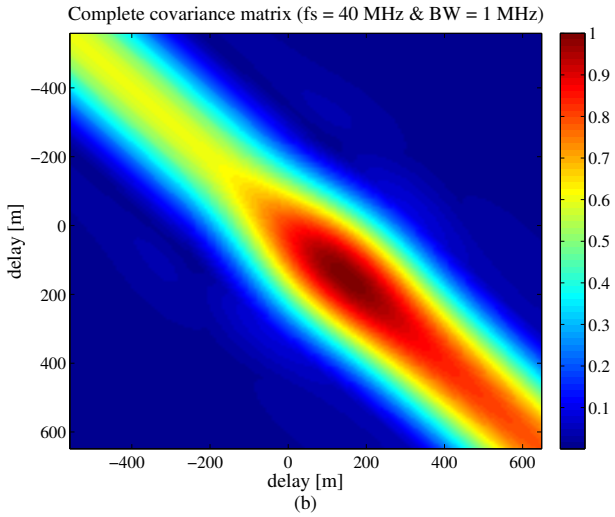

Figure 5.9: (a) Complex cross-correlation statistics (includes both signal and noise terms) for a sampling frequency of 40 MHz and infinite bandwidth, (b) Complex cross correlation statistics (includes both signal and noise terms) for a sampling frequency of 40 MHz and filter bandwidth of 1 MHz.

On the other hand, in Fig. 5.10 it can be observed how the bandwidth impacts on the power waveform (main diagonal of the covariance matrix (Fig. 5.10a)), widering the power waveform, and decreasing the steeper of the leading edge, and also how the receiver bandwidth increases the level of correlation between samples (Fig. 5.10b)). Thus, considering this, it is expected that the receiver bandwidth impacts on the altimetry performance.

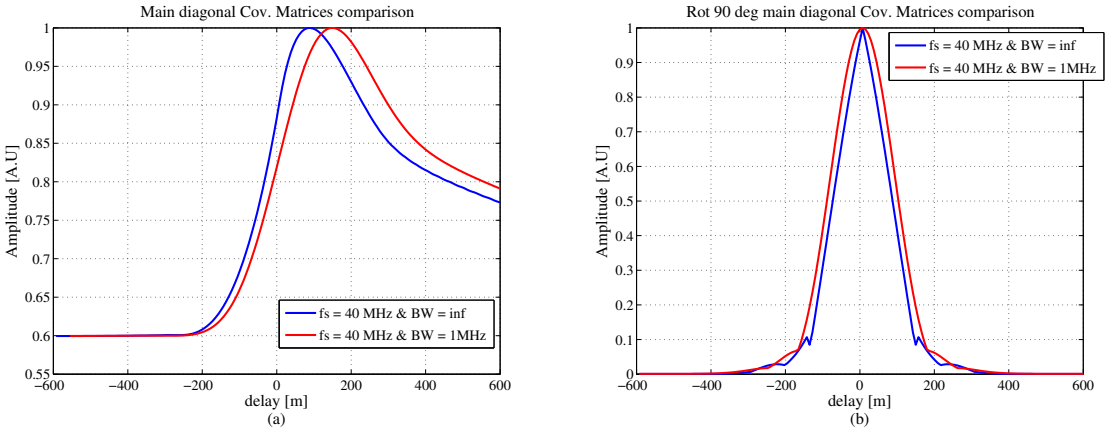

Figure 5.10: (a) Main diagonal covariance matrix comparison, (b) Minor diagonal covariance matrix comparison.

Figure 5.11 shows the altimetry performance by considering Radio Frequency (RF) receiver bandwidths of 20 MHz and 1 MHz. The first consideration that can

be extracted from Fig. 5.11 is that the altimetry performance degrades as the RF bandwidth is reduced. This is again explained by the fact that the bandwidth reduction increases the level of correlation between samples. Note that this is not the case of the uncorrelated data. Since in this case the data is uncorrelated the receiver bandwidth impact in the altimetry performance is much lower. This feature can be better appreciated in Fig. 5.12. Hence, as it can be appreciated in Figs. 5.11 and 5.12, the altimetry performance is limited by the receiver bandwidth, and any increase of sampling frequency beyond the receiver bandwidth does not improve further the performance (in the correlated case). Therefore, this shows an important relationship between the receiver's bandwidth, the sampling frequency, and the expected performance.

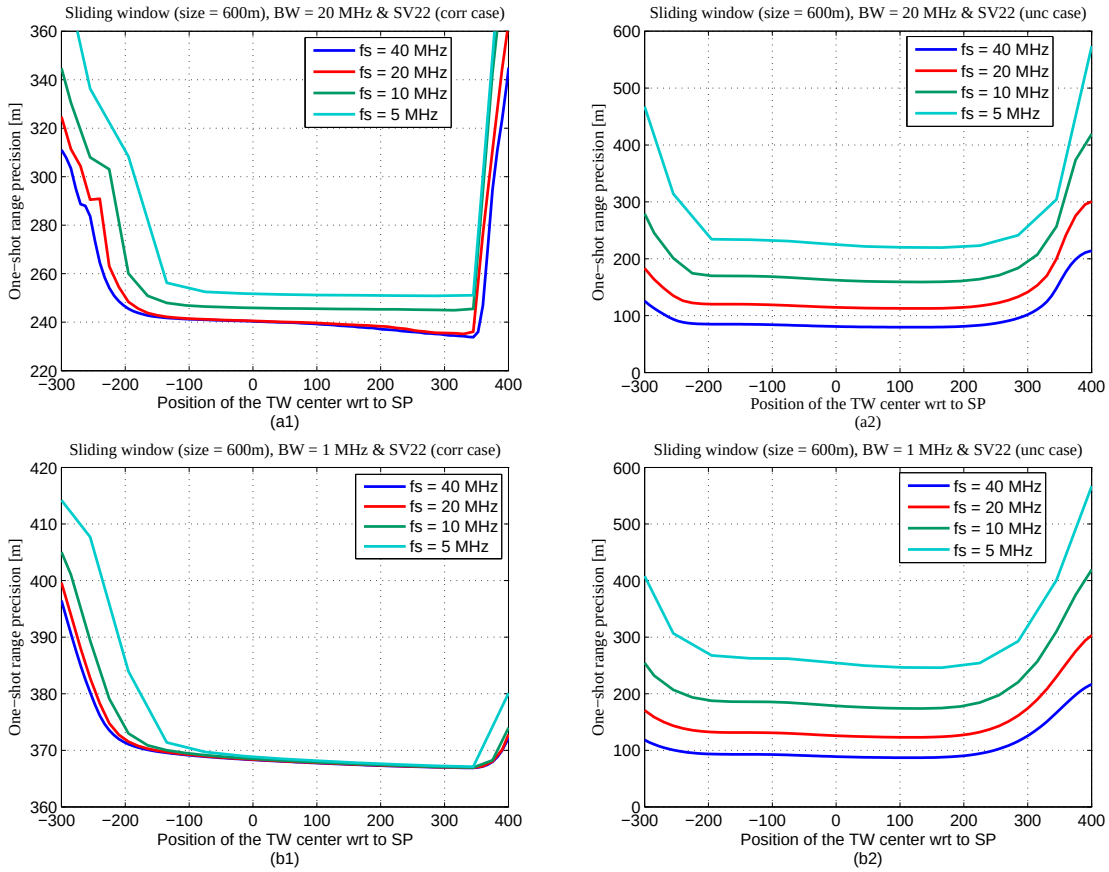

Figure 5.11: One-shot range precision vs, sampling frequency (BW = 20 MHz) for correlated (a1), uncorrelated (a2) and (BW = 1 MHz) for correlated (b1), and uncorrelated (b2).

Figure 5.12 shows the altimetry performance as function of the sampling frequency (remember that the term sampling frequency is defined at the waveform level and not

at signal level before the correlation), considering different receiver bandwidths. As it can be observed, in line with the previous considerations, the altimetry performance does not vary significantly with the sampling frequency for the case of correlated data. This suggests that the RF receiver bandwidth drives the instrument performance. However very different behaviour with respect to the sampling frequency and RF bandwidth is found if the data is assumed uncorrelated. This again shows the importance of taking into account the covariance matrix when estimating the altimetry performance of a GNSS-R system.

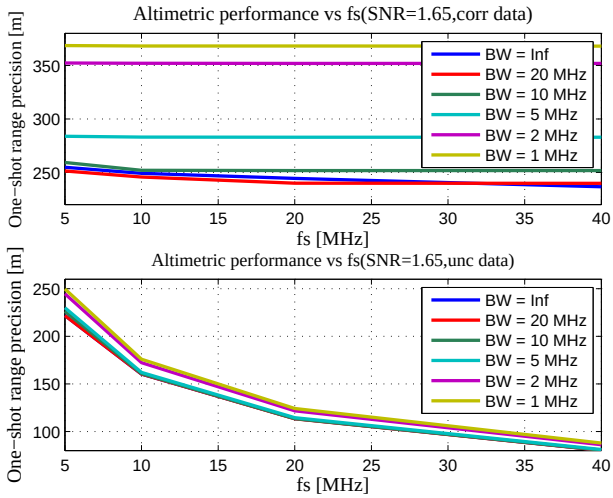

Figure 5.12: One-shot range precision vs. sampling frequency for different BWs, considering the data correlated (top), and considering the data uncorrelated (bottom).

5.3.6 Altimetry performance vs altitude

In this section, the impact of the receiver altitude on the altimetry performance is analysed. Figure 5.13 plots the one shot range precision as a function of the receiver altitude, computed for different receiver bandwidths. From them, the first issue that can be observed is that as expected, the altimetry performance decreases inversely to the height receiver. The second issue, that can be appreciated is that the impact of the height receiver decreases with the receiver bandwidth. Hence, when an ideal case (no filtering applied) is considered, it is obtained an one shot range precision around 200 m approx at 300 km, whereas at 1500 km it is around 252 m, it implies that the altimetry performance get worse by a factor of 1.25. Analogously, when is considered a receiver bandwidth of 1 MHz, the one-shot range precisions obtained are around 350 and 371 m (for 300 and 1500 km respectively). Thus, in this case the one shot range precision has degraded by a 6% factor.

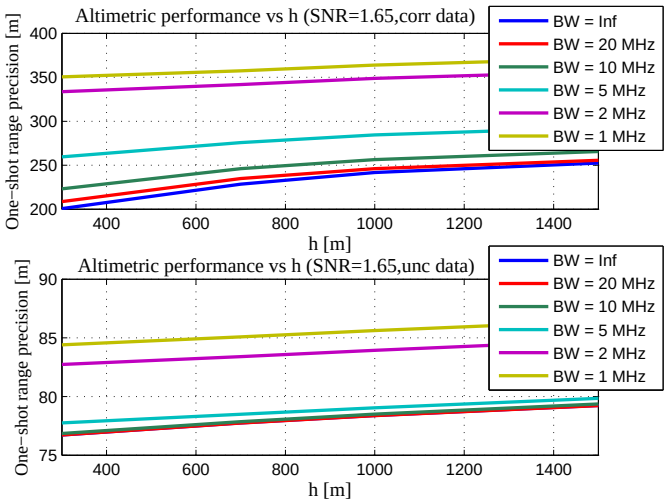

Figure 5.13: One-shot range precision vs. altitude for different recever BWs, considering the data correlated (top), and considering the data uncorrelated (bottom).

5.3.7 Altimetry performance vs incidence angle

The incidence angle is another parameter that can be affected the altimetry performance. Hence, in this section the impact that the incidence angle has on the altimetry performance is evaluated. Figure 5.14 plots the one shot range precision computed as a function of the incidence angle, considering different receiver bandwidths (as in the previous section). From it, a similar trend with respect to the receiver altitude can be observed. The main difference is that the impact that the incidence angle has, is lower than the one due to the receiver altitude. Therefore, considering an ideal case (no filtering) the one shot range precision goes from 225 m approx (at nadir) to a 240 m approx (at 30°), being the degradation around a 6% factor. On the other hand, if its considered the 1 MHz receiver bandwidth, this degradation is around a 2% factor (equivalent to pass from a one shot range precision of 355 m to a 364 m).

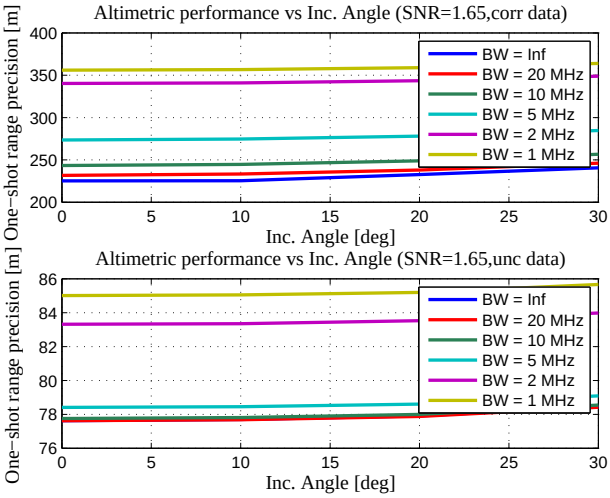

Figure 5.14: One-shot range precision vs. incidence angle for different recever BWs, considering the data correlated (top), and considering the data uncorrelated (bottom).

5.3.8 Altimetry performance vs Wind Speed

In this section, the impact of the wind speed on the altimetry performance is analysed. Figure 5.15 plots the one shot range precision computed as a function of the wind speed considering different receiver bandwidths. From it, the first issue that can be appreciated is that the impact that the wind speed has on the altimetry performance is small (a degradation around a 0.6% factor is obtained from a wind speed of 3 m/s to a wind speed of 20 m/s).

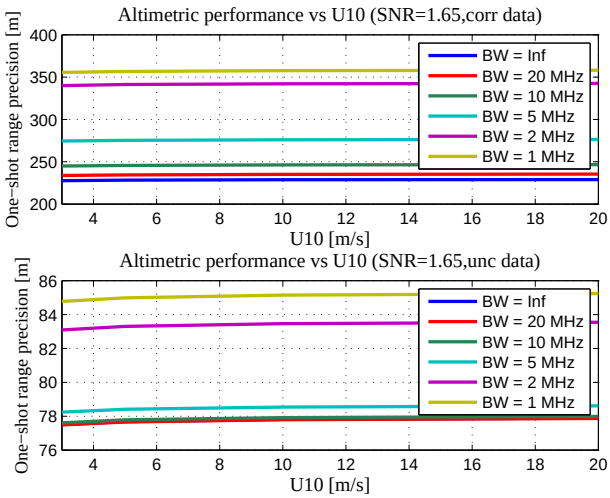

Figure 5.15: One-shot range precision vs. wind speed for different recever BWs, considering the data correlated (top), and considering the data uncorrelated (bottom).

On the other hand, Figure 5.16 repeats the analysis, considering different receiver altitudes 300, 700, 1000, and 1500 km. From it, the impact that has the wind speed on the altimetry performance considering the different altitudes is very small, even more if it is compared with the impact due to the receiver bandwidth or altitude. On the other hand, it can be also appreciated that the impact due to the wind speed is lower as a measure that the receiver altitude increases. Hence, at 300 km the degradation by a factor of 1.09 due to the wind speed is obtained, whereas at 1500 km this degradation is around a 0.93.

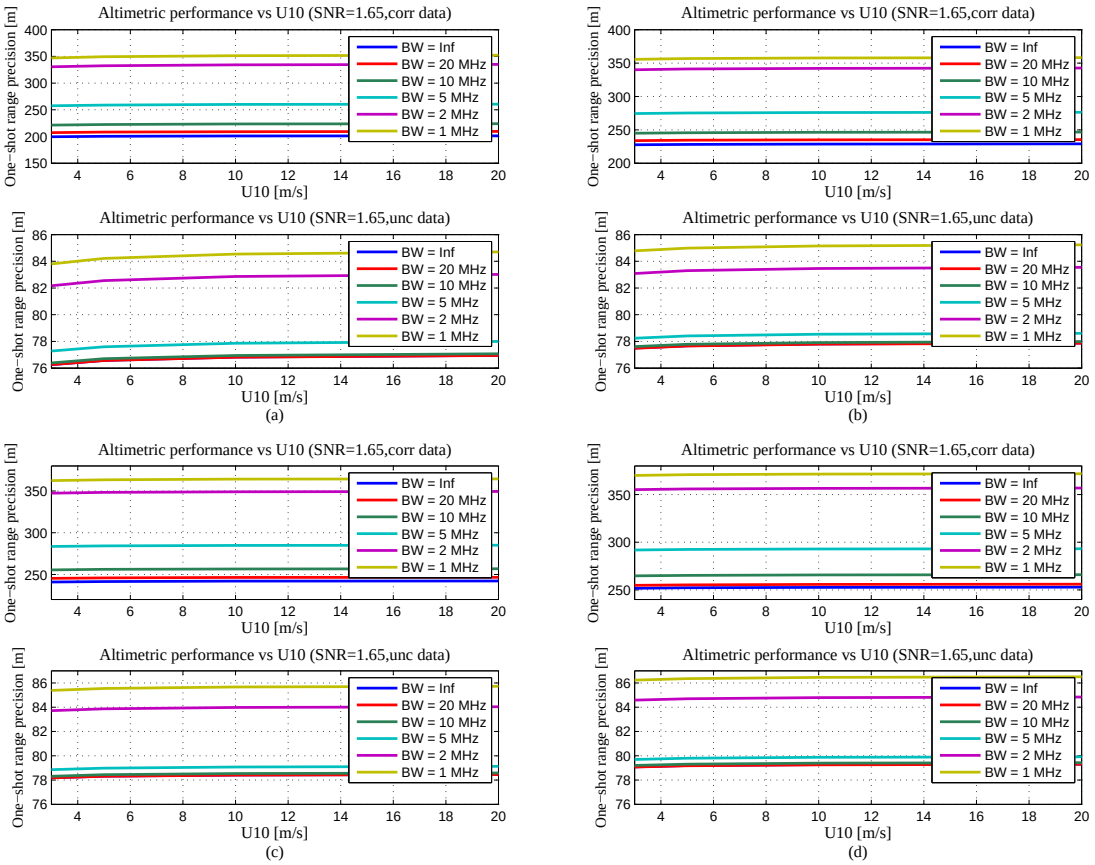

Figure 5.16: One-shot range precision vs wind speed (a) h = 300 km, (b) h = 700 km, (c) h = 1000 km, (d) h = 1500 km

5.4 Analysis of the altimetry performance (iGNSS-R case

In this section a similar analysis to the one performed for the cGNSS-R tehcnique is repeated for the iGNSS-R technique. The main objective is evaluate the impact that the main system parameters have on the altimetry performance when the iGNSS-R

technique is considered. Is important to remark, that the objective of this section is not to compare the altimetry performance obtained in the iGNSS-R with the one obtained using the cGNSS-R, but how the different system parameters impacts the performance in both techniques.

5.4.1 Altimetry performance vs tracking-region considered

In this Section, the impact that the "Tracking Window"(TW) has on the altimetry performance is analyzed for the iGNSS-R technique. As for the cGNSS-R case, here four different tracking-window sizes 150, 300, 450, and 600 m are considered. However, in this case a sampling frequency of 80 MHz, and an initial SNR of 5 dB (equivalent to consider an altitude of 700 km, antenna gain of 22 dBi, and a system noise temperature of 450K [37]) has considered. Note, that these system parameters will be considered as default in the following sections. In addition, is important to remark that in this section, the impact of the receiver bandwidth has not been considered. This impact, will be addressed in the next sections.

Figure 5.17 plots the one-shot (i.e. $T_{coh} = 1$ ms observation, and $N_{incoh} = 1$) range precision obtained for the different TW. From it, it can be observed that the minimum one-shot range precision is obtained closer to the specular point. On the other hand, as in the cGNSS-R case, the size tracking-window has a small impact on the actual performance. Therefore as it occurs in the cGNSS-R case, increasing the tracking-window size beyond the width of the Auto-Correlation Function (i.e. 300 m) does not bring any significant improvement.

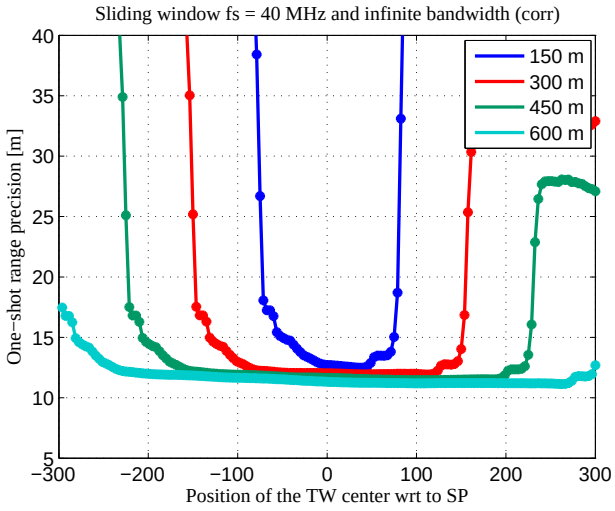

Figure 5.17: One-shot Range precision for each point of the sliding windows.

5.4.2 Altimetry Performance vs Sampling Frequency

In this section the impact of the sampling frequency on the altimetry performance is analysed. As in the case of the cGNSS-R technique, this analysis is very important in order to derive requirements for the sampling to be used on-board for the measured GNSS-R waveform. Hence, the one-shot range precision has been computed by considering four different sampling frequencies (80, 40, 20, 10 and 5 MHz), and a SNR = 5 dB. Figure 5.18 shows the complete covariance matrices for the 80, 20, 10 and 5 MHz cases.

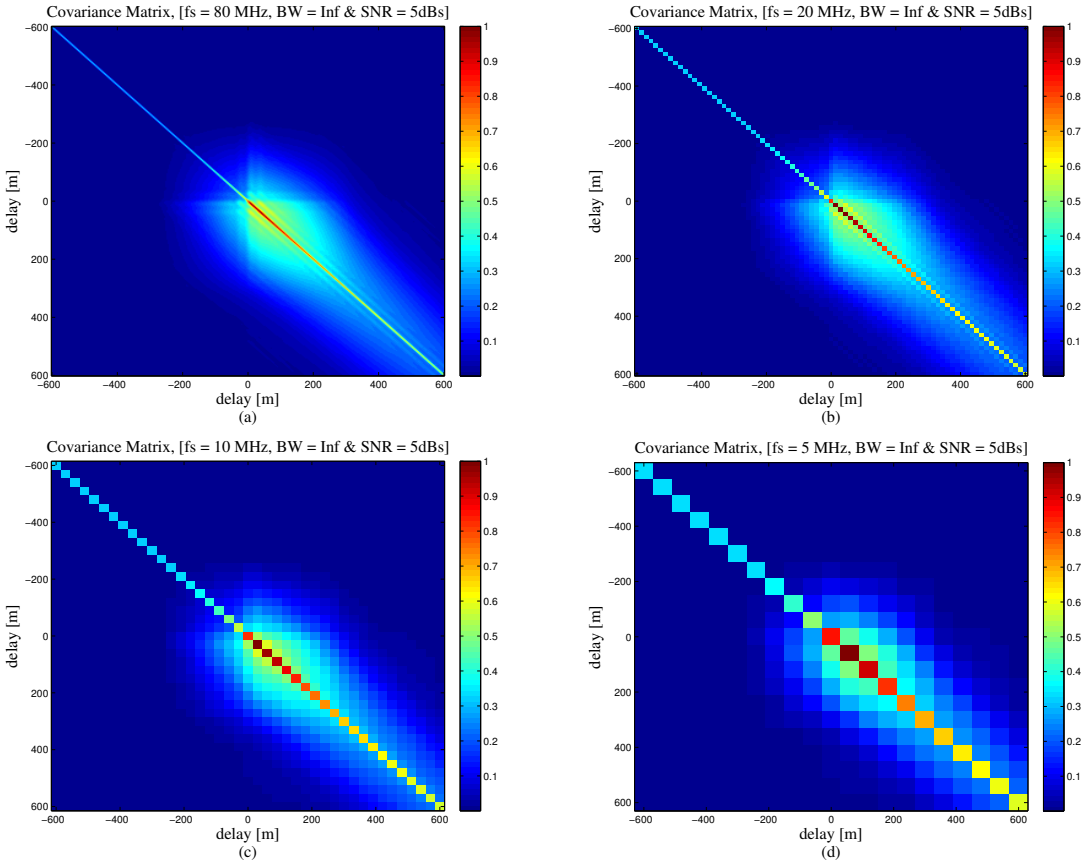

Figure 5.18: Complete Covariance Matrices (a) fs = 80 MHz, (b) fs = 20 MHz, (c) fs = 10 MHz, (d) fs = 5 MHz.

From Fig. 5.19, as it can be appreciated, the dependence with the sampling frequency is different than in the cGNSS-R, where increasing the sampling frequency didn't imply increasing the amount of information. However, in this case is not like this. This issue can be observed in Figs. 5.20, and 5.21, where the ACF and the minor diagonal of the complete covariance matrix (which depends on the ACF) are plotted for the different sampling frequencies. From it, small differences between the

ACF sampled at 80 MHz and 40 MHz can be observed, being thus its impact in the altimetry performance not critical. However, this changes start to be relevant at 20 MHz, and consequently its impact in the altimetry performance.

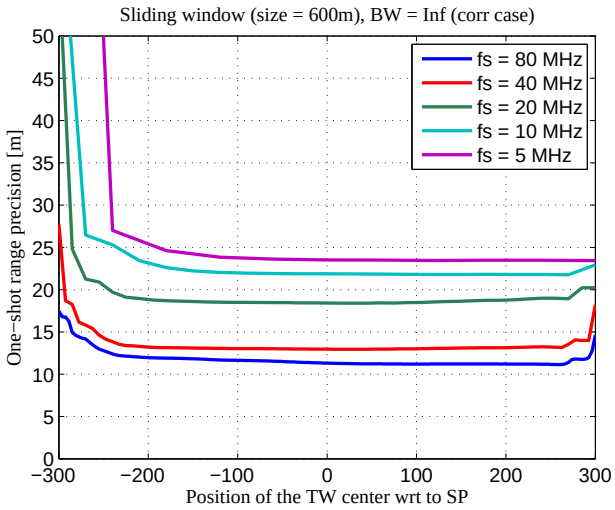

Figure 5.19: One-shot range precision vs sampling frequency for correlated data.

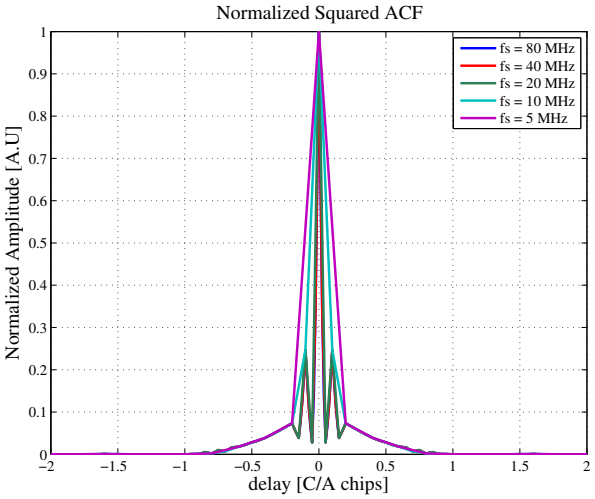

Figure 5.20: Normalized Squared ACF comparison.

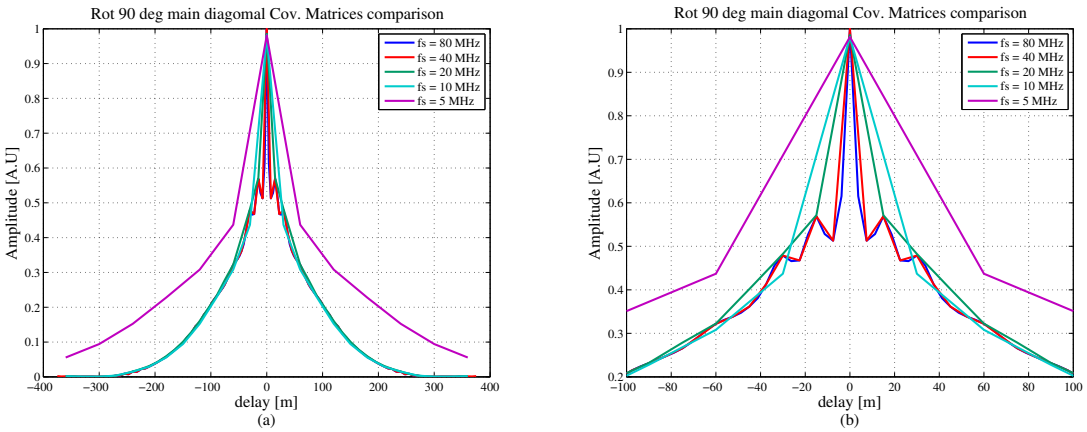

Figure 5.21: (a) Rotated main diagonal complete covariance matrix, (b) zoom of (a).

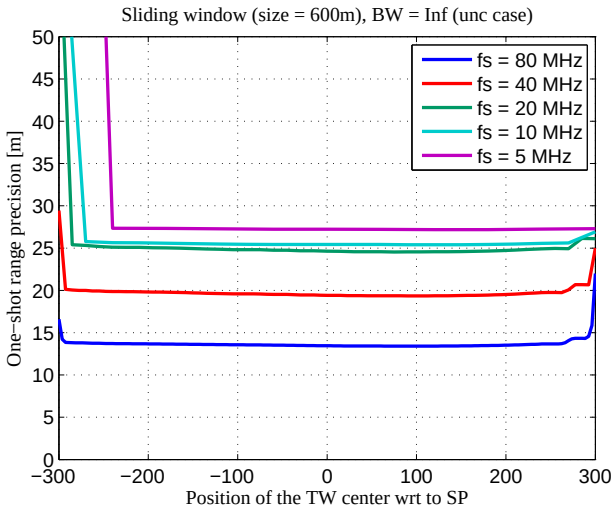

Figure 5.22: One-shot range precision vs sampling frequency for uncorrelated data.

5.4.3 Altimetry performance vs SNR

As it is well know, the SNR is an important parameter to consider in the altimetry performance. Hence, in this section is evaluated the impact that the SNR has in the iGNSS-R technique. Is important to consider, that as in the cGNSS-R case, the "noise" term refers only to the thermal noise.

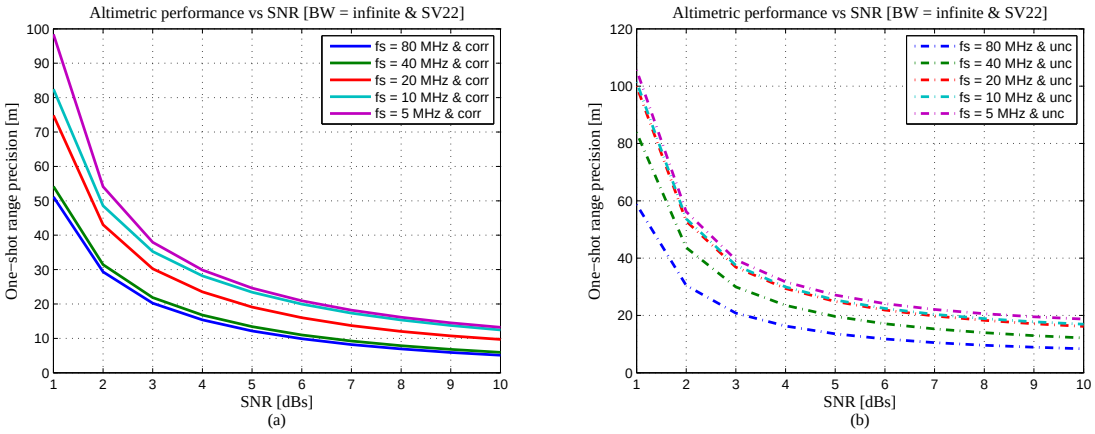

Figure 5.23: One-shot range precision computed vs SNR for different sampling frequencies (a) correlated data, (b) uncorrelated data.

Figure 5.23 plots the one-shot range precision in function of the SNR, considering different sampling frequencies. From it, it can be appreciated the importance that the SNR has in the altimetry performnance. On the other hand, the one shot altimetry performance, can be approximated as an exponential function, by $\sigma_p = a \cdot \exp(b \cdot x) + c \cdot \exp(d \cdot x)$, where x is the SNR, and the parameters a, b, c, and d are summarized in the next table. To finish, it can be observed that the impact that has the correlation between lags in this case is lower than in the cGNSS-R case (Fig. 5.8). This is done basically for the different behaviour that has the sampling frequency over the one-shot range precision in this case (as it has shown in the previous section).

Table 5.2: Coefficients to parametrize the one-shot range precision as a function of the SNR

	a	b	c	d
fs = 80 MHz (corr)	117.4	-1.10	21.86	-0.10
fs = 40 MHz (corr)	166.7	-1.10	31.53	-0.09
fs = 20 MHz (corr)	195.7	-1.09	37.79	-0.08
fs = 10 MHz (corr)	198.3	-1.08	37.58	-0.08
fs = 5 MHz (corr)	205.3	-1.07	38.52	-0.07
fs = 80 MHz (unc)	78.72	-1.06	28.66	-0.17
fs = 40 MHz (unc)	81.98	-1.03	29.54	-0.16
fs = 20 MHz (unc)	118.3	-1.02	36.87	-0.13
fs = 10 MHz (unc)	128.1	-1.07	43.94	-0.13
fs = 5 MHz (unc)	176.6	-1.11	47.1	-0.12

5.4.4 Altimetry performance vs bandwidth

In the two previous sections, the influence of the receiver bandwidth has not been considered. However, as it has been showed for the cGNSS-R, the receiver bandwidth is an important parameter that should be taken into account, even more in the iGNSS-R technique, where the receiver bandwidth impacts the shape of the ACF (as the receiver bandwidth is reduced, the sharper of the ACF becomes wider, and thus, the improvement achieved by this technique is lost, as it has shown on Chapter 3). Hence, in this section the impact that the receiver bandwidth has in the altimetry performance is analysed.

Figure 5.24 shows the complete covariance matrices computed for different receiver bandwidths (ideal case (no filter), BW = 40 MHz, BW = 20 MHz, BW = 10 MHz, BW = 5 MHz, and BW = 1 MHz). From it, not significant changes are appreciated between the ideal case (no filtering), and the case where the receiver bandwidth is 40 MHz (remember that a 80 MHz sampling frequency has been considered in the simulations). For the 20 MHz receiver bandwidth, the central part of the covariance matrix is spread a bit. This impact is more obvious, for the 10 MHz and 5 MHz receiver bandwidths (as a measure that the receiver bandwidth is reduced, the covariance matrix becomes wider). On the other hand, for the 1 MHz case, the covariance matrix obtained is very close to the one obtained in the cGNSS-R case (basically because at 1 MHz, the ACF is very close to the C/A ACF, as it was shown on Chapter 3).

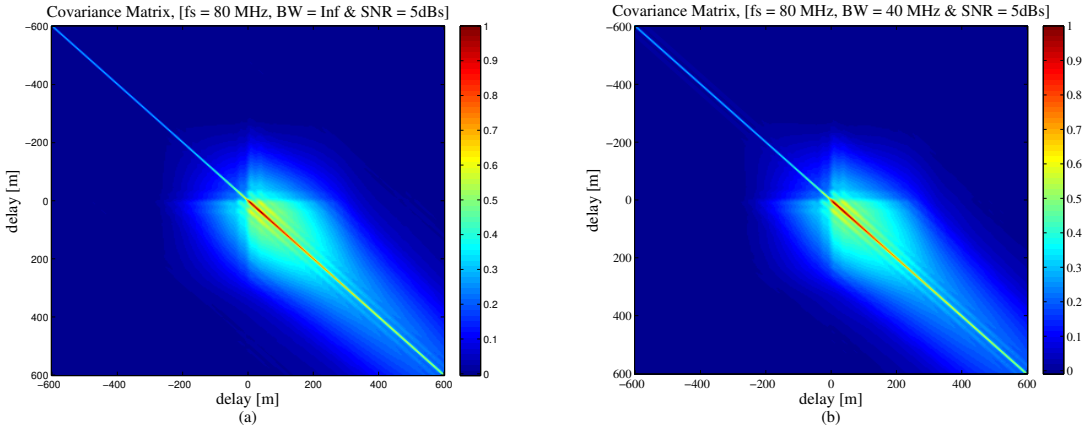

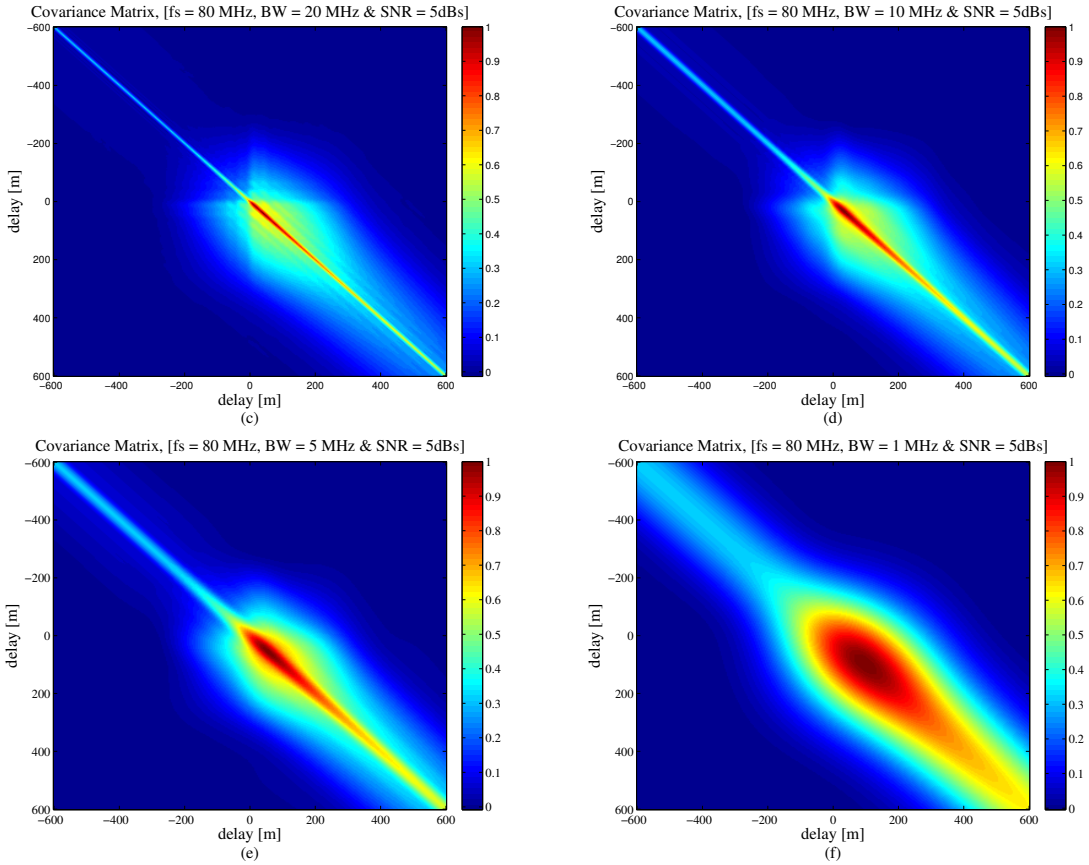

Figure 5.24: Complete Covariance Matrices for different receiver bandwidths (a) No filtering, (b) BW = 40 MHz, (c) BW = 20 MHz, (d) BW = 10 MHz, (e) BW = 5 MHz, (f) BW = 1 MHz.

Figure 5.25 plots the altimetry performance considering RF receiver bandwidths of 40 MHz, 10 MHz and 1 MHz. As it can be appreciated, for the correlated data the receiver bandwidth drives the instrument performance (as it was expected, and as it occurred in the cGNSS-R case), where any increase in terms of sampling frequency beyond the receiver bandwidth does not improve further the performance. On the other hand, for the uncorrelated case, the impact that the receiver bandwidth has is much lower. This results are confirmed in Fig. 5.26 where the one-shot range precision has been plotted as a function of the SNR, considering receiver bandwidths of 40 MHz, 10 MHz and 1 MHz. In addition, and as in the previous cases analysed, the one shot range precision as a function of the SNR can be approximated by an exponential, as $\sigma_p = a \cdot \exp(b \cdot x) + c \cdot \exp(d \cdot x)$, where x is the SNR, and the parameters a, b, c, and d are summarized in the next tables.

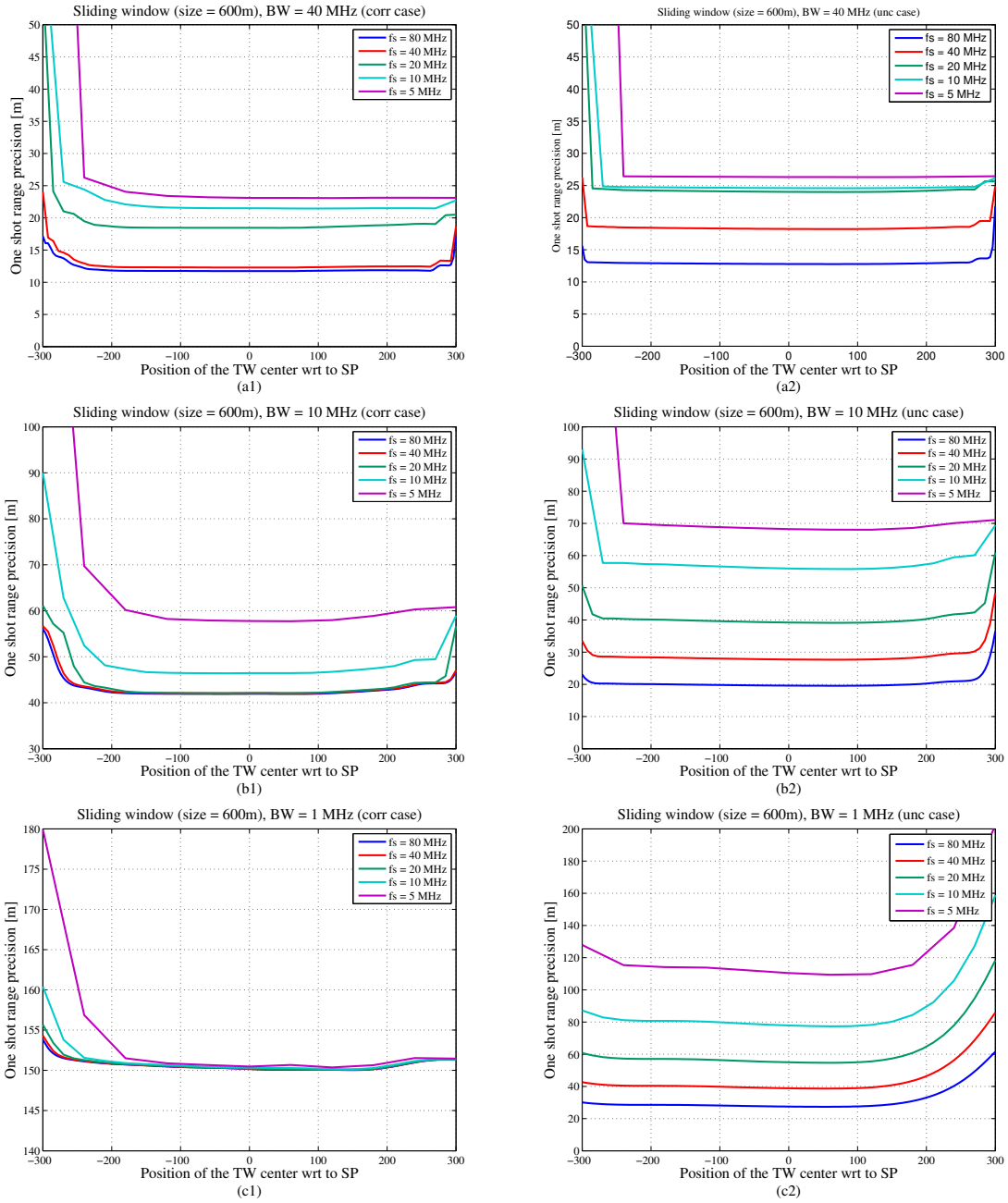

Figure 5.25: One-shot range precision vs sampling frequency (a1) BW = 40 MHz (correlated), (a2) BW = 40 MHz (uncorrelated), (b1) BW = 10 MHz (correlated), (b2) BW = 10 MHz (uncorrelated), (c1) BW = 1 MHz (correlated), (c2) BW = 1 MHz (uncorrelated).

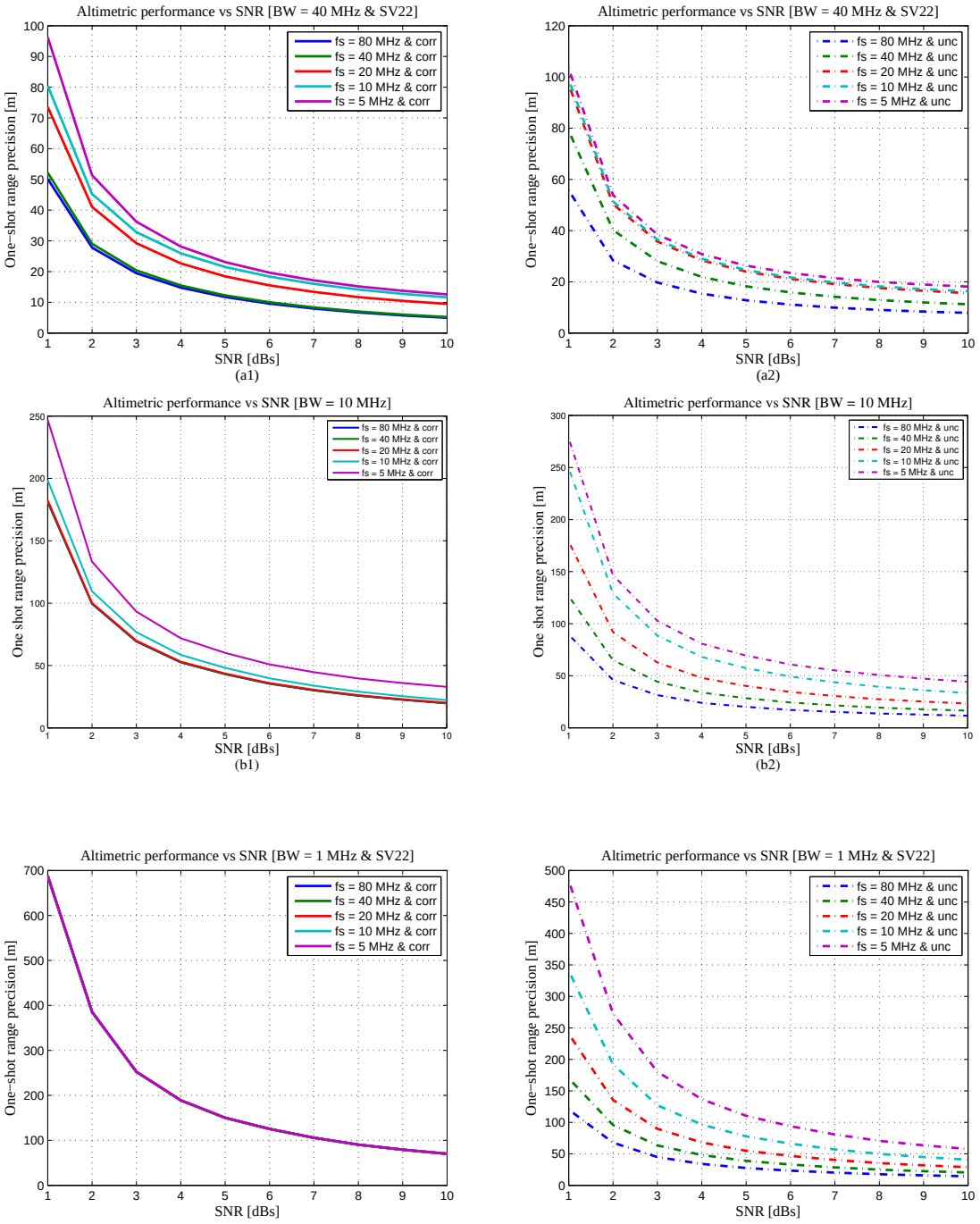

Figure 5.26: One-shot range precision computed vs SNR for different sampling frequencies (a1) BW = 40 MHz (correlated), (a2) BW = 40 MHz (uncorrelated), (b1) BW = 10 MHz (correlated), (b2) BW = 10 MHz (uncorrelated), (c1) BW = 1 MHz (correlated), (c2) BW = 1 MHz (uncorrelated).

Table 5.3: Coefficients to parametrize the one-shot range precision as a function of the SNR (BW = 40 MHz)

	a	b	c	d
fs = 80 MHz (corr)	78.72	-1.06	28.66	-0.17
fs = 40 MHz (corr)	81.98	-1.03	29.54	-0.16
fs = 20 MHz (corr)	118.3	-1.02	36.87	-0.13
fs = 10 MHz (corr)	128.1	-1.07	43.94	-0.13
fs = 5 MHz (corr)	176.6	-1.11	46.1	-0.13
fs = 80 MHz (unc)	117.4	-1.11	21.86	-0.10
fs = 40 MHz (unc)	166.7	-1.11	31.53	-0.09
fs = 20 MHz (unc)	195.7	-1.09	37.79	-0.08
fs = 10 MHz (unc)	198.3	-1.08	37.58	-0.08
fs = 5 MHz (unc)	205.3	-1.07	38.52	-0.07

Table 5.4: Coefficients to parametrize the one-shot range precision as a function of the SNR (BW = 10 MHz)

	a	b	c	d
fs = 80 MHz (corr)	303	-1.14	90.64	-0.16
fs = 40 MHz (corr)	303.7	-1.14	90.95	-0.16
fs = 20 MHz (corr)	304.8	-1.14	90.94	-0.16
fs = 10 MHz (corr)	328.4	-1.14	99.72	-0.15
fs = 5 MHz (corr)	436.2	-1.09	104.3	-0.12
fs = 80 MHz (unc)	175.1	-1.123	33.13	-0.11
fs = 40 MHz (unc)	247.7	-1.123	46.85	-0.11
fs = 20 MHz (unc)	350.3	-1.123	66.27	-0.11
fs = 10 MHz (unc)	486.2	-1.126	94.08	-0.11
fs = 5 MHz (unc)	539.9	-1.112	104.5	-0.09

Table 5.5: Coefficients to parametrize the one-shot range precision as a function of the SNR (BW = 1 MHz)

	a	b	c	d
fs = 80 MHz (corr)	1132	-0.95	288.2	-0.14
fs = 40 MHz (corr)	1132	-0.95	288.2	-0.14
fs = 20 MHz (corr)	1132	-0.95	288.4	-0.14
fs = 10 MHz (corr)	1132	-0.95	288.6	-0.14
fs = 5 MHz (corr)	1135	-0.95	288.8	-0.14
fs = 80 MHz (unc)	199.3	-0.93	46.72	-0.12
fs = 40 MHz (unc)	281.7	-0.93	66.04	-0.12
fs = 20 MHz (unc)	398.8	-0.93	93.47	-0.12
fs = 10 MHz (unc)	565.1	-0.93	132.4	-0.12
fs = 5 MHz (unc)	802.5	-0.93	188	-0.12

5.4.5 Altimetry performance vs altitude

In this section, the impact that the receiver altitude has on the altimetry performance is analysed. Figure 5.27 plots the one-shot range precision computed as a function of the receiver altitude considering different receiver bandwidths. As it can be expected, the performance gets worst with the receiver altitude. On the other hand, and in agreement with the results showed on Chapter 3, the impact that the receiver altitude has in the iGNSS-R is a bit higher than in the cGNSS-R. As for example, if it is considered the ideal case (no filtering applied), the degradation due to the height receiver is around 1.3 times (in the cGNSS-R case it was around 1.25). If it is considered a receiver bandwidth of 1 MHz, the degradation obtained here is around 1.08 (in the cGNSS-R case it was around 1.06).

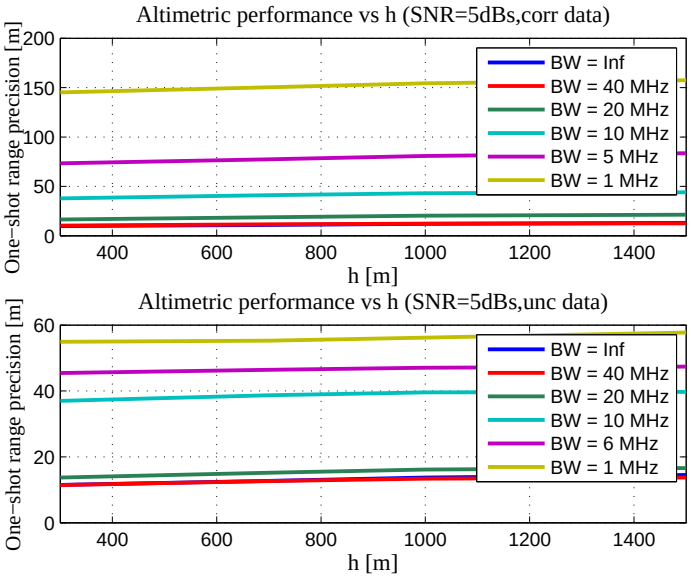

Figure 5.27: One-shot range precision vs altitude for different recever BWs, considering the data correlated (top) and considering the data uncorrelated (bottom).

5.4.6 Altimetry performance vs incidence angle

In this section, the impact of the incidence angle on the altimetry performance is evaluated. Fig 5.28 plots the one-shot range precision computed as a function of the receiver altitude considering different receiver BWs. As it occurred in the cGNSS-R, the incidence angle tends to reduce the altimetry performance. In any case, as it occurred for the cGNSS-R technique, and as it was shown in Chapter 3, the impact

that the incidence angle has over the altimetry performance is lower that the one that the receiver height has.

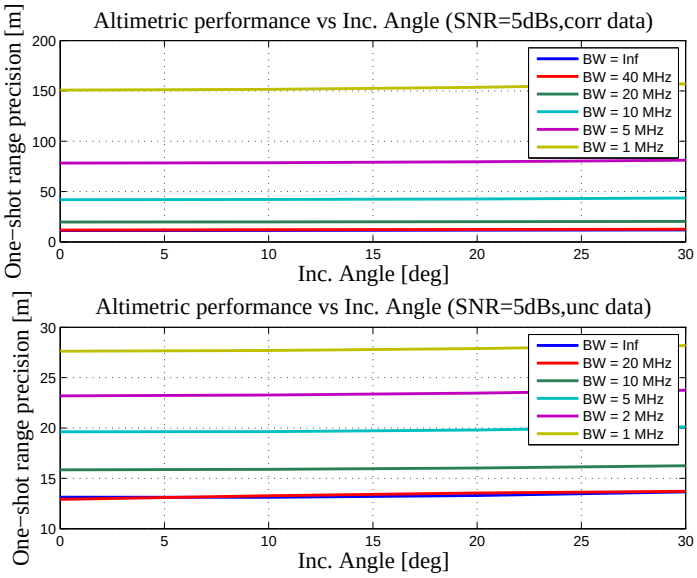

Figure 5.28: One-shot range precision vs incidence angle for different recever BWs, considering the data correlated (top) and considering the data uncorrelated (bottom).

5.4.7 Altimetry performance vs Wind Speed

In this section, the impact of the wind speed on the altimetry performance is analysed for the iGNSS-R technique. Hence, Fig 5.13 plots the one-shot range precision computed as a function of the wind speed considering different receiver bandwidths. From the results plotted on Fig 5.29, it can be appreciated that, as occurred in the cGNSS-R case, the impact that the wind speed has on the altimetry performance is very low (negligible if it is compared with the impact that has the receiver bandwidth for example). These results are also in agreement with the ones showed on Chapter 3.

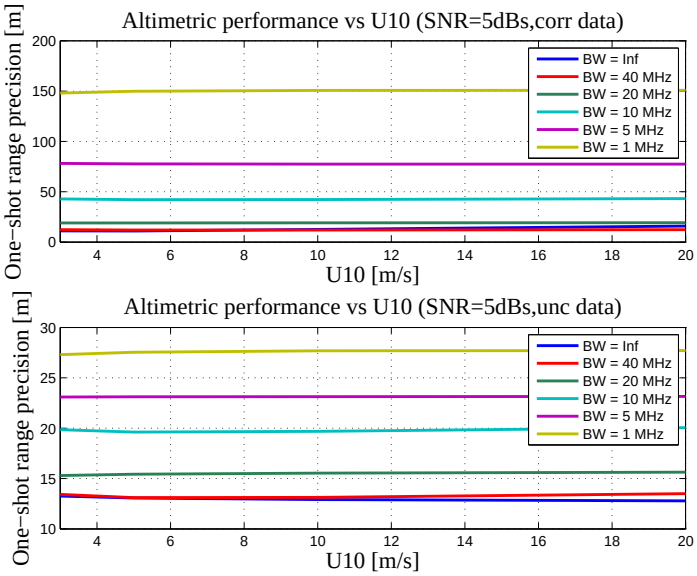

Figure 5.29: One-shot range precision vs wind speed for different recever BWs, considering the data correlated (top) and considering the data uncorrelated (bottom).

Figure 5.30 repeats the analysis, considering different receiver altitudes (300, 700, 1000, and 1500 km). As in the case of the cGNSS-R technique, the impact of the wind speed is very low (almost negligible) for the different receiver altitudes considered here.

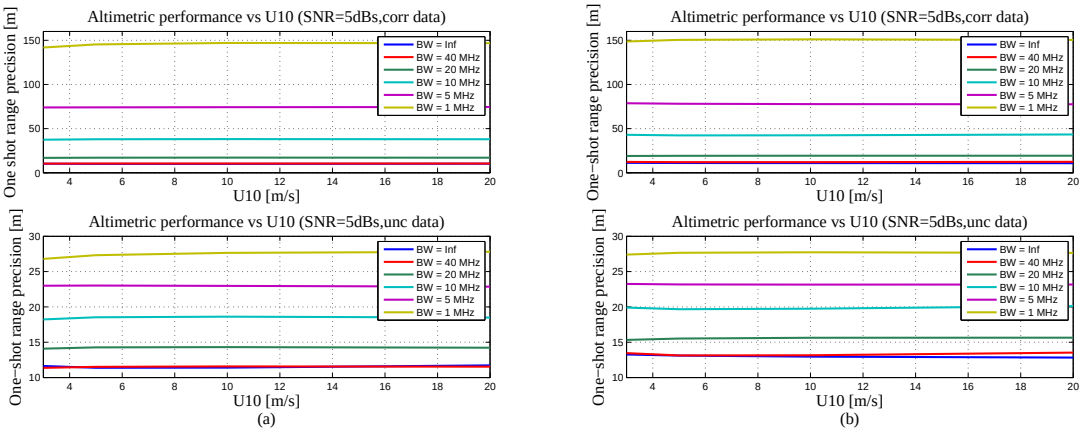

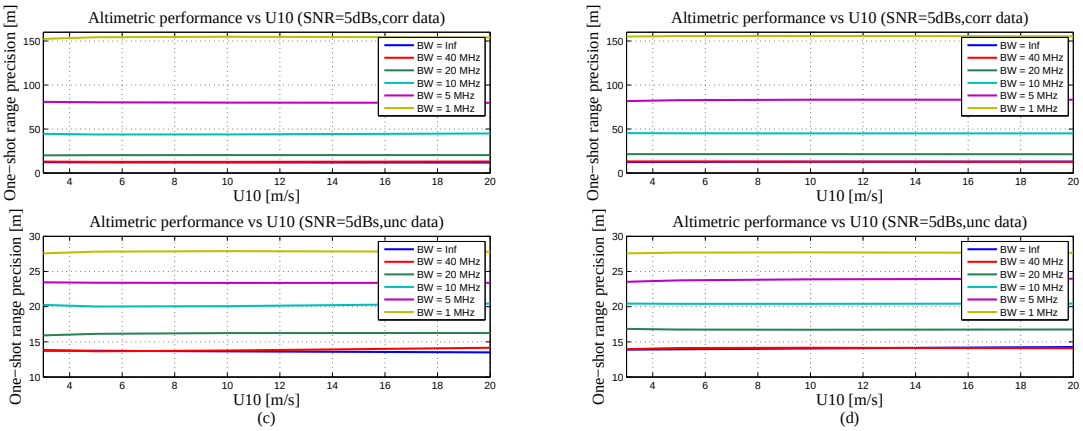

Figure 5.30: One-shot range precision vs wind speed (BW = Inf) (a) h = 300 km, (b) h = 700 km, (c) h = 1000 km, (d) h = 1500 km.

5.5 Comparison of GNSS-R processing techniques

In this section a comprehensive comparison between the cGNSS-R and iGNSS-R technique is provided, highlighting the possible achieved performance for a typical spaceborne case. The performance comparison of the techniques will be carried out by analysing the Cramer-Rao Bound [57], which takes into account the full statistical properties of the reflected signals (i.e. sample-to-sample correlation within a waveform, Covariance matrix, presented on Chapter 4).

The comparison has performed, considering a typical spaceborne case, with a 700 km receiver altitude, and nadir observations, with an intial wind speed of 7 m/s. Respect to the instrument characteristics, it has assumed an antenna gain of 22 dBi, a system noise temperature of 450 K, and an equivalent noise bandwidth of 24 MHz. Table summarizes the main system parameters used in the simulations.

Table 5.6: Simulation System Parameters

Parameter	**Value**	**Unit**
GPS altitude	20200	km
Receiver altitude	700	km
GPS velocity	3.87	km/s
Receiver velocity	7.5	km/s
Incidence angle (θ_i)	0	deg
Antenna Gain (G)	22	dBi
Wind Speed (U_{10})	7	m/s
Coherent Int. Time (T_c)	1	ms

From these system parameters an initial SNR of ~ 9 dB and ~ 5 dB is obtained for the cGNSS-R and iGNSS-R respectively [37]. Figures 5.31 and 5.32 show the covariance matrices obtained for each case, considering the SNRs mentioned. Figure 5.33 shows the Power Waveforms obtained in each case (main diagonal of the covariance matrix).

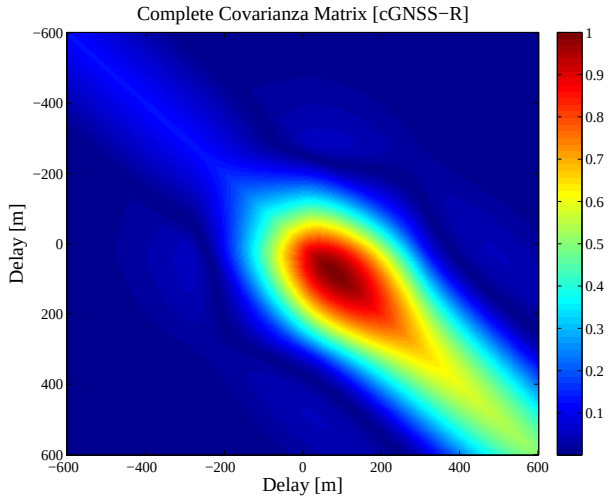

Figure 5.31: Complete covariance matrix for the cGNSS-R technique

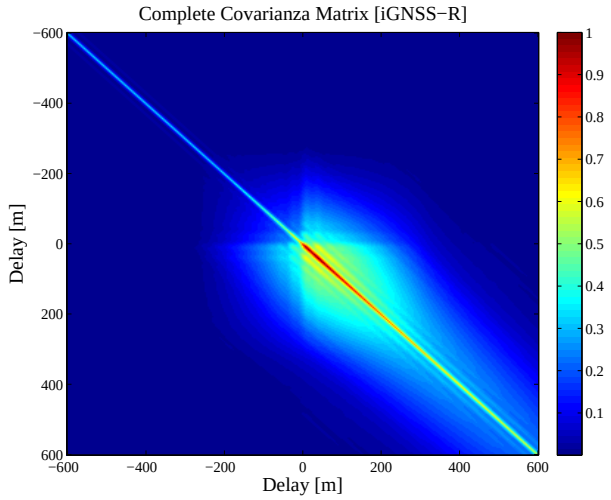

Figure 5.32: Complete covariance matrix for the iGNSS-R technique

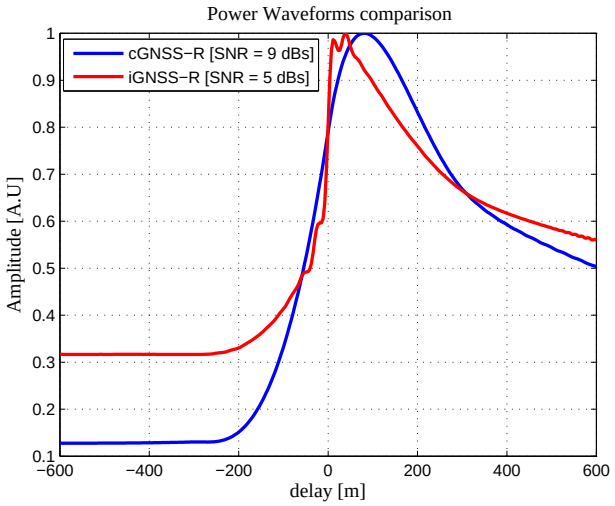

Figure 5.33: Power Waveforms comparison

Figure 5.34 shows the one-shot range precision as a function of the SNR obtained for each case. As it can be observed for the same SNR, the altimetry performance obtained for the iGNSS-R is ∼6-7 times better than the one for the cGNSS-R. However, this is not the real case, since for the same system parameters, the iGNSS-R case will present a lower SNR. Hence, a degradation between 3 and 5 dBs in the SNR can be expected for the iGNSS-R case for a typical spaceborne scenario, like the one considered in this section. Figure 5.35 shows the improvement achieved for the iGNSS-R with respect the cGNSS-R. This improvement has computed as a function of the SNR, considering a 4 dBs impact in the SNR of the iGNSS-R technique.

From Fig. 5.35 it can be appreciated, that as the SNR increases, increases the improvement achieved by the interferometric approach. Considering the reference case here presented ($SNR_c = 9$ dB, and $SNR_i = 5$ dB), the improvement achieved is about 3.25, which is in agreement with previous results [66]-[67].

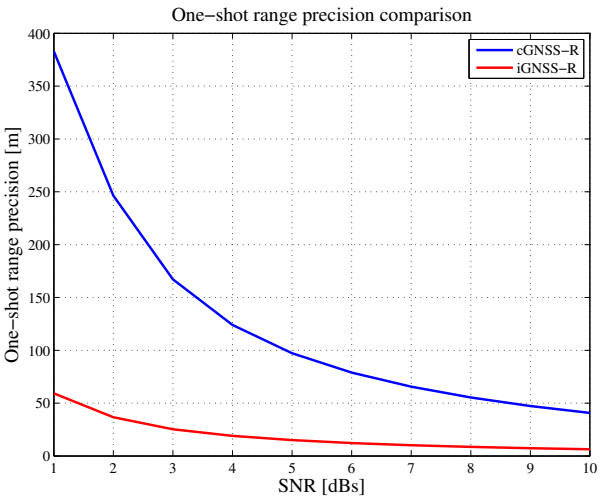

Figure 5.34: One-shot range precision vs SNR for both cGNSS-R and iGNSS-R techniques

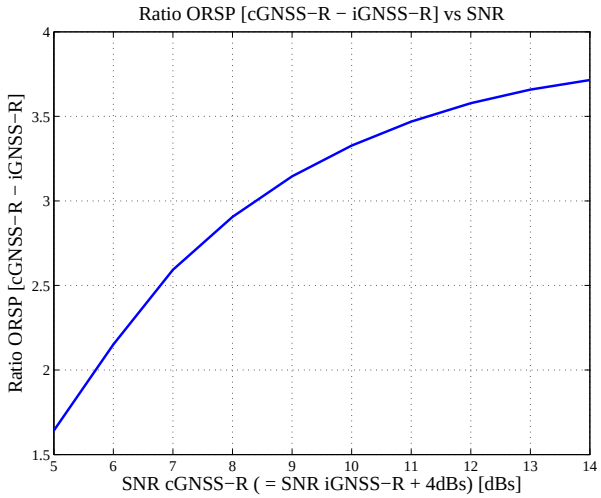

Figure 5.35: Improvement in the altimetry performance, achieved for the iGNS-R with respect the cGNSS-R technique, considering an initial degradation of 4 dBs in the SNR

5.6 Conclusions

The Cramer-Rao Bound has been evaluated for a wide variety of parameters concerning the overall observation system, including instrument, on-board and on-ground processing aspects, for both the cGNSS-R and the iGNSS-R techniques. The most important parameters that have been studied include the sampling frequency, the

RF receiver bandwidth, the signal-to-noise-ratio, and the position and width of the tracking-window to be used for range estimation. More in general, the impact of correlation between samples on the altimetry performance has also been assessed, and the impact that the receiver height, incidence angle or wind speed can have in the altimetry performance.

It can be concluded that, in order to ensure marginal performance degradation, the RF bandwidth shall be at least 10 MHz for the case of GPS C/A code signal, and ideally 40 MHz (20 MHz in the worst case) for the L1 composite signal. Concerning the sampling frequency, it can be concluded that, as general rule, it shall be at least the same as the RF bandwidth in order to not cause performance degradation. Larger values of sampling frequency are not bringing any additional performance improvement.

Concerning the on-ground processing, it has been shown that a minimum tracking-window width comparable to the width of the Auto-Correlation Function is sufficient to guarantee a good performance, centering it around the specular point.

On the other hand, it has been shown that the SNR is a critical parameter, where its impact over the altimetry performance can be approximated by an exponential function. On the other hand, is important to remark, that for a low SNRs a small increase of SNR gives a large improvement in performance, whereas for higher values, the improvement achieved increasing the SNR is marginal.

Respect to the geometry, it has shown that the altimetry performance decreases with the receiver altitude, being this impact a bit higher in the iGNSS-R than in the cGNSS-R. In the same way, the incidence angle tends to reduce the altimetry performance, but the impact that is lower that the one due to the receiver altitude. On the other hand the impact that presents the wind speed is not critical, even more if it is compared with the impact that the receiver bandwidth or altitude has.

To finish, an initial estimation of the altimetric performance has been derived for both the cGNSS-R and iGNSS-R considering a spaceborne case. Results presented shows better performance for the interferometric. At the time to evaluate the real improvement achieved by this technique (iGNSS-R), is important to consider the degradation in terms of SNR, due to the presence of noise in both the up- and down-looking channels. For the reference scenario considered in this chapter (typical spaceborne case), and assuming a 4 dBs degradation in the SNR, an improvement of abouth 3.25 times has been obatined.

Concluding, the analyses reported constitute an important basis for the optimization of the design and performance of future GNSS-R altimeters, including both the

cGNSS-R and iGNSS-R technique.

Chapter 6

Typhoon Investigation using GNSS-R Interferometric Signals experiment

This chapter is addressed to the Typhoon Investigation using GNSS-R Interferometric Signals (TIGRIS) experiment, conducted in the framework of an ESA-China cooperation. This chapter starts with a short introduction to the TIGRIS experiment, including a brief description of the experiment set-up. The chapter follows, showing some pecularities of the data analysed, i.e. direct signal cross-talk, or GNSS multipath contamination, and the main results obtained during the USAGI's period. The chapter ends with the main conclusions.

6.1 Introduction

As it has been introduced previously, GNSS-R was first proposed for mesoscale altimetry applications by the European Space Agency in 1993 (named PARIS - Passive Reflectometry and Interferometry System) to exploit GNSS reflected signals [6], as a complementary technique to classical nadir-looking radar altimetry. The concept has been later proposed for other applications, such as ocean wind-speed retrieval, ice altimetry, soil moisture, and biomass.

Recently, NASA has started the development of the Cyclone Global Navigation Satellite System (CYGNSS) [61], which is a spaceborne mission focused on tropical cyclones. CYGNSS consists of a constellation of 8 nanosatellites at Low Earth orbits (LEO) (500 km) with an inclination of 35°, which will allow to obtain frequent and accurate measurements of ocean surface winds through the life cycle of tropical storms

and hurricanes. One of the main goals of CYGNSS aims to improve extreme weather predictions, i.e. hurricanes.

Within the framework of the ESA-China cooperation in GNSS Reflectometry, during the summer 2013, the TIGRIS Experiment was conducted at the Xichong Bay (East of China)(see Fig. 6.1). This initiative has involved different institutions as the National Remote Sensing Center of China (NRSCC), the Chinese Meteorological Administration (CMA), the European Space Agency (ESA), and the Institute of Space Studies from Catalonia (IEEC).

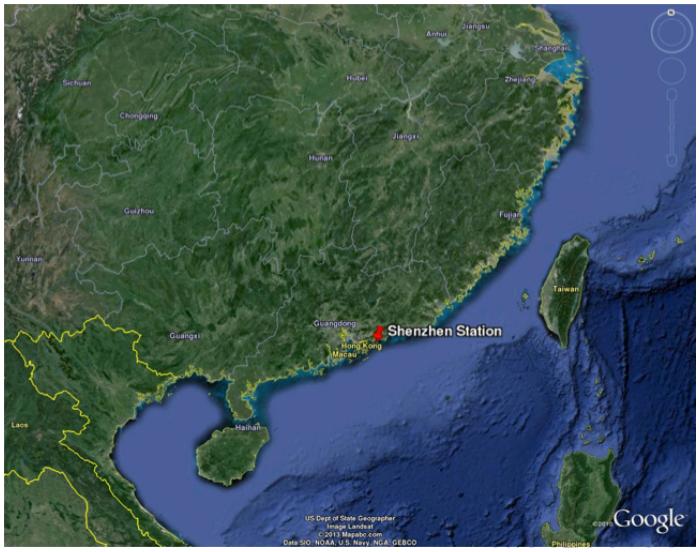

Figure 6.1: Xichong Bay (East of China) (Credits: IEEC).

The main purpose of TIGRIS is to do research on GNSS-R towards remote sensing of typhoons, providing recommendations for future GNSS-R space-based missions, as for example GYGNSS. In this chapter, the data acquired during the TIGRIS experiment is analyzed (i.e direct cross-talk contamination, GNSS multipath contamination, etc), and the main results (focus during USAGI's period) are provided.

6.2 TIGRIS experiment Set-up

The TIGRIS experiment was conducted at the East of China (Xichong Bay) during the summer 2013. The campaign started at July and ended on September. During this period, two typhoons (UTOR of category-4 and USAGI of category-5), and one tropical storm (JEB1) took place.

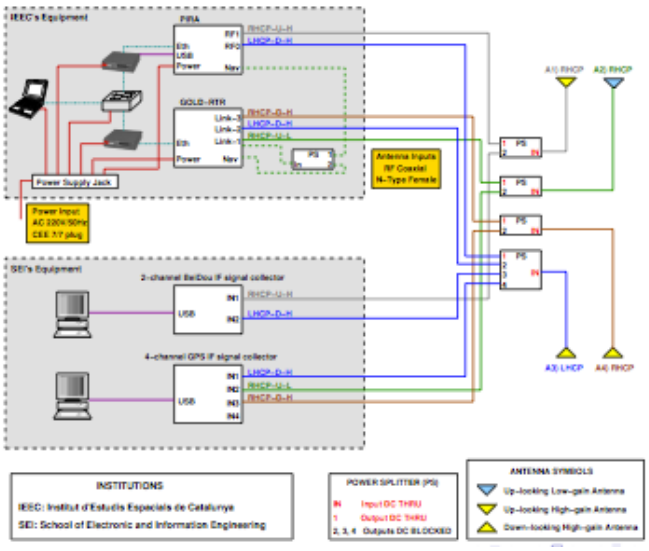

Figure 6.2: Set up of the TIGRIS experiment (Credits: IEEC).

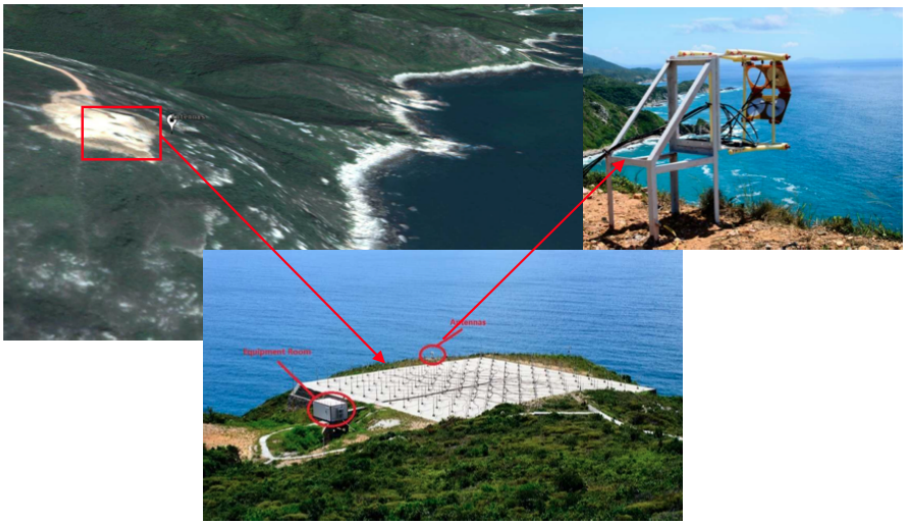

Figure 6.3: Antennas installation (Credits: IEEC).

Data were acquired using the two IEEC GNSS-R receivers. The GOLD - RTR (GPS Open Loop Differential Real Time Receiver) based on the classical GNSS-R approach (cGNSS-R) [65] and the PIR (PARIS Interferometric Receiver) based on the interferometric GNSS-R (iGNSS-R) approach [67]. Figure 6.2 shows the set up of the experiment, and Fig. 6.3 shows the antennas installation in Shenzhen site.

In addition to the IEEC GNSS-R receivers, two signal recorders with software-based receivers from the Beihang University were also collecting GNSS reflected signals, including BeiDou.

6.2.1 PIR instrument

Figure 6.4 provides a simplified user-model view of the PIR receiver. Between the different elements it can be distinguish, the Up/Down antennas, the navigation antenna, the GPS receiver, the user time and frequency, A/D converters, the PIR Signal Processor (PIR-SP), and the correlation channel. As follows, the different parts are described.

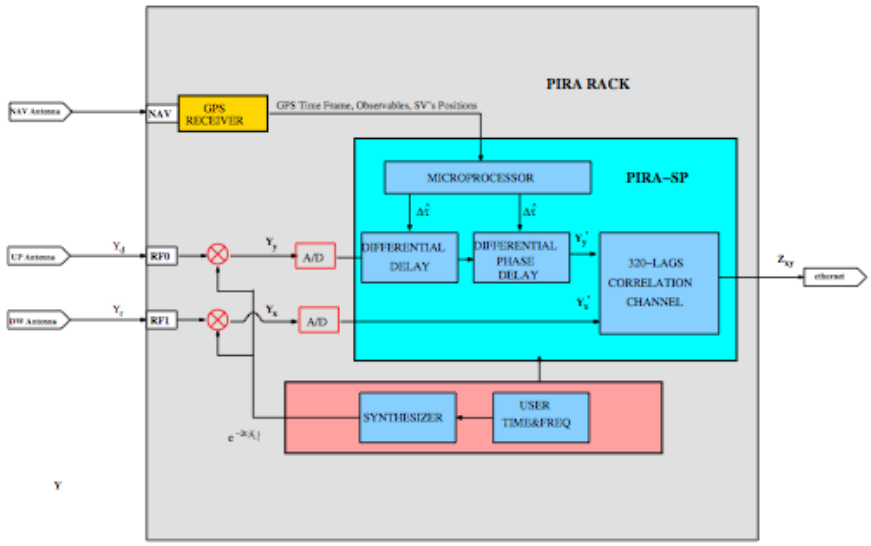

Figure 6.4: PIR receiver details (Credits: IEEC).

1. UP/DOWN Antennas. Both antennas presents an elongated radiation pattern, with a peak gain of $\approx$ 15 dBi. The antennas were placed at the Shenzhen site (Fig. 6.3), at an altitude of 121.81 m pointing towards the sea surface with an azimuth of 120° and elevation of 33°.

2. Navigation antenna, provides sigals to the GPS receiver.

3. GPS receiver, delivers the 1 pps GPS time to the other PIR subsystems. Additionally it provides the Up-looking antenna position and the GPS SV's positions and pseudorange/Doppler observables at 1 Hz rate.

4. User Time and Frequency, provides the system clock and a reference signal to a synthetizer, which produces a signal to downconvert the collected up and down sigals (Y_d,Y_r) to the corresponding analytic signals (Y_x,Y_y)

5. A/D converters, provides one-bit samples of (Y_x, Y_y) at 80 Msamples/second.

6. PIR Signal Processor (PIR-SP), alligns $Y_y(t)$ with $Y_x(t)$ in order to perform the cross-correlation. With this purpose two transformations are applied to $Y_y(t)$,

   (a) a delay (box DIFFERENTIAL DELAY BLOCK).

   (b) counter rotation (box DIFFERENTIAL PHASE DELAY BLOCK).

7. A correlation channel, implements,

$$Z_{x,y}(\tau_{lag}, T_w) = \int_{u=T_w-T_c/2}^{u=T_w+T_c/2} Y'_x \cdot Y'^{*}_y(u - \tau_{lag})du, \tag{6.1}$$

6.3 Preliminary results

Initial results from the data acquired by the PIR receiver reveal three peculiarities. The first one is related with some time gaps, where there is not data acquired by the receiver The second one, is a direct cross-talk contamination produced as a consequence of the geometry. To end, there is a contamination caused from others GNSS signals (i.e. BeiDou, Galileo and QZSS).

6.3.1 Masking the data

As it has been commented, during the acquisition of the data by the receiver, there are some time gaps in where the receiver is not recording the data. In particular, every minute there are some seconds in which no data is stored. Hence, Fig. 6.5 plots the power waveforms acquired during 60 seconds (note that $T_{coh} = 1$ ms and $N_{incoh} = 1$). From it, easily can be identify the seconds in where the receiver is not acquiring data (in this case from second 29 to second 35).

Figures 6.6 and 6.7 show the Power Waveforms obtained at SoW = 432000 (normal case), and at SoW = 432031 (case in where the receiver is not acquiring data). Respect to this, is important identify and mask the times gaps where there is not data (ie Fig. 6.7), in order to avoid obtain wrong results when the power waveforms will be averaged.

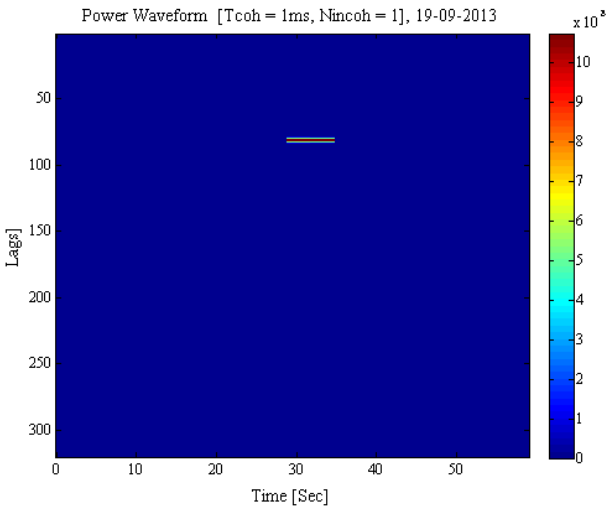

Figure 6.5: Power Waveforms for September 19^{th} without mask.

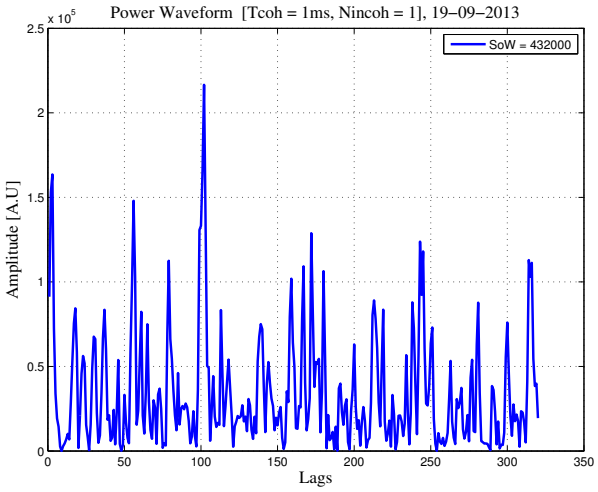

Figure 6.6: Power Waveforms for September 19^{th} 2013 at SoW = 432000.

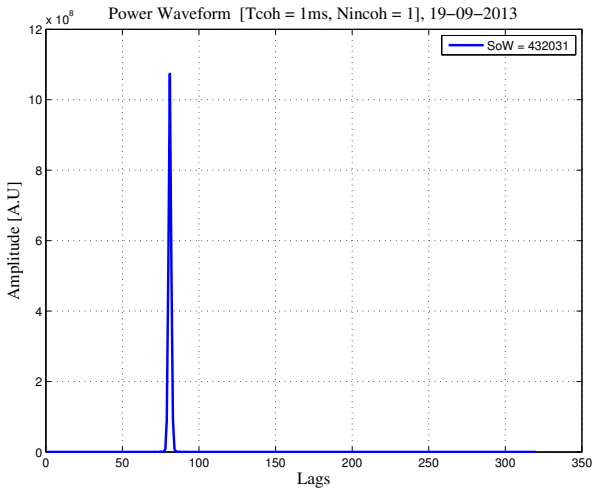

Figure 6.7: Power Waveforms for September 14^{th} 2013 at SoW = 432031.

6.3.2 Mitigation of Direct Signal Cross-Talk

One of the important issues detected is the presence of a direct signal cross-talk contamination in the data, as a consequence of the geometry of the scenario (receiver altitude at 121.81 m), in which case a complete separation of the C/A code in the differential range delay cannot be achieved ($2\rho_{CA}$ = 600 m). Considering that the delay between the direct and reflected signals can be approximated by:

$$\delta\tau = 2h_R sin(\theta_{elev}), \tag{6.2}$$

where h_R is the altitude of the receiver (h_R =121.81 m), and θ_{elev} is the elevation angle. Therefore, the maximum separation that can be achiveved in this case is around 243 m approx (when $\theta_{elev} = 90°$)

Figure 6.8 plots the Power Waveform of September 15^{th} at 00:05:09 (SoW = 309 seg) after averaging 40792 independent Power Waveforms. From that, two peaks can be distinguished. The first one, at lag 0, corresponds to the direct signal contamination (the axis of the Waveform has been centered in the peak of the direct signal). The second one, around lag 21, is related to the peak of the GPS Power Waveform. From the geometry of the scenario, and the time at which the waveform has been acquired (00:05), the GPS SV in view is SAT-ID-31, which presents an elevation angle of 19.27. Hence, from Equ. 6.2, a delay between the direct and the reflected signals of 80.41 m approximately is obtained (equivalent to 21 lags considering that the sampling frequency of the PIR is 80 MHz). Therefore, this result is in agreement with Fig. 6.8, where the distance between the two peaks is 21 lags

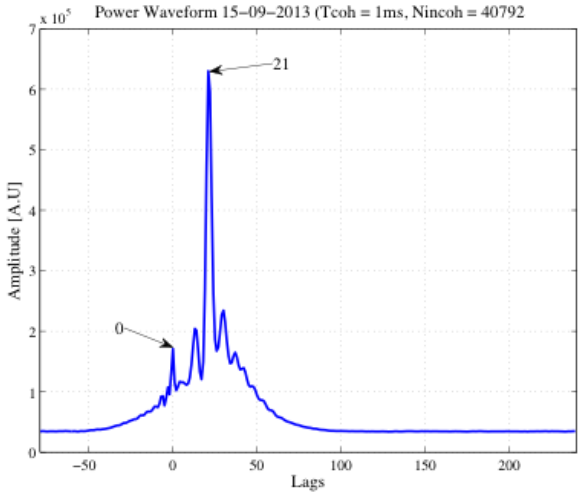

Figure 6.8: Power Waveform obtained from an incoherent average of 40792 individual Power Waveforms.

In order to mitigate this direct signal contamination, the computation of the variance is proposed as an alternative to the incoherent averaging. The variance is given by:

$$Var(X) = E[X^2] - \mu^2, \tag{6.3}$$

where X is the observable and μ is the mean of the observable. Therefore, considering the voltage waveform $Y(\tau)$ as the observable, its variance can be estimated from a finite number of realizations as,

$$Var(Y(\tau)) = \frac{1}{N}\sum |Y(t_{o,j},\tau)|^2 - |\frac{1}{N}\sum (Y(t_{o,j},\tau)|^2, \tag{6.4}$$

where the first term of Eqn. (6.4) is the classical averaged power waveform, whereas the second term of Eqn. (6.4) is the power waveform obtained considering a coherent integration time (T_{coh}) equal to the number of independent waveforms N (i.e the coherent waveform [29]). Figure 6.9 shows the variance of the 40792 complex waveforms used to produce the averaged power waveform in Fig.6.8. As it can be observed, the peak at lag 0 has disappeared, since the coherent part of the signal has been subtracted.

Figure 6.10 presents the coherent part of the signal, i.e. the last term in 6.4. As it can be appreciated, the main contribution comes from the cross-talk of the direct signal (around lag 0). A secondary contribution around the central part is related to the coherent part of the reflected signal itself (related with the speckle noise). It

is important to remark that the coherent component of the reflected signal will vary with the geometry (i.e altitude of the receiver), and the sea state (this feature will be show later). On the other hand, is important to note the difference between the amplitude of the incoherent and coherent components. While the peak amplitude of the incoherent waveforms is around $6 \cdot 10^6$, the amplitude of the coherent component is only of $1.8 \cdot 10^4$, which gives a coherent-to-incoherent amplitude ratio of about 3%.

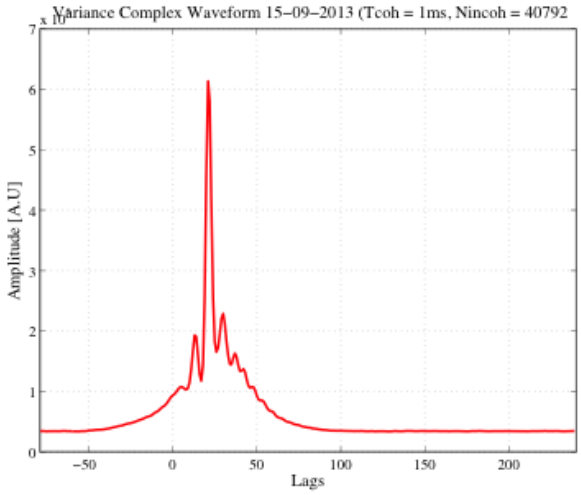

Figure 6.9: Variance Waveform obtained applying from 40792 individual complex Waveforms.

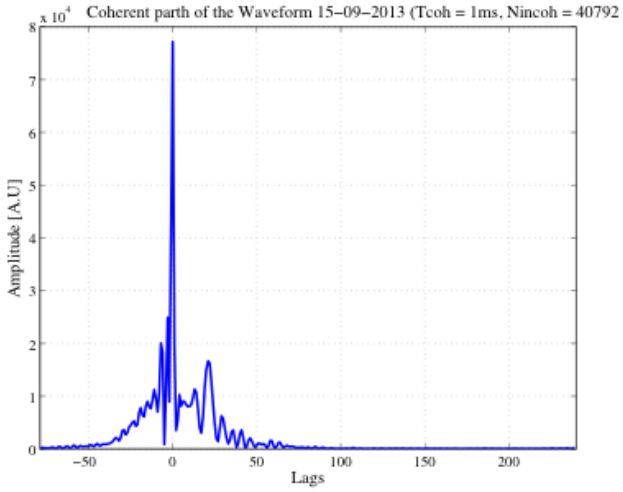

Figure 6.10: Coherent Power Waveform.

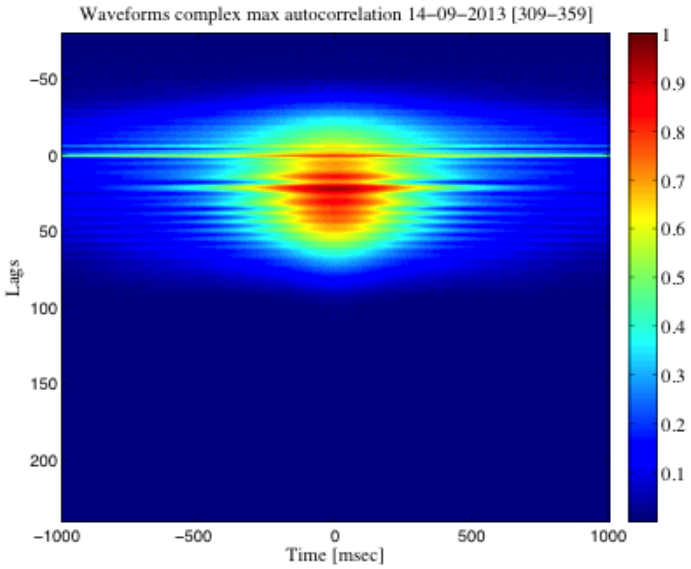

Figure 6.11: Autocorrelation of the complex waveforms.

In order to retry the level of correlation that presents each lag, the autocorrelation function has computed. Thus, Fig. 6.11 stacks the temporal autocorrelation function for each lag. As it can be observed and as it can be expected, the highest level of correlation is obtained around the direct signal (lag 0), and around the peak of the Waveform (around lag 21), which agree with Fig. 6.10.

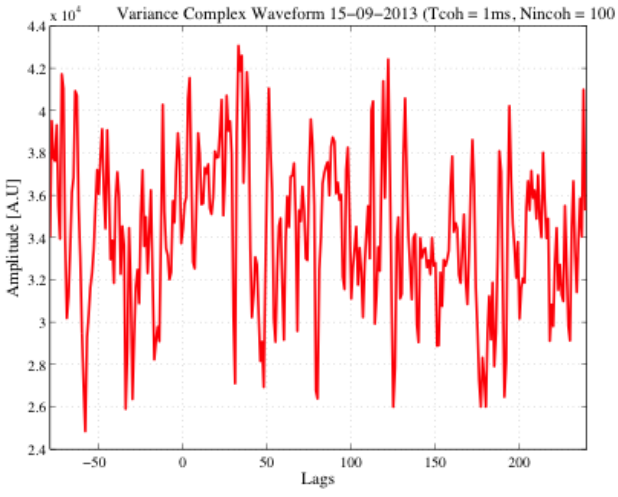

Figure 6.12: Power Waveform estimated using the variance of 100 individual waveforms.

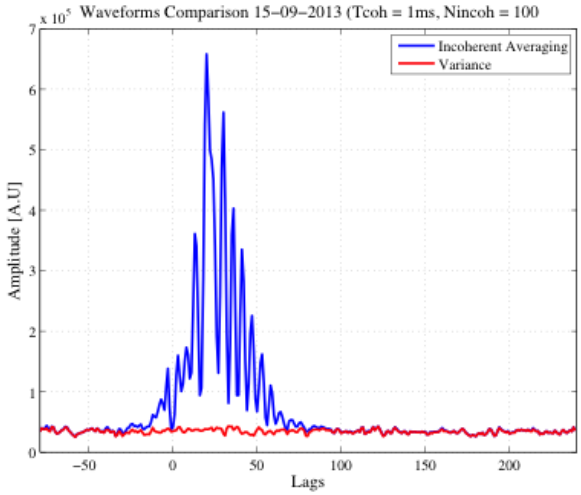

Figure 6.13: Power Waveform comparison obtained applying the incoherent averaging and the variance technique using 100 individual waveforms.

If now the variance is computed considering a small number N of independent waveforms (i.e $N = 100$), but sufficiently high so as to remove the coherent component, the resulting power waveform is dominated by thermal noise (Fig. 6.12). This issue can be better appreciated in Fig. 6.13 , where both the incoherently averaged power waveform and the variance of the complex waveforms have been plotted.

On the other hand, and as it has been commented previously, the coherent component of the reflected signal will vary with the geometry (i.e altitude of the receiver), and the sea state. Hence, the next two examples are used to show how the level of correlation changes as a function of the geometry. Additionally, these two examples will serve to demostrate that the approach presented here, does not modify the results in scenarios where not direct signal contamination is produced, since in that cases, any distortion is introduced due to the lack of components more coherent (as it can be the direct signal). Therefore, the same procedure has been repeated using two data sets from an airborne and spaceborne scenarios.

The second data set consists of a two-hour long airborne experiment performed over the Gulf of Finland near Helsinki on Nov 11^{th} 2011 [51]. For that data, the waveform obtained using the variance and the incoherent power waveform is nearly the same (Fig. 6.14), since in this case there isn't direct signal contamination, and the level of correlation of the reflected signal is much lower than the one of the ground-based TIGRIS experiment. These features, can be observed in Figs. 6.15 and 6.16, where the temporal autocorrelation function for each lag and the coherent power waveform are plotted. This results fully agree with that obtained in [69]. On

the other hand, the ratio obtained between the coherent and incoherent component is around 0.4%, which is substantially lower than the one obtained in the TIGRIS case, basically because in this case the coherent component is lower respect to the ground-base case. It is important to consider that the coherent component varies with the geometry, being the receiver altitude one of the parameters that impact on the coherent component (lower altitudes higher coherence).

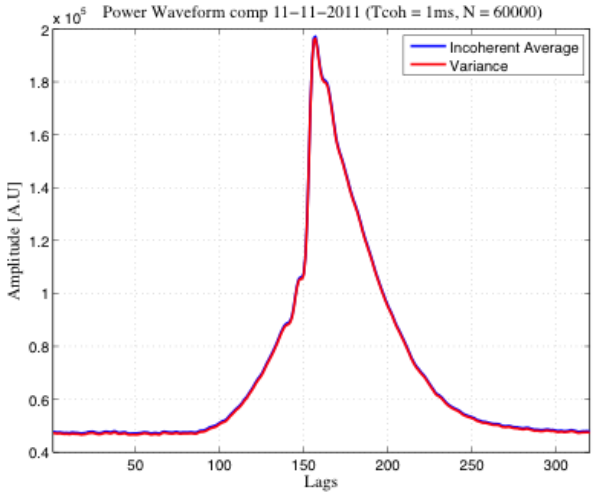

Figure 6.14: Power Waveform comparison obtained applying the incoherent averaging and the variance technique using 60000 individual waveforms. Baltic airborne experiment.

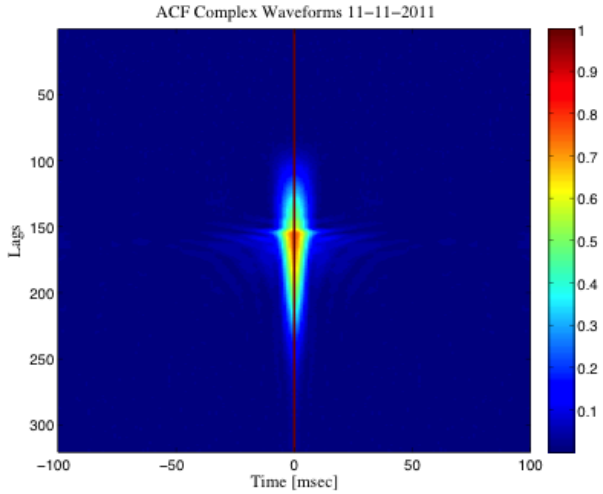

Figure 6.15: Auto-correlation of the complex waveforms (Baltic flight 11-11-2011)

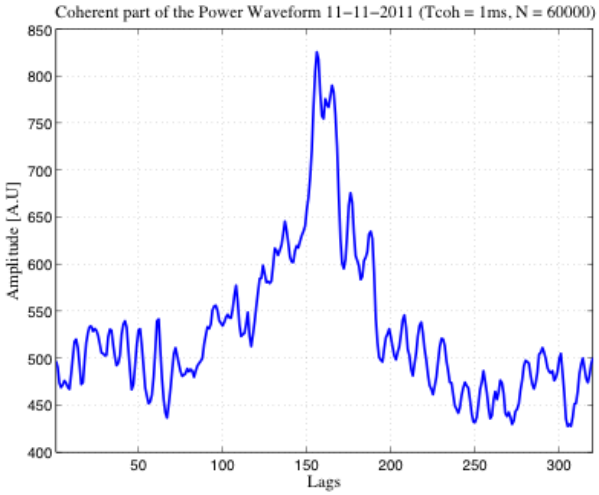

Figure 6.16: Coherent Power Waveform (Baltic Flight, 11-11-2011).

The third data set used is 12 seconds of reflected signals acquired by the GNSS-R receiver on-board the UK-DMC satellite [68]-[19]. The reflected signals were collected during November 2004 in the North-West Pacific. Differently to the previous two data sets, the UK-DMC data set is based on the cGNSS-R technique. In this case, the different 1 ms power waveforms are fully uncorrelated (Fig. 6.17) in agreement with the results shown in the Chapter 3. Since the data is totally uncorrelated, the variance and the incoherently averaged waveforms are the same [29], as it can be appreciated in Fig. 6.18, On the other hand, Fig. 6.19 shows the coherent part of the waveforms. As it can be observed, it is very small, nearly negligible. Thus, the ratio between the coherent and incoherent component obtained in this case is around 0.08%, which again is substantially lower even if it is compared with the airborne case. The reason is because for a spaceborne case (like this) the coherence is much lower (in this case waveforms are fully uncorrelated, dominating the thermal noise respect the speckle noise, as it has shown in the Chapter 3) Therefore, it can be concluded that this ratio decreases as a function of the receiver altitude.

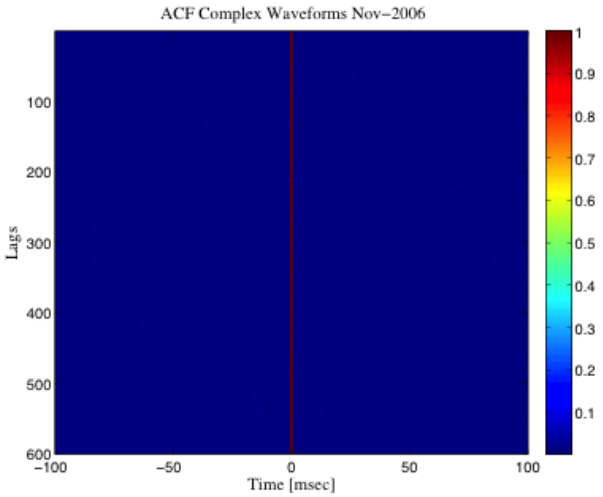

Figure 6.17: Auto-correlation function of the UK-DMC complex waveforms (Nov-2004).

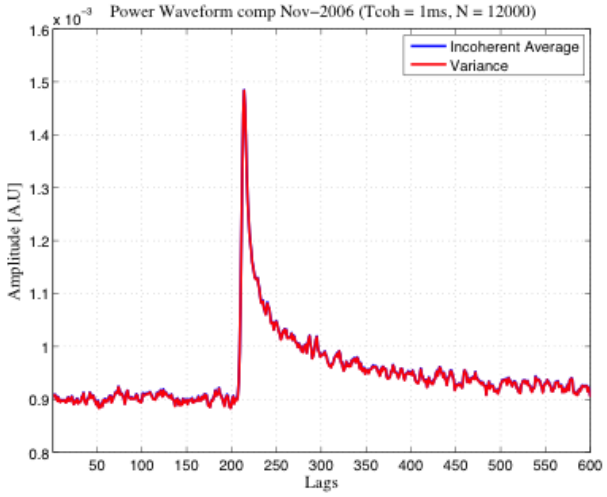

Figure 6.18: Power Waveform comparison obtained applying the incoherent averaging and the variance technique over 60000 individual Waveforms.

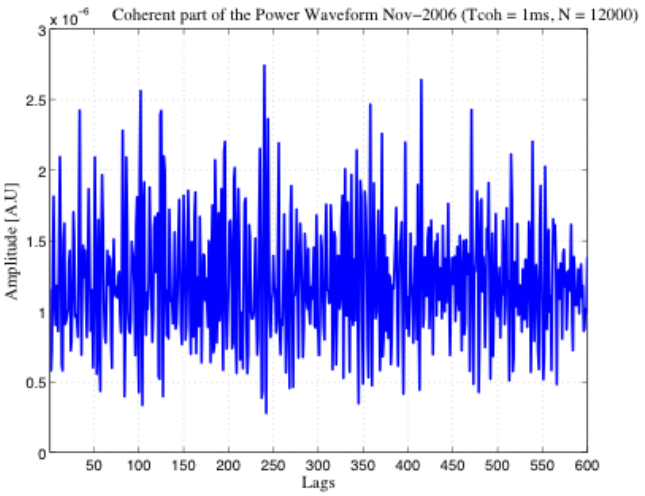

Figure 6.19: Coherent Power Waveform (UK-DMC Nov-2004).

To finish, the effectiveness of this technique is shown. Figure 6.20 represents the power waveforms computed incoherently on September 15^{th}, considering a $T_{coh} = 1$ ms and a $N = 20000$. From it, it can be easily identified the impact that the direct signal has on the waveforms (the vertical strip line that appears around lag 81). On the other hand, Fig. 6.21 represents the power waveforms that results from the application of the variance instead of the incoherent averaging. As it can be appreciated, with using the variance the strip line around the lag 81 is removed. Figure 6.22 represents the coherent part of the signal, that results from substract the waveforms obtained by the variance to the ones obtained by the incoherent averaging.

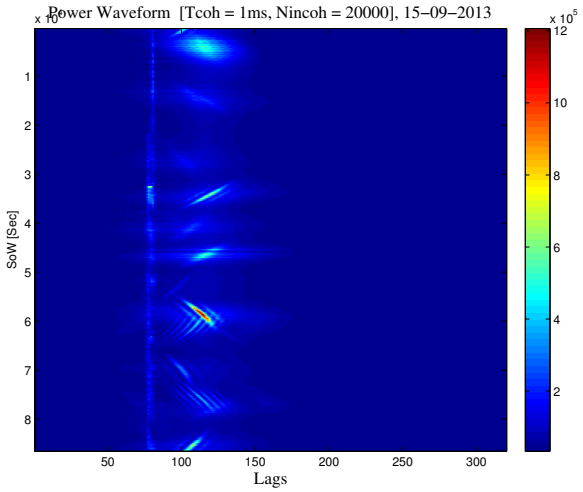

Figure 6.20: Power Waveforms obtained for September 15^{th} 2013 using the incoherent averaging.

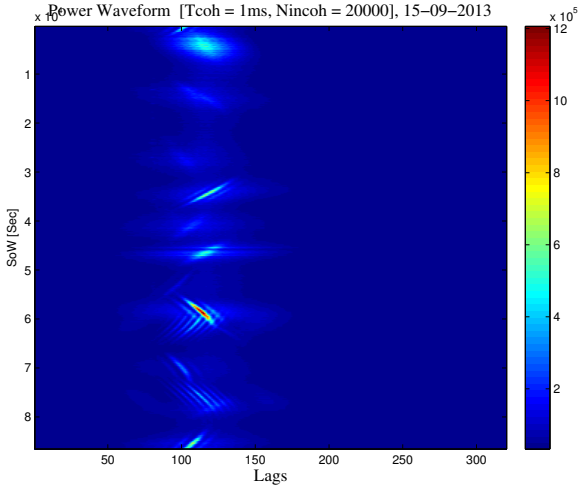

Figure 6.21: Power Waveforms obtained for September 15^{th} 2013 using the variance.

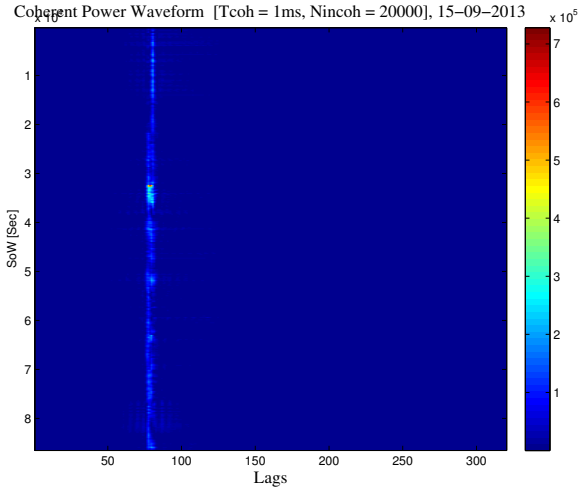

Figure 6.22: Coherent component of the Waveforms obtained for September 15^{th} 2013.

6.3.3 GNSS multipath contamination

As it has been introduced in the previous chapters, the iGNSS-R techique performs the cross-correlation between the direct and the reflected signals. Therefore, the cross-correlation is performed between all the incoming signals from the up- and down-looking antennas. This feature, can be critical above all in ground-based scenarios, where the final waveform, is the result of the cross-correlation of different GNSS signals simultaneously (i.e. GPS, Galileo, BeiDou, and QZSS). Preliminary results obtained in the TIGRIS experiment, confirm this issue.

Figure 6.23 represents the power waveform obtained from September 15^{th} at SoW = 1740 (00:29). From that waveform, two main peaks can be identified. The first one around lags 95-96 (related to GPS signal) and the second one around lag 110 (related to BeiDou and QZSS signals). On the other hand, Fig. 6.24 shows the geometry computed for September 15^{th} at SoW = 1740. As it can be appreciated, at that instant of time (SoW = 1740) there are four GNSS satellites under vision (GPS SAT-ID 32, BeiDou SAT-ID 4, BeiDou SAT-ID 6, and QZSS). From these four GNSS satellites, the main contribution comes from GPS SAT-ID 32, BeiDou SAT-ID-4 and QZSS, which respectively present an elevation angle of 12.35°, 33.45° and 25.58°, and an azimuth angle of 122.74°, 109.94° and 138.63°. Considering the elevation angles, the delay difference between the direct and the reflected signals can be computed using Eq. (6.2). Thus, the delay difference obtained is around 52.10 m for the GPS signal, and 105.2 m for the QZSS signal, which is equivalent to 14 lags (GPS signal), and to 28 lags (QZSS signal). Hence, considering that the direct signal is set up by default at lag 81, and the delay differences computed, the peak of the GPS should be around lag 95, and the peak of the QZSS around lag 110 approximately. These results are in agreement with the positions of the peaks observed in Fig. 6.23. On the other hand, BeiDou SAT-ID 4 is a geostationary satelly, its peak is around lag 111. BeiDou SAT-ID 6 contribution at the end waveform is not relevant, since the elevation and azimuth angles are far from the ones where the receiver antenna are pointing (remember that the antenna are pointing towards the sea with an elevation angle of 32°, and azimuth angle of 120°).

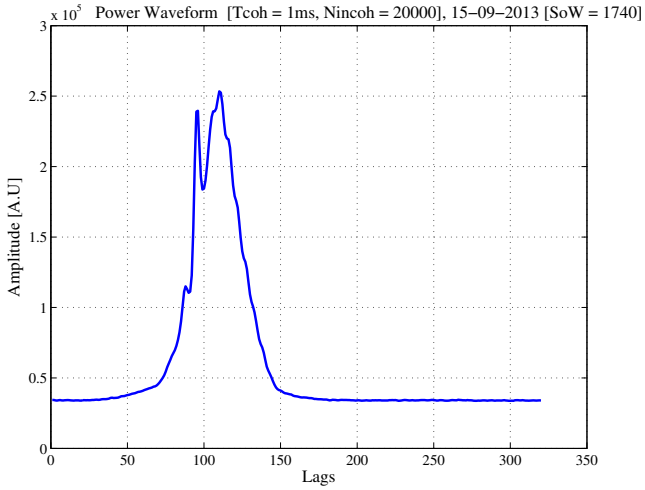

Figure 6.23: Power Waveform obtained for September 15^{th} 2013 at SoW = 1740.

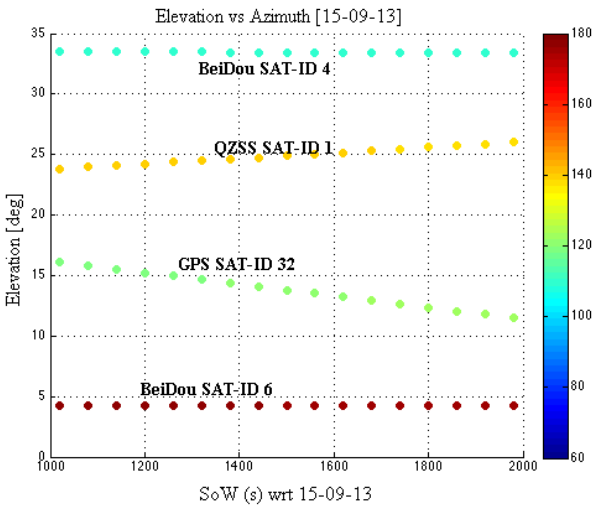

Figure 6.24: Geometry computed for September 15^{th} 2013 at SoW = 1740.

Figure 6.25 represents another example of multipath. The power waveform corresponds to the same day but now at SoW = 73020 (19:32). At that instant of time, the main GNSS signals under vision are GPS SAT-ID 22 and 29, BeiDou SAT-ID 4, QZSS SAT-ID 1 and Galileo SAT-ID 12 are under vision, which present an elevation angle of 28.82°, 23.03°, 33.54°, 18° and 19.37°, respectively, and an azimuth angle of 175.84°, 82.09°, 109.92°, 166.47° and 133.21°, respectively. Figure 6.26 shows the evolution of the elevation and azimuth angles from these GNSS satellites. According to the geometry computed, the main contribution is produced by the Galileo satellite, which is the one that presents the elevation and azimuth angles closer to the ones of the receiver antennas. For that elevation angle, the peak of the waveform is obtained around lag 102, in agreement with Fig. 6.25. On the other hand the distortion in the waveform is produced by the contribution of the GPS, BeiDou and QZSS signals.

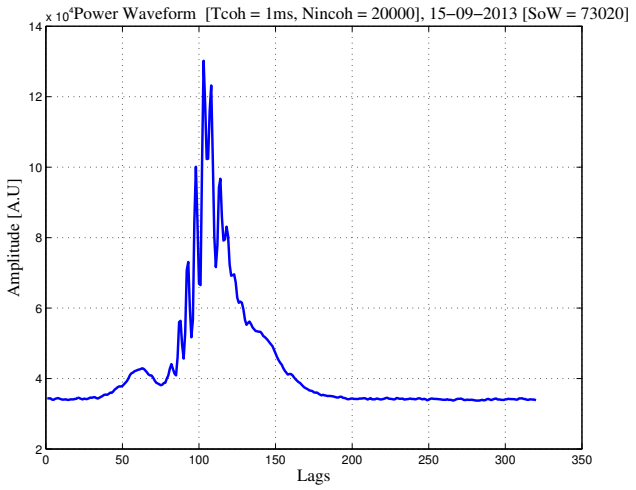

Figure 6.25: Geometry computed for September 15^{th} 2013 at SoW = 73020.

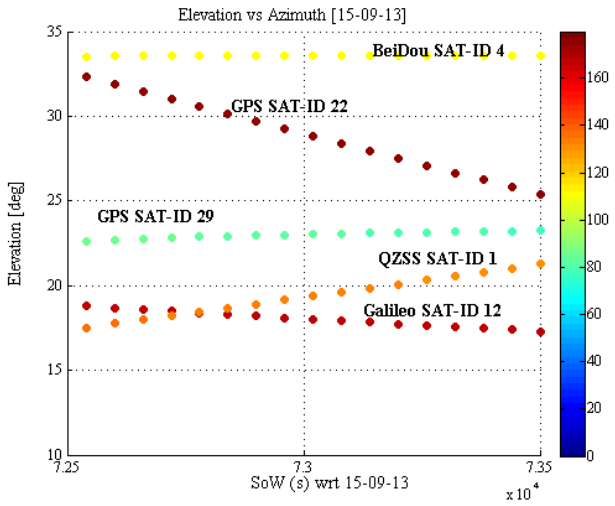

Figure 6.26: Geometry computed for September 15^{th} at SoW = 73020.

The last two examples illustrate perfectly the impact that the GNSS multipath has on the resulting power waveform. It is important to remark, that the major part of the data processed, are affected by this GNSS multipath. Therefore, doing a proper representation of the geometry can be very useful, in order to determine the impact that the different GNSS signals has on the resulting power waveform. In addition, an accurate computation of the geometry can help in the identification of these epoch times when one GNSS satellite (i.e. GPS, BeiDou, Galileo, etc) dominates over others. Next plots serve as a good example of that, where GPS, BeiDou or Galileo are the dominating signals. All of them are obtained from September 15^{th}, 2013.

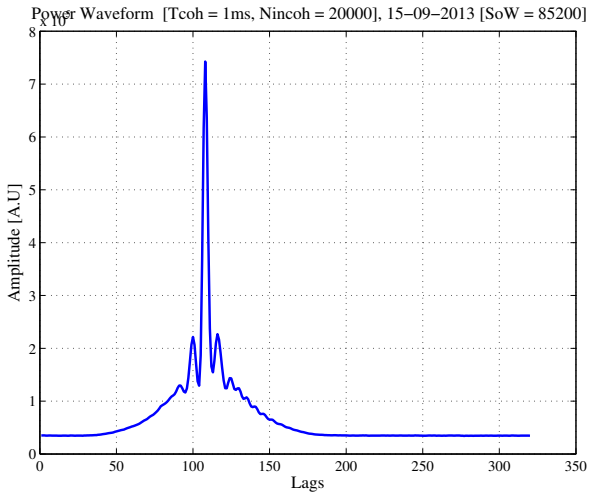

Figure 6.27: Power Waveform computed for September 15^{th} 2013 at SoW = 85200.

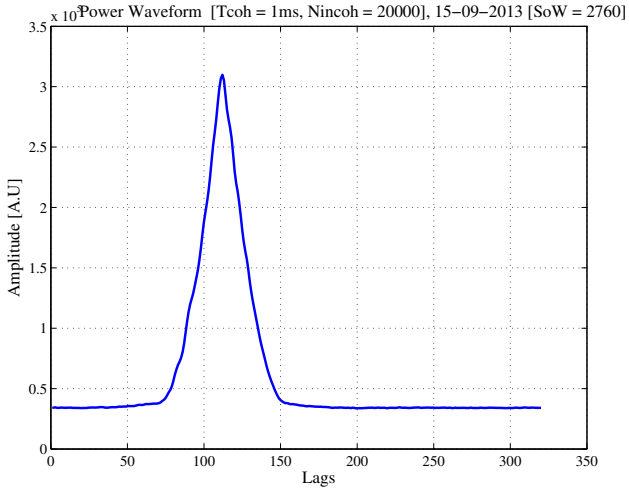

Figure 6.28: Power Waveform computed for September 15^{th} 2013 at SoW = 2760.

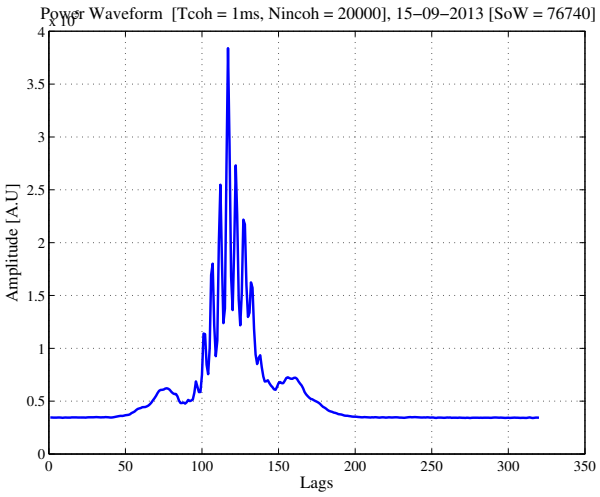

Figure 6.29: Power Waveform computed for September 15^{th} 2013 at SoW = 76740.

6.3.4 Impact of the direct signal cross-talk contamination and geometry

Mitigating the direct signal cross-talk contamination is an important issue, that should be considered since the end results can be impacted by this contamination. Figures 6.30 and 6.31, are clear examples of that.

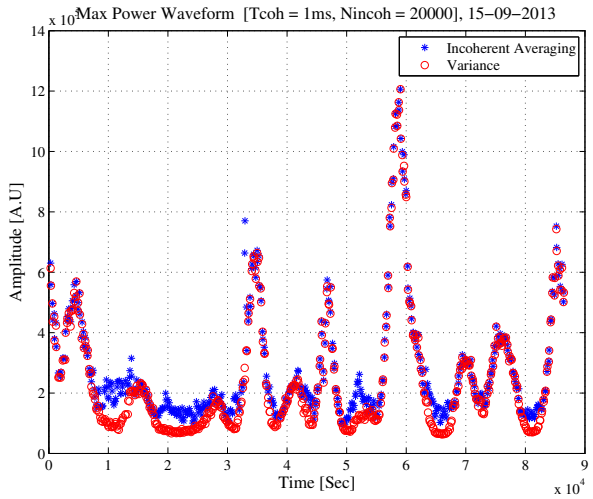

Figure 6.30: Peak power Waveforms obtained for September 15^{th} 2013.

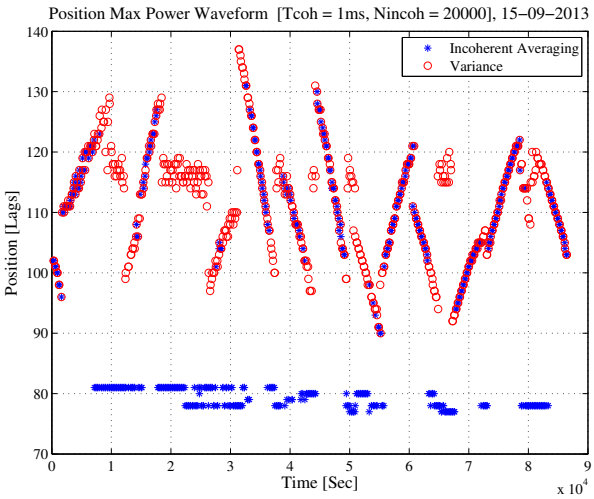

Figure 6.31: Position peak power Waveforms obtained for September 15^{th} 2013.

Figure 6.30 represents the peak of the power waveform, whereas Fig. 6.31 plots the lag position of this peak. From that, some differences can be appreciated between the amplitude and lag position. Additionally, it can be easily identified that the major impact occurs for the lower amplitude values, which corresponds to the cases where the reflected signal is lower than the direct one. Therefore, at that time epochs the amplitude of the direct signal is dominating over the reflected signal.

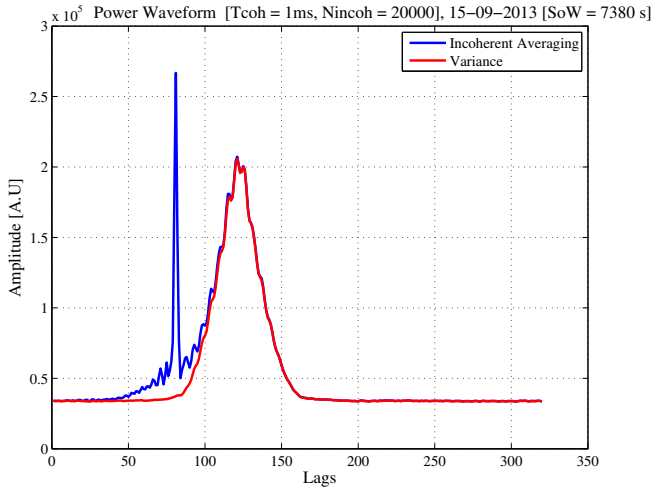

Figure 6.32: Power Waveforms obtained for September 15^{th} 2013 at SoW = 7380.

Figure 6.32 serves as an example. It represents the power waveforms computed using the incoherent averaging and the variance for the SoW = 7380. For that particular instant, the GNSS satellites under visibility are GPS SAT-ID 16, BeiDou

SAT-ID 4, and QZSS, being the QZSS the dominant one (elevation angle equal to 40.33° (peak around lag 121) and azimuth angle equal to 127.47°). On the other hand, the GPS signal is to low (elevation angle equal to 18.71° and azimuth angle equal to 76.43°). Therefore in cases like this, the amplitude of the direct signal is higher than the amplitude of the reflected signal. This feature can be clearly identified in Fig. 6.32.

The importance of the computation of the geometry has been introduced in order to identify the impact that the different GNSS signals have on the resulting power waveform. Geometry will be also relevant in the evaluation of some observables. Thus, parameters such as the amplitude of the power waveform (related to the wind speed), or the coherence time (related to the significant wave height), will depend on the geometry.

Figure 6.33 shows several examples on how the geometry impacts the main observables (color indicates the elevation or azimuth angle during its visibility window). Hence, from Fig. 6.33 it can be observed that the amplitude of the peak waveform varies as a function of the elevation and azimuth angles, where the maximum is obtained for an elevation angle of $\sim 30°$ and an azimuth angle of $\sim 120°$. As measure that the elevation and azimuth angles distances from that values, the amplitude decreases as well the contribution of the GPS signal in the waveform, starting to be noticeable the contribution from other GNSS signals. In a similar way, the position of the specular delay varies as a function of the elevation angle, as it can clearly observed in Fig. 6.33. To finish, it can be also note that for the same SWH, the coherence time varies as a function of the elevation angle.

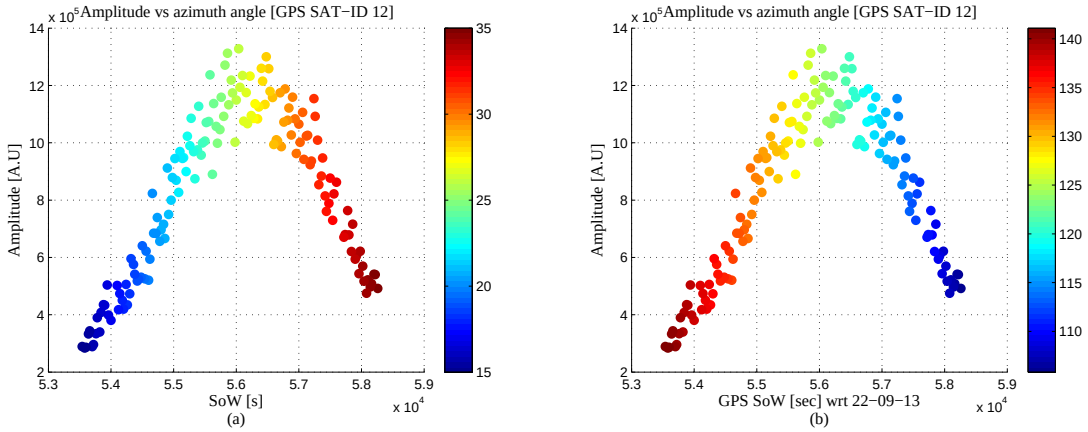

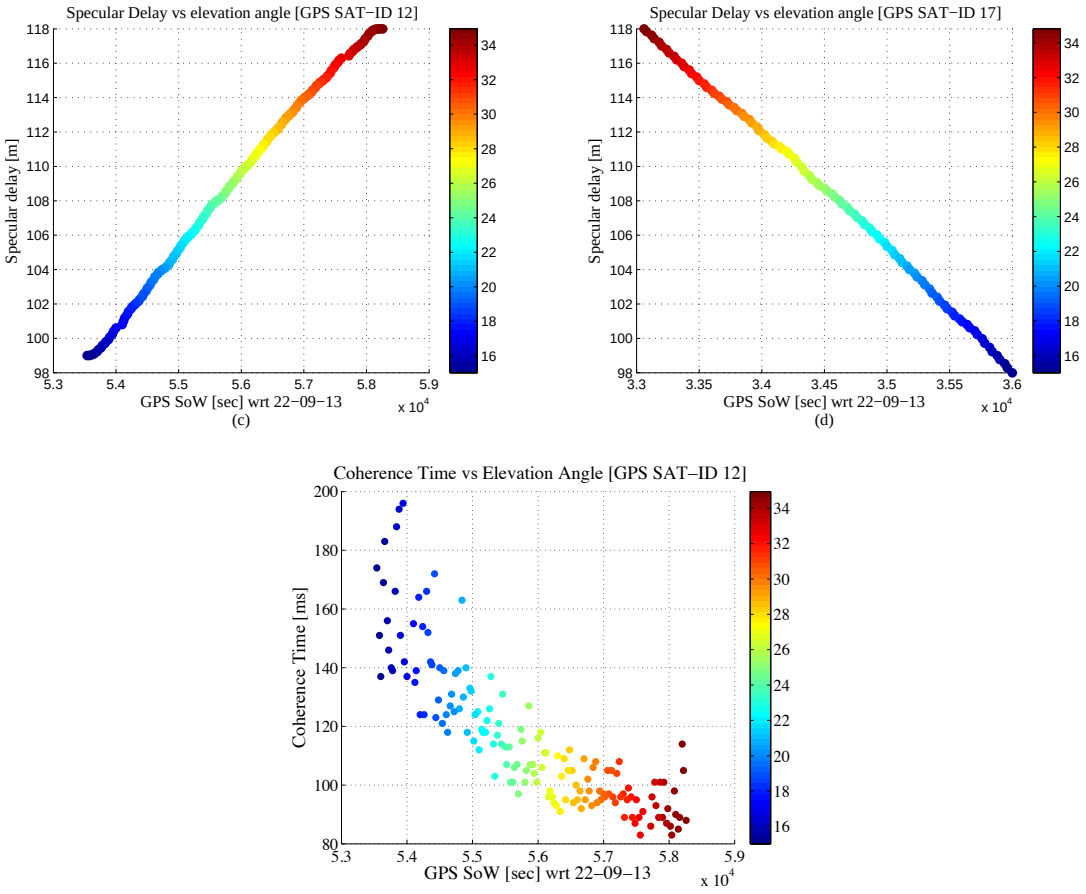

Figure 6.33: Impact of the geometry on the main observables: (a) amplitude vs elevation and (b) azimuth angles for the GPS SAT-ID 12, (c) specular delay vs elevation angle for the GPS SAT-ID 12, and (d) GPS SAT-ID 17, and (e) coherence time vs elevation angle.

6.4 Main results

As previously introduced, one of the main objectives of the TIGRIS experiment, is explore the capabilities of the GNSS-R technique for typhoon monitoring. Hence, in this section the main results obtained during September 10^{th} and September 23^{rd}, concerning to the Usagis typhon are analyzed.

Three main observables will be used in this section. The peak amplitude of the power waveforms, which decreases with increasing the wind speed, the coherence time, which decreases with increasing the significant wave height, and a new observable, based on the computation of the estimated ratio (R) of the number of incoherent averages and the effective number of incoherent averages at the peak of the waveform (introduced on Chapter 3), which will decrease with increasing the significant wave

height, in a similar way to the coherence time. Ground truth data is used in order to validate the results obtained in this section. About the ground truth data is important to consider the following issues. The wind speed was collected by a cup anemometer near to the PIR receiver ($\sim$ 1 km), located at the top of a hill. Therefore this data could be affected by the terrain itself. In this sense is important to remark that access to the data collected by the buoys has not been possible. On the other hand, the significant wave height, has been collected by stations situated far away from the PIR receiver.

Previously to analyze the results, the direct cross-talk contamination has been mitigated using the variance approach presented in the previous section. On the other hand the computation fo the geometry has been considered in order to identify the time epochs in where there is one signal dominating respect the others, and in order to discriminate the impact due to variations in the elevation and azimuth angles. In this sense three GPS signals can be identified; GPS-SAT-ID 12, GPS-SAT-ID 17, and GPS-SAT-ID 2 (without M code). Is important to analyze them separately, since each one is affected in a different way by the geometry, as well the EIRP will be different for example for GPS-SAT-ID 12 than for GPS-SAT-ID 2.

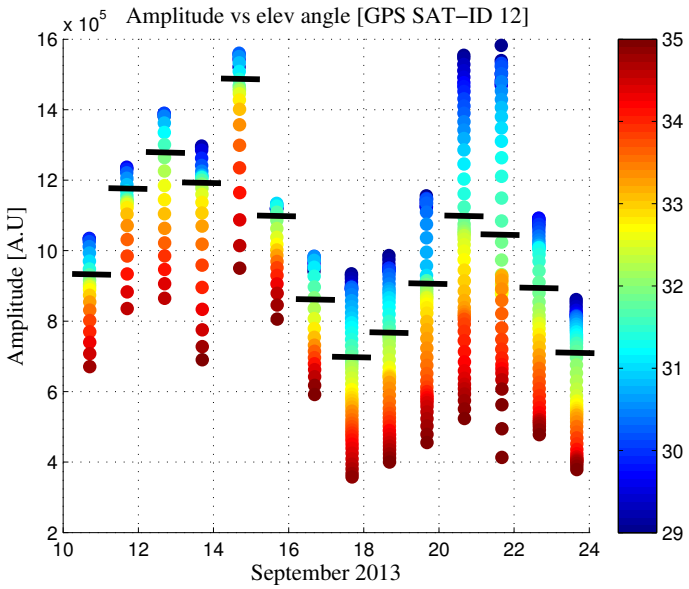

Figure 6.34: Peak power waveforms for the GPS-SAT-ID 12 as a function of the elevation angle.

Figure 6.34 shows the peak amplitude of the power waveforms as a function of the elevation angle, for the GPS-SAT-ID 12 during the USAGI's period. As the PIR

receiver is pointing towards the sea with an elevation angle of 31° and azimuth angle of 120°, these are the reference values that have been considered in this case (marked in the figure with a black line). Remember that the peak amplitude is dependent on both the elevation and azimuth angles, as it can be observed in Fig. 6.35.

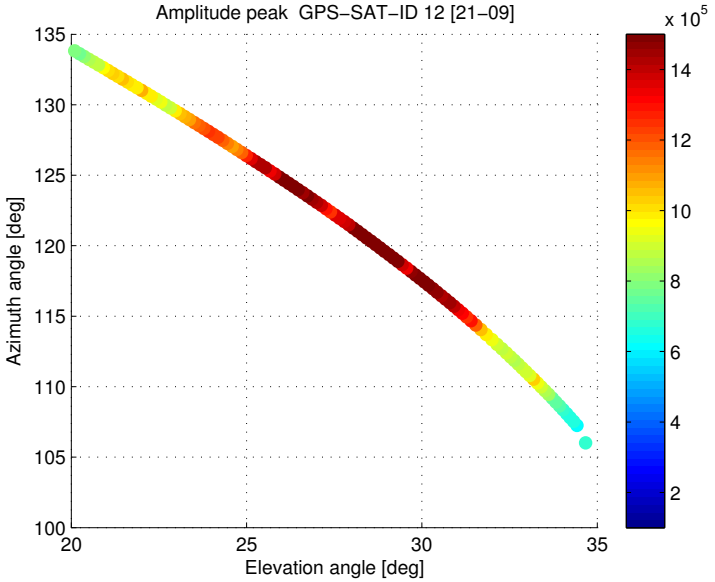

Figure 6.35: Peak power waveforms for the GPS-SAT-ID 12 as a function of the elevation angle and azimuth angle for September 21^{st}.

Figure represents the wind speed measured by the cup anemometer. In red the equivalent wind speeds of the peak amplitudes shown in Fig. 6.34 are marked. Comparing both figures, it can be appreciated that the general trend that the peak amplitude present is inverse of that with the wind speed evolution. It can be appreciated that the peak amplitude evolution shows an inverse trend respect to the wind speed evolution. It is important to note that some pecularities can impact the results, such as the variation of the actual sea surface height as a consequence of the wind speed, the non Gaussianity and non linearity of the waves in coastal areas, above all during the typhoon (short fetch). On the other hand, other than swell, the multipath due to the coast for elevation angles higher than 32°, or the wind direction are parameters that can affect the waveforms.

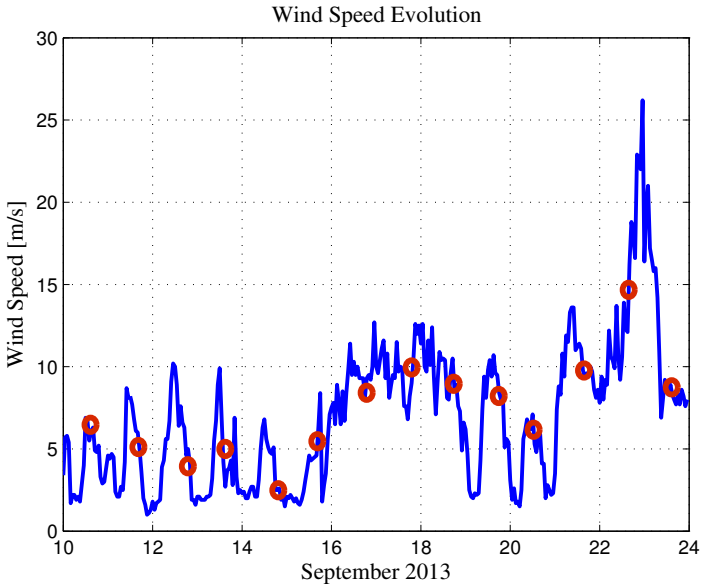

Figure 6.36: Wind speed measured by a cup anemometer closer to the PIR receiver.

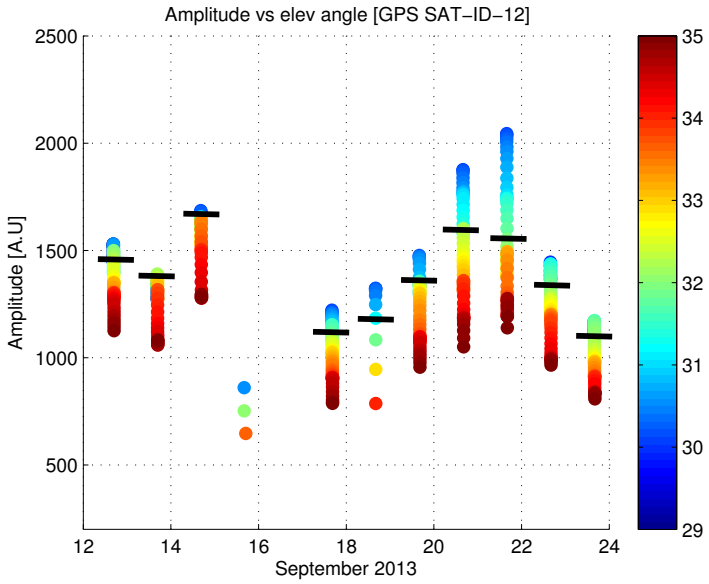

Figure 6.37: Peak power waveforms for the GPS-SAT-ID 12 as a function of the elevation angle.

The same procedure has been repeated, but now considering the cGNSS-R case. With this purpose, data acquired from the GOLD-RTR receiver has been processed. Figure 6.37 plots the peak amplitude obtained for GPS-SAT-ID 12, for the cGNSS-R case. As it can be appreciated, these results show a similar trend to the ones obtained for the iGNSS-R case.

Figure 6.38 shows the coherence time computed for GPS-SAT-ID 12 considering the iGNSS-R case. The coherence time is plotted as a function of the elevation angle. As it can be observed and as expected, the coherence time decreases as a function of the elevation angle.

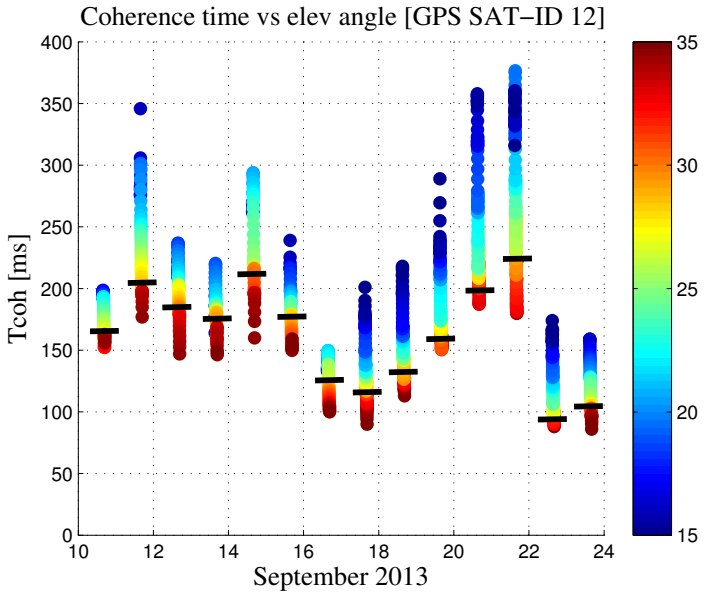

Figure 6.38: Coherence time for the GPS-SAT-ID 12 as a function of the elevation angle.

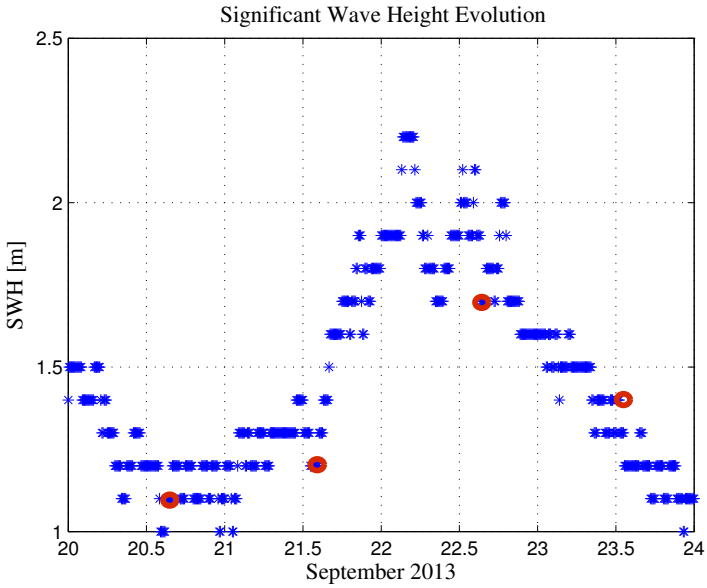

Figure 6.39: Significant Wave Height collected during the USAGI's typhoon.

Figure 6.39 shows the significant wave height available to validate the results. Is important to consider, that the data was collected from one station far away with respect the PIR receiver. On the other hand, data from September 20^{th} to September 24^{th} is only available. From Fig. 6.39 it can be observed how the coherence time presents an inverse trend with respect to the significant wave height.

In the same way the coherence time has been computed considering the cGNSS-R case. Figure 6.40 plots the coherence time computed as a function of the elevation angle. As it can be observed, the coherence time computed for the cGNSS-R case follows a similar trend to the computed previously for the iGNSS-R case, being the results in this iGNSS-R case a bit clear (something similar occurs for the amplitude peaks of the power waveforms). In any case a similar evolution of the coherence time can be identified.

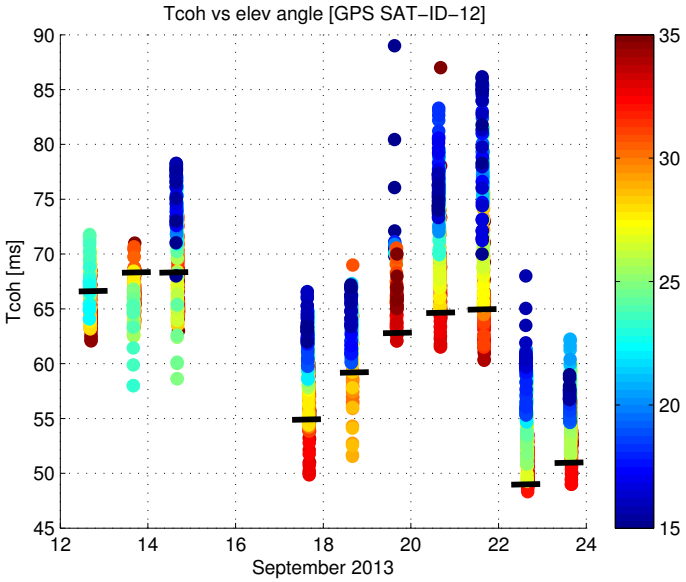

Figure 6.40: Coherence time for the GPS-SAT-ID 12 as a function of the elevation angle.

On the other hand, if Fig. 6.34 is compared to Fig. 6.38, it can be appreciated that both cases presents a similar trend, and the same occurs if Fig. 6.37 is compared with Fig. 6.40.

To end the estimated ratio (R) of the number of incoherent averages and the effective number of incoherent averages at the peak of the waveform has been used as a new observable. As it has been introduced in Chapter 3, in order to reduce the standard deviation of the amplitude of the reflected power wave due to the speckle and thermal noises, incoherent averaging is applied. For the thermal noise, the reduction

achieved with the incoherent averaging is proportional to $\sqrt{N}$, since the thermal noise is uncorrelated sample to sample. However, in the speckle noise, the effectiveness of the incoherent averaging depends on the level of correlation between consecutive waveforms which, as it was shown, varies with geometry, the sea conditions, and also the lag. Thus, in this case the SNR will increase approximately as $\sqrt{N_{incoh}/R}$, where R is the ratio between the number of incoherent averages and the effective number of incoherent averages ($R = N_{incoh}/N_{incoh,eff}$). Thus, focusing in the lag where the amplitude of the waveform is maximum (high impact of the speckle noise), changes in the ratio along the time, can be addressed to the Significant Wave Height, in the same way of the coherence time. As an example, Fig. 6.41 shows the coherence time and the ratio computed for September 16^{th}. For the computation of the ratio, it has been considered a $N_{incoh} = 100$ and MC (Monte Carlo)= 200.

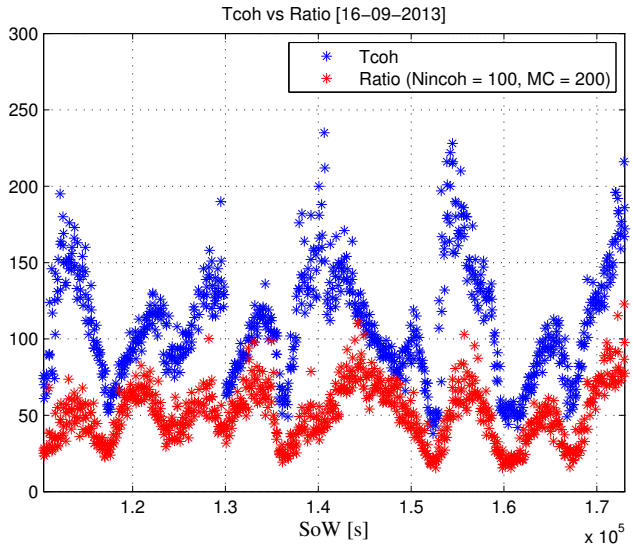

Figure 6.41: Tcoh vs Ratio between the number of incoherent averages and the effective number of incoherent averages, for a $N_{incoh} = 100$ and $MC = 200$.

As it can be appreciated, the ratio follows the trends of the coherence time. If now is repeated the same comparison but now considering a $N_{incoh} = 200$ and $MC = 100$, it can be observed how the ratio has increased. In this sense, the ratio depends on the N_{incoh}, increasing with it. Figure 6.43 can be useful to understand this issue. If the signal will be fully uncorrelated the SNR will increase proportionally to $\sqrt{N_{incoh}}$, as occurs in the area where the thermal noise is dominating (blue line in Fig. 6.43). On the other hand the increase in the part of the waveform dominated by speckle noise is not proportional to $\sqrt{N_{incoh}}$. Therefore, as measure that $\sqrt{N_{incoh}}$ increases

the ratio increases. This issue can be clearly identified on Fig. 6.43 (all this study has been introduced previously in Chapter 3). In any case, the most important issue is that the ratio is following the trend of the coherence time, and thus it can be related to the significant wave height. In the same way, similar results are obtained for the cGNSS-R case.

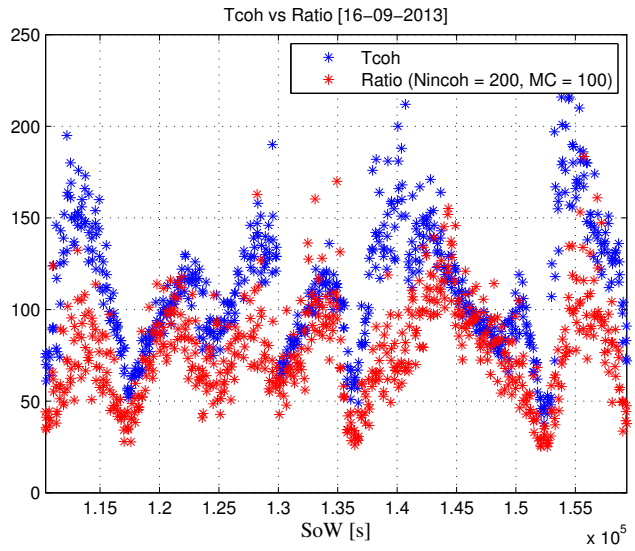

Figure 6.42: Tcoh vs Ratio between the number of incoherent averages and the effective number of incoherent averages, for a $N_{incoh} = 200$ and $MC = 100$.

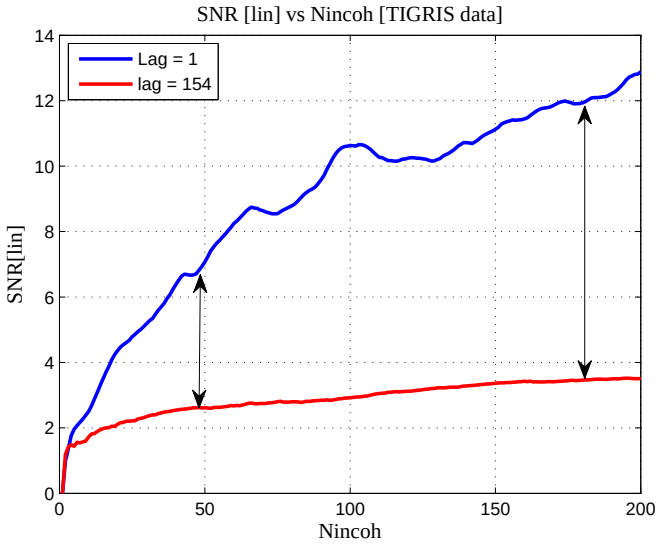

Figure 6.43: SNR for Lags 1 and 154.

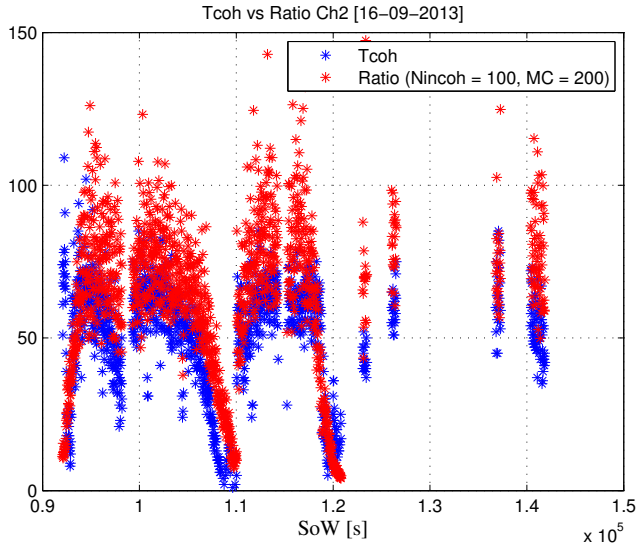

Figure 6.44: Tcoh vs Ratio between the number of incoherent averages and the effective number of incoherent averages, for a $N_{incoh} = 100$ and $MC = 200$, for the GOLD-RTR receiver using the channel 2.

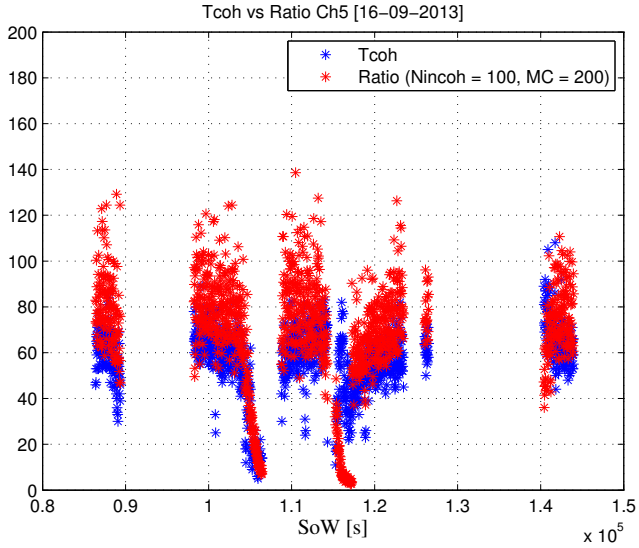

Figure 6.45: Tcoh vs Ratio between the number of incoherent averages and the effective number of incoherent averages, for a $N_{incoh} = 200$ and $MC = 100$ for the GOLD-RTR receiver using the channel 5.

To finish, Fig. 6.46 shows the evolution of the Ratio between the number of incoherent averages and the effective number of incoherent averages (for a $N_{incoh} = 100$ and $MC = 200$) for the GPS-SAT ID 12, and the coherence time for the same satellite, during USAGIs period. As it can be appreciated, both observables show

similar trends. Hence, from these results, it can be concluded that the Ratio between the number of incoherent averages and the effective number of incoherent averages, can be used as an alternative to the coherence time. One of the advantages that this method presents is that for the cGNSS-R case, it is not necessary compensate the navigation bit.

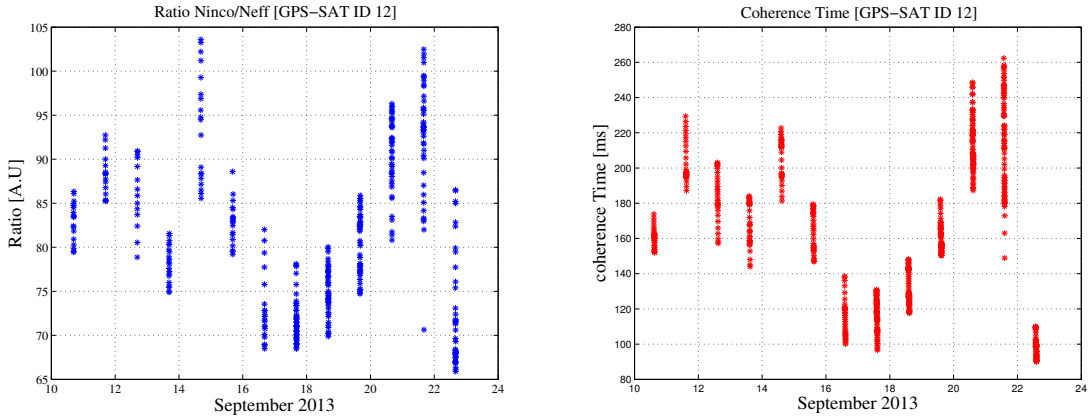

Figure 6.46: (a) Ratio evolution computed for GPS-SAT ID 12, (b) Tcoh evolution computed for GPS-SAT ID 12.

6.5 Conclusions

This Chapter has presented the preliminary results obtained for the TIGRIS experiment using the iGNSS-R technique. From those, two peculiarities has been identified. For one hand, a direct signal contamination as a consequence of the geometry of the scenario (receiver altitude equal to around 121m), which has been mitigated using the variance instead of the incoherent averaging. On the other hand, a contamination caused from others GNSS signals that are on field of view of the receiver. In this case a proper computation of the geometry becomes critical. By means the geometry is possible to identify the impact that has the different GNSS signals on the resultant power waveform. In addition, the geometry should be considered, in order to determine the impact that has on the end results, since as it has been showed in this chapter, the main observables (i.e. amplitude of the power waveform, specular delay, or coherence time) are dependent on the geometry.

Initial results computed for the iGNSS-R, shows that the Waveform peak amplitude is inversely proportional to wind speed. On the other hand, the coherence time obtained decreases with increasing the Significant Wave Height. Similar results has

been obtained for the cGNSS-R case, confirming thus the feasibility of the GNSS-R technique for monitoring typhoons.

To finish a novel observable based on the Ratio between the number of incoherent averages and the effective number of incoherent averages has been proposed as an alternative observable to infer the coherence time of the sea surface. Initial results shows a similar behavior with respect to the coherence time. Therefore, this new observable can be related to the Significant Wave Height.

Chapter 7

Summary, conclusions, and future work

This PhD dissertation, has analysed the boundaries of the GNSS-R technique to perform ocean mesoscale altimetry, where a wide variety of parameters concerning the overall observation system, including instrument, on-board and on-ground processing aspects have been addressed.

Hece, a comprehensive analysis of the GNSS-R cross-correlation waveform properties has been done. From it, an initial better performance of the iGNSS-R has been identified, due to the ACF of the L1 composite signal, which is much narrower than the C/A code alone, obtaining as a consequence a steeper power waveform. In this sense, the bandwidth plays an importat role, since as the bandwidth is reduced, the ACF becomes wider, and the waveform shape approximates to the conventional GNSS-R using the C/A code.In addition a bias in the peak derivative is produced (which starts to be relevant at 10 MHz (20 MHz in RF)), and a reduction in its amplitude. Regarding to the bias that the wind speed introduces, this is quite small, even more if it is compared to the one obtained by the receiver bandwidth.

Thermal and speckle noises have also been analysed for both the interferometric and conventional processing, using real measurements from UK-DMC and PIT-POC data. From it has been stablished that fot airborne scenarios the thermal noise is not a limiting factor (the system is not limited by thermal SNR, due to the very low height of the receiver $\sim$3 km). On the other hand, it has been verified that the speckle noise correlation is about 1 ms for the cGNSS-R technique, considering an altitude of 700 km, whereas for an altitude of 3 km, the speckle noise has been estimated to be about 6 ms for both cGNSS-R and iGNSS-R.

Detailed analytical model of the correlation between samples within a GNSS-R waveform (fast-time correlation), including complex and power waveforms, and

covering both the cGNSS-R and iGNSS-R techniques, has been also addressed in this PhD work. Hence, a theoretical derivation of the model has been described in detail and validated against real data from the UK-DMC, PIT-POC second flight and TIGRIS experiment. The model was found to be in very good agreement with real observations, with errors well within 10%. The availability of such detailed covariance model has been used to assess the performance of a GNSS-R spaceborne altimeter, as a function of important system parameters, using the statistics of the signal.

Hence, the Cramer-Rao Bound has been used to evaluate the performance model of the altimetry precision for a wide variety of parameters concerning the overall observation system, including instrument, on-board and on-ground processing aspects, for both the cGNSS-R and the iGNSS-R techniques.

From this analysis, it has been shown that in order to ensure marginal performance degradation, the RF bandwidth shall be at least 10 MHz for the case of GPS C/A code signal, and ideally 40 MHz for the L1 composite signal (20 MHz in the worst case). Concerning the sampling frequency, it can be concluded that, as general rule, it shall be at least the same as the RF bandwidth in order to not cause performance degradation. Therefore, larger values of sampling frequency are not bringing any additional performance improvement.

Concerning the on-ground processing, it has been shown that a minimum tracking-window width comparable to the width of the Auto-Correlation Function is sufficient to guarantee a good performance, centering it around the specular point.

On the other hand, it has been shown that the SNR is a critical parameter, and its impact over the altimetry performance can be approximated by an exponential function. In this sense, is important to remark, that for a low SNRs a small increase of SNR gives a large improvement in performance, whereas for higher values, the improvement achieved increasing the SNR is marginal.

Regarding to the geometry, it has been shown that the altimetry performance decreases with the receiver altitude, being this impact a bit higher in the iGNSS-R than in the cGNSS-R. In the same way, the incidence angle tends to reduce the altimetry performance, but the impact is lower that the one due to the receiver altitude. On the other hand the impact of the wind speed is not critical, even more if it is compared with to the impact that the receiver bandwidth or altitude have.

To finish, an initial estimation of the altimetric performance has been derived for both the cGNSS-R and iGNSS-R considering a spaceborne case, where a better performance has been obtained for the interferometric case (an improvement of about 3.25 time has been obtained).

Therefore, considering the analysis here conducted, an initial iGNSS-R mission (considering the composite L1 GPS signals) could be defined according to the system parameters sumarized on table 7.1.

Table 7.1: Simulation System Parameters

Parameter	**Value**	**Unit**
Receiver altitude	700	km
Receiver velocity	7.5	km/s
Incidence angle (θ_i)	0	deg
Antenna Gain (G)	22	dBi
System Noise Temperature (T_{sys})	450	k
Receiver Bandwidth (BW)	24	MHz
Coherent Int. Time (T_c)	1	ms

Ending an analysis of experimental data from the Typhoon Investigation using GNSS-R Interferometric Signals (TIGRIS) experiment has been performed. Initial results computed for the iGNSS-R, shows that the Waveform peak amplitude is inversely proportional to wind speed. On the other hand, the coherence time obtained decreases with increasing the Significant Wave Height. Similar results has been obtained for the cGNSS-R case, confirming thus the feasibility of the GNSS-R technique for monitoring typhoons.

In addition, an alternative method to the incoherent averaging based on the computation of the variance has been proposed as an effective method to mitigate the direct signal contamination that can be present in some scenarios, and a novel observable based on the Ratio between the number of incoherent averages, and the effective number of incoherent averages has been proposed as an alternative observable to infer the coherence time of the sea surface. Initial results have shown a similar behavior with respect to the coherence time.

As a future work, the analytical proposed model based on the statistics of the signal, can be also adopted to analyse the correlation properties of delay-Doppler Maps (DDM), and to evaluate the benefit of using the full DDM for altimetry applications. The presented method could also be used to assess the performance of other GNSS-R applications such as scatterometry or soil moisture retrieval.

On the other hand, the analysis based on the Cramer-Rao Bound has been conducted considering θ as an scalar parameter. The computation of the Cramer-Rao Bound, can be repeated considering θ a vector parameter. In addition, the analysis performed, can extended to Galileo signals, or to alternative GNSS-R approaches, as for example the partially interferometric processing [70].

Appendix A

cGNSS-R complex cross-correlation

In this appendix, the computation of the complex cross-correlation statistics is performed. It will be performed for the conventional GNSS-R case, where the received ocean scattered GNSS Signal is cross-correlated with a clean replica generated onboard the satellite.

A.1 Complex Cross-Correlation

A.1.1 Signal Voltage Cross-Correlation

Defining the received direct signal ($s_{d,c}$) and the received reflected signal ($s_{r,c}$) as,

$$s_{d,c} = 2u(t - T_s)e^{j\varphi_o}e^{j2\pi f_s(t-T_s)}, \tag{A.1}$$

$$s_{r,c} = \sqrt{2}\int_{\theta,\varphi} W_{\theta,\varphi,t}u(t - \tau_{r,\theta,\varphi,t})e^{-j2\pi f_o\tau_{r,\theta,\varphi,t}}e^{j\varphi_o}d\Omega, \tag{A.2}$$

the signal voltage cross-correlation $Y_s(t,\tau)$, can be computed as,

$$\begin{aligned}
Y_s(t,\tau) =& \frac{1}{T_c}\int_{-T_c/2}^{T_c/2} s_{[}r,c](t+t')s^*_{d,c}(t+t'-\tau)dt' \\
=& \frac{1}{t_c}\int_{-T_c/2}^{T_c/2}\sqrt{2}\int_{\theta,\varphi} W_{\theta,\varphi,t+t'}u(t+t'-\tau_{r,\theta,\varphi,t+t'})e^{-j2\pi f_o\tau_{r,\theta,\varphi,t+t'}}e^{j\varphi_o}d\Omega \\
& \cdot\sqrt{2}u^*(t+t'-\tau-T_s)e^{-j\varphi_o}e^{j2\pi f_s(t+t'-\tau-T_s)}dt' \\
=& \frac{2}{T_c}\int_{-T_c/2}^{T_c/2}\int_{\theta,\varphi} W_{\theta,\varphi,t+t'}u(t+t'-\tau_{r,\theta,\varphi,t+t'})u^*(t+t'-\tau-T_s) \\
& \cdot e^{-j2\pi f_o\tau_{r,\theta,\varphi,t+t'}}e^{-j2\pi f_s(t+t'-\tau-T_s)}dt'd\Omega.
\end{aligned} \tag{A.3}$$

Assuming that:

$$W_{\theta,\varphi,t+t'} \approx W_{\theta,\varphi,t},$$
$$\tau_{r,\theta,\varphi,t+t'} \approx \tau_{r,\theta,\varphi,t} - \frac{f_{Dr,\theta,\varphi,t}}{f_o}t', \tag{A.4}$$

where $f_{Dr,\theta,\varphi,t}$ is the Doppler frequency of the generic reflecting path impinging the sea surface at position (θ,φ) and received at the receiver satellite at time t_s, Equ. (A.3) becomes

$$\begin{aligned} Y_s(t,\tau) =& \frac{2}{T_c}\int_{\theta,\varphi,t}\int_{-T_c/2}^{T_c/2} ut+t'-\tau_{r,\theta,\varphi,t+t'}u(t+t'-\tau-T_s) \\ & \cdot e^{-j2\pi f_o(\tau_{r,\theta,\varphi,t}-\tau_{r,\theta,\varphi,t}-\frac{f_{Dr,\theta,\varphi,t}}{f_o}t')}e^{-j2\pi f_s t' dt'}e^{-j2\pi f_s(t-\tau-T_s)}d\Omega \\ =& \frac{2}{T_c}\int_{\theta,\varphi}\int_{-T_c/2}^{T_c/2} u(t+t'-\tau_{r,\theta,\varphi,t+t'})u^*(t+t'-\tau-T_s) \\ & \cdot e^{-j2\pi f_o\tau_{r,\theta,\varphi,t}}e^{j2\pi(f_{Dr,\theta,\varphi,t}-f_s)t'}e^{-j2\pi f_s(t-\tau-T_s)}d\Omega. \end{aligned} \tag{A.5}$$

Considering that the WAF ($\chi(\Delta\tau,\Delta f,t)$) is defined as:

$$\chi(\Delta\tau,\Delta f,t) = \frac{1}{T_c}\int_{-T_c/2}^{T_c/2} u(t+t')u(t+t'-\Delta\tau)e^{-j2\pi\Delta f t'}dt' \tag{A.6}$$

where:

$$\begin{aligned} \Delta\tau =& -\tau_{r,\theta,\varphi,t}-(-\tau-T_s) = -\tau_{r,\theta,\varphi,t}+\tau+T_s \\ \Delta f =& -(f_{Dr,\theta,\varphi,t}-f_s) = -f_{Dr,\theta,\varphi,t}+f_s, \end{aligned} \tag{A.7}$$

Equatio (A.5) can be rewritten as:

$$Y_s(t,\tau) = 2\int_{\theta,\varphi} W_{\theta,\varphi,t}\chi(\Delta\tau,\Delta f,t)e^{-j2\pi f_o\tau_{r,\theta,\varphi,t}}e^{-j2\pi f_s(t-\tau-T_s)}d\Omega. \tag{A.8}$$

A.1.2 Direct Signal and Down-Looking Noise Voltage Cross-Correlation

Considering Eqn. (A.1) and the thermal noise introduced by the receiver in the down-looking chain ($n_{r,c} = n_r(t)e^{j\varphi_o}e^{-j2\pi f_o t}$), the direct signal and down-looking noise voltage cross-correlation $Y_{Nr}(t,\tau)$, can be performed as,

$$Y_{Nr}(t,\tau) = \frac{1}{T_c}\int_{-T_c/2}^{T_c/2} n_{r,c}(t+t')s^*_{d,c}(t+t'-\tau)dt'$$

$$= \frac{1}{T_c}\int_{-T_c/2}^{T_c/2} n_{r,c}(t+t')e^{j\varphi_o}e^{-j2\pi f_o(t+t')}\sqrt{2}u^*(t+t'-\tau-T_s)e^{-j\varphi_o}e^{-j2\pi f_s(t+t'-\tau-T_s)}dt'$$

$$= \frac{\sqrt{2}}{T_c}\int_{-T_c/2}^{T_c/2}\int_{-T_c/2}^{T_c/2} n_{r,c}(t+t')e^{-j2\pi f_o(t+t')}u^*(t+t'-\tau-T_s)e^{-j2\pi f_s(t+t'-\tau-T_s)}dt'. \tag{A.9}$$

A.2 Complex Cross-Correlation Statistics

Considering that the signal and the down-looking thermal noise component are uncorrelated, the statistics at the correlator output can be represented as:

$$\langle Y(\tau_1)Y^*(\tau_2)\rangle = \langle Y_s(\tau_1)Y_s^*(\tau_2)\rangle + \langle Y_{Nr}(\tau_1)Y_{Nr}^*(\tau_2)\rangle\,, \tag{A.10}$$

where $\tau_1 = \tau$ and $\tau_2 = \tau + \tilde{\tau}$.

A.2.1 Signal-Times-Signal Statistics

Taking Eqn. (A.8), the signal-times-signal statistics can be performed as,

$$\begin{aligned}\langle Y_s(\tau)Y_s^*(\tau+\tilde{\tau})\rangle \\ =&\Big\langle 2\int_{\theta_i\varphi_i} W_{i,t}\chi(\Delta\tau,\Delta f,t)e^{-j2\pi f_o\tau_{r,i,t}}e^{-j2\pi f_s(t-\tau-T_s)}d\Omega_i \\ &\cdot 2\int_{\theta_j\varphi_j} W_{j,t}^*\chi^*(\Delta\tau,\Delta f,t)e^{j2\pi f_o\tau_{r,j,t}}e^{j2\pi f_s(t-\tau-\tilde{\tau}-T_s)}d\Omega_j\Big\rangle,\end{aligned} \tag{A.11}$$

where the dependence on the spatial coordinates θ_i, φ_i and θ_j, φ_j has been expressed by subscripts i and j. Applying the statistical average inside the spatial integrals Eqn. (A.11) becomes:

$$\begin{aligned}\langle Y_s(\tau)Y_s^*(\tau+\tilde{\tau})\rangle \\ =&4\int_{\theta_i\varphi_i}\int_{\theta_j\varphi_j}\Big\langle W_{i,t}W_{j,t}^*\chi(\Delta\tau,\Delta f,t)\chi^*(\Delta(\tau+\tilde{\tau}),\Delta f,t) \\ &\cdot e^{-j2\pi f_o(\tau_{r,j,t}-\tau_{r,i,t})}\Big\rangle e^{j2\pi f_s(-\tilde{\tau})}d\Omega_i d\Omega_j,\end{aligned} \tag{A.12}$$

Considering that the height is spatially uncorrelated for any point of the surface $(\theta_i, \varphi_i) \neq (\theta_j, \varphi_j)$, and that the spatial integrals are nonnegligible only for $(\theta_i, \varphi_i) = (\theta_j, \varphi_j)$, Eqn. (A.12) becomes,

$$\begin{aligned}\langle Y_s(\tau)Y_s^*(\tau+\tilde{\tau})\rangle =&4\int_{\theta,\varphi}\left\langle W_{\theta,\varphi,t}W_{\theta,\varphi,t}^*\right\rangle\chi(\Delta\tau,\Delta f,t)\chi^*(\Delta(\tau+\tilde{\tau}),\Delta f,t)e^{-j2\pi f_s\tilde{\tau}}d\Omega \\ =&4\left\langle W_{\theta,\varphi,t}W_{\theta,\varphi,t}^*\right\rangle\chi(\Delta\tau,\Delta f,t)\chi^*(\Delta(\tau+\tilde{\tau}),\Delta f,t)e^{-j2\pi f_s\tilde{\tau}}d\Omega,\end{aligned} \tag{A.13}$$

A.2.2 Down-Looking Noise-Times Signal Statistics

Taking Eqn. (A.9) the down-looking noise-times-signal statistics can be performed as:

$$\begin{aligned}\left\langle Y_{Nr}(\tau)Y_{Nr}^{*}(\tau+\tilde{\tau})\right\rangle =&\Big\langle\frac{\sqrt{2}}{T_c}\int_{-T_c/2}^{T_c/2} n_r(t+t')u^{*}(t+t'-\tau-T_s)\\ &\cdot e^{-j2\pi f_o(t+t')}e^{-j2\pi f_s(t+t'-\tau-T_s)}dt'\\ &\cdot\frac{\sqrt{2}}{T_c}\int_{-T_c/2}^{T_c/2} n_r^{*}(t+t'')u(t+t''-\tau-\tilde{\tau}-T_s)\\ &\cdot e^{j2\pi f_o(t+t'')}e^{j2\pi f_s(t+t''-\tau-\tilde{\tau}-T_s)}dt''\Big\rangle\\ =&\frac{2}{T_c^2}\int_{-T_c/2}^{T_c/2}\int_{-T_c/2}^{T_c/2}\Big\langle n_r(t+t')n_r^{*}(t+t'')\\ &\cdot u^{*}(t+t'-\tau-T_s)u(t+t''-\tau-\tilde{\tau}-T_s)\\ &\cdot e^{-j2\pi f_o(t+t')}e^{-j2\pi f_s(t+t'-\tau-T_s)}dt'\\ &\cdot e^{j2\pi f_o(t+t'')}e^{j2\pi f_s(t+t''-\tau-\tilde{\tau}-T_s)}dt''\Big\rangle,\end{aligned}\tag{A.14}$$

where the band-limited noise can be expressed as:

$$\langle nr(t+t')n_r^{*}(t+t'')\rangle = 2kT_{Nr}\frac{\sin(2\pi B(t+t''))}{\pi(t+t''}.\tag{A.15}$$

Replacing Eqn. (A.15) on Eqn. (A.14) and considering that $BT_c \gg 1$ the noise ACF can be simplified to a Dirac delta function. Thus, Eqn. (A.14) becomes:

$$\begin{aligned}\left\langle Y_{Nr}(\tau)Y_{Nr}^{*}(\tau+\tilde{\tau})\right\rangle =&\frac{2}{T_c^2}\Big\langle 2kT_{Nr}\int_{-T_c/2}^{T_c/2} u^{*}(t+t'-\tau-T_s)u(t-\tau-\tilde{\tau}-T_s)\\ &\cdot e^{-j2\pi f_o(t+t')}e^{-j2\pi f_s(t+t'-\tau-T_s)}\\ &\cdot e^{j2\pi f_o(t+t')}e^{j2\pi f_s(t+t'-\tau-\tilde{\tau}-T_s)}\Big\rangle dt'\\ =&\frac{4}{T_c}\Big\langle kT_{Nr}\frac{1}{T_c}\int_{-T_c/2}^{T_c/2} u^{*}(t+t'-\tau-T_s)u(t-\tau-\tilde{\tau}-T_s)\\ &\cdot e^{-j2\pi f_s\tilde{\tau}}\Big\rangle dt',\end{aligned}\tag{A.16}$$

Equation (A.16) can be expressed as a function of the WAF at $\Delta f = 0$, which can be approximate by the function triangle function ($\Lambda(\Delta\tau)$),

$$\left\langle Y_{Nr}(\tau)Y_{Nr}^{*}(\tau+\tilde{\tau})\right\rangle = \frac{2}{T_c}2kT_{Nr}\Lambda(\Delta\tau)e^{-j2\pi f_s\tilde{\tau}},\tag{A.17}$$

Appendix B

iGNSS-R complex cross-correlation

In this appendix, the computation of the complex cross-correlation statistics is performed for the interferometric GNSS-R case, where the received ocean scattered GNSS Signal is cross-correlated with the received direct signal.

B.1 Complex Cross-Correlation

B.1.1 Signal Voltage Cross-Correlation

Defining the received direct signal ($s_{d,c}$) and the received reflected signal ($s_{r,c}$) as,

$$s_{d,c}(t) = \sqrt{2}A_d u(t - \tau_d - T_s)e^{-j2\pi f_o \tau_d} e^{j\phi_o} e^{j2\pi f_s (t-T_s)}, \tag{B.1}$$

$$s_{r,c} = \sqrt{2}\int_{\theta,\varphi} W_{\theta,\varphi,t} u(t - \tau_{r,\theta,\varphi,t}) e^{-j2\pi f_o \tau_{r,\theta,\varphi,t}} e^{j\varphi_o} d\Omega, \tag{B.2}$$

the signal voltage cross-correlation $Y_s(t,\tau)$, can be computed as,

$$\begin{aligned}
Y_s(t,\tau) =& \frac{1}{T_c}\int_{-\frac{T_c}{2}}^{\frac{T_c}{2}} s_{r,c}(t+t')s^*_{d,c}(t+t'-\tau)dt' \\
=& \frac{1}{T_c}\int_{-\frac{T_c}{2}}^{\frac{T_c}{2}} \sqrt{2}\int_{\theta,\phi} W_{\theta,\phi,t+t'} u(t+t'-\tau_{r,\theta,\phi,t+t'}) \\
& \cdot e^{j2\pi f_o (t+t'-\tau_{r,\theta,\phi,t+t'})} e^{j\phi_o} e^{-j2\pi f_o (t+t')} d\Omega \\
& \cdot \sqrt{2}A_d u^*(t+t'-\tau-\tau_{d,t+t'-\tau-T_s}) \\
& \cdot e^{j2\pi f_o \tau_{d,t+t'-\tau}} e^{-j\phi_o} e^{-j2\pi f_s (t+t'-\tau-T_s)} dt' \\
=& \frac{2A_d}{T_c}\int_{-\frac{T_c}{2}}^{\frac{T_c}{2}} \int_{\theta\phi} W_{\theta,\phi,t+t'} u(t+t'-\tau_{r,\theta,\phi,t+t'}) u^*(t+t'-\tau-\tau_{d,t+t'-\tau-T_s}) \\
& \cdot e^{j2\pi f_o (t+t'-\tau_{r,\theta,\phi,t+t'})} e^{-j2\pi f_o (t+t')} e^{j2\pi f_o \tau_{d,t+t'-\tau}} e^{-j2\pi f_s (t+t'-\tau-T_s)} dt' d\Omega,
\end{aligned} \tag{B.3}$$

where it can be assumed that

$$\begin{aligned} W_{\theta,\phi,t+t'} &\sim W_{\theta,\phi,t} \\ \tau_{r,\theta,\phi,t+t'} &\sim \tau_{r,\theta,\phi,t} - \frac{f_{Dr,\theta,\phi}}{f_o}t' \\ \tau_{d,t+t'-\tau} &\sim \tau_{d,t+t'-\tau} - \frac{f_{Dr,t-\tau}}{f_o}t' \end{aligned} \tag{B.4}$$

thus Eqn.(B.3) can be rewritte as:

$$\begin{aligned} Y_s(t,\tau) =& \frac{2A_d}{T_c}\int_{-\frac{T_c}{2}}^{\frac{T_c}{2}}\int_{\theta\phi} W_{\theta,\phi,t+t'}u(t+t'-\tau_{r,\theta,\phi,t+t'})u^*(t+t'-\tau-\tau_{d,t+t'-\tau-T_s}) \\ &\cdot e^{j2\pi f_o(t+t'-\tau_{r,\theta,\phi,t}-\frac{f_{Dr,\theta,\phi}}{f_o}t')}e^{j2\pi f_o(t+t')} \\ &\cdot e^{j2\pi f_o(\tau_{d,t-\tau}-\frac{f_{Dd,t-\tau}}{t_o}t')}e^{-j2\pi f_s(t+t'-\tau-T_s)}dt'd\Omega \end{aligned} \tag{B.5}$$

from Eqn.(B.5)

$$\begin{aligned} \chi(\Delta\tau,\Delta f,t) \approx& \frac{1}{T_c}\int_{-\frac{T_c}{2}}^{\frac{T_c}{2}} u(t+t'-\tau_{r,\theta,\phi,t+t'})u^*(t+t'-\tau-\tau_{d,t+t'-\tau-T_s}) \\ &\cdot e^{j2\pi(f_{Dr,\theta,\phi}-f_{Dd,})t'}e^{-j2\pi f_s t'}dt' \end{aligned} \tag{B.6}$$

where

$$\begin{aligned} \Delta\tau &= -\tau_{r,\theta,\phi,t} + \tau + \tau_{d,t+-\tau} + T_s, \\ \Delta f &= f_{Dr,\theta,\phi} - f_{Dd,} + f_s, \end{aligned} \tag{B.7}$$

Hence Eqn.(B.5) becomes,

$$Y_s(t,\tau) = 2A_d\int_{\theta\phi} W_{\theta,\phi,t}\chi(\Delta\tau,\Delta f,t)e^{j2\pi f_o(\tau_{d,t-\tau}-\tau_{r,\theta,\phi})}e^{-j2\pi f_s(t-\tau-T_s)}d\Omega. \tag{B.8}$$

B.1.2 Reflected Signal and Up-looking Noise Voltage Cross-Correlation

Considering Equ.(B.2) and the thermal noise introduced by the receiver in the up-looking chain ($n_{d,c} = n_d(t-T_s)e^{j\phi_o}e^{-j2\pi(f_o-f_s)(t-T_s)}$), the reflected signal and up-

looking noise voltage cross-correlation $Y_{Nd}(t,\tau)$, can be performed as:

$$\begin{aligned}
Y_{Nd}(t,\tau) =& \frac{1}{T_c}\int_{-\frac{T_c}{2}}^{\frac{T_c}{2}} s_{r,c}(t+t')n_{d,c}^*(t+t'-\tau)dt' \\
=& \frac{\sqrt{2}}{T_c}\int_{-\frac{T_c}{2}}^{\frac{T_c}{2}}\int_{\theta,\phi} W_{\theta,\phi,t+t'}u(t+t'-\tau_{r,\theta,\phi,t+t'})e^{j2\pi f_o(t+t'-\tau_{r,\theta,\phi,t+t'})}e^{j\phi_o}e^{-j2\pi f_o(t+t')}d\Omega \\
& \cdot n_d^*(t+t'-\tau-T_s)e^{-j\phi_o}e^{j2\pi(f_o-f_s)(t+t'-\tau-T_s)}dt' \\
=& \frac{\sqrt{2}}{T_c}\int_{\theta,\phi} W_{\theta,\phi,t+t'}\int_{-\frac{T_c}{2}}^{\frac{T_c}{2}} u(t+t'-\tau_{r,\theta,\phi,t+t'})e^{j2\pi f_o(-\tau_{r,\theta,\phi,t}+\frac{f_{Dr,\theta,\phi}}{f_o}t')}d\Omega \\
& \cdot e^{-j2\pi f_o\tau_{r,\theta,\phi,t}}e^{j2\pi(f_o-f_s)(t-\tau-T_s)}d\Omega.
\end{aligned} \tag{B.9}$$

B.1.3 Direct Signal and Down-looking Noise Voltage Cross-Correlation

Considering Equ.(B.1) and the thermal noise introduced by the receiver in the down-looking chain ($n_{r,c} = n_r(t)e^{j\phi_o}e^{-j2\pi f_o t}$), the direct signal and down-looking noise voltage cross-correlation $Y_{Nr}(t,\tau)$, can be performed as,

$$\begin{aligned}
Y_{Nr}(t,\tau) =& \frac{1}{T_c}\int_{-\frac{T_c}{2}}^{\frac{T_c}{2}} n_{r,c}(t+t')s_{d,c}^*(t+t'-\tau)dt' \\
=& \frac{\sqrt{2}A_d}{T_c}\int_{-\frac{T_c}{2}}^{\frac{T_c}{2}} n_r(t+t')e^{j\phi_o}e^{-j2\pi f_o(t+t')} \\
& \cdot u^*(t+t'-\tau-\tau_{d,t+t'-\tau})e^{j2\pi f_o\tau_{d,t+t'-\tau}}e^{-j\phi_o}e^{-j2\pi f_s(t+t'-\tau-T_s)}dt' \\
=& \frac{\sqrt{2}A_d}{T_c}\int_{-\frac{T_c}{2}}^{\frac{T_c}{2}} n_r(t+t')u^*(t+t'-\tau-\tau_{d,t+t'-\tau}) \\
& \cdot e^{-j2\pi f_o(t+t')}e^{j2\pi f_o\tau_{d,t+t'-\tau}}e^{-j2\pi f_s(t+t'-\tau-T_s)}dt'.
\end{aligned} \tag{B.10}$$

B.1.4 Up-looking Noise and Down-looking Noise Voltage Cross-Correlation

Considering the thermal noise introduced by the receiver in both chains, the up-looking signal and down-looking noise voltage cross-correlation $Y_{Ndr}(t,\tau)$, can be

performed as,

$$\begin{aligned} Y_{Ndr}(t,\tau) &= \frac{1}{T_c}\int_{-\frac{T_c}{2}}^{\frac{T_c}{2}} n_{r,c}(t+t')n^*_{d,c}(t+t'-\tau-T_s)dt' \\ &= \frac{1}{T_c}\int_{-\frac{T_c}{2}}^{\frac{T_c}{2}} n_r(t+t')e^{j\phi_o}e^{-j2\pi f_o(t+t')} \\ &\cdot n^*_d(t+t'-\tau-T_s)^* e^{-j\phi_o}e^{j2\pi(f_o-f_s)(t+t'-\tau-T_s)}dt' \\ &= \frac{1}{T_c}\int_{-\frac{T_c}{2}}^{\frac{T_c}{2}} n_r(t+t')n^*_d(t+t'-\tau-T_s) \\ &\cdot e^{-j2\pi f_o(t+t')}e^{j2\pi(f_o-f_s)(t+t'-\tau-T_s)}dt'. \end{aligned} \tag{B.11}$$

B.2 Complex Cross-Correlation Statistics

The complex waveform at the output of the correlator can be expressed as:

$$Y(t,\tau) = Y_s(t,\tau) + Y_{Nr}(t,\tau) + Y_{Nd}(t,\tau) + Y_{Ndr}(t,\tau) \tag{B.12}$$

From Eqn.B.12 the statistics at the output of the cross-correlator are given by:

$$\begin{aligned} \big\langle Y(\tau)Y^*(\tau+\tilde{\tau})\big\rangle =& \big\langle (Y_s(t,\tau) + Y_{Nr}(t,\tau) + Y_{Nd}(t,\tau) + Y_{Ndr}(t,\tau)) \\ & (Y_s(t,\tau)^* + Y^*_{Nr}(t,\tau) + Y^*_{Nd}(t,\tau) + Y^*_{Ndr}(t,\tau))\big\rangle \\ =& \big\langle Y_s(\tau)Y^*_s(\tau+\tilde{\tau})\big\rangle + \big\langle Y_s(\tau)Y^*_{nr}(\tau+\tilde{\tau})\big\rangle \\ & + \big\langle Y_s(\tau)Y^*_{Nd}(\tau+\tilde{\tau})\big\rangle + \big\langle Y_s(\tau)Y^*_{Ndr}(\tau+\tilde{\tau})\big\rangle \\ & + \big\langle Y_{Nr}(\tau)Y^*_s(\tau+\tilde{\tau})\big\rangle + \big\langle Y_{Nr}(\tau)Y^*_{Nr}(\tau+\tilde{\tau})\big\rangle \\ & + \big\langle Y_{Nr}(\tau)Y^*_{Nd}(\tau+\tilde{\tau})\big\rangle + \big\langle Y_{Nr}(\tau)Y^*_{Ndr}(\tau+\tilde{\tau})\big\rangle \\ & + \big\langle Y_{Nd}(\tau)Y^*_s(\tau+\tilde{\tau})\big\rangle + \big\langle Y_{nr}(\tau)Y^*_{Nd}(\tau+\tilde{\tau})\big\rangle \\ & + \big\langle Y_{Nd}(\tau)Y^*_{Nd}(\tau+\tilde{\tau})\big\rangle + \big\langle Y_{nd}(\tau)Y^*_{Ndr}(\tau+\tilde{\tau})\big\rangle \\ & + \big\langle Y_{Ndr}(\tau)Y^*_s(\tau+\tilde{\tau})\big\rangle + \big\langle Y_{Nr}(\tau)Y^*_{Ndr}(\tau+\tilde{\tau})\big\rangle \\ & + \big\langle Y_{Ndr}(\tau)Y^*_{Nd}(\tau+\tilde{\tau})\big\rangle + \big\langle Y_{Ndr}(\tau)Y^*_{Ndr}(\tau+\tilde{\tau})\big\rangle. \end{aligned} \tag{B.13}$$

Considering that the signal and the up- and down-looking thermal noises components are uncorrelated to each other, Eqn.(B.14) can be expressed as,

$$\begin{aligned} \big\langle Y(\tau)Y^*(\tau+\tilde{\tau})\big\rangle =& \big\langle Y_s(\tau)Y^*_s(\tau+\tilde{\tau})\big\rangle + \big\langle Y_{nr}(\tau)Y^*_{nr}(\tau+\tilde{\tau})\big\rangle \\ & + \big\langle Y_{nd}(\tau)Y^*_{nd}(\tau+\tilde{\tau})\big\rangle + \big\langle Y_{ndr}(\tau)Y^*_{ndr}(\tau+\tilde{\tau})\big\rangle, \end{aligned} \tag{B.14}$$

B.2.1 Signal-Times-Signal Statistics

Taking Eqn.(B.8), the signal-times-signal statistics can be written as,

$$\begin{aligned}\left\langle Y_s(\tau)Y_s^*(\tau+\tilde{\tau})\right\rangle =&\Big\langle 2A_d\int_{\theta_i,\phi_i} W_{\theta_i,\phi_i,t}\chi(\Delta\tau,\Delta f,t)\\ &\cdot e^{j2\pi f_o(\tau_{d,t-\tau}-\tau_r,\theta_i,\phi_i)}e^{-j2\pi f_s(t-\tau-T_s)}d\Omega_i\\ &\cdot 2A_d\int_{\theta_j,\phi_j} W^*_{\theta_j,\phi_j,t}\chi^*(\Delta(\tau+\tilde{\tau}),\Delta f,t)\\ &\cdot e^{-j2\pi f_o(\tau_{d,t-\tau-\tilde{\tau}}-\tau_r,\theta_j,\phi_j)}e^{j2\pi f_s(t-\tau-\tilde{\tau}-T_s)}d\Omega_j\Big\rangle,\end{aligned} \tag{B.15}$$

For the sake of simplicity, the subscripts θ_i, ϕ_i and θ_j, ϕ_j will be expressed by the subscripts i, j. Thus Eqn. (B.15) becomes,

$$\begin{aligned}\left\langle Y_s(\tau)Y_s^*(\tau+\tilde{\tau})\right\rangle =&4A_d^2\int_{\theta_i,\phi_i}\int_{\theta_j,\phi_j}\left\langle W_{i,t}W^*_{j,t}\chi_{i,t}\chi^*_{j,t}e^{j2\pi f_o(\tau_{r,j,t}-\tau_{r,i,t})}\right\rangle\\ &\cdot e^{j2\pi f_o(\tau_{d,t-\tau}-\tau_{d,t-\tau-\tilde{\tau}})}e^{j2\pi f_s\tilde{\tau}}d\Omega_i d\Omega_j,\end{aligned} \tag{B.16}$$

considering,

$$\tau_{d,t-\tau-\tilde{\tau}} = \tau_{d,t-\tau} - \frac{f_{Dd,t-\tau}}{f_o}(-\tilde{\tau}), \tag{B.17}$$

Eqn. (B.16) becomes,

$$\begin{aligned}\left\langle Y_s(\tau)Y_s^*(\tau+\tilde{\tau})\right\rangle =&4A_d^2\int_{\theta_i,\phi_i}\int_{\theta_j,\phi_j}\left\langle W_{i,t}W^*_{j,t}\right\rangle\left\langle \chi_{i,t}\chi^*_{j,t}e^{j2\pi f_o(\tau_{r,j,t}-\tau_{r,i,t})}\right\rangle\\ &\cdot e^{j2\pi f_o(\tau_{d,t-\tau}-\tau_{d,t-\tau}+\frac{f_{Dd,t-\tau}}{f_o}(-\tilde{\tau}))}e^{j2\pi f_s\tilde{\tau}}d\Omega_i d\Omega_j.\end{aligned} \tag{B.18}$$

Considering that the height is spatially uncorrelated for any point of the surface $(\theta_i, \phi_i) \neq (\theta_j, \phi_j)$ and that the spatial integrals are non negligible only for $(\theta_i, \phi_i) = (\theta_j, \phi_j)$, Eqn. (B.18) reduces to,

$$\begin{aligned}\left\langle Y_s(\tau)Y_s^*(\tau+\tilde{\tau})\right\rangle =&4A_d^2\left\langle W_{\theta,\phi,t}W^*_{\theta,\phi,t}\right\rangle\chi(\Delta\tau,\Delta f,t)\chi^*(\Delta(\tau+\tilde{\tau}),\Delta f,t)\\ &\cdot e^{j2\pi(-f_{Dd,t-\tau}+f_s)\tilde{\tau}}\end{aligned} \tag{B.19}$$

assuming that $f_D \approx f_s$, Eqn. (B.19) becomes

$$\left\langle Y_s(\tau)Y_s^*(\tau+\tilde{\tau})\right\rangle = 4A_d^2\left\langle W_{\theta,\phi,t}W^*_{\theta,\phi,t}\right\rangle\chi(\Delta\tau,\Delta f,t)\chi^*(\Delta(\tau+\tilde{\tau}),\Delta f,t) \tag{B.20}$$

B.2.2 Up-looking Noise-Times-Signal Statistics

Taking Eqn.(B.9), the up-looking noise-times-signal statistics can be written as,

$$\begin{aligned}\big\langle Y_{Nd}(\tau)Y_{Nd}^*(\tau+\tilde{\tau})\big\rangle =&\big\langle \frac{\sqrt{2}}{T_c}\int_{\theta_i,\phi_i} W_{i,t}\int_{-\frac{T_c}{2}}^{\frac{T_c}{2}} u(t+t'-\tau_{r,i,t+t'})n_d^*(t+t'-\tau-T_s)\\ &\cdot e^{j2\pi(f_{Dr,i,t}+f_o-f_s)t'}dt' e^{-j2\pi f_o\tau_{r,i,t}}e^{j2\pi(f_o-f_s)(t-\tau-T_s)}d\Omega_i\\ &\cdot \frac{\sqrt{2}}{T_c}\int_{\theta_j,\phi_j} W_{j,t}^*\int_{-\frac{T_c}{2}}^{\frac{T_c}{2}} u^*(t+t''-\tau_{r,j,t+t''})n_d(t+t'-\tau-T_s)\\ &\cdot e^{-j2\pi(f_{Dr,j,t}+f_o-f_s)t''}dt'' e^{j2\pi f_o\tau_{r,j,t}}e^{j2\pi(f_o-f_s)(t-\tau-\tilde{\tau}-T_s)}d\Omega_j\big\rangle\\ =&2\int_{\theta_i,\phi_i}\int_{\theta_j,\phi_j}\big\langle W_{i,t}W_{j,t}^*\big\rangle\big\langle\frac{1}{T_c^2}\int_{-\frac{T_c}{2}}^{\frac{T_c}{2}}\int_{-\frac{T_c}{2}}^{\frac{T_c}{2}} u(t+t'-\tau_{r,i,t+t'})\\ &\cdot u^*(t+t''-\tau_{r,j,t+t''})\langle n_d^*(t+t'-\tau-T_s)n_d(t+t''-\tau-\tilde{\tau}-T_s)\rangle\\ &\cdot e^{j2\pi(f_{Dri,t}+f_o-f_s)t'}e^{-j2\pi(f_{Drj,t}+f_o-f_s)t''}dt'dt''\\ &\cdot e^{j2\pi f_o(-\tau_r i+\tau_r j)}e^{-j2\pi(f_o-f_s)(\tilde{\tau})}d\Omega_i d\Omega_j\big\rangle, \end{aligned}\tag{B.21}$$

where:

$$\big\langle n_d^*(t+t'-\tau-T_s)n_d(t+t''-\tau-\tilde{\tau}-T_s)\big\rangle = 2kT_{Nd}\frac{sin(2\pi B(t'-t''+\tilde{\tau}))}{\pi(t'-t''+\tilde{\tau})},\tag{B.22}$$

hence Eqn.(B.21) becomes,

$$\begin{aligned}\big\langle Y_{Nd}(\tau)Y_{Nd}^*(\tau+\tilde{\tau})\big\rangle =&2\int_{\theta_i,\phi_i}\int_{\theta_j,\phi_j}\big\langle W_{i,t}W_{j,t}^*\big\rangle\big\langle\frac{2kT_{Nd}}{T_c^2}\int_{-\frac{T_c}{2}}^{\frac{T_c}{2}} u(t+t'-\tau_{r,t+t'})\\ &\cdot u^*(t+t'+\tilde{\tau}-\tau_{r,t+t'})e^{j2\pi(f_{Dri}+f_o-f_s)t'}e^{-j2\pi(f_{Drj}+f_o-f_s)t'}dt'\\ &\cdot e^{j2\pi f_o(-\tau_{ri}+\tau_{rj})}e^{-j2\pi(f_o-f_s)(-\tilde{\tau})}d\Omega_i d\Omega_j\big\rangle, \end{aligned}\tag{B.23}$$

where

$$\frac{1}{T_c}\int_{-\frac{T_c}{2}}^{\frac{T_c}{2}} u(t+t'-\tau_{ri,t+t'})u^*(t+t'-\tilde{\tau}-\tau_{rj,t+t'-\tilde{\tau}})dt' = ACF(\Delta\tau),\tag{B.24}$$

thus the up-looking noise - times - signal statistics can be expressed as,

$$\big\langle Y_{Nd}(\tau)Y_{Nd}^*(\tau+\tilde{\tau})\big\rangle =2\big\langle W_{\theta\phi}W_{\theta\phi}^*\big\rangle\big\langle 2\frac{kT_{Nd}}{T_c}ACF(\tau)e^{-j2\pi(f_o-f_s)(\tilde{\tau})}\big\rangle,\tag{B.25}$$

B.2.3 Down-looking Noise-Times-Signal Statistics

Taking Eqn.(B.10), the down-looking noise-times-signal statistics can be written as,

$$\begin{aligned}\big\langle Y_{Nr}(\tau)Y_{Nr}^*(\tau+\tilde{\tau})\big\rangle =&\big\langle \frac{\sqrt{2}A_d}{T_c}\int_{-\frac{T_c}{2}}^{\frac{T_c}{2}} n_r(t+t')u^*(t+t'-\tau-\tau_{dt+t'-\tau})\\ &\cdot e^{-j2\pi f_o(t+t')}e^{j2\pi f_o\tau_{dt+t'-\tau}}e^{-j2\pi f_s(t+t'-\tau-T_s)}dt'\\ &\cdot \frac{\sqrt{2}A_d}{T_c}\int_{-\frac{T_c}{2}}^{\frac{T_c}{2}} n_r^*(t+t'')u(t+t''-\tau-\tilde{\tau}-\tau_{dt+t''-\tau-\tilde{\tau}})\\ &\cdot e^{j2\pi f_o(t+t'')}e^{-j2\pi f_o\tau_{dt+t''-\tau-\tilde{\tau}}}e^{j2\pi f_s(t+t''-\tau-\tilde{\tau}-T_s)}dt''\big\rangle\\ =&\frac{2A_d^2}{T_c^2}\big\langle \int_{-\frac{T_c}{2}}^{\frac{T_c}{2}}\int_{-\frac{T_c}{2}}^{\frac{T_c}{2}} n_r(t+t')n_r^*(t+t'')\\ &\cdot u^*(t+t'-\tau-\tau_{dt+t'-\tau})u(t+t''-\tau-\tilde{\tau}-\tau_{dt+t''-\tau-\tilde{\tau}})\\ &\cdot e^{-j2\pi f_o(t+t')}e^{j2\pi f_o\tau_{dt+t'-\tau}}e^{-j2\pi f_s(t+t'-\tau-T_s)}dt'\\ &\cdot e^{j2\pi f_o(t+t'')}e^{-j2\pi f_o\tau_{dt+t''-\tau-\tilde{\tau}}}e^{j2\pi f_s(t+t''-\tau-\tilde{\tau}-T_s)}dt''\big\rangle, \end{aligned} \tag{B.26}$$

considering

$$\big\langle n_r(t+t')n_r^*(t+t'')\big\rangle = 2kT_{Nr}\frac{sin(2\pi B(t'-t''))}{\pi(t'-t'')}, \tag{B.27}$$

Eqn. (B.26) becomes,

$$\begin{aligned}\big\langle Y_{Nr}(\tau)Y_{Nr}^*(\tau+\tilde{\tau})\big\rangle =&\frac{2A_d^2 2kT_{Nr}}{T_c}\big\langle \frac{1}{T_c}\int_{-\frac{T_c}{2}}^{\frac{T_c}{2}} u^*(t+t'-\tau-\tau_{dt+t'-\tau})\\ &\cdot u(t+t'-\tau-\tilde{\tau}-\tau_{dt+t'-\tau-\tilde{\tau}})\\ &\cdot e^{-j2\pi f_o(t+t')}e^{j2\pi f_o\tau_{dt+t'-\tau}}e^{-j2\pi f_s(t+t'-\tau-T_s)}dt'\\ &\cdot e^{j2\pi f_o(t+t')}e^{-j2\pi f_o\tau_{dt+t'-\tau-\tilde{\tau}}}e^{j2\pi f_s(t+t'-\tau-\tilde{\tau}-T_s)}dt'\big\rangle, \end{aligned} \tag{B.28}$$

where

$$\tau_{dt+t'-\tau\tilde{\tau}} = \tau_{dt+t'-\tau} - \frac{f_{Ddt-\tau}}{f_o}(-\tilde{\tau}), \tag{B.29}$$

thus Eqn.(B.28) becomes,

$$\begin{aligned}\left\langle Y_{Nr}(\tau)Y_{Nr}^{*}(\tau+\tilde{\tau})\right\rangle =&\frac{2A_d^2 2kT_{Nr}}{T_c}\Big\langle\frac{1}{T_c}\int_{-\frac{T_c}{2}}^{\frac{T_c}{2}}u^{*}(t+t'-\tau-\tau_{dt+t'-\tau})\\&\cdot u(t+t'-\tau-\tilde{\tau}-\tau_{dt+t'-\tau-\tilde{\tau}})\\&\cdot e^{j2\pi f_o\tau_{dt+t'-\tau}}e^{-j2\pi f_s(t+t'-\tau-T_s)}dt'\\&\cdot e^{-j2\pi f_o(\tau_{dt+t'-\tau}-\frac{f_{Ddt-\tau}}{f_o}(-\tilde{\tau}))}e^{j2\pi f_s(t+t'-\tau-\tilde{\tau}-T_s)}dt'\Big\rangle\\=&\frac{4A_d^2 kT_{Nr}}{T_c}\Big\langle\frac{1}{T_c}\int_{-\frac{T_c}{2}}^{\frac{T_c}{2}}u^{*}(t+t'-\tau-\tau_{dt+t'-\tau})\\&\cdot u(t+t'-\tau-\tilde{\tau}-\tau_{dt+t'-\tau-\tilde{\tau}})e^{j2\pi(f_{Ddt}-f_s)(\tilde{\tau})}dt'\Big\rangle,\end{aligned}\tag{B.30}$$

where:

$$\frac{1}{T_c}\int_{-\frac{T_c}{2}}^{\frac{T_c}{2}}u^{*}(t+t'-\tau-\tau_{dt+t'-\tau})u(t+t'-\tau-\tilde{\tau}-\tau_{dt+t'-\tau-\tilde{\tau}})dt'=ACF(\Delta\tau),\tag{B.31}$$

hence

$$\left\langle Y_{Nr}(\tau)Y_{Nr}^{*}(\tau+\tilde{\tau})\right\rangle ==\qquad\frac{4A_d^2 kT_{Nr}}{T_c}ACF(\Delta\tau)e^{j2\pi(f_{Ddt}-f_s)(\tilde{\tau})}.\tag{B.32}$$

B.2.4 Noise-Times-Noise Statistics

Taking Eqn.(B.11), the noise-times-noise statistics can be written as:

$$\begin{aligned}\left\langle Y_{Ndr}(\tau)Y_{Ndr}^{*}(\tau+\tilde{\tau})\right\rangle =&\frac{1}{T_c}\int_{-\frac{T_c}{2}}^{\frac{T_c}{2}}n_r(t+t')n_d^{*}(t+t'-\tau-T_s)\\&\cdot e^{-j2\pi f_o(t+t')}e^{j2\pi(f_o-f_s)(t+t'-\tau-T_s)}dt'\\&\cdot\frac{1}{T_c}\int_{-\frac{T_c}{2}}^{\frac{T_c}{2}}n_r^{*}(t+t'')n_d(t+t''-\tau-\tilde{\tau}-T_s)\\&\cdot e^{j2\pi f_o(t+t'')}e^{-j2\pi(f_o-f_s)(t+t''-\tau-\tilde{\tau}-T_s)}dt',\end{aligned}\tag{B.33}$$

where:

$$\left\langle n_r(t+t')n_r^{*}(t+t'')\right\rangle=2kT_{Nr}\frac{sin(2\pi B(t'-t''))}{\pi(t'-t'')},\tag{B.34}$$

and

$$\left\langle n_d^{*}(t+t'-\tau-T_s)n_d(t+t''-\tau-\tilde{\tau}-T_s)\right\rangle=2kT_{Nd}\frac{sin(2\pi B(t'-t''+\tilde{\tau}))}{\pi(t'-t''+\tilde{\tau})},\tag{B.35}$$

therefore, Eqn.(B.33) becomes,

$$\begin{aligned}\left\langle Y_{Ndr}(\tau)Y^{*}_{Ndr}(\tau+\tilde{\tau})\right\rangle =&\frac{2kT_{Nr}2kT_{Nd}}{T_c^2}\int_{-\frac{T_c}{2}}^{\frac{T_c}{2}}\int_{-\frac{T_c}{2}}^{\frac{T_c}{2}}\frac{sin(2\pi B(t'-t''))}{\pi(t'-t'')}\\ &\cdot\frac{sin(2\pi B(t'-t''+\tilde{\tau}))}{\pi(t'-t''+\tilde{\tau})}e^{j2\pi(f_o+f_s)(t''-t')j2\pi f_s(-\tilde{\tau})}dt'dt''\Big\rangle\end{aligned} \tag{B.36}$$

Appendix C

Fourth order moments of complex circular Gaussian random variables

In this appendix it is shown that the power statistics, can be expressed as a 4^{th} order moments of circular Gaussian complex random variables. The domonstration presented for the cGNSS-R technique, can be extrapolate in the same way for the iGNSS-R technique.

C.1 Power Cross-Correlation

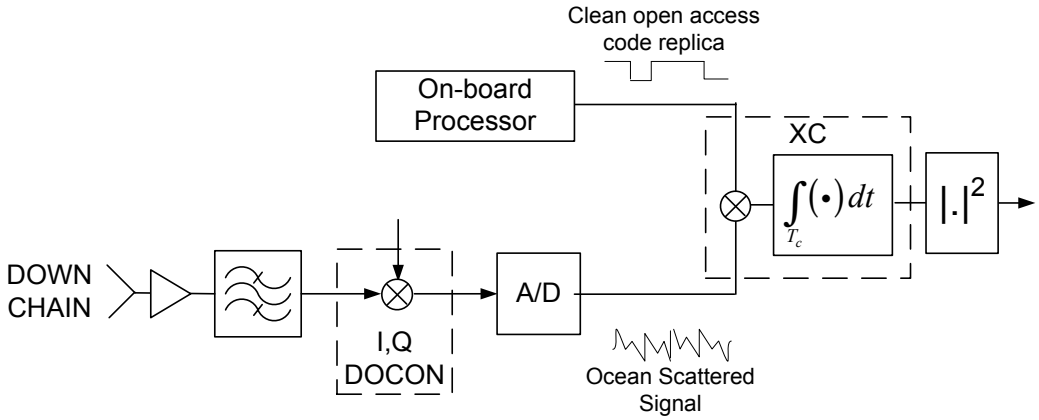

Figure C.1: Schematic diagram of a classical GNSS-R altimeter processor.

Figure C.1 shows the schematic diagram for the cGNSS-R approach. As it can be appreciated, cross-correlator (XC) performs the correlation between the signal at the up-link channel (in this case the clean replica) and rhe signal at the down-link channel (the scattered signal plus the noise introudced by the receiver). Therefore, a complex waveform is obtained at the output of the cross-correlator, that can be expressed in

a simple way as,

$$Y(\tau) = a_\tau \cdot (b_\tau + n_\tau) = a_\tau b_\tau + a_\tau n_\tau, \tag{C.1}$$

where a in this case is referred to the clean replica, b to the scattered signal, and n to the thermal noise, being b and n (complex gaussian), and a not. Hence, considering the special properties of the Gaussian random variables, any linear combination of jointly Gaussian random variables, dependent nor independent, results in a Gaussian random variable [60]. Therefore, the products ab and an becomes Gaussian, and can be expressed as,

$$Y_s(\tau) = a_\tau b_\tau, \tag{C.2}$$

and

$$Y_{Nr}(\tau) = a_\tau n_\tau, \tag{C.3}$$

thus the complex waveform is Gaussian. Considering Eqn. C.1, the complex statistics can be expressed as:

$$\begin{aligned}\left\langle Y(\tau)Y(\tau+\tilde{\tau})\right\rangle =& \left\langle (a_\tau b_\tau + a_\tau n_\tau)\cdot(a^*_{\tau+\tilde{\tau}} b^*_{\tau+\tilde{\tau}} + a^*_{\tau+\tilde{\tau}} n^*_{\tau+\tilde{\tau}})\right\rangle \\ =& \left\langle a_\tau b_\tau a^*_{\tau+\tilde{\tau}} b^*_{\tau+\tilde{\tau}}\right\rangle + \left\langle a_\tau b_\tau a^*_{\tau+\tilde{\tau}} n^*_{\tau+\tilde{\tau}}\right\rangle \\ &+ \left\langle a_\tau n_\tau a^*_{\tau+\tilde{\tau}} b^*_{\tau+\tilde{\tau}}\right\rangle + \left\langle a_\tau n_\tau a^*_{\tau+\tilde{\tau}} n^*_{\tau+\tilde{\tau}}\right\rangle,\end{aligned} \tag{C.4}$$

considering Eqn. C.2 and Eqn. C.3, Eqn. C.4 can be expressed as,

$$\begin{aligned}\left\langle Y(\tau)Y(\tau+\tilde{\tau})\right\rangle =& \left\langle Y_s(\tau)Y^*_s(\tau+\tilde{\tau})\right\rangle + \left\langle Y_s(\tau)Y^*_{Nr}(\tau+\tilde{\tau})\right\rangle \\ &+ \left\langle Y_{Nr}(\tau)Y^*_s(\tau+\tilde{\tau})\right\rangle + \left\langle Y_{Nr}(\tau)Y^*_{Nr}(\tau+\tilde{\tau})\right\rangle\end{aligned} \tag{C.5}$$

where as it has been commented previously, Y_s and Y_{Nr} are complex and Gaussian random variables.

The power waveform is the result of squaring the in-phase and -quadrature components of the complex waveforms obtained at the output of the cross-correlator. Thus, it can be expressed as:

$$\begin{aligned}|Y(\tau)|^2 =& |a_\tau b_\tau + a_\tau n_\tau|^2 \\ =& (a_\tau b_\tau + a_\tau n_\tau)(a^*_\tau b^*_\tau + a^*_\tau n^*_\tau) \\ =& a_\tau b_\tau a^*_{\tau+\tilde{\tau}} b^*_{\tau+\tilde{\tau}} + a_\tau b_\tau a^*_{\tau+\tilde{\tau}} n^*_{\tau+\tilde{\tau}} \\ &+ a_\tau n_\tau a^*_{\tau+\tilde{\tau}} b^*_{\tau+\tilde{\tau}} + a_\tau n_\tau a^*_{\tau+\tilde{\tau}} n^*_{\tau+\tilde{\tau}},\end{aligned} \tag{C.6}$$

Hence, the statistics of the power waveforms can be written as,

$$\begin{aligned}\left\langle |Y(\tau)|^2 |Y(\tau+\tilde{\tau})|^2 \right\rangle =& \big\langle (a_\tau b_\tau a^*_{\tau+\tilde{\tau}} b^*_{\tau+\tilde{\tau}} + a_\tau b_\tau a^*_{\tau+\tilde{\tau}} n^*_{\tau+\tilde{\tau}} + a_\tau n_\tau a^*_{\tau+\tilde{\tau}} b^*_{\tau+\tilde{\tau}} + a_\tau n_\tau a^*_{\tau+\tilde{\tau}} n^*_{\tau+\tilde{\tau}}) \\ & \cdot (a^*_\tau b^*_\tau a_{\tau+\tilde{\tau}} b_{\tau+\tilde{\tau}} + a^*_\tau b^*_\tau a_{\tau+\tilde{\tau}} n_{\tau+\tilde{\tau}} + a^*_\tau n^*_\tau a_{\tau+\tilde{\tau}} b_{\tau+\tilde{\tau}} + a^*_\tau n^*_\tau a_{\tau+\tilde{\tau}} n_{\tau+\tilde{\tau}}) \big\rangle \\ =& \left\langle a_\tau b_\tau a^*_\tau b^*_\tau a^*_{\tau+\tilde{\tau}} b^*_{\tau+\tilde{\tau}} a_{\tau+\tilde{\tau}} b_{\tau+\tilde{\tau}} \right\rangle + \left\langle a_\tau b_\tau a^*_\tau b^*_\tau a^*_{\tau+\tilde{\tau}} b^*_{\tau+\tilde{\tau}} a_{\tau+\tilde{\tau}} n_{\tau+\tilde{\tau}} \right\rangle \\ & + \left\langle a_\tau b_\tau a^*_\tau b^*_\tau a^*_{\tau+\tilde{\tau}} n^*_{\tau+\tilde{\tau}} a_{\tau+\tilde{\tau}} b_{\tau+\tilde{\tau}} \right\rangle + \left\langle a_\tau b_\tau a^*_\tau b^*_\tau a^*_{\tau+\tilde{\tau}} n^*_{\tau+\tilde{\tau}} a_{\tau+\tilde{\tau}} n_{\tau+\tilde{\tau}} \right\rangle \\ & + \left\langle a_\tau b_\tau a^*_\tau n^*_\tau a^*_{\tau+\tilde{\tau}} b^*_{\tau+\tilde{\tau}} a_{\tau+\tilde{\tau}} b_{\tau+\tilde{\tau}} \right\rangle + \left\langle a_\tau b_\tau a^*_\tau n^*_\tau a^*_{\tau+\tilde{\tau}} b^*_{\tau+\tilde{\tau}} a_{\tau+\tilde{\tau}} n_{\tau+\tilde{\tau}} \right\rangle \\ & + \left\langle a_\tau b_\tau a^*_\tau n^*_\tau a^*_{\tau+\tilde{\tau}} n^*_{\tau+\tilde{\tau}} a_{\tau+\tilde{\tau}} b_{\tau+\tilde{\tau}} \right\rangle + \left\langle a_\tau b_\tau a^*_\tau n^*_\tau a^*_{\tau+\tilde{\tau}} n^*_{\tau+\tilde{\tau}} a_{\tau+\tilde{\tau}} n_{\tau+\tilde{\tau}} \right\rangle \\ & + \left\langle a_\tau n_\tau a^*_\tau b^*_\tau a^*_{\tau+\tilde{\tau}} b^*_{\tau+\tilde{\tau}} a_{\tau+\tilde{\tau}} b_{\tau+\tilde{\tau}} \right\rangle + \left\langle a_\tau n_\tau a^*_\tau b^*_\tau a^*_{\tau+\tilde{\tau}} b^*_{\tau+\tilde{\tau}} a_{\tau+\tilde{\tau}} n_{\tau+\tilde{\tau}} \right\rangle \\ & + \left\langle a_\tau n_\tau a^*_\tau b^*_\tau a^*_{\tau+\tilde{\tau}} n^*_{\tau+\tilde{\tau}} a_{\tau+\tilde{\tau}} b_{\tau+\tilde{\tau}} \right\rangle + \left\langle a_\tau n_\tau a^*_\tau b^*_\tau a^*_{\tau+\tilde{\tau}} n^*_{\tau+\tilde{\tau}} a_{\tau+\tilde{\tau}} n_{\tau+\tilde{\tau}} \right\rangle \\ & + \left\langle a_\tau n_\tau a^*_\tau n^*_\tau a^*_{\tau+\tilde{\tau}} b^*_{\tau+\tilde{\tau}} a_{\tau+\tilde{\tau}} b_{\tau+\tilde{\tau}} \right\rangle + \left\langle a_\tau n_\tau a^*_\tau n^*_\tau a^*_{\tau+\tilde{\tau}} b^*_{\tau+\tilde{\tau}} a_{\tau+\tilde{\tau}} n_{\tau+\tilde{\tau}} \right\rangle \\ & + \left\langle a_\tau n_\tau a^*_\tau n^*_\tau a^*_{\tau+\tilde{\tau}} n^*_{\tau+\tilde{\tau}} a_{\tau+\tilde{\tau}} b_{\tau+\tilde{\tau}} \right\rangle + \left\langle a_\tau n_\tau a^*_\tau n^*_\tau a^*_{\tau+\tilde{\tau}} n^*_{\tau+\tilde{\tau}} a_{\tau+\tilde{\tau}} n_{\tau+\tilde{\tau}} \right\rangle \end{aligned} \tag{C.7}$$

where $a_\tau b_\tau = Y_s(\tau)$, $a_\tau n_\tau = Y_{Nr}(\tau)$, $a^*_\tau b^*_\tau = Y^*_s(\tau)$, $a^*_\tau n^*_\tau = Y^*_{Nr}(\tau)$, $a_{\tau+\tilde{\tau}} b_{\tau+\tilde{\tau}} = Y_s(\tau+\tilde{\tau})$, $a_{\tau+\tilde{\tau}} n_{\tau+\tilde{\tau}} = Y_{Nr}(\tau+\tilde{\tau})$, $a^*_{\tau+\tilde{\tau}} b^*_{\tau+\tilde{\tau}} = Y^*_s(\tau+\tilde{\tau})$, and $a^*_{\tau+\tilde{\tau}} n^*_{\tau+\tilde{\tau}} = Y^*_{Nr}(\tau+\tilde{\tau})$, being complex and Gaussians. Therefore, Eqn. C.7 can be expressed as a complex gaussians four momenths,

$$\begin{aligned}\left\langle |Y(\tau)|^2 |Y(\tau+\tilde{\tau})|^2 \right\rangle =& \left\langle Y_s(\tau) Y^*_s(\tau) Y^*_s(\tau+\tilde{\tau}) Y_s(\tau+\tilde{\tau}) \right\rangle \\ & + \left\langle Y_s(\tau) Y^*_s(\tau) Y^*_s(\tau+\tilde{\tau}) Y_{Nr}(\tau+\tilde{\tau}) \right\rangle \\ & + \left\langle Y_s(\tau) Y^*_s(\tau) Y^*_{Nr}(\tau+\tilde{\tau}) Y_s(\tau+\tilde{\tau}) \right\rangle \\ & + \left\langle Y_s(\tau) Y^*_s(\tau) Y^*_{Nr}(\tau+\tilde{\tau}) Y_{Nr}(\tau+\tilde{\tau}) \right\rangle \\ & + \left\langle Y_s(\tau) Y^*_{Nr}(\tau) Y^*_s(\tau+\tilde{\tau}) Y_s(\tau+\tilde{\tau}) \right\rangle \\ & + \left\langle Y_s(\tau) Y^*_{Nr}(\tau) Y^*_s(\tau+\tilde{\tau}) Y_{Nr}(\tau+\tilde{\tau}) \right\rangle \\ & + \left\langle Y_s(\tau) Y^*_{Nr}(\tau) Y^*_{Nr}(\tau+\tilde{\tau}) Y_s(\tau+\tilde{\tau}) \right\rangle \\ & + \left\langle Y_s(\tau) Y^*_{Nr}(\tau) Y^*_{Nr}(\tau+\tilde{\tau}) Y_{Nr}(\tau+\tilde{\tau}) \right\rangle \\ & + \left\langle Y_{Nr}(\tau) Y^*_s(\tau) Y^*_s(\tau+\tilde{\tau}) Y_s(\tau+\tilde{\tau}) \right\rangle \\ & + \left\langle Y_{Nr}(\tau) Y^*_s(\tau) Y^*_s(\tau+\tilde{\tau}) Y_{Nr}(\tau+\tilde{\tau}) \right\rangle \\ & + \left\langle Y_{Nr}(\tau) Y^*_s(\tau) Y^*_{Nr}(\tau+\tilde{\tau}) Y_s(\tau+\tilde{\tau}) \right\rangle \\ & + \left\langle Y_{Nr}(\tau) Y^*_s(\tau) Y^*_{Nr}(\tau+\tilde{\tau}) Y_{Nr}(\tau+\tilde{\tau}) \right\rangle \\ & + \left\langle Y_{Nr}(\tau) Y^*_{Nr}(\tau) Y^*_s(\tau+\tilde{\tau}) Y_s(\tau+\tilde{\tau}) \right\rangle \\ & + \left\langle Y_{Nr}(\tau) Y^*_{Nr}(\tau) Y^*_s(\tau+\tilde{\tau}) Y_{Nr}(\tau+\tilde{\tau}) \right\rangle \end{aligned}$$

$$+\left\langle Y_{Nr}(\tau)Y_{Nr}^{*}(\tau)Y_{Nr}^{*}(\tau+\tilde{\tau})Y_{s}(\tau+\tilde{\tau})\right\rangle$$
$$+\left\langle Y_{Nr}(\tau)Y_{Nr}^{*}(\tau)Y_{Nr}^{*}(\tau+\tilde{\tau})Y_{Nr}(\tau+\tilde{\tau})\right\rangle \tag{C.8}$$

Appendix D

cGNSS-R power cross-correlation

In this appendix, the computation of the power cross-correlation statistics is performed for the classical GNSS-R case.

D.1 Power Cross-Correlation

The complex cross-correlation at the output of the correlator at a given delay τ and acquiered at a time instant t, can be expressed as the sum of two terms as:

$$Y(t,\tau) = Y_s(t,\tau) + Y_{Nr}(t,\tau), \tag{D.1}$$

where $Y_s(t,\tau)$ is the Signal Voltage Cross-Correlation, and $Y_{Nr}(t,\tau)$ is the Noise Voltage Cross-Correlation (see Appendix A). Thus, from Eqn. (E.1), the power waveform obtained at the output of the cross-correlator can be written as,

$$\begin{aligned} |Y(t,\tau)|^2 =& |Y_s(t,\tau) + Y_{Nr}(t,\tau)|^2, \\ =& |Y_s(t,\tau)|^2 + |Y_{Nr}(t,\tau)|^2 + Y_s(t,\tau)Y_{Nr}^*(t,\tau) + Y_s^*(t,\tau)Y_{Nr}(t,\tau), \end{aligned} \tag{D.2}$$

Therefore, the cross-correlation statistics are given by:

$$\begin{aligned} C =& \left\langle |Y(\tau)|^2 |Y(\tau+\tilde{\tau})|^2 \right\rangle \\ =& \Big\langle (|Y_s(\tau)|^2 + |Y_{Nr}(\tau)|^2 + Y_s(\tau)Y_{Nr}^*(\tau) + Y_s^*(t,\tau)Y_{Nr}(t,\tau)) \\ & \cdot (|Y_s(\tau+\tilde{\tau})|^2 + |Y_{Nr}(\tau+\tilde{\tau})|^2 + Y_s^*(\tau+\tilde{\tau})Y_{Nr}(\tau+\tilde{\tau}) + Y_s(\tau+\tilde{\tau})Y_{Nr}^*(\tau+\tilde{\tau})) \Big\rangle \\ =& \left\langle |Y_s(\tau)|^2 |Y_s(\tau+\tilde{\tau})|^2 \right\rangle + \left\langle |Y_s(\tau)|^2 |Y_{Nr}(\tau+\tilde{\tau})|^2 \right\rangle + \left\langle |Y_s(\tau)|^2 Y_s^*(\tau+\tilde{\tau}) Y_{Nr}(\tau+\tilde{\tau}) \right\rangle \\ & + \left\langle |Y_s(\tau)|^2 Y_s(\tau+\tilde{\tau}) Y_{Nr}^*(\tau+\tilde{\tau}) + \left\langle |Y_{Nr}(\tau)|^2 |Y_s(\tau+\tilde{\tau})|^2 \right\rangle + \left\langle |Y_{Nr}(\tau)|^2 |Y_{Nr}(\tau+\tilde{\tau})|^2 \right\rangle \right. \\ & + \left\langle |Y_{Nr}(\tau)|^2 Y_s^*(\tau+\tilde{\tau}) Y_{Nr}(\tau+\tilde{\tau}) \right\rangle + \left\langle |Y_{Nr}(\tau)|^2 Y_s(\tau+\tilde{\tau}) Y_{Nr}^*(\tau+\tilde{\tau}) \right\rangle \\ & + \left\langle Y_s(\tau) Y_{Nr}^*(\tau) |Y_s(\tau+\tilde{\tau})|^2 \right\rangle + \left\langle Y_s(\tau) Y_{Nr}^*(\tau) |Y_{Nr}(\tau+\tilde{\tau})|^2 \right\rangle \end{aligned}$$

$$+\left\langle Y_s(\tau)Y_{Nr}^*(\tau)Y_s^*(\tau+\tilde{\tau})Y_{Nr}(\tau+\tilde{\tau})\right\rangle+\left\langle Y_s(\tau)Y_{Nr}^*(\tau)Y_s(\tau+\tilde{\tau})Y_{Nr}^*(\tau+\tilde{\tau})\right\rangle$$
$$+\left\langle Y_s^*(\tau)Y_{Nr}(\tau)|Y_s(\tau+\tilde{\tau})|^2\right\rangle+\left\langle Y_s^*(\tau)Y_{Nr}(\tau)|Y_{Nr}(\tau+\tilde{\tau})|^2\right\rangle$$
$$+\left\langle Y_s^*(\tau)Y_{Nr}(\tau)Y_s^*(\tau+\tilde{\tau})Y_{Nr}(\tau+\tilde{\tau})\right\rangle+\left\langle Y_s^*(\tau)Y_{Nr}(\tau)Y_s(\tau+\tilde{\tau})Y_{Nr}^*(\tau+\tilde{\tau})\right\rangle. \quad \text{(D.3)}$$

Considering that the signals are circular complex random, the fourth-order moments, can be expressed as [60],

$$\left\langle Y_1Y_2Y_3^*Y_4^*\right\rangle=\left\langle Y_1Y_3^*\right\rangle\left\langle Y_2Y_4^*\right\rangle+\left\langle Y_1Y_4^*\right\rangle\left\langle Y_2Y_3^*\right\rangle, \quad \text{(D.4)}$$

the different terms of Eqn.(E.2) can be written as,

$$\begin{aligned}&\left\langle|Y_s(\tau)|^2|Y_s(\tau+\tilde{\tau})|^2\right\rangle\\&\quad=\left\langle Y_s(\tau)Y_s^*(\tau)Y_s(\tau+\tilde{\tau})Y_s^*(\tau+\tilde{\tau})\right\rangle\\&\quad=\left\langle Y_s(\tau)Y_s(\tau+\tilde{\tau})Y_s^*(\tau)Y_s^*(\tau+\tilde{\tau})\right\rangle\\&\quad=\left\langle Y_s(\tau)Y_s^*(\tau)\right\rangle\left\langle Y_s(\tau+\tilde{\tau})Y_s^*(\tau+\tilde{\tau})\right\rangle\\&\qquad+\left\langle Y_s(\tau)Y_s^*(\tau+\tilde{\tau})\right\rangle\left\langle Y_s(\tau)Y_s^*(\tau+\tilde{\tau})\right\rangle, \quad \text{(D.5)}\end{aligned}$$

$$\begin{aligned}&\left\langle|Y_s(\tau)|^2|Y_{Nr}(\tau+\tilde{\tau})|^2\right\rangle\\&\quad=\left\langle Y_s(\tau)Y_s^*(\tau)Y_{Nr}(\tau+\tilde{\tau})Y_{Nr}^*(\tau+\tilde{\tau})\right\rangle\\&\quad=\left\langle Y_s(\tau)Y_{Nr}(\tau+\tilde{\tau})Y_s^*(\tau)Y_{Nr}^*(\tau+\tilde{\tau})\right\rangle\\&\quad=\left\langle Y_s(\tau)Y_s^*(\tau)\right\rangle\left\langle Y_{Nr}(\tau+\tilde{\tau})Y_{Nr}^*(\tau+\tilde{\tau})\right\rangle\\&\qquad+\left\langle Y_s(\tau)Y_{Nr}^*(\tau+\tilde{\tau})\right\rangle\left\langle Y_s(\tau)Y_{Nr}^*(\tau+\tilde{\tau})\right\rangle\\&\quad=\left\langle Y_s(\tau)Y_s^*(\tau)\right\rangle\left\langle Y_{Nr}(\tau+\tilde{\tau})Y_{Nr}^*(\tau+\tilde{\tau})\right\rangle, \quad \text{(D.6)}\end{aligned}$$

$$\begin{aligned}&\left\langle|Y_s(\tau)|^2Y_s^*(\tau+\tilde{\tau})Y_{Nr}(\tau+\tilde{\tau})\right\rangle\\&\quad=\left\langle Y_s(\tau)Y_s^*(\tau)Y_s^*(\tau+\tilde{\tau})Y_{Nr}(\tau+\tilde{\tau})\right\rangle\\&\quad=\left\langle Y_s(\tau)Y_{Nr}(\tau+\tilde{\tau})Y_s^*(\tau)Y_s^*(\tau+\tilde{\tau})\right\rangle\\&\quad=\left\langle Y_s(\tau)Y_s^*(\tau)\right\rangle\left\langle Y_{Nr}(\tau+\tilde{\tau})Y_s^*(\tau+\tilde{\tau})\right\rangle\\&\qquad+\left\langle Y_s(\tau)Y_s^*(\tau+\tilde{\tau})\right\rangle\left\langle Y_{Nr}(\tau)Y_{Nr}^*(\tau+\tilde{\tau})\right\rangle\\&\quad=\left\langle Y_s(\tau)Y_s^*(\tau+\tilde{\tau})\right\rangle\left\langle Y_{Nr}(\tau)Y_{Nr}^*(\tau+\tilde{\tau})\right\rangle, \quad \text{(D.7)}\end{aligned}$$

$$\begin{aligned}
&\big\langle |Y_s(\tau)|^2 Y_s(\tau+\tilde{\tau}) Y_{Nr}^*(\tau+\tilde{\tau})\big\rangle \\
&\qquad =\big\langle Y_s(\tau) Y_s^*(\tau) Y_s(\tau+\tilde{\tau}) Y_{Nr}^*(\tau+\tilde{\tau})\big\rangle \\
&\qquad =\big\langle Y_s(\tau) Y_s(\tau+\tilde{\tau}) Y_s^*(\tau) Y_{Nr}^*(\tau+\tilde{\tau})\big\rangle \\
&\qquad =\big\langle Y_s(\tau) Y_s^*(\tau)\big\rangle\big\langle Y_s(\tau+\tilde{\tau}) Y_{Nr}^*(\tau+\tilde{\tau})\big\rangle \\
&\qquad\quad +\big\langle Y_s(\tau) Y_{Nr}^*(\tau+\tilde{\tau})\big\rangle\big\langle Y_s(\tau+\tilde{\tau}) Y_s^*(\tau)\big\rangle \\
&\qquad =0, \qquad\qquad (D.8)
\end{aligned}$$

$$\begin{aligned}
&\big\langle |Y_{Nr}(\tau)|^2 |Y_s(\tau+\tilde{\tau})|^2\big\rangle \\
&\qquad =\big\langle Y_{Nr}(\tau) Y_{Nr}^*(\tau) Y_s(\tau+\tilde{\tau}) Y_s^*(\tau+\tilde{\tau})\big\rangle \\
&\qquad =\big\langle Y_{Nr}(\tau) Y_s(\tau+\tilde{\tau}) Y_{Nr}^*(\tau) Y_s^*(\tau+\tilde{\tau})\big\rangle \\
&\qquad =\big\langle Y_{Nr}(\tau) Y_{Nr}^*(\tau)\big\rangle\big\langle Y_s(\tau+\tilde{\tau}) Y_{Nr}^*(\tau)\big\rangle \\
&\qquad\quad +\big\langle Y_{Nr}(\tau) Y_s^*(\tau+\tilde{\tau})\big\rangle\big\langle Y_s(\tau+\tilde{\tau}) Y_{Nr}^*(\tau)\big\rangle \\
&\qquad =0, \qquad\qquad (D.9)
\end{aligned}$$

$$\begin{aligned}
&\big\langle |Y_{Nr}(\tau)|^2 |Y_{Nr}(\tau+\tilde{\tau})|^2\big\rangle \\
&\qquad =\big\langle Y_{Nr}(\tau) Y_{Nr}^*(\tau) Y_{Nr}(\tau+\tilde{\tau}) Y_{Nr}^*(\tau+\tilde{\tau})\big\rangle \\
&\qquad =\big\langle Y_{Nr}(\tau) Y_{Nr}(\tau+\tilde{\tau}) Y_{Nr}^*(\tau) Y_{Nr}^*(\tau+\tilde{\tau})\big\rangle \\
&\qquad =\big\langle Y_{Nr}(\tau) Y_{Nr}^*(\tau)\big\rangle\big\langle Y_{Nr}(\tau+\tilde{\tau}) Y_{Nr}^*(\tau+\tilde{\tau})\big\rangle \\
&\qquad\quad +\big\langle Y_{Nr}(\tau) Y_{Nr}^*(\tau+\tilde{\tau})\big\rangle\big\langle Y_{Nr}(\tau) Y_{Nr}^*(\tau+\tilde{\tau})\big\rangle, \qquad (D.10)
\end{aligned}$$

$$\begin{aligned}
&\big\langle |Y_{Nr}(\tau)|^2 Y_s^*(\tau+\tilde{\tau}) Y_{Nr}(\tau+\tilde{\tau})\big\rangle \\
&\qquad =\big\langle Y_{Nr}(\tau) Y_{Nr}^*(\tau) Y_s^*(\tau+\tilde{\tau}) Y_{Nr}(\tau+\tilde{\tau})\big\rangle \\
&\qquad =\big\langle Y_{Nr}(\tau) Y_{Nr}(\tau+\tilde{\tau}) Y_{Nr}^*(\tau) Y_s^*(\tau+\tilde{\tau})\big\rangle \\
&\qquad =\big\langle Y_{Nr}(\tau) Y_{Nr}^*(\tau)\big\rangle\big\langle Y_{Nr}(\tau+\tilde{\tau}) Y_s^*(\tau+\tilde{\tau})\big\rangle \\
&\qquad\quad +\big\langle Y_{Nr}(\tau) Y_s^*(\tau+\tilde{\tau})\big\rangle\big\langle Y_{Nr}(\tau+\tilde{\tau}) Y_{Nr}^*(\tau)\big\rangle \\
&\qquad =0, \qquad\qquad (D.11)
\end{aligned}$$

$$\begin{aligned}
&\big\langle |Y_{Nr}(\tau)|^2 Y_s(\tau+\tilde{\tau}) Y_{Nr}^*(\tau+\tilde{\tau})\big\rangle \\
&\qquad =\big\langle Y_{Nr}(\tau) Y_{Nr}^*(\tau) Y_s(\tau+\tilde{\tau}) Y_{Nr}^*(\tau+\tilde{\tau})\big\rangle \\
&\qquad =\big\langle Y_{Nr}(\tau) Y_s(\tau+\tilde{\tau}) Y_{Nr}^*(\tau) Y_{Nr}^*(\tau+\tilde{\tau})\big\rangle \\
&\qquad =\big\langle Y_{Nr}(\tau) Y_{Nr}^*(\tau)\big\rangle\big\langle Y_s(\tau+\tilde{\tau}) Y_{Nr}^*(\tau+\tilde{\tau})\big\rangle \\
&\qquad\quad +\big\langle Y_{Nr}(\tau) Y_{Nr}^*(\tau+\tilde{\tau})\big\rangle\big\langle Y_s(\tau+\tilde{\tau}) Y_{Nr}^*(\tau)\big\rangle \\
&\qquad =0, \qquad\qquad (D.12)
\end{aligned}$$

$$\begin{aligned}
&\Big\langle Y_s(\tau)Y_{Nr}^*(\tau)|Y_s(\tau+\tilde{\tau})|^2\Big\rangle \\
&\quad=\Big\langle Y_s(\tau)Y_{Nr}^*(\tau)Y_s(\tau+\tilde{\tau})Y_s^*(\tau+\tilde{\tau})\Big\rangle \\
&\quad=\Big\langle Y_s(\tau)Y_s(\tau+\tilde{\tau})Y_{Nr}^*(\tau)Y_s^*(\tau+\tilde{\tau})\Big\rangle \\
&\quad=\Big\langle Y_s(\tau)Y_{Nr}^*(\tau)\Big\rangle\Big\langle Y_s(\tau+\tilde{\tau})Y_s^*(\tau+\tilde{\tau})\Big\rangle \\
&\qquad+\Big\langle Y_s(\tau)Y_s^*(\tau+\tilde{\tau})\Big\rangle\Big\langle Y_s(\tau+\tilde{\tau})Y_{Nr}^*(\tau)\Big\rangle \\
&\quad=0,
\end{aligned} \tag{D.13}$$

$$\begin{aligned}
&\Big\langle Y_s(\tau)Y_{Nr}^*(\tau)|Y_{Nr}(\tau+\tilde{\tau})|^2\Big\rangle \\
&\quad=\Big\langle Y_s(\tau)Y_{Nr}^*(\tau)Y_{Nr}(\tau+\tilde{\tau})Y_{Nr}^*(\tau+\tilde{\tau})\Big\rangle \\
&\quad=\Big\langle Y_s(\tau)Y_{Nr}(\tau+\tilde{\tau})Y_{Nr}^*(\tau)Y_{Nr}^*(\tau+\tilde{\tau})\Big\rangle \\
&\quad=\Big\langle Y_s(\tau)Y_{Nr}^*(\tau)\Big\rangle\Big\langle Y_{Nr}(\tau+\tilde{\tau})Y_{Nr}^*(\tau+\tilde{\tau})\Big\rangle \\
&\qquad+\Big\langle Y_s(\tau)Y_{Nr}^*(\tau+\tilde{\tau})\Big\rangle\Big\langle Y_{Nr}(\tau+\tilde{\tau})Y_{Nr}^*(\tau)\Big\rangle \\
&\quad=0,
\end{aligned} \tag{D.14}$$

$$\begin{aligned}
&\Big\langle Y_s(\tau)Y_{Nr}^*(\tau)Y_s^*(\tau+\tilde{\tau})Y_{Nr}(\tau+\tilde{\tau})\Big\rangle \\
&\quad=\Big\langle Y_s(\tau)Y_{Nr}^*(\tau)Y_{Nr}^*(\tau+\tilde{\tau})Y_s^*(\tau+\tilde{\tau})\Big\rangle \\
&\quad=\Big\langle Y_s(\tau)Y_{Nr}(\tau+\tilde{\tau})Y_{Nr}^*(\tau)Y_s^*(\tau+\tilde{\tau})\Big\rangle \\
&\quad=\Big\langle Y_s(\tau)Y_{Nr}^*(\tau)\Big\rangle\Big\langle Y_{Nr}(\tau+\tilde{\tau})Y_s^*(\tau+\tilde{\tau})\Big\rangle \\
&\qquad+\Big\langle Y_s(\tau)Y_s^*(\tau+\tilde{\tau})\Big\rangle\Big\langle Y_{Nr}(\tau+\tilde{\tau})Y_{Nr}^*(\tau)\Big\rangle \\
&\quad=+\Big\langle Y_s(\tau)Y_s^*(\tau+\tilde{\tau})\Big\rangle\Big\langle Y_{Nr}(\tau+\tilde{\tau})Y_{Nr}^*(\tau)\Big\rangle,
\end{aligned} \tag{D.15}$$

$$\begin{aligned}
&\Big\langle Y_s(\tau)Y_{Nr}^*(\tau)Y_s(\tau+\tilde{\tau})Y_{Nr}^*(\tau+\tilde{\tau})\Big\rangle \\
&\quad=\Big\langle Y_s(\tau)Y_s(\tau+\tilde{\tau})Y_{Nr}^*(\tau)Y_{Nr}^*(\tau+\tilde{\tau})\Big\rangle \\
&\quad=\Big\langle Y_s(\tau)Y_{Nr}^*(\tau)\Big\rangle\Big\langle Y_s(\tau+\tilde{\tau})Y_{Nr}^*(\tau+\tilde{\tau})\Big\rangle \\
&\qquad+\Big\langle Y_s(\tau)Y_{Nr}^*(\tau+\tilde{\tau})\Big\rangle\Big\langle Y_s(\tau+\tilde{\tau})Y_{Nr}^*(\tau)\Big\rangle \\
&\quad=0,
\end{aligned} \tag{D.16}$$

$$\begin{aligned}
&\Big\langle Y_s^*(\tau)Y_{Nr}(\tau)|Y_s(\tau+\tilde{\tau})|^2\Big\rangle \\
&\quad=\Big\langle Y_s^*(\tau)Y_{Nr}(\tau)Y_s(\tau+\tilde{\tau})Y_s^*(\tau+\tilde{\tau})\Big\rangle \\
&\quad=\Big\langle Y_{Nr}(\tau)Y_s(\tau+\tilde{\tau})Y_s^*(\tau)Y_s^*(\tau+\tilde{\tau})\Big\rangle \\
&\quad=\Big\langle Y_{Nr}(\tau)Y_s^*(\tau)\Big\rangle\Big\langle Y_s(\tau+\tilde{\tau})Y_s^*(\tau+\tilde{\tau})\Big\rangle \\
&\qquad+\Big\langle Y_{Nr}(\tau)Y_s^*(\tau+\tilde{\tau})\Big\rangle\Big\langle Y_s(\tau+\tilde{\tau})Y_s^*(\tau)\Big\rangle \\
&\quad=0,
\end{aligned} \tag{D.17}$$

$$\begin{aligned}
&\left\langle Y_s^*(\tau)Y_{Nr}(\tau)|Y_{Nr}(\tau+\tilde{\tau})|^2\right\rangle \\
&\quad=\left\langle Y_s^*(\tau)Y_{Nr}(\tau)Y_{Nr}(\tau+\tilde{\tau})Y_{Nr}^*(\tau+\tilde{\tau})\right\rangle \\
&\quad=\left\langle Y_{Nr}(\tau)Y_{Nr}(\tau+\tilde{\tau})Y_s^*(\tau)Y_{Nr}^*(\tau+\tilde{\tau})\right\rangle \\
&\quad=\left\langle Y_{Nr}(\tau)Y_s^*(\tau)\right\rangle\left\langle Y_{Nr}(\tau+\tilde{\tau})Y_{Nr}^*(\tau+\tilde{\tau})\right\rangle \\
&\qquad+\left\langle Y_{Nr}(\tau)Y_{Nr}^*(\tau+\tilde{\tau})\right\rangle\left\langle Y_{Nr}(\tau+\tilde{\tau})Y_s^*(\tau)\right\rangle \\
&\quad=0,
\end{aligned}\tag{D.18}$$

$$\begin{aligned}
&\left\langle Y_s^*(\tau)Y_{Nr}(\tau)Y_s^*(\tau+\tilde{\tau})Y_{Nr}(\tau+\tilde{\tau})\right\rangle \\
&\quad=\left\langle Y_{Nr}^*(\tau)Y_{Nr}(\tau+\tilde{\tau})Y_s^*(\tau)Y_s^*(\tau+\tilde{\tau})\right\rangle \\
&\quad=\left\langle Y_{Nr}(\tau)Y_s^*(\tau)\right\rangle\left\langle Y_{Nr}(\tau+\tilde{\tau})Y_s^*(\tau+\tilde{\tau})\right\rangle \\
&\qquad+\left\langle Y_{Nr}(\tau)Y_s^*(\tau+\tilde{\tau})\right\rangle\left\langle Y_{Nr}(\tau+\tilde{\tau})Y_s^*(\tau)\right\rangle \\
&\quad=0,
\end{aligned}\tag{D.19}$$

and

$$\begin{aligned}
&\left\langle Y_s^*(\tau)Y_{Nr}(\tau)Y_s(\tau+\tilde{\tau})Y_{Nr}^*(\tau+\tilde{\tau})\right\rangle \\
&\quad=\left\langle Y_{Nr}^*(\tau)Y_s(\tau+\tilde{\tau})Y_s^*(\tau)Y_{Nr}^*(\tau+\tilde{\tau})\right\rangle \\
&\quad=\left\langle Y_{Nr}(\tau)Y_s^*(\tau)\right\rangle\left\langle Y_s(\tau+\tilde{\tau})Y_{Nr}^*(\tau+\tilde{\tau})\right\rangle \\
&\qquad+\left\langle Y_{Nr}(\tau)Y_{Nr}^*(\tau+\tilde{\tau})\right\rangle\left\langle Y_s(\tau+\tilde{\tau})Y_s^*(\tau)\right\rangle \\
&\quad=+\left\langle Y_{Nr}(\tau)Y_{Nr}^*(\tau+\tilde{\tau})\right\rangle\left\langle Y_s(\tau+\tilde{\tau})Y_s^*(\tau)\right\rangle,
\end{aligned}\tag{D.20}$$

Thus substituting all that terms on Eqn. (E.2), it becomes,

$$\begin{aligned}
C=&\left\langle |Y(\tau)|^2|Y(\tau+\tilde{\tau})|^2\right\rangle \\
=&\left\langle Y_s(\tau)Y_s^*(\tau)\right\rangle\left\langle Y_s(\tau+\tilde{\tau})Y_s^*(\tau+\tilde{\tau})\right\rangle+\left\langle Y_s(\tau)Y_s^*(\tau+\tilde{\tau})\right\rangle\left\langle Y_s(\tau+\tilde{\tau})Y_s^*(\tau)\right\rangle \\
&+\left\langle Y_s(\tau)Y_s^*(\tau)\right\rangle\left\langle Y_{Nr}(\tau+\tilde{\tau})Y_{Nr}^*(\tau+\tilde{\tau})\right\rangle+\left\langle Y_{Nr}(\tau)Y_{Nr}^*(\tau)\right\rangle\left\langle Y_s(\tau+\tilde{\tau})Y_s^*(\tau+\tilde{\tau})\right\rangle \\
&+\left\langle Y_{Nr}(\tau)Y_{Nr}^*(\tau)\right\rangle\left\langle Y_{Nr}(\tau+\tilde{\tau})Y_{Nr}^*(\tau+\tilde{\tau})\right\rangle+\left\langle Y_{Nr}(\tau)Y_{Nr}^*(\tau+\tilde{\tau})\right\rangle\left\langle Y_{Nr}(\tau+\tilde{\tau})Y_{Nr}^*(\tau)\right\rangle \\
&+\left\langle Y_s(\tau)Y_s^*(\tau+\tilde{\tau})\right\rangle\left\langle Y_{Nr}(\tau+\tilde{\tau})Y_{NR}s^*(\tau)\right\rangle+\left\langle Y_{Nr}(\tau)Y_{Nr}^*(\tau+\tilde{\tau})\right\rangle\left\langle Y_s(\tau+\tilde{\tau})Y_s^*(\tau)\right\rangle
\end{aligned}\tag{D.21}$$

Equation.(D.21)

$$\begin{aligned}
C=&\left\langle |Y(\tau)|^2|Y(\tau+\tilde{\tau})|^2\right\rangle \\
=&|C_{Y_s}(\tilde{\tau})|^2+|C_{Y_{Nr}}(\tilde{\tau})|^2+2C_{Y_s}(\tilde{\tau})C_{Y_{Nr}}(\tilde{\tau}) \\
&+|C_{Y_s}(0)|^2+|C_{Y_{Nr}}(0)|^2+2C_{Y_s}(0)C_{Y_{Nr}}(0),
\end{aligned}\tag{D.22}$$

where

$$|C_Y(\tilde{\tau})|^2 = \big\langle Y(\tau)Y^*(\tau+\tilde{\tau})\big\rangle\big\langle Y(\tau+\tilde{\tau})Y^*(\tau)\big\rangle. \tag{D.23}$$

$$|C_Y(0)|^2 = \big\langle Y(\tau)Y^*(\tau)\big\rangle\big\langle Y(\tau+\tilde{\tau})Y^*(\tau+\tilde{\tau})\big\rangle. \tag{D.24}$$

Appendix E

iGNSS-R power cross-correlation

In this appendix, the computation of the power cross-correlation statistics is performed for the interferometric GNSS-R case.

E.1 Power Cross-Correlation

The complex waveform at the output of the cross correlator can be expressed as the sum of four terms (Y_s, Y_{Nr}, Y_{Nd}, and Y_{Ndr}). Thus, the power waveform obtained at the output, can be written as:

$$\begin{aligned}|Y(t,\tau)|^2 =&|Y_s(t,\tau)+Y_{Nr}(t,\tau)+Y_{Nd}(t,\tau)+Y_{Ndr}(t,\tau)|^2\\ =&|Y_s(t,\tau)|^2+Y_s(t,\tau)Y_{Nr}^*(t,\tau)+Y_s(t,\tau)Y_{Nd}^*(t,\tau)+Y_s(t,\tau)Y_{Ndr}^*(t,\tau)\\ &\cdot Y_{Nr}(t,\tau)Y_{Ns}^*(t,\tau)+|Y_{Nr}(t,\tau)|^2+Y_{Nr}(t,\tau)Y_{Nd}^*(t,\tau)+Y_{Nr}(t,\tau)Y_{Ndr}^*(t,\tau)\\ &\cdot Y_{Nd}(t,\tau)Y_{Ns}^*(t,\tau)+Y_{Nd}(t,\tau)Y_{Nr}^*(t,\tau)+|Y_{Nd}(t,\tau)|^2+Y_{Nd}(t,\tau)Y_{Ndr}^*(t,\tau)\\ &\cdot Y_{Ndr}(t,\tau)Y_s^*(t,\tau)+Y_{Ndr}(t,\tau)Y_{Nr}^*(t,\tau)+Y_{Ndr}(t,\tau)Y_{Nd}^*(t,\tau)+|Y_{Ndr}(t,\tau)|^2.\end{aligned} \tag{E.1}$$

Hence, the cross-correlation statistics are given by:

$$\begin{aligned}C =&\left\langle |Y(\tau)|^2|Y(\tau+\tilde{\tau})|^2\right\rangle\\ =&\big\langle(|Y_s(\tau)|^2+Y_s(\tau)Y_{Nr}^*(\tau)+Y_s(\tau)Y_{Nd}^*(\tau)+Y_s(\tau)Y_{Ndr}^*(\tau)\\ &\cdot Y_{Nr}(\tau)Y_{Ns}^*(\tau)+|Y_{Nr}(\tau)|^2+Y_{Nr}(\tau)Y_{Nd}^*(\tau)+Y_{Nr}(\tau)Y_{Ndr}^*(\tau)\\ &\cdot Y_{Nd}(\tau)Y_{Ns}^*(\tau)+Y_{Nd}(\tau)Y_{Nr}^*(\tau)+|Y_{Nd}(\tau)|^2+Y_{Nd}(\tau)Y_{Ndr}^*(\tau)\\ &\cdot Y_{Ndr}(\tau)Y_s^*(\tau)+Y_{Ndr}(\tau)Y_{Nr}^*(\tau)+Y_{Ndr}(\tau)Y_{Nd}^*(\tau)+|Y_{Ndr}(\tau)|^2)\\ &(|Y_s(\tau+\tilde{\tau})|^2+Y_s^*(\tau+\tilde{\tau})Y_{Nr}(\tau+\tilde{\tau})+Y_s^*(\tau+\tilde{\tau})Y_{Nd}(\tau+\tilde{\tau})+Y_s^*(\tau+\tilde{\tau})Y_{Ndr}(\tau+\tilde{\tau})\end{aligned}$$

$$\cdot Y^*_{Nr}(\tau+\tilde{\tau})Y_{Ns}(\tau+\tilde{\tau}) + |Y_{Nr}(\tau+\tilde{\tau})|^2 + Y^*_{Nr}(\tau+\tilde{\tau})Y_{Nd}(\tau+\tilde{\tau}) + Y^*_{Nr}(\tau+\tilde{\tau})Y_{Ndr}(\tau+\tilde{\tau})$$
$$\cdot Y^*_{Nd}(\tau+\tilde{\tau})Y_{Ns}(\tau+\tilde{\tau}) + Y^*_{Nd}(\tau+\tilde{\tau})Y_{Nr}(\tau+\tilde{\tau}) + |Y_{Nd}(\tau+\tilde{\tau})|^2 + Y^*_{Nd}(\tau+\tilde{\tau})Y_{Ndr}(\tau+\tilde{\tau})$$
$$\cdot Y^*_{Ndr}(\tau+\tilde{\tau})Y_s(\tau+\tilde{\tau}) + Y^*_{Ndr}(\tau+\tilde{\tau})Y_{Nr}(\tau+\tilde{\tau}) + Y^*_{Ndr}(\tau+\tilde{\tau})Y_{Nd}(\tau+\tilde{\tau}) + |Y_{Ndr}(\tau+\tilde{\tau})|^2)\big\rangle \tag{E.2}$$

where it can be expanded as:

$$\begin{aligned}
=&\big\langle |Y_s(\tau)|^2|Y_s(\tau+\tilde{\tau})|^2\big\rangle + \big\langle |Y_s(\tau)|^2 Y^*_s(\tau+\tilde{\tau})Y_{Nr}(\tau+\tilde{\tau})\big\rangle \\
&+ \big\langle |Y_s(\tau)|^2 Y^*_s(\tau+\tilde{\tau})Y_{Nd}(\tau+\tilde{\tau})\big\rangle + \big\langle |Y_s(\tau)|^2 Y^*_s(\tau+\tilde{\tau})Y_{Ndr}(\tau+\tilde{\tau})\big\rangle \\
&+ \big\langle |Y_s(\tau)|^2 Y^*_{Nr}(\tau+\tilde{\tau})Y_s(\tau+\tilde{\tau})\big\rangle + \big\langle |Y_s(\tau)|^2|Y_{Nr}(\tau+\tilde{\tau})|^2\big\rangle \\
&+ \big\langle |Y_s(\tau)|^2 Y^*_{Nr}(\tau+\tilde{\tau})Y_{Nd}(\tau+\tilde{\tau})\big\rangle + \big\langle |Y_s(\tau)|^2 Y^*_{Nr}(\tau+\tilde{\tau})Y_{Ndr}(\tau+\tilde{\tau})\big\rangle \\
&+ \big\langle |Y_s(\tau)|^2 Y^*_{Nd}(\tau+\tilde{\tau})Y_s(\tau+\tilde{\tau})\big\rangle + \big\langle |Y_s(\tau)|^2 Y^*_{Nd}(\tau+\tilde{\tau})Y_{Nr}(\tau+\tilde{\tau})\big\rangle \\
&+ \big\langle |Y_s(\tau)|^2|Y_{Nd}(\tau+\tilde{\tau})|^2\big\rangle + \big\langle |Y_s(\tau)|^2 Y^*_{Nd}(\tau+\tilde{\tau})Y_{Ndr}(\tau+\tilde{\tau})\big\rangle \\
&+ \big\langle |Y_s(\tau)|^2 Y^*_{Ndr}(\tau+\tilde{\tau})Y_s(\tau+\tilde{\tau})\big\rangle + \big\langle |Y_s(\tau)|^2 Y^*_{Ndr}(\tau+\tilde{\tau})Y_{Nr}(\tau+\tilde{\tau})\big\rangle \\
&+ \big\langle |Y_s(\tau)|^2 Y^*_{Ndr}(\tau+\tilde{\tau})Y_{Nd}(\tau+\tilde{\tau})\big\rangle + \big\langle |Y_s(\tau)|^2|Y^*_{Ndr}(\tau+\tilde{\tau})|^2\big\rangle \\
&+ \big\langle Y_s(\tau)Y^*_{Nr}(\tau)|Y_s(\tau+\tilde{\tau})|^2\big\rangle + \big\langle Y_s(\tau)Y^*_{Nr}(\tau)Y^*_s(\tau+\tilde{\tau})Y_{Nr}(\tau+\tilde{\tau})\big\rangle \\
&+ \big\langle Y_s(\tau)Y^*_{Nr}(\tau)Y^*_s(\tau+\tilde{\tau})Y_{Nd}(\tau+\tilde{\tau})\big\rangle + \big\langle Y_s(\tau)Y^*_{Nr}(\tau)Y^*_s(\tau+\tilde{\tau})Y_{Ndr}(\tau+\tilde{\tau})\big\rangle \\
&+ \big\langle Y_s(\tau)Y^*_{Nr}(\tau)Y^*_{Nr}(\tau+\tilde{\tau})Y_s(\tau+\tilde{\tau})\big\rangle + \big\langle Y_s(\tau)Y_{Nr}(\tau)|Y^*_s(\tau+\tilde{\tau})|^2\big\rangle \\
&+ \big\langle Y_s(\tau)Y^*_{Nr}(\tau)Y^*_{Nr}(\tau+\tilde{\tau})Y_{Nd}(\tau+\tilde{\tau})\big\rangle + \big\langle Y_s(\tau)Y^*_{Nr}(\tau)Y^*_{Nr}(\tau+\tilde{\tau})Y_{Ndr}(\tau+\tilde{\tau})\big\rangle \\
&+ \big\langle Y_s(\tau)Y^*_{Nr}(\tau)Y^*_{Nd}(\tau+\tilde{\tau})Y_s(\tau+\tilde{\tau})\big\rangle + \big\langle Y_s(\tau)Y^*_{Nr}(\tau)Y^*_{Nd}(\tau+\tilde{\tau})Y_{Nr}(\tau+\tilde{\tau})\big\rangle \\
&+ \big\langle Y_s(\tau)Y^*_{Nr}(\tau)|Y_{Nd}(\tau+\tilde{\tau})|^2\big\rangle + \big\langle Y_s(\tau)Y^*_{Nr}(\tau)Y^*_{Nd}(\tau+\tilde{\tau})Y_{Ndr}(\tau+\tilde{\tau})\big\rangle \\
&+ \big\langle Y_s(\tau)Y^*_{Nr}(\tau)Y^*_{Ndr}(\tau+\tilde{\tau})Y_s(\tau+\tilde{\tau})\big\rangle + \big\langle Y_s(\tau)Y^*_{Nr}(\tau)Y^*_{Ndr}(\tau+\tilde{\tau})Y_{Nr}(\tau+\tilde{\tau})\big\rangle \\
&+ \big\langle Y_s(\tau)Y^*_{Nr}(\tau)Y^*_{Ndr}(\tau+\tilde{\tau})Y_{Nd}(\tau+\tilde{\tau})\big\rangle + \big\langle Y_s(\tau)Y^*_{Nr}(\tau)|Y_{Ndr}(\tau+\tilde{\tau})|^2\big\rangle \\
&+ \big\langle Y_s(\tau)Y^*_{Nd}(\tau)|Y_s(\tau+\tilde{\tau})|^2\big\rangle + \big\langle Y_s(\tau)Y^*_{Nr}(\tau)Y^*_s(\tau+\tilde{\tau})Y_{Nr}(\tau+\tilde{\tau})\big\rangle \\
&+ \big\langle Y_s(\tau)Y^*_{Nr}(\tau)Y^*_s(\tau+\tilde{\tau})Y_{Nd}(\tau+\tilde{\tau})\big\rangle + \big\langle Y_s(\tau)Y^*_{Nr}(\tau)Y^*_s(\tau+\tilde{\tau})Y_{Ndr}(\tau+\tilde{\tau})\big\rangle \\
&+ \big\langle Y_s(\tau)Y^*_{Nr}(\tau)Y^*_{Nr}(\tau+\tilde{\tau})Y_s(\tau+\tilde{\tau})\big\rangle + \big\langle Y_s(\tau)Y^*_{Nd}(\tau)|Y_{NR}(\tau+\tilde{\tau})|^2\big\rangle \\
&+ \big\langle Y_s(\tau)Y^*_{Nr}(\tau)Y^*_{Nr}(\tau+\tilde{\tau})Y_{Nd}(\tau+\tilde{\tau})\big\rangle + \big\langle Y_s(\tau)Y^*_{Nr}(\tau)Y^*_{Nr}(\tau+\tilde{\tau})Y_{Ndr}(\tau+\tilde{\tau})\big\rangle \\
&+ \big\langle Y_s(\tau)Y^*_{Nr}(\tau)Y^*_{Nd}(\tau+\tilde{\tau})Y_s(\tau+\tilde{\tau})\big\rangle + \big\langle Y_s(\tau)Y^*_{Nr}(\tau)Y^*_{Nd}(\tau+\tilde{\tau})Y_{Nr}(\tau+\tilde{\tau})\big\rangle \\
&+ \big\langle Y_s(\tau)Y^*_{Nr}(\tau)|Y_{Nd}(\tau+\tilde{\tau})|^2\big\rangle + \big\langle Y_s(\tau)Y^*_{Nr}(\tau)Y^*_{Nd}(\tau+\tilde{\tau})Y_{Ndr}(\tau+\tilde{\tau})\big\rangle \\
&+ \big\langle Y_s(\tau)Y^*_{Nd}(\tau)|Y_s(\tau+\tilde{\tau})|^2\big\rangle + \big\langle Y_s(\tau)Y^*_{Nr}(\tau)Y^*_s(\tau+\tilde{\tau})Y_{Nr}(\tau+\tilde{\tau})\big\rangle \\
&+ \big\langle Y_s(\tau)Y^*_{Nr}(\tau)Y^*_s(\tau+\tilde{\tau})Y_{Nd}(\tau+\tilde{\tau})\big\rangle + \big\langle Y_s(\tau)Y^*_{Nr}(\tau)Y^*_s(\tau+\tilde{\tau})Y_{Ndr}(\tau+\tilde{\tau})\big\rangle \\
&+ \big\langle Y_s(\tau)Y^*_{Nr}(\tau)Y^*_{Nr}(\tau+\tilde{\tau})Y_s(\tau+\tilde{\tau})\big\rangle + \big\langle Y_s(\tau)Y^*_{Nd}(\tau)|Y_{Nr}(\tau+\tilde{\tau})|^2\big\rangle
\end{aligned}$$

$$+\left\langle Y_s(\tau)Y^*_{Nr}(\tau)Y^*_{Nr}(\tau+\tilde\tau)Y_{Nd}(\tau+\tilde\tau)\right\rangle+\left\langle Y_s(\tau)Y^*_{Nr}(\tau)Y^*_{Nr}(\tau+\tilde\tau)Y_{Ndr}(\tau+\tilde\tau)\right\rangle$$
$$+\left\langle Y_s(\tau)Y^*_{Nr}(\tau)Y^*_{Nd}(\tau+\tilde\tau)Y_s(\tau+\tilde\tau)\right\rangle+\left\langle Y_s(\tau)Y^*_{Nr}(\tau)Y^*_{Nd}(\tau+\tilde\tau)Y_{Nr}(\tau+\tilde\tau)\right\rangle$$
$$+\left\langle Y_s(\tau)Y^*_{Nr}(\tau)|Y_{Nd}(\tau+\tilde\tau)|^2\right\rangle+\left\langle Y_s(\tau)Y^*_{Nr}(\tau)Y^*_{Nd}(\tau+\tilde\tau)Y_{Ndr}(\tau+\tilde\tau)\right\rangle$$
$$+\left\langle Y_s(\tau)Y^*_{Nr}(\tau)Y^*_{Ndr}(\tau+\tilde\tau)Y_s(\tau+\tilde\tau)\right\rangle+\left\langle Y_s(\tau)Y^*_{Nr}(\tau)Y^*_{Ndr}(\tau+\tilde\tau)Y_{Nr}(\tau+\tilde\tau)\right\rangle$$
$$+\left\langle Y_s(\tau)Y^*_{Nr}(\tau)Y^*_{Ndr}(\tau+\tilde\tau)Y_{Nd}(\tau+\tilde\tau)\right\rangle+\left\langle Y_s(\tau)Y^*_{Nr}(\tau)|Y_{Ndr}(\tau+\tilde\tau)|^2\right\rangle$$
$$+\left\langle Y_s(\tau)Y^*_{Nd}(\tau)|Y_s(\tau+\tilde\tau)|^2\right\rangle+\left\langle Y_s(\tau)Y^*_{Nd}(\tau)Y^*_s(\tau+\tilde\tau)Y_{Nr}(\tau+\tilde\tau)\right\rangle$$
$$+\left\langle Y_s(\tau)Y^*_{Nd}(\tau)Y^*_s(\tau+\tilde\tau)Y_{Nd}(\tau+\tilde\tau)\right\rangle+\left\langle Y_s(\tau)Y^*_{Nd}(\tau)Y^*_s(\tau+\tilde\tau)Y_{Ndr}(\tau+\tilde\tau)\right\rangle$$
$$+\left\langle Y_s(\tau)Y^*_{Nd}(\tau)Y^*_{Nr}(\tau+\tilde\tau)Y_s(\tau+\tilde\tau)\right\rangle+\left\langle Y_s(\tau)Y^*_{Nd}(\tau)|Y_{Nr}(\tau+\tilde\tau)|^2\right\rangle$$
$$+\left\langle Y_s(\tau)Y^*_{Nd}(\tau)Y^*_{Nr}(\tau+\tilde\tau)Y_{Nd}(\tau+\tilde\tau)\right\rangle+\left\langle Y_s(\tau)Y^*_{Nd}(\tau)Y^*_{Nr}(\tau+\tilde\tau)Y_{Ndr}(\tau+\tilde\tau)\right\rangle$$
$$+\left\langle Y_s(\tau)Y^*_{Nd}(\tau)Y^*_{Nd}(\tau+\tilde\tau)Y_s(\tau+\tilde\tau)\right\rangle+\left\langle Y_s(\tau)Y^*_{Nd}(\tau)Y^*_{Nd}(\tau+\tilde\tau)Y_{Nr}(\tau+\tilde\tau)\right\rangle$$
$$+\left\langle Y_s(\tau)Y^*_{Nd}(\tau)|Y^*_{Nd}(\tau+\tilde\tau)|^2\right\rangle+\left\langle Y_s(\tau)Y^*_{Nd}(\tau)Y^*_{Nd}(\tau+\tilde\tau)Y_{Ndr}(\tau+\tilde\tau)\right\rangle$$
$$+\left\langle Y_s(\tau)Y^*_{Nd}(\tau)Y^*_{Ndr}(\tau+\tilde\tau)Y_s(\tau+\tilde\tau)\right\rangle+\left\langle Y_s(\tau)Y^*_{Nd}(\tau)Y^*_{Ndr}(\tau+\tilde\tau)Y_{Nr}(\tau+\tilde\tau)\right\rangle$$
$$+\left\langle Y_s(\tau)Y^*_{Nd}(\tau)Y^*_{Ndr}(\tau+\tilde\tau)Y_{Nd}(\tau+\tilde\tau)\right\rangle+\left\langle Y_s(\tau)Y^*_{Nd}(\tau)|Y^*_{Ndr}(\tau+\tilde\tau)|^2\right\rangle$$
$$+\left\langle Y_s(\tau)Y^*_{Ndr}(\tau)|Y^*_s(\tau+\tilde\tau)|^2\right\rangle+\left\langle Y_s(\tau)Y^*_{Ndr}(\tau)Y^*_s(\tau+\tilde\tau)Y_{Nr}(\tau+\tilde\tau)\right\rangle$$
$$+\left\langle Y_s(\tau)Y^*_{Ndr}(\tau)Y^*_s(\tau+\tilde\tau)Y_{Nd}(\tau+\tilde\tau)\right\rangle+\left\langle Y_s(\tau)Y^*_{Ndr}(\tau)Y^*_s(\tau+\tilde\tau)Y_{Ndr}(\tau+\tilde\tau)\right\rangle$$
$$+\left\langle Y_s(\tau)Y^*_{Ndr}(\tau)Y^*_{Nr}(\tau+\tilde\tau)Y_s(\tau+\tilde\tau)\right\rangle+\left\langle Y_s(\tau)Y^*_{Ndr}(\tau)|Y^*_{Nr}(\tau+\tilde\tau)|^2\right\rangle$$
$$+\left\langle Y_s(\tau)Y^*_{Ndr}(\tau)Y^*_{Nr}(\tau+\tilde\tau)Y_{Nd}(\tau+\tilde\tau)\right\rangle+\left\langle Y_s(\tau)Y^*_{Ndr}(\tau)Y^*_{Nr}(\tau+\tilde\tau)Y_{Ndr}(\tau+\tilde\tau)\right\rangle$$
$$+\left\langle Y_s(\tau)Y^*_{Ndr}(\tau)Y^*_{Nd}(\tau+\tilde\tau)Y_s(\tau+\tilde\tau)\right\rangle+\left\langle Y_s(\tau)Y^*_{Ndr}(\tau)Y^*_{Nd}(\tau+\tilde\tau)Y_{Nr}(\tau+\tilde\tau)\right\rangle$$
$$+\left\langle Y_s(\tau)Y^*_{Ndr}(\tau)|Y^*_{Nd}(\tau+\tilde\tau)|^2\right\rangle+\left\langle Y_s(\tau)Y^*_{Ndr}(\tau)Y^*_{Nd}(\tau+\tilde\tau)Y_{Ndr}(\tau+\tilde\tau)\right\rangle$$
$$+\left\langle Y_s(\tau)Y^*_{Ndr}(\tau)Y^*_{Ndr}(\tau+\tilde\tau)Y_s(\tau+\tilde\tau)\right\rangle+\left\langle Y_s(\tau)Y^*_{Ndr}(\tau)Y^*_{Ndr}(\tau+\tilde\tau)Y_{Nr}(\tau+\tilde\tau)\right\rangle$$
$$+\left\langle Y_s(\tau)Y^*_{Ndr}(\tau)Y^*_{Ndr}(\tau+\tilde\tau)Y_{Nd}(\tau+\tilde\tau)\right\rangle+\left\langle Y_s(\tau)Y^*_{Ndr}(\tau)|Y^*_{Ndr}(\tau+\tilde\tau)|^2\right\rangle$$
$$+\left\langle Y_{Nr}(\tau)Y^*_s(\tau)|Y_s(\tau+\tilde\tau)|^2\right\rangle+\left\langle Y_{Nr}(\tau)Y^*_a(\tau)Y^*_s(\tau+\tilde\tau)Y_{Nr}(\tau+\tilde\tau)\right\rangle$$
$$+\left\langle Y_{Nr}(\tau)Y^*_s(\tau)Y^*_s(\tau+\tilde\tau)Y_{Nd}(\tau+\tilde\tau)\right\rangle+\left\langle Y_{Nr}(\tau)Y^*_a(\tau)Y^*_s(\tau+\tilde\tau)Y_{Ndr}(\tau+\tilde\tau)\right\rangle$$
$$+\left\langle Y_{Nr}(\tau)Y^*_s(\tau)Y^*_{Nr}(\tau+\tilde\tau)Y_s(\tau+\tilde\tau)\right\rangle+\left\langle Y_{Nr}(\tau)Y^*_s(\tau)|Y_{Nr}(\tau+\tilde\tau)|^2\right\rangle$$
$$+\left\langle Y_{Nr}(\tau)Y^*_s(\tau)Y^*_{Nr}(\tau+\tilde\tau)Y_{Nd}(\tau+\tilde\tau)\right\rangle+\left\langle Y_{Nr}(\tau)Y^*_s(\tau)Y^*_{Nr}(\tau+\tilde\tau)Y_{Ndr}(\tau+\tilde\tau)\right\rangle$$
$$+\left\langle Y_{Nr}(\tau)Y^*_s(\tau)Y^*_{Nd}(\tau+\tilde\tau)Y_s(\tau+\tilde\tau)\right\rangle+\left\langle Y_{Nr}(\tau)Y^*_s(\tau)Y^*_{Nd}(\tau+\tilde\tau)Y_{Nr}(\tau+\tilde\tau)\right\rangle$$
$$+\left\langle Y_{Nr}(\tau)Y^*_s(\tau)|Y_{Nd}(\tau+\tilde\tau)|^2\right\rangle+\left\langle Y_{Nr}(\tau)Y^*_s(\tau)Y^*_{Nd}(\tau+\tilde\tau)Y_{Ndr}(\tau+\tilde\tau)\right\rangle$$
$$+\left\langle Y_{Nr}(\tau)Y^*_s(\tau)Y^*_{Ndr}(\tau+\tilde\tau)Y_s(\tau+\tilde\tau)\right\rangle+\left\langle Y_{Nr}(\tau)Y^*_s(\tau)Y^*_{Ndr}(\tau+\tilde\tau)Y_{Nr}(\tau+\tilde\tau)\right\rangle$$
$$+\left\langle Y_{Nr}(\tau)Y^*_s(\tau)Y^*_{Ndr}(\tau+\tilde\tau)Y_{Nd}(\tau+\tilde\tau)\right\rangle+\left\langle Y_{Nr}(\tau)Y^*_s(\tau)|Y_{Ndr}(\tau+\tilde\tau)|^2\right\rangle$$
$$+\left\langle |Y_{Nr}(\tau)|^2|Y_s(\tau+\tilde\tau)|^2\right\rangle+\left\langle |Y_{Nr}(\tau)|^2Y^*_s(\tau+\tilde\tau)Y_{Nr}(\tau+\tilde\tau)\right\rangle$$
$$+\left\langle |Y_{Nr}(\tau)|^2Y^*_s(\tau+\tilde\tau)Y_{Nd}(\tau+\tilde\tau)\right\rangle+\left\langle |Y_{Nr}(\tau)|^2Y^*_s(\tau+\tilde\tau)Y_{Ndr}(\tau+\tilde\tau)\right\rangle$$

$$
\begin{aligned}
&+ \left\langle |Y_{Nr}(\tau)|^2 Y^*_{Nr}(\tau+\tilde{\tau}) Y_s(\tau+\tilde{\tau}) \right\rangle + \left\langle |Y_{Nr}(\tau)|^2 |Y_{Nr}(\tau+\tilde{\tau})|^2 \right\rangle \\
&+ \left\langle |Y_{Nr}(\tau)|^2 Y^*_{Nr}(\tau+\tilde{\tau}) Y_{Nd}(\tau+\tilde{\tau}) \right\rangle + \left\langle |Y_{Nr}(\tau)|^2 Y^*_{Nr}(\tau+\tilde{\tau}) Y_{Ndr}(\tau+\tilde{\tau}) \right\rangle \\
&+ \left\langle |Y_{Nr}(\tau)|^2 Y^*_{Nd}(\tau+\tilde{\tau}) Y_s(\tau+\tilde{\tau}) \right\rangle + \left\langle |Y_{Nr}(\tau)|^2 Y^*_{Nd}(\tau+\tilde{\tau}) Y_{Nr}(\tau+\tilde{\tau}) \right\rangle \\
&+ \left\langle |Y_{Nr}(\tau)|^2 |Y_{Nd}(\tau+\tilde{\tau})|^2 \right\rangle + \left\langle |Y_{Nr}(\tau)|^2 Y^*_{Nd}(\tau+\tilde{\tau}) Y_{Ndr}(\tau+\tilde{\tau}) \right\rangle \\
&+ \left\langle |Y_{Nr}(\tau)|^2 Y^*_{Ndr}(\tau+\tilde{\tau}) Y_s(\tau+\tilde{\tau}) \right\rangle + \left\langle |Y_{Nr}(\tau)|^2 Y^*_{Ndr}(\tau+\tilde{\tau}) Y_{Nr}(\tau+\tilde{\tau}) \right\rangle \\
&+ \left\langle |Y_{Nr}(\tau)|^2 Y^*_{Ndr}(\tau+\tilde{\tau}) Y_{Nd}(\tau+\tilde{\tau}) \right\rangle + \left\langle |Y_{Nr}(\tau)|^2 |Y_{Ndr}(\tau+\tilde{\tau})|^2 \right\rangle \\
&+ \left\langle Y_{Nr}(\tau) Y^*_{Nd}(\tau) |Y_s(\tau+\tilde{\tau})|^2 \right\rangle + \left\langle Y_{Nr}(\tau) Y^*_{Nd}(\tau) Y^*_s(\tau+\tilde{\tau}) Y_{Nr}(\tau+\tilde{\tau}) \right\rangle \\
&+ \left\langle Y_{Nr}(\tau) Y^*_{Nd}(\tau) Y^*_s(\tau+\tilde{\tau}) Y_{Nd}(\tau+\tilde{\tau}) \right\rangle + \left\langle Y_{Nr}(\tau) Y^*_{Nd}(\tau) Y^*_s(\tau+\tilde{\tau}) Y_{Ndr}(\tau+\tilde{\tau}) \right\rangle \\
&+ \left\langle Y_{Nr}(\tau) Y^*_{Nd}(\tau) Y^*_{Nr}(\tau+\tilde{\tau}) Y_s(\tau+\tilde{\tau}) \right\rangle + \left\langle Y_{Nr}(\tau) Y^*_{Nd}(\tau) |Y_{Nr}(\tau+\tilde{\tau})|^2 \right\rangle \Big\rangle \\
&+ \left\langle Y_{Nr}(\tau) Y^*_{Nd}(\tau) Y^*_{Nr}(\tau+\tilde{\tau}) Y_{Nd}(\tau+\tilde{\tau}) \right\rangle + \left\langle Y_{Nr}(\tau) Y^*_{Nd}(\tau) Y^*_{Nr}(\tau+\tilde{\tau}) Y_{Ndr}(\tau+\tilde{\tau}) \right\rangle \\
&+ \left\langle Y_{Nr}(\tau) Y^*_{Nd}(\tau) Y^*_{Nd}(\tau+\tilde{\tau}) Y_s(\tau+\tilde{\tau}) \right\rangle + \left\langle Y_{Nr}(\tau) Y^*_{Nd}(\tau) Y^*_{Nd}(\tau+\tilde{\tau}) Y_{Nr}(\tau+\tilde{\tau}) \right\rangle \\
&+ \left\langle Y_{Nr}(\tau) Y^*_{Nd}(\tau) |Y^*_{Nd}(\tau+\tilde{\tau})|^2 \right\rangle + \left\langle Y_{Nr}(\tau) Y^*_{Nd}(\tau) Y^*_{Nd}(\tau+\tilde{\tau}) Y_{Ndr}(\tau+\tilde{\tau}) \right\rangle \\
&+ \left\langle Y_{Nr}(\tau) Y^*_{Nd}(\tau) Y^*_{Ndr}(\tau+\tilde{\tau}) Y_s(\tau+\tilde{\tau}) \right\rangle + \left\langle Y_{Nr}(\tau) Y^*_{Nd}(\tau) Y^*_{Ndr}(\tau+\tilde{\tau}) Y_{Nr}(\tau+\tilde{\tau}) \right. \\
&+ \left\langle Y_{Nr}(\tau) Y^*_{Nd}(\tau) Y^*_{Ndr}(\tau+\tilde{\tau}) Y_{Nd}(\tau+\tilde{\tau}) \right\rangle + \left\langle Y_{Nr}(\tau) Y^*_{Nd}(\tau) |Y_{Ndr}(\tau+\tilde{\tau})|^2 \right\rangle \\
&+ \left\langle Y_{Nr}(\tau) Y^*_{Ndr}(\tau) |Y_s(\tau+\tilde{\tau})|^2 \right\rangle + \left\langle Y_{Nr}(\tau) Y^*_{Ndr}(\tau) Y^*_s(\tau+\tilde{\tau}) Y_{Nr}(\tau+\tilde{\tau}) \right\rangle \\
&+ \left\langle Y_{Nr}(\tau) Y^*_{Ndr}(\tau) Y^*_s(\tau+\tilde{\tau}) Y_{Nd}(\tau+\tilde{\tau}) \right\rangle \left\langle Y_{Nr}(\tau) Y^*_{Ndr}(\tau) Y^*_s(\tau+\tilde{\tau}) Y_{Ndr}(\tau+\tilde{\tau}) \right\rangle \\
&+ \left\langle Y_{Nr}(\tau) Y^*_{Ndr}(\tau) Y^*_{Nr}(\tau+\tilde{\tau}) Y_s(\tau+\tilde{\tau}) \right\rangle + \left\langle Y_{Nr}(\tau) Y^*_{Ndr}(\tau) |Y_{Nr}(\tau+\tilde{\tau})|^2 \right\rangle \\
&+ \left\langle Y_{Nr}(\tau) Y^*_{Ndr}(\tau) Y^*_{Nr}(\tau+\tilde{\tau}) Y_{Nd}(\tau+\tilde{\tau}) \right\rangle \left\langle Y_{Nr}(\tau) Y^*_{Ndr}(\tau) Y^*_{Nr}(\tau+\tilde{\tau}) Y_{Ndr}(\tau+\tilde{\tau}) \right\rangle \\
&+ \left\langle Y_{Nr}(\tau) Y^*_{Ndr}(\tau) Y^*_{Nd}(\tau+\tilde{\tau}) Y_s(\tau+\tilde{\tau}) \right\rangle \left\langle Y_{Nr}(\tau) Y^*_{Ndr}(\tau) Y^*_{Nd}(\tau+\tilde{\tau}) Y_{Nr}(\tau+\tilde{\tau}) \right\rangle \\
&+ \left\langle Y_{Nr}(\tau) Y^*_{Ndr}(\tau) Y^*_{Nd}(\tau+\tilde{\tau}) Y_s(\tau+\tilde{\tau}) \right\rangle \left\langle Y_{Nr}(\tau) Y^*_{Ndr}(\tau) Y^*_{Nd}(\tau+\tilde{\tau}) Y_{Nr}(\tau+\tilde{\tau}) \right\rangle \\
&+ \left\langle Y_{Nr}(\tau) Y^*_{Ndr}(\tau) |Y^*_{Nd}(\tau+\tilde{\tau})|^2 \right\rangle \left\langle Y_{Nr}(\tau) Y^*_{Ndr}(\tau) Y^*_{Nd}(\tau+\tilde{\tau}) Y_{Ndr}(\tau+\tilde{\tau}) \right\rangle \\
&+ \left\langle Y_{Nr}(\tau) Y^*_{Ndr}(\tau) Y^*_{Ndr}(\tau+\tilde{\tau}) Y_s(\tau+\tilde{\tau}) \right\rangle \left\langle Y_{Nr}(\tau) Y^*_{Ndr}(\tau) Y^*_{Ndr}(\tau+\tilde{\tau}) Y_{Nr}(\tau+\tilde{\tau}) \right\rangle \\
&+ \left\langle Y_{Nr}(\tau) Y^*_{Ndr}(\tau) Y^*_{Ndr}(\tau+\tilde{\tau}) Y_{Nd}(\tau+\tilde{\tau}) \right\rangle + \left\langle Y_{Nr}(\tau) Y^*_{Ndr}(\tau) |Y_{Ndr}(\tau+\tilde{\tau})|^2 \right\rangle \\
&+ \left\langle Y_{Nd}(\tau) Y^*_s(\tau) |Y_s(\tau+\tilde{\tau})|^2 \right\rangle + \left\langle Y_{Nd}(\tau) Y^*_s(\tau) Y^*_s(\tau+\tilde{\tau}) Y_{Nr}(\tau+\tilde{\tau}) \right\rangle \\
&+ \left\langle Y_{Nd}(\tau) Y^*_s(\tau) Y^*_s(\tau+\tilde{\tau}) Y_{Nd}(\tau+\tilde{\tau}) \right\rangle + \left\langle Y_{Nd}(\tau) Y^*_s(\tau) Y^*_s(\tau+\tilde{\tau}) Y_{Ndr}(\tau+\tilde{\tau}) \right\rangle \\
&+ \left\langle Y_{Nd}(\tau) Y^*_s(\tau) Y^*_{Nr}(\tau+\tilde{\tau}) Y_s(\tau+\tilde{\tau}) \right\rangle + \left\langle Y_{Nd}(\tau) Y^*_s(\tau) |Y_{Nr}(\tau+\tilde{\tau})|^2 \right\rangle \\
&+ \left\langle Y_{Nd}(\tau) Y^*_s(\tau) Y^*_{Nr}(\tau+\tilde{\tau}) Y_{Nd}(\tau+\tilde{\tau}) \right\rangle + \left\langle Y_{Nd}(\tau) Y^*_s(\tau) Y^*_{Nr}(\tau+\tilde{\tau}) Y_{Ndr}(\tau+\tilde{\tau}) \right\rangle \\
&+ \left\langle Y_{Nd}(\tau) Y^*_s(\tau) Y^*_{Nd}(\tau+\tilde{\tau}) Y_s(\tau+\tilde{\tau}) \right\rangle + \left\langle Y_{Nd}(\tau) Y^*_s(\tau) Y^*_{Nd}(\tau+\tilde{\tau}) Y_{Nr}(\tau+\tilde{\tau}) \right\rangle \\
&+ \left\langle Y_{Nd}(\tau) Y^*_s(\tau) |Y_{Nd}(\tau+\tilde{\tau})|^2 \right\rangle + \left\langle Y_{Nd}(\tau) Y^*_s(\tau) Y^*_{Nd}(\tau+\tilde{\tau}) Y_{Ndr}(\tau+\tilde{\tau}) \right\rangle
\end{aligned}
$$

$$
\begin{aligned}
&+ \left\langle Y_{Nd}(\tau)Y_s^*(\tau)Y_{Ndr}^*(\tau+\tilde{\tau})Y_s(\tau+\tilde{\tau})\right\rangle + \left\langle Y_{Nd}(\tau)Y_s^*(\tau)Y_{Ndr}^*(\tau+\tilde{\tau})Y_{Nr}(\tau+\tilde{\tau})\right\rangle \\
&+ \left\langle Y_{Nd}(\tau)Y_s^*(\tau)Y_{Ndr}^*(\tau+\tilde{\tau})Y_{Nd}(\tau+\tilde{\tau})\right\rangle + \left\langle Y_{Nd}(\tau)Y_s^*(\tau)|Y_{Ndr}(\tau+\tilde{\tau})|^2\right\rangle \\
&+ \left\langle Y_{Nd}(\tau)Y_{Nr}^*(\tau)|Y_s(\tau+\tilde{\tau})|^2\right\rangle + \left\langle Y_{Nd}(\tau)Y_{Nr}^*(\tau)Y_s^*(\tau+\tilde{\tau})Y_{Nr}(\tau+\tilde{\tau})\right\rangle \\
&+ \left\langle Y_{Nd}(\tau)Y_{Nr}^*(\tau)Y_s^*(\tau+\tilde{\tau})Y_{Nd}(\tau+\tilde{\tau})\right\rangle + \left\langle Y_{Nd}(\tau)Y_{Nr}^*(\tau)Y_s^*(\tau+\tilde{\tau})Y_{Ndr}(\tau+\tilde{\tau})\right\rangle \\
&+ \left\langle Y_{Nd}(\tau)Y_{Nr}^*(\tau)Y_{Nr}^*(\tau+\tilde{\tau})Y_s(\tau+\tilde{\tau})\right\rangle + \left\langle Y_{Nd}(\tau)Y_{Nr}^*(\tau)|Y_{Nr}(\tau+\tilde{\tau})|^2\right\rangle \\
&+ \left\langle Y_{Nd}(\tau)Y_{Nr}^*(\tau)Y_{Nr}^*(\tau+\tilde{\tau})Y_{Nd}(\tau+\tilde{\tau})\right\rangle + \left\langle Y_{Nd}(\tau)Y_{Nr}^*(\tau)Y_{Nr}^*(\tau+\tilde{\tau})Y_{Ndr}(\tau+\tilde{\tau})\right\rangle \\
&+ \left\langle Y_{Nd}(\tau)Y_{Nr}^*(\tau)Y_{Nd}^*(\tau+\tilde{\tau})Y_s(\tau+\tilde{\tau})\right\rangle + \left\langle Y_{Nd}(\tau)Y_{Nr}^*(\tau)Y_{Nd}^*(\tau+\tilde{\tau})Y_{Nr}(\tau+\tilde{\tau})\right\rangle \\
&+ \left\langle Y_{Nd}(\tau)Y_{Nr}^*(\tau)|Y_{Nd}(\tau+\tilde{\tau})|^2\right\rangle + \left\langle Y_{Nd}(\tau)Y_{Nr}^*(\tau)Y_{Nd}^*(\tau+\tilde{\tau})Y_{Ndr}(\tau+\tilde{\tau})\right\rangle \\
&+ \left\langle Y_{Nd}(\tau)Y_{Nr}^*(\tau)Y_{Ndr}^*(\tau+\tilde{\tau})Y_s(\tau+\tilde{\tau})\right\rangle + \left\langle Y_{Nd}(\tau)Y_{Nr}^*(\tau)Y_{Ndr}^*(\tau+\tilde{\tau})Y_{Nr}(\tau+\tilde{\tau})\right\rangle \\
&+ \left\langle Y_{Nd}(\tau)Y_{Nr}^*(\tau)Y_{Ndr}^*(\tau+\tilde{\tau})Y_{Nd}(\tau+\tilde{\tau})\right\rangle + \left\langle Y_{Nd}(\tau)Y_{Nr}^*(\tau)|Y_{Ndr}(\tau+\tilde{\tau})|^2\right\rangle \\
&+ \left\langle |Y_{Nd}(\tau)|^2|Y_s(\tau+\tilde{\tau})|^2\right\rangle + \left\langle |Y_{Nd}(\tau)|^2Y_s^*(\tau+\tilde{\tau})Y_{Nr}(\tau+\tilde{\tau})\right\rangle \\
&+ \left\langle |Y_{Nd}(\tau)|^2Y_s^*(\tau+\tilde{\tau})Y_{Nd}(\tau+\tilde{\tau})\right\rangle + \left\langle |Y_{Nd}(\tau)|^2Y_s^*(\tau+\tilde{\tau})Y_{Ndr}(\tau+\tilde{\tau})\right\rangle \\
&+ \left\langle |Y_{Nd}(\tau)|^2Y_{Nr}^*(\tau+\tilde{\tau})Y_s(\tau+\tilde{\tau})\right\rangle + \left\langle |Y_{Nd}(\tau)|^2|Y_{Nr}(\tau+\tilde{\tau})|^2\right\rangle\rangle \\
&+ \left\langle |Y_{Nd}(\tau)|^2Y_{Nr}^*(\tau+\tilde{\tau})Y_{Nd}(\tau+\tilde{\tau})\right\rangle + \left\langle |Y_{Nd}(\tau)|^2Y_{Nr}^*(\tau+\tilde{\tau})Y_{Ndr}(\tau+\tilde{\tau})\right\rangle \\
&+ \left\langle |Y_{Nd}(\tau)|^2Y_{Nd}^*(\tau+\tilde{\tau})Y_s(\tau+\tilde{\tau})\right\rangle + \left\langle |Y_{Nd}(\tau)|^2Y_{Nd}^*(\tau+\tilde{\tau})Y_{Nr}(\tau+\tilde{\tau})\right\rangle \\
&+ \left\langle |Y_{Nd}(\tau)|^2|Y_{Nd}(\tau+\tilde{\tau})|^2\right\rangle + \left\langle |Y_{Nd}(\tau)|^2Y_{Nd}^*(\tau+\tilde{\tau})Y_{Ndr}(\tau+\tilde{\tau})\right\rangle \\
&+ \left\langle |Y_{Nd}(\tau)|^2Y_{Ndr}^*(\tau+\tilde{\tau})Y_s(\tau+\tilde{\tau})\right\rangle + \left\langle |Y_{Nd}(\tau)|^2Y_{Ndr}^*(\tau+\tilde{\tau})Y_{Nr}(\tau+\tilde{\tau})\right\rangle \\
&+ \left\langle |Y_{Nd}(\tau)|^2Y_{Ndr}^*(\tau+\tilde{\tau})Y_{Nd}(\tau+\tilde{\tau})\right\rangle + \left\langle |Y_{Nd}(\tau)|^2|Y_{Ndr}(\tau+\tilde{\tau})|^2\right\rangle\rangle \\
&+ \left\langle Y_{Nd}(\tau)Y_{Ndr}^*(\tau)|Y_s(\tau+\tilde{\tau})|^2\right\rangle + \left\langle Y_{Nd}(\tau)Y_{Ndr}^*(\tau)Y_s^*(\tau+\tilde{\tau})Y_{Nr}(\tau+\tilde{\tau})\right\rangle \\
&+ \left\langle Y_{Nd}(\tau)Y_{Ndr}^*(\tau)Y_{Nr}^*(\tau+\tilde{\tau})Y_s(\tau+\tilde{\tau})\right\rangle + \left\langle Y_{Nd}(\tau)Y_{Ndr}^*(\tau)|Y_{Nr}(\tau+\tilde{\tau})|^2\right\rangle \\
&+ \left\langle Y_{Nd}(\tau)Y_{Ndr}^*(\tau)Y_{Nr}^*(\tau+\tilde{\tau})Y_{Nd}(\tau+\tilde{\tau})\right\rangle + \left\langle Y_{Nd}(\tau)Y_{Ndr}^*(\tau)Y_{Nr}^*(\tau+\tilde{\tau})Y_{Ndr}(\tau+\tilde{\tau})\right\rangle\rangle \\
&+ \left\langle Y_{Nd}(\tau)Y_{Ndr}^*(\tau)Y_{Nd}^*(\tau+\tilde{\tau})Y_s(\tau+\tilde{\tau})\right\rangle + \left\langle Y_{Nd}(\tau)Y_{Ndr}^*(\tau)Y_{Nd}^*(\tau+\tilde{\tau})Y_{Nr}(\tau+\tilde{\tau})\right\rangle\rangle \\
&+ \left\langle Y_{Nd}(\tau)Y_{Ndr}^*(\tau)|Y_{Nd}(\tau+\tilde{\tau})|^2\right\rangle + \left\langle Y_{Nd}(\tau)Y_{Ndr}^*(\tau)Y_{Nd}^*(\tau+\tilde{\tau})Y_{Ndr}(\tau+\tilde{\tau})\right\rangle\rangle \\
&+ \left\langle Y_{Nd}(\tau)Y_{Ndr}^*(\tau)Y_{Ndr}^*(\tau+\tilde{\tau})Y_s(\tau+\tilde{\tau})\right\rangle + \left\langle Y_{Nd}(\tau)Y_{Ndr}^*(\tau)Y_{Ndr}^*(\tau+\tilde{\tau})Y_{Nr}(\tau+\tilde{\tau})\right\rangle \\
&+ \left\langle Y_{Nd}(\tau)Y_{Ndr}^*(\tau)Y_{Ndr}^*(\tau+\tilde{\tau})Y_{Nd}(\tau+\tilde{\tau})\right\rangle + \left\langle Y_{Nd}(\tau)Y_{Ndr}^*(\tau)|Y_{Ndr}(\tau+\tilde{\tau})|^2\right\rangle \\
&+ \left\langle Y_{Ndr}(\tau)Y_s^*(\tau)|Y_s(\tau+\tilde{\tau})|^2\right\rangle + \left\langle Y_{Ndr}(\tau)Y_s^*(\tau)Y_s^*(\tau+\tilde{\tau})Y_{Nr}(\tau+\tilde{\tau})\right\rangle \\
&+ \left\langle Y_{Ndr}(\tau)Y_s^*(\tau)Y_s^*(\tau+\tilde{\tau})Y_{Nd}(\tau+\tilde{\tau})\right\rangle + \left\langle Y_{Ndr}(\tau)Y_s^*(\tau)Y_s^*(\tau+\tilde{\tau})Y_{Ndr}(\tau+\tilde{\tau})\right\rangle \\
&+ \left\langle Y_{Ndr}(\tau)Y_s^*(\tau)Y_{Nr}^*(\tau+\tilde{\tau})Y_s(\tau+\tilde{\tau})\right\rangle + \left\langle Y_{Ndr}(\tau)Y_s^*(\tau)|Y_{Nr}(\tau+\tilde{\tau})|^2\right\rangle \\
&+ \left\langle Y_{Ndr}(\tau)Y_s^*(\tau)Y_{Nr}^*(\tau+\tilde{\tau})Y_{Nd}(\tau+\tilde{\tau})\right\rangle + \left\langle Y_{Ndr}(\tau)Y_s^*(\tau)Y_{Nr}^*(\tau+\tilde{\tau})Y_{Ndr}(\tau+\tilde{\tau})\right\rangle
\end{aligned}
$$

$$
\begin{aligned}
&+\left\langle Y_{Ndr}(\tau)Y_s^*(\tau)Y_{Nd}^*(\tau+\tilde{\tau})Y_s(\tau+\tilde{\tau})\right\rangle + \left\langle Y_{Ndr}(\tau)Y_s^*(\tau)Y_{Nd}^*(\tau+\tilde{\tau})Y_{Nr}(\tau+\tilde{\tau})\right\rangle \\
&+\left\langle Y_{Ndr}(\tau)Y_s^*(\tau)|Y_{Nd}(\tau+\tilde{\tau})|^2\right\rangle + \left\langle Y_{Ndr}(\tau)Y_s^*(\tau)Y_{Nd}^*(\tau+\tilde{\tau})Y_{Ndr}(\tau+\tilde{\tau})\right\rangle \\
&+\left\langle Y_{Ndr}(\tau)Y_s^*(\tau)Y_{Ndr}^*(\tau+\tilde{\tau})Y_s(\tau+\tilde{\tau})\right\rangle + \left\langle Y_{Ndr}(\tau)Y_s^*(\tau)Y_{Ndr}^*(\tau+\tilde{\tau})Y_{Nr}(\tau+\tilde{\tau})\right\rangle \\
&+\left\langle Y_{Ndr}(\tau)Y_s^*(\tau)Y_{Ndr}^*(\tau+\tilde{\tau})Y_{Nd}(\tau+\tilde{\tau})\right\rangle + \left\langle Y_{Ndr}(\tau)Y_s^*(\tau)|Y_{Ndr}(\tau+\tilde{\tau})|^2\right\rangle \\
&+\left\langle Y_{Ndr}(\tau)Y_{Nr}^*(\tau)|Y_s(\tau+\tilde{\tau})|^2\right\rangle + \left\langle Y_{Ndr}(\tau)Y_{Nr}^*(\tau)Y_s^*(\tau+\tilde{\tau})Y_{Nr}(\tau+\tilde{\tau})\right\rangle \\
&+\left\langle Y_{Ndr}(\tau)Y_{Nr}^*(\tau)Y_s^*(\tau+\tilde{\tau})Y_{Nd}(\tau+\tilde{\tau})\right\rangle + \left\langle Y_{Ndr}(\tau)Y_{Nr}^*(\tau)Y_s^*(\tau+\tilde{\tau})Y_{Ndr}(\tau+\tilde{\tau})\right\rangle \\
&+\left\langle Y_{Ndr}(\tau)Y_{Nr}^*(\tau)Y_{Nr}^*(\tau+\tilde{\tau})Y_s(\tau+\tilde{\tau})\right\rangle + \left\langle Y_{Ndr}(\tau)Y_{Nr}^*(\tau)|Y_{Nr}(\tau+\tilde{\tau})|^2\right\rangle \\
&+\left\langle Y_{Ndr}(\tau)Y_{Nr}^*(\tau)Y_{Nr}^*(\tau+\tilde{\tau})Y_{Nd}(\tau+\tilde{\tau})\right\rangle + \left\langle Y_{Ndr}(\tau)Y_{Nr}^*(\tau)Y_{Nr}^*(\tau+\tilde{\tau})Y_{Ndr}(\tau+\tilde{\tau})\right\rangle \\
&+\left\langle Y_{Ndr}(\tau)Y_{Nr}^*(\tau)Y_{Nd}^*(\tau+\tilde{\tau})Y_s(\tau+\tilde{\tau})\right\rangle + \left\langle Y_{Ndr}(\tau)Y_{Nr}^*(\tau)Y_{Nd}^*(\tau+\tilde{\tau})Y_{Nr}(\tau+\tilde{\tau})\right\rangle \\
&+\left\langle Y_{Ndr}(\tau)Y_{Nr}^*(\tau)|Y_{Nd}(\tau+\tilde{\tau})|^2\right\rangle + \left\langle Y_{Ndr}(\tau)Y_{Nr}^*(\tau)Y_{Nd}^*(\tau+\tilde{\tau})Y_{Ndr}(\tau+\tilde{\tau})\right\rangle \\
&+\left\langle Y_{Ndr}(\tau)Y_{Nr}^*(\tau)Y_{Ndr}^*(\tau+\tilde{\tau})Y_s(\tau+\tilde{\tau})\right\rangle + \left\langle Y_{Ndr}(\tau)Y_{Nr}^*(\tau)Y_{Ndr}^*(\tau+\tilde{\tau})Y_{Nr}(\tau+\tilde{\tau})\right\rangle \\
&+\left\langle Y_{Ndr}(\tau)Y_{Nr}^*(\tau)Y_{Ndr}^*(\tau+\tilde{\tau})Y_{Nd}(\tau+\tilde{\tau})\right\rangle + \left\langle Y_{Ndr}(\tau)Y_{Nr}^*(\tau)|Y_{Ndr}(\tau+\tilde{\tau})|^2\right\rangle \\
&+\left\langle Y_{Ndr}(\tau)Y_{Nd}^*(\tau)|Y_s(\tau+\tilde{\tau})|^2\right\rangle + \left\langle Y_{Ndr}(\tau)Y_{Nd}^*(\tau)Y_s^*(\tau+\tilde{\tau})Y_{Nr}(\tau+\tilde{\tau})\right\rangle \\
&+\left\langle Y_{Ndr}(\tau)Y_{Nd}^*(\tau)Y_s^*(\tau+\tilde{\tau})Y_{Nd}(\tau+\tilde{\tau})\right\rangle + \left\langle Y_{Ndr}(\tau)Y_{Nd}^*(\tau)Y_s^*(\tau+\tilde{\tau})Y_{Ndr}(\tau+\tilde{\tau})\right\rangle \\
&+\left\langle Y_{Ndr}(\tau)Y_{Nd}^*(\tau)Y_{Nr}^*(\tau+\tilde{\tau})Y_s(\tau+\tilde{\tau})\right\rangle + \left\langle Y_{Ndr}(\tau)Y_{Nd}^*(\tau)|Y_{Nr}(\tau+\tilde{\tau})|^2\right\rangle \\
&+\left\langle Y_{Ndr}(\tau)Y_{Nd}^*(\tau)Y_{Nr}^*(\tau+\tilde{\tau})Y_{Nd}(\tau+\tilde{\tau})\right\rangle + \left\langle Y_{Ndr}(\tau)Y_{Nd}^*(\tau)Y_{Nr}^*(\tau+\tilde{\tau})Y_{Ndr}(\tau+\tilde{\tau})\right\rangle \\
&+\left\langle Y_{Ndr}(\tau)Y_{Nd}^*(\tau)Y_{Nd}^*(\tau+\tilde{\tau})Y_s(\tau+\tilde{\tau})\right\rangle + \left\langle Y_{Ndr}(\tau)Y_{Nd}^*(\tau)Y_{Nd}^*(\tau+\tilde{\tau})Y_{Nr}(\tau+\tilde{\tau})\right\rangle \\
&+\left\langle Y_{Ndr}(\tau)Y_{Nd}^*(\tau)|Y_{Nd}(\tau+\tilde{\tau})|^2\right\rangle + \left\langle Y_{Ndr}(\tau)Y_{Nd}^*(\tau)Y_{Nd}^*(\tau+\tilde{\tau})Y_{Ndr}(\tau+\tilde{\tau})\right\rangle \\
&+\left\langle Y_{Ndr}(\tau)Y_{Nd}^*(\tau)Y_{Ndr}^*(\tau+\tilde{\tau})Y_s(\tau+\tilde{\tau})\right\rangle + \left\langle Y_{Ndr}(\tau)Y_{Nd}^*(\tau)Y_{Ndr}^*(\tau+\tilde{\tau})Y_{Nr}(\tau+\tilde{\tau})\right\rangle \\
&+\left\langle Y_{Ndr}(\tau)Y_{Nd}^*(\tau)Y_{Ndr}^*(\tau+\tilde{\tau})Y_{Nd}(\tau+\tilde{\tau})\right\rangle + \left\langle Y_{Ndr}(\tau)Y_{Nd}^*(\tau)|Y_{Ndr}(\tau+\tilde{\tau})|^2\right\rangle \\
&+\left\langle |Y_{Ndr}(\tau)|^2|Y_s(\tau+\tilde{\tau})|^2\right\rangle + \left\langle |Y_{Ndr}(\tau)|^2Y_s^*(\tau+\tilde{\tau})Y_{Nr}(\tau+\tilde{\tau})\right\rangle \\
&+\left\langle |Y_{Ndr}(\tau)|^2Y_s^*(\tau+\tilde{\tau})Y_{Nd}(\tau+\tilde{\tau})\right\rangle + \left\langle |Y_{Ndr}(\tau)|^2Y_s^*(\tau+\tilde{\tau})Y_{Ndr}(\tau+\tilde{\tau})\right\rangle \\
&+\left\langle |Y_{Ndr}(\tau)|^2Y_{Nr}^*(\tau+\tilde{\tau})Y_s(\tau+\tilde{\tau})\right\rangle + \left\langle |Y_{Ndr}(\tau)|^2|Y_{Nr}(\tau+\tilde{\tau})|^2\right\rangle \\
&+\left\langle |Y_{Ndr}(\tau)|^2Y_{Nr}^*(\tau+\tilde{\tau})Y_{Nd}(\tau+\tilde{\tau})\right\rangle + \left\langle |Y_{Ndr}(\tau)|^2Y_{Nr}^*(\tau+\tilde{\tau})Y_{Ndr}(\tau+\tilde{\tau})\right\rangle \\
&+\left\langle |Y_{Ndr}(\tau)|^2Y_{Nd}^*(\tau+\tilde{\tau})Y_s(\tau+\tilde{\tau})\right\rangle + \left\langle |Y_{Ndr}(\tau)|^2Y_{Nd}^*(\tau+\tilde{\tau})Y_{Nr}(\tau+\tilde{\tau})\right\rangle \\
&+\left\langle |Y_{Ndr}(\tau)|^2|Y_{Nd}(\tau+\tilde{\tau})|^2\right\rangle + \left\langle |Y_{Ndr}(\tau)|^2Y_{Nd}^*(\tau+\tilde{\tau})Y_{Ndr}(\tau+\tilde{\tau})\right\rangle \\
&+\left\langle |Y_{Ndr}(\tau)|^2Y_{Ndr}^*(\tau+\tilde{\tau})Y_s(\tau+\tilde{\tau})\right\rangle + \left\langle |Y_{Ndr}(\tau)|^2Y_{Ndr}^*(\tau+\tilde{\tau})Y_{Nr}(\tau+\tilde{\tau})\right\rangle \\
&+\left\langle |Y_{Ndr}(\tau)|^2Y_{Ndr}^*(\tau+\tilde{\tau})Y_{Nd}(\tau+\tilde{\tau})\right\rangle + \left\langle |Y_{Ndr}(\tau)|^2|Y_{Ndr}(\tau+\tilde{\tau})|^2\right\rangle
\end{aligned}
\tag{E.3}
$$

following the same procedure of Appendix D, Equ. (E.3) is reduced to:

$$
\begin{aligned}
C =&\big\langle |Y(\tau)|^2 |Y(\tau+\tilde{\tau})|^2 \big\rangle \\
=&|C_{Y_s}(\tilde{\tau})|^2 + |C_{Y_s}(0)|^2 + C_{Y_s}(0)C_{Y_{Nr}}(0) + C_{Y_s}(0)C_{Y_{Nd}}(0) + C_{Y_s}(0)C_{Y_{Ndr}}(0) \\
&+ C_{Y_s}(\tilde{\tau})C_{Y_{Nr}}(\tilde{\tau}) + C_{Y_s}(\tilde{\tau})C_{Y_{Nd}}(\tilde{\tau}) + C_{Y_s}(\tilde{\tau})C_{Y_{Ndr}}(\tilde{\tau}) + C_{Y_s}(\tilde{\tau})C_{Y_{Nr}}(\tilde{\tau}) \\
&+ C_{Y_{Nr}}(0)C_{Y_s}(0) + |C_{Y_{Nr}}(0)|^2 + |C_{Y_{Nr}}(\tilde{\tau})|^2 + C_{Y_{Nr}}(0)C_{Y_{Nd}}(0) + C_{Y_{Nr}}(0)C_{Y_{Ndr}}(0) \\
&+ C_{Y_{Nr}}(\tilde{\tau})C_{Y_{Nd}}(\tilde{\tau}) + C_{Y_{Nr}}(\tilde{\tau})C_{Y_{Ndr}}(\tilde{\tau}) + C_{Y_{Nd}}(\tilde{\tau})C_{Y_s}(\tilde{\tau}) + C_{Y_{Nd}}(\tilde{\tau})C_{Y_{Nr}}(\tilde{\tau}) \\
&+ C_{Y_{Nd}}(0)C_{Y_s}(0) + C_{Y_{Nd}}(0)C_{Y_{Nr}}(0) + |C_{Y_{Nd}}(0)|^2 + |C_{Y_{Nd}}(\tilde{\tau})|^2 + C_{Y_{Nd}}(\tilde{\tau})C_{Y_{Ndr}}(\tilde{\tau}) \\
&+ C_{Y_{Nd}}(\tilde{\tau})C_{Y_{Ndr}}(\tilde{\tau}) + C_{Y_{Ndr}}(\tilde{\tau})C_{Y_s}(\tilde{\tau}) + C_{Y_{Ndr}}(\tilde{\tau})C_{Y_{Nr}}(\tilde{\tau}) + C_{Y_{Ndr}}(\tilde{\tau})C_{Y_{Nd}}(\tilde{\tau}) \\
&+ C_{Y_{Ndr}}(0)C_{Y_s}(0) + C_{Y_{Ndr}}(0)C_{Y_{Nr}}(0) + C_{Y_{Ndr}}(0)C_{Y_{Nd}}(0) + |C_{Y_{Ndr}}(0)|^2 + |C_{Y_{Ndr}}(\tilde{\tau})|^2 \\
=&|C_{Y_s}(\tilde{\tau})|^2 + |C_{Y_{Nr}}(\tilde{\tau})|^2 + |C_{Y_{Nd}}(\tilde{\tau})|^2 + |C_{Y_{Ndr}}(\tilde{\tau})|^2 \\
&+ 2C_{Y_s}(\tilde{\tau})C_{Y_{Nr}}(\tilde{\tau}) + 2C_{Y_s}(\tilde{\tau})C_{Y_{Nd}}(\tilde{\tau}) + 2C_{Y_s}(\tilde{\tau})C_{Y_{Ndr}}(\tilde{\tau}) \\
&+ 2C_{Y_{Nr}}(\tilde{\tau})C_{Y_{Nd}}(\tilde{\tau}) + 2C_{Y_{Nr}}(\tilde{\tau})C_{Y_{Ndr}}(\tilde{\tau}) + 2C_{Y_{Nd}}(\tilde{\tau})C_{Y_{Ndr}}(\tilde{\tau}) \\
&+ |C_{Y_s}(0)|^2 + |C_{Y_{Nr}}(0)|^2 + |C_{Y_{Nd}}(0|^2 + |C_{Y_{Ndr}}(0)|^2 \\
&+ 2C_{Y_s}(0)C_{Y_{Nr}}(0) + 2C_{Y_s}(0)C_{Y_{Nd}}(0) + 2C_{Y_s}(0)C_{Y_{Ndr}}(0) \\
&+ 2C_{Y_{Nr}}(0)C_{Y_{Nd}}(0) + 2C_{Y_{Nr}}(0)C_{Y_{Ndr}}(0) + 2C_{Y_{Nd}}(0)C_{Y_{Ndr}}(0) \\
=&|C_{Y_s}(\tilde{\tau}) + C_{Y_{Nr}}(\tilde{\tau}) + C_{Y_{Nd}}(\tilde{\tau}) + C_{Y_{Ndr}}(\tilde{\tau})|^2 + |C_{Y_s}(0) + C_{Y_{Nr}}(0) + C_{Y_{Nd}}(0) + C_{Y_{Ndr}}(0)|^2,
\end{aligned}
\tag{E.4}
$$

where as in Appendix D:

$$
|C_Y(\tilde{\tau})|^2 = \big\langle Y(\tau)Y^*(\tau+\tilde{\tau})\big\rangle\big\langle Y(\tau+\tilde{\tau})Y^*(\tau)\big\rangle, \tag{E.5}
$$

$$
|C_Y(0)|^2 = \big\langle Y(\tau)Y^*(\tau)\big\rangle\big\langle Y(\tau+\tilde{\tau})Y^*(\tau+\tilde{\tau})\big\rangle, \tag{E.6}
$$

Appendix F

Derivation of CRLB for Circular Gaussian Random Processes

In this appendix the derivation of the CRLB for the case of Circular Gaussian random processes is detailed.

F.1 Derivation of CRLB

By means of the Cramer-Rao Bound (CRB), the minimum variance of an unbiased estimator can be evaluated. Then, the CRB is given by,

$$var(\tilde{\theta}) \geq \frac{1}{I(\theta)}, \tag{F.1}$$

where θ is the parameter to be estimated and $I(\theta)$ is the so-called Fisher Information Matrix, that can be expressed as,

$$I(\theta) = -E[\frac{\delta \ln(p(x;\theta)}{\partial \theta_i} \frac{\partial \ln(p(x;\theta)}{\partial \theta_j}], \tag{F.2}$$

Considering the case of Circular Gaussian random processes, where $\tilde{\boldsymbol{x}} \approx CN(\boldsymbol{\mu(\theta)})$, $\boldsymbol{C(\theta)}$, where $\tilde{x}$ is a complex random vector ($\tilde{x} = [\tilde{x}_1, \tilde{x}_2, \cdots, \tilde{N}]^T$) with $\tilde{x}_1 = u + jv$, mean $\tilde{\mu}(\theta) = E[u] + jE[v]$ and covariance matrix (as an Hermitian Matrix) $C^H(\theta) = C(\theta)$, the Circular Gaussian probability density function (pdf) can be written as:

$$p(\tilde{\boldsymbol{x}};\boldsymbol{\theta}) = \frac{1}{(\pi)^N |\boldsymbol{C(\theta)}|} \exp[-(\tilde{\boldsymbol{x}} - \tilde{\boldsymbol{\mu}}(\boldsymbol{\theta}))^H \boldsymbol{C}^{-1}(\boldsymbol{\theta})(\tilde{\boldsymbol{x}} - \tilde{\boldsymbol{\mu}}(\boldsymbol{\theta})], \tag{F.3}$$

and thus the first derivative of the natural logarithm of the PDF can be expressed as,

$$\frac{\partial \ln p(\tilde{\boldsymbol{x}}, \boldsymbol{\theta})}{\partial \boldsymbol{\theta}} = -\frac{\partial |\boldsymbol{C(\theta)}|}{\partial \boldsymbol{\theta}} - \frac{\partial (\tilde{\boldsymbol{x}} - \tilde{\boldsymbol{\mu}}(\boldsymbol{\theta}))^H \boldsymbol{C}^{-1}(\tilde{\boldsymbol{x}} - \tilde{\boldsymbol{\mu}}(\boldsymbol{\theta}))}{\partial \boldsymbol{\theta}} \tag{F.4}$$

where the first term of Eqn. F.4 becomes:

$$\frac{\partial|\boldsymbol{C}^{-1}(\boldsymbol{\theta})|}{\partial\boldsymbol{\theta}} = tr(\boldsymbol{C}^{-1}(\boldsymbol{\theta})\frac{\partial\boldsymbol{C}(\boldsymbol{\theta})}{\partial\boldsymbol{\theta}}), \tag{F.5}$$

and the second term of Eqn. (F.3) becomes:

$$\begin{aligned}\frac{\partial(\tilde{\boldsymbol{x}}-\tilde{\boldsymbol{\mu}}(\boldsymbol{\theta}))^H\boldsymbol{C}^{-1}(\tilde{\boldsymbol{x}}-\tilde{\boldsymbol{\mu}}(\boldsymbol{\theta}))}{\partial\boldsymbol{\theta}} =& -\frac{\partial\boldsymbol{\mu}^H(\boldsymbol{\theta})}{\partial\boldsymbol{\theta}}(\boldsymbol{C}^{-1}(\boldsymbol{\theta})(\tilde{\boldsymbol{x}}-\tilde{\boldsymbol{\mu}}(\boldsymbol{\theta}))\\ &+(\tilde{\boldsymbol{x}}-\tilde{\boldsymbol{\mu}}(\boldsymbol{\theta}))^H\frac{\partial(\boldsymbol{C}^{-1}(\boldsymbol{\theta})(\tilde{\boldsymbol{x}}-\tilde{\boldsymbol{\mu}}(\boldsymbol{\theta})))}{\partial\boldsymbol{\theta}},\end{aligned} \tag{F.6}$$

where:

$$\frac{\partial(\boldsymbol{C}^{-1}(\boldsymbol{\theta})(\tilde{\boldsymbol{x}}-\tilde{\boldsymbol{\mu}}(\boldsymbol{\theta})))}{\partial\boldsymbol{\theta}} = \frac{\partial\boldsymbol{C}^{-1}(\boldsymbol{\theta})}{\partial\boldsymbol{\theta}}(\tilde{\boldsymbol{x}}-\tilde{\boldsymbol{\mu}}(\boldsymbol{\theta})) - \boldsymbol{C}^{-1}(\theta)\frac{\partial\tilde{\boldsymbol{\mu}}(\boldsymbol{\theta})}{\partial\boldsymbol{\theta}}, \tag{F.7}$$

thus Equ.(F.6) becomes:

$$\begin{aligned}\frac{\partial(\tilde{\boldsymbol{x}}-\tilde{\boldsymbol{\mu}}(\boldsymbol{\theta}))^H\boldsymbol{C}^{-1}(\tilde{\boldsymbol{x}}-\tilde{\boldsymbol{\mu}}(\boldsymbol{\theta}))}{\partial\boldsymbol{\theta}} =& -\frac{\partial\boldsymbol{\mu}^H(\boldsymbol{\theta})}{\partial\boldsymbol{\theta}}(\boldsymbol{C}^{-1}(\boldsymbol{\theta})(\tilde{\boldsymbol{x}}-\tilde{\boldsymbol{\mu}}(\boldsymbol{\theta}))\\ &+(\tilde{\boldsymbol{x}}-\tilde{\boldsymbol{\mu}}(\boldsymbol{\theta}))(\frac{\partial\boldsymbol{C}^{-1}(\boldsymbol{\theta})}{\partial\boldsymbol{\theta}}(\tilde{\boldsymbol{x}}-\tilde{\boldsymbol{\mu}}(\boldsymbol{\theta})) - \boldsymbol{C}^{-1}(\theta)\frac{\partial\tilde{\boldsymbol{\mu}}(\boldsymbol{\theta})}{\partial\boldsymbol{\theta}}),\end{aligned} \tag{F.8}$$

substituting Eqn. (F.5) and Equ.(F.8) on Eqn. (F.4), is obtained that:

$$\begin{aligned}\frac{\partial\ln p(\tilde{\boldsymbol{x}},\boldsymbol{\theta})}{\partial\boldsymbol{\theta}} =& -tr(\boldsymbol{C}^{-1}(\boldsymbol{\theta})\frac{\partial\boldsymbol{C}(\boldsymbol{\theta})}{\partial\boldsymbol{\theta}})\\ &+\frac{\partial\boldsymbol{\mu}^H(\boldsymbol{\theta})}{\partial\boldsymbol{\theta}}(\boldsymbol{C}^{-1}(\boldsymbol{\theta})(\tilde{\boldsymbol{x}}-\tilde{\boldsymbol{\mu}}(\boldsymbol{\theta}))\\ &-(\tilde{\boldsymbol{x}}-\tilde{\boldsymbol{\mu}}(\boldsymbol{\theta}))(\frac{\partial\boldsymbol{C}^{-1}(\boldsymbol{\theta})}{\partial\boldsymbol{\theta}}(\tilde{\boldsymbol{x}}-\tilde{\boldsymbol{\mu}}(\boldsymbol{\theta})) - \boldsymbol{C}^{-1}(\theta)\frac{\partial\tilde{\boldsymbol{\mu}}(\boldsymbol{\theta})}{\partial\boldsymbol{\theta}}),\end{aligned} \tag{F.9}$$

where:

$$\frac{\partial\boldsymbol{C}(\boldsymbol{\theta})}{\partial\boldsymbol{\theta}}\boldsymbol{C}^{-1}(\boldsymbol{\theta}) = -\boldsymbol{C}(\boldsymbol{\theta})\frac{\partial\boldsymbol{C}^{-1}(\boldsymbol{\theta})}{\partial\boldsymbol{\theta}} \rightarrow \frac{\partial\boldsymbol{C}^{-1}(\boldsymbol{\theta})}{\partial\boldsymbol{\theta}} = -\boldsymbol{C}^{-1}(\boldsymbol{\theta})\frac{\partial\boldsymbol{C}(\boldsymbol{\theta})}{\partial\boldsymbol{\theta}}\boldsymbol{C}^{-1}(\boldsymbol{\theta}), \tag{F.10}$$

thus Eqn. (F.9) becomes:

$$\begin{aligned}\frac{\partial\ln p(\tilde{\boldsymbol{x}},\boldsymbol{\theta})}{\partial\boldsymbol{\theta}} =& -tr(\boldsymbol{C}^{-1}(\boldsymbol{\theta})\frac{\partial\boldsymbol{C}(\boldsymbol{\theta})}{\partial\boldsymbol{\theta}})\\ &+\frac{\partial\boldsymbol{\mu}^H(\boldsymbol{\theta})}{\partial\boldsymbol{\theta}}(\boldsymbol{C}^{-1}(\boldsymbol{\theta})(\tilde{\boldsymbol{x}}-\tilde{\boldsymbol{\mu}}(\boldsymbol{\theta}))\\ &+(\tilde{\boldsymbol{x}}-\boldsymbol{\mu}(\boldsymbol{\theta}))^H\boldsymbol{C}^{-1}(\boldsymbol{\theta})\frac{\partial\boldsymbol{C}(\boldsymbol{\theta})}{\partial\boldsymbol{\theta}}\boldsymbol{C}^{-1}(\boldsymbol{\theta})(\tilde{\boldsymbol{x}}-\boldsymbol{\mu}(\boldsymbol{\theta}))\\ &+(\tilde{\boldsymbol{x}}-\boldsymbol{\mu}(\boldsymbol{\theta}))^H\boldsymbol{C}^{-1}(\boldsymbol{\theta})\frac{\partial\tilde{\boldsymbol{\mu}}(\boldsymbol{\theta})}{\partial\boldsymbol{\theta}}.\end{aligned} \tag{F.11}$$

Substituting Eqn. (F.11) in Eqn. (F.2),

$$
\begin{aligned}
I(\boldsymbol{\theta}) =& tr(\boldsymbol{C}^{-1}(\boldsymbol{\theta})\frac{\partial \boldsymbol{C}(\boldsymbol{\theta})}{\partial \boldsymbol{\theta}_i})tr(\boldsymbol{C}^{-1}(\boldsymbol{\theta})\frac{\partial \boldsymbol{C}(\boldsymbol{\theta})}{\partial \boldsymbol{\theta}_j}) \\
&- tr(\boldsymbol{C}^{-1}(\boldsymbol{\theta})\frac{\partial \boldsymbol{C}(\boldsymbol{\theta})}{\partial \boldsymbol{\theta}_i})E|\frac{\partial \boldsymbol{\mu}^H(\boldsymbol{\theta})}{\partial \boldsymbol{\theta}_j}(\boldsymbol{C}^{-1}(\boldsymbol{\theta})(\tilde{\boldsymbol{x}} - \tilde{\boldsymbol{\mu}}(\boldsymbol{\theta})))| \\
&- tr(\boldsymbol{C}^{-1}(\boldsymbol{\theta})\frac{\partial \boldsymbol{C}(\boldsymbol{\theta})}{\partial \boldsymbol{\theta}_i})E|(\tilde{\boldsymbol{x}} - \tilde{\boldsymbol{\mu}}(\boldsymbol{\theta}))^H\boldsymbol{C}^{-1}(\boldsymbol{\theta})\frac{\partial \boldsymbol{C}(\boldsymbol{\theta})}{\partial \boldsymbol{\theta}_j}\boldsymbol{C}^{-1}(\boldsymbol{\theta})(\tilde{\boldsymbol{x}} - \tilde{\boldsymbol{\mu}}(\boldsymbol{\theta}))| \\
&- tr(\boldsymbol{C}^{-1}(\boldsymbol{\theta})\frac{\partial \boldsymbol{C}(\boldsymbol{\theta})}{\partial \boldsymbol{\theta}_i})E|(\tilde{\boldsymbol{x}} - \tilde{\boldsymbol{\mu}}(\boldsymbol{\theta}))^H\boldsymbol{C}^{-1}(\boldsymbol{\theta})\frac{\partial \tilde{\boldsymbol{\mu}}(\boldsymbol{\theta})}{\partial \boldsymbol{\theta}_j}| \\
&- E|\frac{\partial \boldsymbol{\mu}^H(\boldsymbol{\theta})}{\partial \boldsymbol{\theta}_i}(\boldsymbol{C}^{-1}(\boldsymbol{\theta})(\tilde{\boldsymbol{x}} - \tilde{\boldsymbol{\mu}}(\boldsymbol{\theta})))|tr(\boldsymbol{C}^{-1}(\boldsymbol{\theta})\frac{\partial \boldsymbol{C}(\boldsymbol{\theta})}{\partial \boldsymbol{\theta}_j}) \\
&+ E|\frac{\partial \boldsymbol{\mu}^H(\boldsymbol{\theta})}{\partial \boldsymbol{\theta}_i}(\boldsymbol{C}^{-1}(\boldsymbol{\theta})(\tilde{\boldsymbol{x}} - \tilde{\boldsymbol{\mu}}(\boldsymbol{\theta})))\frac{\partial \boldsymbol{\mu}^H(\boldsymbol{\theta})}{\partial \boldsymbol{\theta}_j}(\boldsymbol{C}^{-1}(\boldsymbol{\theta})(\tilde{\boldsymbol{x}} - \tilde{\boldsymbol{\mu}}(\boldsymbol{\theta})))| \\
&+ E|\frac{\partial \boldsymbol{\mu}^H(\boldsymbol{\theta})}{\partial \boldsymbol{\theta}_i}(\boldsymbol{C}^{-1}(\boldsymbol{\theta})(\tilde{\boldsymbol{x}} - \tilde{\boldsymbol{\mu}}(\boldsymbol{\theta})))(\tilde{\boldsymbol{x}} - \tilde{\boldsymbol{\mu}}(\boldsymbol{\theta}))^H\boldsymbol{C}^{-1}(\boldsymbol{\theta})\frac{\partial \boldsymbol{C}(\boldsymbol{\theta})}{\partial \boldsymbol{\theta}_j}\boldsymbol{C}^{-1}(\boldsymbol{\theta})(\tilde{\boldsymbol{x}} - \tilde{\boldsymbol{\mu}}(\boldsymbol{\theta}))| \\
&+ E|\frac{\partial \boldsymbol{\mu}^H(\boldsymbol{\theta})}{\partial \boldsymbol{\theta}_i}(\boldsymbol{C}^{-1}(\boldsymbol{\theta})(\tilde{\boldsymbol{x}} - \tilde{\boldsymbol{\mu}}(\boldsymbol{\theta})))(\tilde{\boldsymbol{x}} - \boldsymbol{\mu}(\boldsymbol{\theta}))^H\boldsymbol{C}^{-1}(\boldsymbol{\theta})\frac{\partial \tilde{\boldsymbol{\mu}}(\boldsymbol{\theta})}{\partial \boldsymbol{\theta_j}}| \\
&- E|(\tilde{\boldsymbol{x}} - \tilde{\boldsymbol{\mu}}(\boldsymbol{\theta}))^H\boldsymbol{C}^{-1}(\boldsymbol{\theta})\frac{\partial \boldsymbol{C}(\boldsymbol{\theta})}{\partial \boldsymbol{\theta}_i}\boldsymbol{C}^{-1}(\boldsymbol{\theta})(\tilde{\boldsymbol{x}} - \tilde{\boldsymbol{\mu}}(\boldsymbol{\theta}))|tr(\boldsymbol{C}^{-1}(\boldsymbol{\theta})\frac{\partial \boldsymbol{C}(\boldsymbol{\theta})}{\partial \boldsymbol{\theta}_j}) \\
&+ E|(\tilde{\boldsymbol{x}} - \tilde{\boldsymbol{\mu}}(\boldsymbol{\theta}))^H\boldsymbol{C}^{-1}(\boldsymbol{\theta})\frac{\partial \boldsymbol{C}(\boldsymbol{\theta})}{\partial \boldsymbol{\theta}_i}\boldsymbol{C}^{-1}(\boldsymbol{\theta})(\tilde{\boldsymbol{x}} - \tilde{\boldsymbol{\mu}}(\boldsymbol{\theta}))\frac{\partial \boldsymbol{\mu}^H(\boldsymbol{\theta})}{\partial \boldsymbol{\theta}_j}(\boldsymbol{C}^{-1}(\boldsymbol{\theta})(\tilde{\boldsymbol{x}} - \tilde{\boldsymbol{\mu}}(\boldsymbol{\theta})))| \\
&+ E|(\tilde{\boldsymbol{x}} - \tilde{\boldsymbol{\mu}}(\boldsymbol{\theta}))^H\boldsymbol{C}^{-1}(\boldsymbol{\theta})\frac{\partial \boldsymbol{C}(\boldsymbol{\theta})}{\partial \boldsymbol{\theta}_i}\boldsymbol{C}^{-1}(\boldsymbol{\theta})(\tilde{\boldsymbol{x}} - \tilde{\boldsymbol{\mu}}(\boldsymbol{\theta})) \\
&\cdot (\tilde{\boldsymbol{x}} - \tilde{\boldsymbol{\mu}}(\boldsymbol{\theta}))^H\boldsymbol{C}^{-1}(\boldsymbol{\theta})\frac{\partial \boldsymbol{C}(\boldsymbol{\theta})}{\partial \boldsymbol{\theta}_j}\boldsymbol{C}^{-1}(\boldsymbol{\theta})(\tilde{\boldsymbol{x}} - \tilde{\boldsymbol{\mu}}(\boldsymbol{\theta}))| \\
&+ E|(\tilde{\boldsymbol{x}} - \tilde{\boldsymbol{\mu}}(\boldsymbol{\theta}))^H\boldsymbol{C}^{-1}(\boldsymbol{\theta})\frac{\partial \boldsymbol{C}(\boldsymbol{\theta})}{\partial \boldsymbol{\theta}_i}\boldsymbol{C}^{-1}(\boldsymbol{\theta})(\tilde{\boldsymbol{x}} - \tilde{\boldsymbol{\mu}}(\boldsymbol{\theta}))(\tilde{\boldsymbol{x}} - \tilde{\boldsymbol{\mu}}(\boldsymbol{\theta}))^H\boldsymbol{C}^{-1}(\boldsymbol{\theta})\frac{\partial \tilde{\boldsymbol{\mu}}(\boldsymbol{\theta})}{\partial \boldsymbol{\theta}_j}| \\
&- E|(\tilde{\boldsymbol{x}} - \tilde{\boldsymbol{\mu}}(\boldsymbol{\theta}))^H\boldsymbol{C}^{-1}(\boldsymbol{\theta})\frac{\partial \tilde{\boldsymbol{\mu}}(\boldsymbol{\theta})}{\partial \boldsymbol{\theta}_j}|tr(\boldsymbol{C}^{-1}(\boldsymbol{\theta})\frac{\partial \boldsymbol{C}(\boldsymbol{\theta})}{\partial \boldsymbol{\theta}_i}) \\
&+ E|(\tilde{\boldsymbol{x}} - \tilde{\boldsymbol{\mu}}(\boldsymbol{\theta}))^H\boldsymbol{C}^{-1}(\boldsymbol{\theta})\frac{\partial \tilde{\boldsymbol{\mu}}(\boldsymbol{\theta})}{\partial \boldsymbol{\theta}_j}\frac{\partial \boldsymbol{\mu}^H(\boldsymbol{\theta})}{\partial \boldsymbol{\theta}_j}(\boldsymbol{C}^{-1}(\boldsymbol{\theta})(\tilde{\boldsymbol{x}} - \tilde{\boldsymbol{\mu}}(\boldsymbol{\theta})))| \\
&+ E|(\tilde{\boldsymbol{x}} - \tilde{\boldsymbol{\mu}}(\boldsymbol{\theta}))^H\boldsymbol{C}^{-1}(\boldsymbol{\theta})\frac{\partial \tilde{\boldsymbol{\mu}}(\boldsymbol{\theta})}{\partial \boldsymbol{\theta}_j}\boldsymbol{C}^{-1}(\boldsymbol{\theta})\frac{\partial \boldsymbol{C}(\boldsymbol{\theta})}{\partial \boldsymbol{\theta}_j}\boldsymbol{C}^{-1}(\boldsymbol{\theta})(\tilde{\boldsymbol{x}} - \tilde{\boldsymbol{\mu}}(\boldsymbol{\theta}))| \\
&+ E|(\tilde{\boldsymbol{x}} - \tilde{\boldsymbol{\mu}}(\boldsymbol{\theta}))^H\boldsymbol{C}^{-1}(\boldsymbol{\theta})\frac{\partial \tilde{\boldsymbol{\mu}}(\boldsymbol{\theta})}{\partial \boldsymbol{\theta}_j}(\tilde{\boldsymbol{x}} - \tilde{\boldsymbol{\mu}}(\boldsymbol{\theta}))^H\boldsymbol{C}^{-1}(\boldsymbol{\theta})\frac{\partial \tilde{\boldsymbol{\mu}}(\boldsymbol{\theta})}{\partial \boldsymbol{\theta}_j}|. \qquad \text{(F.12)}
\end{aligned}
$$

Considering that:

$$
(\tilde{\boldsymbol{x}} - \tilde{\boldsymbol{\mu}}(\boldsymbol{\theta}))^H\boldsymbol{C}^{-1}(\boldsymbol{\theta})\frac{\partial \boldsymbol{C}(\boldsymbol{\theta})}{\partial \boldsymbol{\theta}}\boldsymbol{C}^{-1}(\boldsymbol{\theta})(\tilde{\boldsymbol{x}} - \tilde{\boldsymbol{\mu}}(\boldsymbol{\theta})) = tr(\boldsymbol{C}^{-1}(\boldsymbol{\theta})\frac{\partial \boldsymbol{C}(\boldsymbol{\theta})}{\partial \boldsymbol{\theta}}) \qquad \text{(F.13)}
$$

and that all first- and third- order moments of $\tilde{\boldsymbol{y}} = \tilde{\boldsymbol{x}} - \tilde{\boldsymbol{\mu}(\boldsymbol{\theta})}$, are zero, including all second order moments of the form $E(\tilde{\boldsymbol{y}}\tilde{\boldsymbol{y}}^T)$, Eqn. (F.12) becomes:

$$\begin{aligned} I(\boldsymbol{\theta}) =& 2E[\frac{\partial \boldsymbol{\mu}^H(\boldsymbol{\theta})}{\partial \boldsymbol{\theta}_i}\boldsymbol{C}^{-1}(\boldsymbol{\theta})\frac{\partial \boldsymbol{\mu}(\boldsymbol{\theta})}{\partial \boldsymbol{\theta}_j}] - tr(\boldsymbol{C}^{-1}(\boldsymbol{\theta})\frac{\partial \boldsymbol{C}(\boldsymbol{\theta})}{\partial \boldsymbol{\theta}_i})tr(\boldsymbol{C}^{-1}(\boldsymbol{\theta})\frac{\partial \boldsymbol{C}(\boldsymbol{\theta})}{\partial \boldsymbol{\theta}_j}) \\ &+ E|\boldsymbol{y}^H\boldsymbol{C}^{-1}(\boldsymbol{\theta})\frac{\partial \boldsymbol{C}(\boldsymbol{\theta})}{\partial \boldsymbol{\theta}_i}\boldsymbol{C}^{-1}(\boldsymbol{\theta})\boldsymbol{y}\boldsymbol{y}^H\boldsymbol{C}^{-1}(\boldsymbol{\theta})\frac{\partial \boldsymbol{C}(\boldsymbol{\theta})}{\partial \boldsymbol{\theta}_j}\boldsymbol{C}^{-1}(\boldsymbol{\theta})\boldsymbol{y}], \end{aligned} \tag{F.14}$$

considering the following lemma,

$$E(\tilde{\boldsymbol{x}}^H\boldsymbol{A}\tilde{\boldsymbol{x}}\tilde{\boldsymbol{x}}^H\boldsymbol{B}\tilde{\boldsymbol{x}}) = tr(\boldsymbol{AC})tr(\boldsymbol{BC}) + tr(\boldsymbol{ACBC}), \tag{F.15}$$

Eqn. (F.14) becomes,

$$\begin{aligned} I(\boldsymbol{\theta}) =& - tr(\boldsymbol{C}^{-1}(\boldsymbol{\theta})\frac{\partial \boldsymbol{C}(\boldsymbol{\theta})}{\partial \boldsymbol{\theta}_i})tr(\boldsymbol{C}^{-1}(\boldsymbol{\theta})\frac{\partial \boldsymbol{C}(\boldsymbol{\theta})}{\partial \boldsymbol{\theta}_j}) \\ &+ tr(\boldsymbol{C}^{-1}(\boldsymbol{\theta})\frac{\partial \boldsymbol{C}(\boldsymbol{\theta})}{\partial \boldsymbol{\theta}_i}\boldsymbol{C}^{-1}(\boldsymbol{\theta})\boldsymbol{C}(\boldsymbol{\theta}))tr(\boldsymbol{C}^{-1}(\boldsymbol{\theta})\frac{\partial \boldsymbol{C}(\boldsymbol{\theta})}{\partial \boldsymbol{\theta}_j}\boldsymbol{C}^{-1}(\boldsymbol{\theta})\boldsymbol{C}(\boldsymbol{\theta})) \\ &+ tr(\boldsymbol{C}^{-1}(\boldsymbol{\theta})\frac{\partial \boldsymbol{C}(\boldsymbol{\theta})}{\partial \boldsymbol{\theta}_i}\boldsymbol{C}^{-1}(\boldsymbol{\theta})\boldsymbol{C}(\boldsymbol{\theta})\boldsymbol{C}^{-1}(\boldsymbol{\theta})\frac{\partial \boldsymbol{C}(\boldsymbol{\theta})}{\partial \boldsymbol{\theta}_j}\boldsymbol{C}^{-1}(\boldsymbol{\theta})\boldsymbol{C}(\boldsymbol{\theta})) \\ &+ 2E[\frac{\partial \boldsymbol{\mu}^H(\boldsymbol{\theta})}{\partial \boldsymbol{\theta}_i}\boldsymbol{C}^{-1}(\boldsymbol{\theta})\frac{\partial \boldsymbol{\mu}(\boldsymbol{\theta})}{\partial \boldsymbol{\theta}_j}] \\ =& - tr(\boldsymbol{C}^{-1}(\boldsymbol{\theta})\frac{\partial \boldsymbol{C}(\boldsymbol{\theta})}{\partial \boldsymbol{\theta}_i})tr(\boldsymbol{C}^{-1}(\boldsymbol{\theta})\frac{\partial \boldsymbol{C}(\boldsymbol{\theta})}{\partial \boldsymbol{\theta}_j}) + tr(\boldsymbol{C}^{-1}(\boldsymbol{\theta})\frac{\partial \boldsymbol{C}(\boldsymbol{\theta})}{\partial \boldsymbol{\theta}_i}tr(\boldsymbol{C}^{-1}(\boldsymbol{\theta})\frac{\partial \boldsymbol{C}(\boldsymbol{\theta})}{\partial \boldsymbol{\theta}_j}) \\ &+ tr(\boldsymbol{C}^{-1}(\boldsymbol{\theta})\frac{\partial \boldsymbol{C}(\boldsymbol{\theta})}{\partial \boldsymbol{\theta}_i}\boldsymbol{C}^{-1}(\boldsymbol{\theta})\frac{\partial \boldsymbol{C}(\boldsymbol{\theta})}{\partial \boldsymbol{\theta}_j}) + 2E[\frac{\partial \boldsymbol{\mu}^H(\boldsymbol{\theta})}{\partial \boldsymbol{\theta}_i}\boldsymbol{C}^{-1}(\boldsymbol{\theta})\frac{\partial \boldsymbol{\mu}(\boldsymbol{\theta})}{\partial \boldsymbol{\theta}_j}] \\ =& + tr(\boldsymbol{C}^{-1}(\boldsymbol{\theta})\frac{\partial \boldsymbol{C}(\boldsymbol{\theta})}{\partial \boldsymbol{\theta}_i}\boldsymbol{C}^{-1}(\boldsymbol{\theta})\frac{\partial \boldsymbol{C}(\boldsymbol{\theta})}{\partial \boldsymbol{\theta}_j}) + 2E[\frac{\partial \boldsymbol{\mu}^H(\boldsymbol{\theta})}{\partial \boldsymbol{\theta}_i}\boldsymbol{C}^{-1}(\boldsymbol{\theta})\frac{\partial \boldsymbol{\mu}(\boldsymbol{\theta})}{\partial \boldsymbol{\theta}_j}]. \end{aligned} \tag{F.16}$$

Bibliography

[1] V. Rosmorduc, J. Benveniste, O. Lauret, M. Milagro, and N. Picot, "Radar Altimetry Tutorial," 2006.

[2] C.J. Koblinsky, P. Gaspar and G. Lagerloef, "The future of spaceborne altimetry: Oceans and climate change," *Joint oceanographic institutions incorporated*, Washington, D.C., pp. 75, 1992.

[3] P.Y. Le Traon and G. Dibarboure, "Velocity mapping capabilities of present and future altimeter missions: the role of high frequency signals," *Journal of Atmospheric and Oceanic Technology*, vol. 19, pp. 2077-2088, 2002.

[4] M. Martin-Neira, C. Mavrocordatos, and E. Colzi, "Study of a constellation of bistatic radar altimeters for mesoscale ocean applications," *IEEE. Transactions on Geosciences and Remote Sensing.*, vol. 36, no. 6, pp. 1898-1904, Nov. 1998.

[5] C. Hall, and R. Cordy, "Multistatic Scaterrometry," *Proceedings of the IEEE International Geoscience and Remote Sensing Symposium*, Edinburgh, Scotland, 1988.

[6] M. Martin-Neira, "A passive reflectometry and interferometry system(Paris): Application to ocean altimetry." *ESA J.*, vol.17, pp.331-335, 1993.

[7] S. Lowe, C. Zuffada, Y. Chao, P. Kroger, L. Young and J. LaBrecque. "5-cm precision aircraft ocean altimetry using GPS reflections," *Geophysical Research Letters*. vol. 29, no. 10, 2002.

[8] G. Ruffini et al, "The Eddy Experiment: Accurate GNSS-R Ocean Altimetry from Low Altitude Aircraft," *Geophysical and Research Letters*, Vol.31, L12306, 18 June 2004.

[9] J.L. Garrison, A. Komjathy, "Wind speed measurement from bistatically scattered GPS signals," *IEEE Transactions on Geosciences and Remote Sensing*, vol.37, pp.100-110, 1999.

[10] J.L. Garrison, A. Komjathy, V.U. Zavorotny, S.J. Katzberg, "Wind Speed Measurement from Forward Scattered GPS Signals," *IEEE Transactions on Geoscience and Remote Sensing*, vol. 40, no.1, pp.50-65, 2002.

[11] V.U. Zavorotny, A. G. Voronovich, "Scattering of GPS Signals from the Ocean with Wind Remote Sensing Application," *IEEE Transactions on Geosciences and Remote Sensing*, vol.38, no.2, pp.951-964, 2000.

[12] A. Komjathy, M. Armatys, DZD. Masters, P. Axelrad, V.U. Zavorotny, S. Katzberg, "Retrieval of Ocean Surface Wind Speed and Wind Direction Using Reflected GPS Signals," *Journal of Atmospheric and Oceanic Technology*, vol. 21, no. 3, pp-515?526, 2004.

[13] N. Rodriguez-Alvarez, X. Bosch-Lluis, A. Camps, M. Vall-llossera, E. Valencia,J. F. Marchan-Hernandez, I. Ramos-Perez, "Soil Moisture Retrieval Using GNSS-R Techniques: Experimental Results over a Bare Soil Field," *IEEE Transactions on Geoscience and Remote Sensing*, vol. 47, no. 11, pp. 3616-3624, Nov 2009.

[14] D. Masters, "Surface Remote Sensing Applications of GNSS Bistatic Radar: Soil Moisture and Aircraft Atimetry," PhD dissertation, University of Colorado, 2004.

[15] A. Komjathy, J.A. Maslanik, V.U. Zavorotny, P. Axelrad, S.J. Katzberg, "Sea Ice Remote Sensing Using Surface Reflected GPS Signals," *Proceedings of the IEEE international Geosciences and Remote Sensing Symposium (IGARSS 2010)*, Honolulu, Hawaii, 24-28 July, pp. 2855-2857, 2010.

[16] F. Fabra, E. Cardellach, O. Nogues-Correig, S. Oliveras, S. Ribo, A. Rius, M. Belmonte, M. Semmling, C. Macelloni, S. Pettinato, R. Zasso, and S. D'Addio, S, "Monitoring sea ice and dry snow with GNSS reflections," *Proceedings of the IEEE international Geosciences and Remote Sensing Symposium (IGARSS 2010)*, Honolulu, Hawaii, 24-28 July, pp. 3837-2840, 2010.

[17] J. Wickert, G. Beyerle, E. Cardellach, C. Frste, T. Gruber, A. Helm, M.P. Hess, P. Hoeg, N. Jakowski, O. Montenbruck, A. Rius, M. Rothacher, C.K. Shum, "GNSS REflectometry, Radio Occultation and Scatterometry onboard ISS for long-term monitoring of climate observations using innovative space geodetic techniques on-board the International Space Statio n." Proposal in response to Call: ESA Research Announcement for ISS Experiments relevant to study of Global Climate Change(2011).

[18] S. Gleason, "Remote Sensing of Ocean, Ice and Land Surfaces UsingBistatically Scattered GNSS Signals From Low Earth Orbit," Ph.D.Thesis, University of Surrey, 2006.

[19] S. Gleason, S. Hodgart, Y. Sun, C. Gommenginger, S. Mackin, M. Adjrad, and M. Unwin, "Detection and processing of bistatically re?ected GPS signals from low earth orbit for the purpose of ocean remote sensing," *IEEE Transactions on Geosciences and Remote Sensing.*, vol. 43, no. 6, pp. 1229?1241, Jun. 2005.

[20] B. Parkinson, and J. Spilker, "Global Positioning System: Theory and Applications I/II/III." Progress in Astronautics and Aeronautics, 163 (1996).

[21] GPS Navstar interface control documents, available at: http://www.navcen.uscg.gov/gps/ geninfo/, accessed in May 2007.

[22] F. Soulat, "Sea Surface Remote Sensing with GNSS and Sunlights Reflections," Ph.D.Thesis, Universitat Politecnica de Catalunya, 2003.

[23] ARINC, NAVSTAR GPS Space Segment/Navigation User Interfaces, IS-GPS-200D, ARINC Research Corporation, Fountain Valley, CA, December 7, 2004.

[24] E.D. Kaplan, and C.J. Hegarty, (2006). "Understanding GPS Principles and Applications." Artech House, Noorword MA, 2006.

[25] E. Stefan, S. Tholert, and J. Furthner. "L5-The New GPS Signal." German Aerospace Center (DLR) Institute of Communications and Navigation.

[26] ESA (2013). "Galileo Navigation (Next steps)." http://www.esa.int/Our Activities/Navigation/The future Galileo/Next steps.

[27] R. Gold, "Optimal Binary Sequences for Spread Spectrum Multiplexing," *IEEE Trans. on Information Theory*, vol. 33, no. 3, 1967.

[28] China Satellite Navigation Office, (2013). "BeiDou Navigation Satellite System Signal In Space Interface Control Document." Open Service Signal (Version 2.0).

[29] P. Beckmann, and A. Spizzichino, (1987). "The Scattering of Electromagnetic Waves from Rough Surfaces." Artech House.

[30] R. Rice. "Reflection of electromagnetic waves from slightly rough surfaces." *Communications on Pure and Applied Mathematics*, vol. 4 , pp. 351-378, 1951.

[31] G. R. Valenzuela, "Theories for the interaction of electromagnetic and oceanic waves. A review," *Bound.-Layer Meteorol.*, vol. 31, pp. 61-85, 1978.

[32] F. G. Bass and I. M. Fuks, "Wave Scattering from Statistically Rough Surfaces," C. B. Vesecky and J. F. Vesecky, Eds. Oxford, U.K.: Pergamon, 1979, vol. 93.

[33] F. E. Nathanson, "Radar Design Principles." *New York: McGraw-Hill*, 1969.

[34] J. Betz, "Design and Perfomance of Code Tracking for the GPS M Code Signal," The MITRE Corporation Technical Report. New York: McGraw-Hill, 1969

[35] Alenia, "Final report for the constellation of pulse limited nadir looking radar altimeters," IAB/FR/ALS/001, ESTEC Contract 9370/91, 1992.

[36] M. Martn-Neira, S. D´Addio, C. Buck, N. Floury, "The PARIS Ocean Altimeter In-Orbit Demonstrator," *IEEE Transactions on Geoscience and Remote Sensing*, vol. 49, no. 6, pp. 2209-2237, June 2011.

[37] S. D´Addio, M. Martin-Neira, "Comparison of processing techniques for remote sensing of earth-exploiting reflected radio-navigation signals," *Electronics Letters*, vol. 49, no. 4, Feb 2013.

[38] A. Rius, E. Cardellach, and M. Martin-Neira, "Altimetric Analysis of the Sea-Surface GPS-Reflected Signals," *IEEE Transactions on Geoscience and Remote Sensing*, vol. 48, no. 4, pp. 2119?2127, 2010.

[39] F. Martin, A. Camps, H. Park, S. DAddio, M. Martin-Neira, D. Pascual, and H. Park, "Cross- Correlation Waveform Analysis for a conventional and interferometric GNSS-R approaches," *Journal of Selected Topics in Applied Earth Observations and Remote Sensing*, vol. 7, no. 5, pp. 1560-1572, May 2014.

[40] S. J. Katzberg, O. Torres, and G. Ganoe, "Calibration of reflected GPS for tropical storm wind speed retrievals," *Geophys. Res. Lett.*, vol. 33, 2006.

[41] J. F. Marchan. "Stochastic Model for Ocean Surface Reflected GPS Signals and Satellite Remote Sensing Applications." PhD dissertation, Universitat Politectènica de Catalunya, Barcelona, (2009).

[42] R.Treuhaft, S. Lowe, C. Zuffada, and Y. Chao, "2-cm GPS altimetry over Crater Lake," *Geophysical Research Letters.*, vol. 22, no. 23, p. 4343-4346, December 2001.

[43] J. Park, J. T. Johnson, and S. T. Lowe, "A study of the electromagnetic bias in GNSS-R altimetry," *Proceedings of the IEEE international Geosciences and Remote Sensing Symposium (IGARSS 2014)*, Quebec, Canada, July 2014.

[44] A. Ghavidel, D. Schiavulli, A. Camps, " A numerical simulator to evaluate the electromagnetic bias in GNSS-R altimetry ," *Proceedings of the IEEE international Geosciences and Remote Sensing Symposium (IGARSS 2014)*, Quebec, Canada, July 2014.

[45] E. Cardellach, "Sea Surface determination using GNSS−reflected signals," PhD Dissertation, Universitat Politectènica de Catalunya, Barcelona, (2001).

[46] F. T. Ulaby, R. K. Moore, and A. K. Fung, "Microwave Remote Sensing, Active and Passive." Reading, MA: Addison-Wesley, 1982

[47] S. Lowe, J.L LaBrecque, C. Zuffada, L.J. Romans, L.E. Young, G.A. Hajj, "G.A. First spaceborne observation of an earth-reflected GPS signal." *Radio Sci.* 37 (1), doi: 10.1029/2000RS002539, 2002.

[48] A. Papoulis, and S. U. Pillai, "Probability, random variables, and stochastic processes," McGraw-Hill, 2002.

[49] M.J. Unwin, S. Gleason and M. Brennan. "The Space GPS Reflectometry Experiment on the UK Disaster Monitoring Constellation Satellite." *Proc. ION 2003.* Portland, Oregon. September 2002.

[50] H. You, J.L. Garrison, G. Heckler, D. Smajlovic, "The Autocorrelation of Waveforms Generated From Ocean-Scattered GPS Sigmals," *IEEE Transactions on Geoscience and Remote Sensing Letters*, vol. 3, no. 1, pp. 78-82, Jan 2006.

[51] A. Rius et al., "PARIS interferometric technique proof of concept: Sea Slope Measurements," *Proceedings of the IEEE international Geosciences and Remote Sensing Symposium (IGARSS 2012)*, Munich, Germany, July 2012.

[52] A. Camps, H. Park, E. Valencia, D. Pascual, F. Martin, A. Rius, S. Ribo , "Optimization and Performance Analysis of GNSS-R Altimeters," *Journal of Selected Topics in Applied Earth Observations and Remote Sensing*, vol.7, no.5, pp.1436-1451, May 2014.

[53] A. Camps, D. Pascual, H. Park, F. Martin, A. Rius, S. Ribo , J. Benito, A. Andres, P. Saameno, G. Staton, M. Martin-Neira, S. D'Addio, P. Willemsen, "Altimetry Performance and Error Budget of the PARIS In-Orbit Demonstration Mission," *Proceedings of the IEEE international Geosciences and Remote Sensing Symposium (IGARSS 2013)*, Melbourne, Australia, July 2013.

[54] C. Zuffada and V. U. Zavorotny, "Coherence time and statistical properties of the GPS signal scattered off the ocean surface and their impact on the accuracy of remote sensing of sea surface topography and winds," *Proceedings of the IEEE international Geosciences and Remote Sensing Symposium (IGARSS 2001)*, Sydney, Australia, July 2001.

[55] You, et al, "Stochastic Voltage Model and Experimental Measurement of Ocean-Scattered GPS Signal Statistics," *IEEE Transactions on Geoscience and Remote Sensing*, vol. 42, no. 10, pp. 2160-2169, Oct. 2004.

[56] J. Garrison, "Modeling and simulating of bin-bin correlations in GNSS-R waveforms," *Proceedings of the IEEE international Geosciences and Remote Sensing Symposium (IGARSS 2012)*, Munich, Germany, July, 2012.

[57] S.M. Kay, "Fundamentals of Statistical Signal Processing: Estimation Theory," Prentice Hall, Upper Saddle River, NJ 07458, 1993.

[58] O. Germain and G. Rufini, "A revisit to the GNSS-R code range precision," *in Proc. GNSS-R Workshop*, Jun. 14?15, 2006.

[59] F. Fabra, W. Li, M. Martin-Neira, A. Rius, and Y. Dongkai, "TIGRIS Experiment: Characterizating a Typhoon with GNSS-Reflectometry," *URSI Commision F. Microwave Signature*,2013, Espoo, Finland, 28-31.

[60] J. W. Goodman, "Statistical Optics." Wiley Classics Library, 2000.

[61] C. S. Ruf, S. Gleason, Z. Jelenak, S. Katzberg, A. Ridley, R. Rose, J. Scherrer and V. U. Zavorotny, "The CYGNSS nanosatellite constellation hurricane mission," *Proceedings of the IEEE international Geosciences and Remote Sensing Symposium (IGARSS 2012)*, Munich, Germany, July 2012.

[62] J.F. Marchan-Hernandez, A. Camps, N. Rodriguez-Alvarez, E. Valencia, X. Bosch-Lluis, I. Ramos-Perez, "A New Efficient Algorithm to the Simulation of Delay-Doppler Maps of Reflected Global Navigation Satellite System Signals," *IEEE Transactions on Geoscience and Remote Sensing* , 2009.

[63] G. A. Hajj, C. Zuffada "Theoretical description of a bistatic system for ocean altimetry using the GPS signal," *Radio Science* , 2003, 38(5):10-19.

[64] E. Rodriguez "Altimetry for non-Gaussian oceans: Height biases and estimation parameters," *J. Geophys. Res.* , 93(C11), 14, 107-14,120,1988.

[65] O. Nogues, E. Cardellach, J. Sanz, A. Rius, "AGPS-Reflections Receiver That Computes Doppler/Delay Maps in Real Time," *IEEE Transactions on Geoscience and Remote Sensing* ., 45(1):156-174, January 2007.

[66] F. Martin, S. D'Addio, A. Camps, M.Martin-Neira, H.Park, D.Pascual, "Comparison of GNSS-R processing techniques for spaceborne ocaen altimetry,"*Proceedings of the IEEE international Geosciences and Remote Sensing Symposium (IGARSS 2013)*, Melbourne, Australia, July 2013.

[67] E. Cardellach, A. Rius, M. Martn-Neira, F. Fabra, O. Nogues-Correig, S. Rib, J. Kainulainen, A. Camps, and S. D'Addio, "Consolidating the Precision of Interferometric GNSS-R Ocean Altimetry using Airborne Experimental Data," *IEEE Transactions on Geoscience and Remote Sensing.*, 10.1109/TGRS.2013.2286257, 2013.

[68] M.J. Unwin, S. Gleason and M. Brennan, "The Space GPS Reflectometry Experiment on the UK Disaster Monitoring Constellation Satellite," *Proc. ION 2003,*. Portland, Oregon. September 2002.

[69] A. Camps, F. Martin, H. Park, E. Valencia, A. Rius, S. D'Addio, "Interferometric GNSS-R achievable altimetric performance and compression/denoising using the wavelet transform: An experimental study," *Proceedings of the IEEE international Geosciences and Remote Sensing Symposium (IGARSS 2013)*, Munich, Germany, July 2012.

[70] W. Li, D. Yang, S. D'Addio, M. Martin-Neira, "Partial Interferometric Processing of Reflected GNSS Signals for Ocean Altimetry," *IEEE Geoscience and Remote Sensing Letters*, vol. 11, no. 9, pp. 1509-1513, Sept 2014.